THE UNIVERSITY OF WARWICK

AUTHOR: **João Paulo da Silva Bento** DEGREE: **Ph.D.**

TITLE: **Research and development of ground-based transiting extrasolar planet projects**

DATE OF DEPOSIT: .....

I agree that this thesis shall be available in accordance with the regulations governing the University of Warwick theses.

I agree that the summary of this thesis may be submitted for publication.

I **agree** that the thesis may be photocopied (single copies for study purposes only).

Theses with no restriction on photocopying will also be made available to the British Library for microfilming. The British Library may supply copies to individuals or libraries. subject to a statement from them that the copy is supplied for non-publishing purposes. All copies supplied by the British Library will carry the following statement:

> "Attention is drawn to the fact that the copyright of this thesis rests with its author. This copy of the thesis has been supplied on the condition that anyone who consults it is understood to recognise that its copyright rests with its author and that no quotation from the thesis and no information derived from it may be published without the author's written consent."

AUTHOR'S SIGNATURE: .....

USER'S DECLARATION

1. I undertake not to quote or make use of any information from this thesis without making acknowledgement to the author.
2. I further undertake to allow no-one else to use this thesis while it is in my care.

DATE SIGNATURE ADDRESS

.....

.....

.....

.....

.....

Research and development of ground-based transiting extrasolar planet projects

by

João Paulo da Silva Bento

Thesis

Submitted to the University of Warwick

for the degree of

Doctor of Philosophy

Department of Physics

July 2012

THE UNIVERSITY OF WARWICK

Contents

List of Tables

List of Figures

Acknowledgments

I am profoundly grateful to Dr. Peter Wheatley for all his guidance, patience and support throughout my PhD. I would like to thank the University of Warwick Astronomy and Astrophysics Group for making me feel truly at home and Dr. Richard West for maintaining the SuperWASP archive and for being generally a constant source of invaluable help.

A huge thanks goes to a remarkable group of friends who have made the last three years the best of my life (so far). In particular, I would like to thank Simon, Jon, Steve, Lieke, Rachel and Dave for playing a massive part in that, being the best friends anyone could hope to have, and for allowing me to be myself without (too many) questions asked. I gratefully salute the Motorcade crew for all the wonderful times and for giving me the chance to fulfil a life-long dream. A special thanks goes out to Steel Panther, for providing the perfect soundtrack and for being simply awesome.

None of this work would have been possible, of course, without the constant love and support of my family. They have provided me with much needed help and a range of opportunities, for which I am eternally grateful. They have been the foundations of all my achievements and their unending belief and encouragement have inspired me in every aspect of my life.

Declarations

I declare that the work presented in this thesis is my own except where stated otherwise, and was carried out entirely at the University of Warwick, during the period October 2008 to May 2012, under the supervision of Dr. Peter Wheatley. The research reported here has not been submitted, either wholly or in part, in this or any other academic institution for admission to a higher degree.

Conference contributions based on this thesis are:

- National Astronomy Meeting, Glasgow, UK, April 2010, Poster presentation: *Finding smaller planets with SuperWASP.*
- SuperWASP consortium meeting, St. Andrews, UK, September 2010, Oral presentation: *SuperWASP detector map analysis.*
- Extreme Solar Systems II, Jackson Hole, Wyoming, US, September 2011, Poster presentation: *Transmission photometry of WASP-15b and WASP-17b.*

Abstract

The search for exoplanets has gone from the realm of speculation to being one of the most prolific topics of modern astronomy in the space of just 20 years. In particular, the geometric alignment of transiting exoplanets provides the added opportunity to measure a host of properties of these systems, including studies of planetary atmospheres.

The vast majority of known transiting exoplanets to date were found using dedicated ground-based surveys such as the SuperWASP project. Such enterprises comprise of multiple small telescopes designed to perform high-precision photometry over a wide field of view and rely on efficiently compensating for several noise contributions. An analysis of the sources of noise in the SuperWASP light curves was performed, focussing on systematic effects fixed in detector space. A study of a set of *detector maps* produced from the average of the fractional residuals of the light curves in CCD coordinates has revealed that the current flat-fielding strategy is introducing a component of red noise into the light curves due to the wavelength-dependent nature of the CCDs. The possibility of using such maps as a basis for an additional decorrelation step in the software pipeline is discussed.

The next phase in planetary discoveries from ground-based surveys consists of the search for smaller planets and those in longer orbits around their host stars. This process involves an observing strategy that focuses on intensive coverage of particular locations of the sky. We develop simulation software to aid the choice of observed fields for the SuperWASP and Next Generation Transit Survey (NGTS) projects in order to maximise the chances of finding planets at those locations. Moreover, this simulation can be used for comparative studies of the planet finding probability for several design choices and has been used to justify the necessity to commission the NGTS instrument at ESO's Paranal Observatory in order to benefit from one of the World's premier sites.

The increasing number of known transiting planets has triggered a new phase of exoplanet exploration, in which the properties of the atmospheres of these planets are being explored using techniques such as transmission spectroscopy. This process consists of measuring an enhanced transit depth at particular wavelengths due to the presence of opacity sources in the atmospheres of exoplanets. We use the multi-band photometer ULTRACAM to attempt a similar measurement via the technique of *transmission photometry* for the highly inflated planets WASP-15b and WASP-17b. The data are found to be dominated by systematic errors and a detailed study of the possible sources is performed.

Abbreviations

QE Quantum Efficiency

CCD Charged Coupled Devices

S/N Signal-to-noise

NaN Not a Number

ADU Analog/Digital Unit

FWHM Full Width Half Maximum

RMS Root Mean Squared

AU Astronomical Unit

PSF Point Spread Function

Alt/Az Altazimuth mount

FOV Field of view

M_J Jupiter Mass

R_J Jupiter Radius

RV Radial Velocity

NTT New Technology Telescope

WHT William Herschel Telescope

WASP Wide Angle Search for Planets

NGTS Next Generation Transit Survey

HST Hubble Space Telescope

ESO European Southern Observatory

ESA European Space Agency

NASA National Aeronautics and Space Administration

Chapter 1

Introduction

1.1 Exoplanets

The word exoplanet simply means extrasolar planet, which refers to any planet found outside of our Solar System. The existence of such bodies was part of the realm of speculation until 1992, when 3 terrestrial-mass planets were found orbiting the pulsar PSR B1257+12 [Wolszczan & Frail, 1992]. These planets cause a reflex motion on the orbit of the star which lead to the apparent change in the pulsar's rotational frequency as the pulses seem to arrive faster when the star is moving towards the observer and vice-versa. The first discovery of an exoplanet orbiting a main-sequence star came only three years after, when a Jupiter mass body was found to orbit the star 51 Peg [Mayor & Queloz, 1995]. In this case, variations of the radial velocity of the star with respect to the Sun were detected, and the presence of the planet inferred (see Section 1.2 for more details on this method). This discovery was the trigger for a change in the mindset of the astronomical community, where the study of exoplanets is now a major field of scientific research. Many of the planets known today fall under the category of *hot Jupiters*, which are Jupiter mass planets orbiting very close to their parent stars, typically at separations under 0.1AU. The definition is loose and several authors have defined a sub-set of these as *very hot Jupiters* if the orbital period is under 3 days [Beatty & Gaudi, 2008] or the separation is under 0.025AU [Ragozzine & Wolf, 2009]. However, a whole host of smaller examples are being found on a regular basis[1], with $\approx 33\%$ of known planets having masses lower than that of Saturn. The dominance of hot Jupiters comes from the observational bias of current instruments. Massive planets close to their host stars are typically much easier to find than small bodies at large

[1]Information based on exoplanet.eu

separations.

The numbers of known planets, within 20 years of the discovery of the first sub-stellar body outside our Solar System, have risen to close to a thousand. We are entering a new age of exoplanet exploration, where such numbers allow us to perform reliable and meaningful statistics, such as those performed recently by Mayor et al. [2011] or by Wolfgang & Laughlin [2011]. The time has also come to further study the properties of these bodies in more detail. Section 1.5.4 contains an introduction to a potential example of such studies. Throughout this thesis, and indeed in the field of exoplanets in general, the naming convention for any planet outside the Solar System consists of adding a lower case letter to the host star's denomination for each planet, starting with *b*, in order of discovery. For example, if the star is named *WASP-1*, the first planet to be discovered orbiting it will be named *WASP-1b*, the second *WASP-1c* and so on.

1.2 Detection methods

Finding exoplanets is challenging due to the very high contrast between the reflected light from the planet and the stellar emission and the relatively small separation between both. It is therefore extremely hard to image these objects directly, and often astronomers rely on measuring the impact of the planet on its host star. Figure 1.1 shows a plot of the mass as a function of the orbital separation for all confirmed planets discovered by December 2011 (courtesy of Keith Horne). This Figure shows that the majority of planets have been found by radial velocity measurements (named *Doppler* in the Figure), but transiting planets also have contributed considerably to the numbers of known planets. Moreover, direct imaging is responsible for the vast majority of planets at large orbital separations, whereas the microlensing technique yields results with planet masses as low as a few Earth masses, but restricted to a relatively small range of orbital separations. These observational biases are addressed in more detail as each method is explored.

The following Sections describe the most commonly used detection methods of exoplanets to date. Transiting planets are described in more detail in Section 1.3.

1.2.1 Direct Imaging

Despite the high contrast between the flux of the host star and that of the planet, it is possible to image some of these objects directly. This is typically achieved by detecting the thermal emission of the planet at infrared wavelengths, combined with techniques that reduce the stellar contribution, such as angular differ-

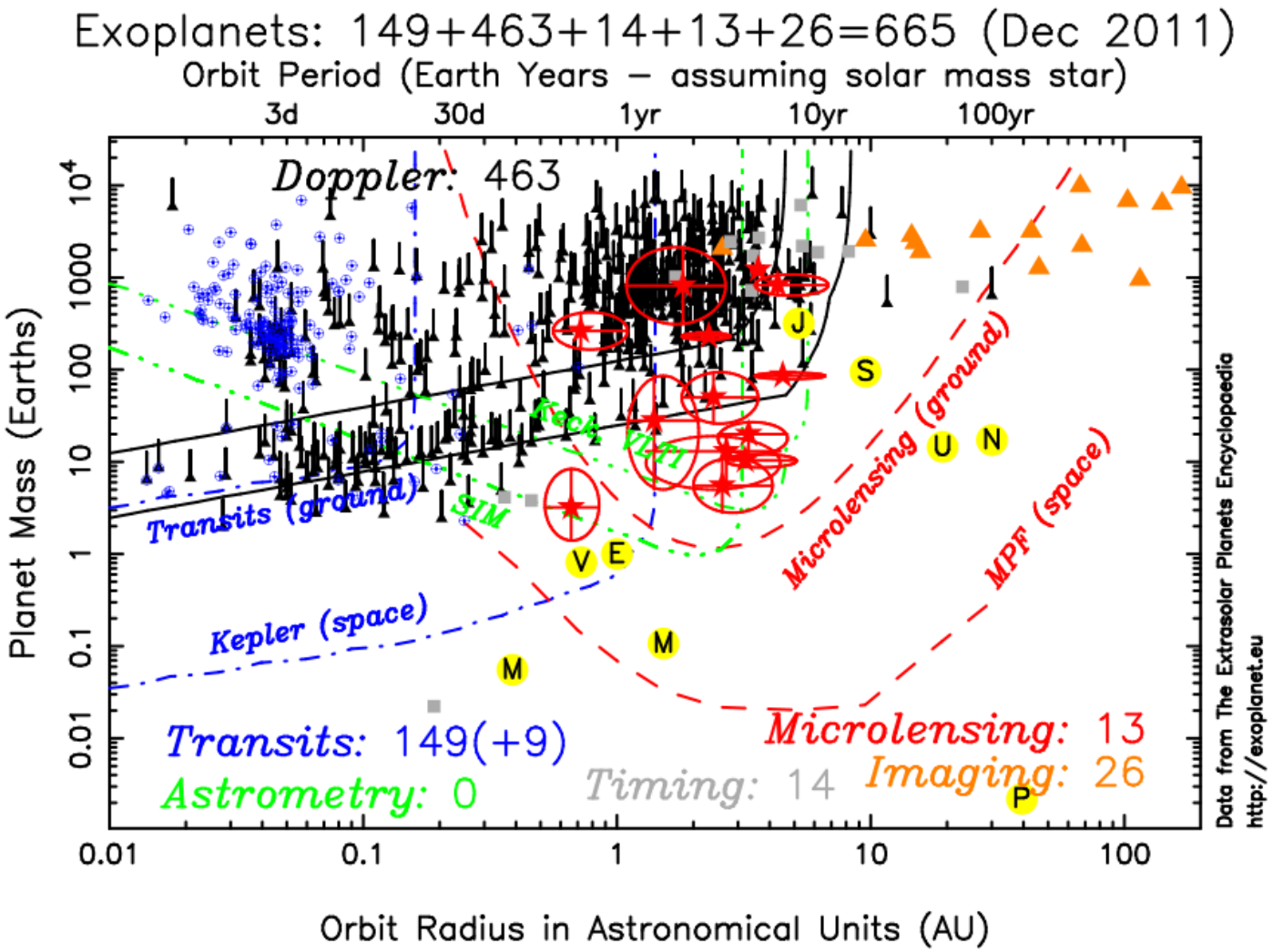

Figure 1.1: Exoplanet detections by all successful methods. This plot shows the mass as a function of orbital separation for all confirmed planets as of 11th December 2011. Different symbols represent the different detection methods, and the Solar System planets have been included (yellow circles with initials) for comparison. Lines indicating the sensitivity regions of each method in this parameter space. Courtesy of Keith Horne.

ential imaging coupled with adaptive optics [Marois et al., 2008]. There is therefore a bias towards young massive planets, since these still have temperatures higher than the equilibrium temperature due to stellar irradiation, thereby exhibiting high thermal emission. This technique is also more sensitive to planets on long orbits (separations of 8-200 AU), as the large separation will help with the limited resolution of the current telescopes. This is evident in Figure 1.1, since the planets detected by direct imaging dominate the higher orbital separation region on the plot. The large periods of these systems and the associated difficulty in directly observing the planet moving around the star on feasible time-scales makes it harder to distinguish these planetary companions from background objects at short angular separations from the target star. This is done by ensuring that the two objects form a common proper-motion pair [Seager, 2010b, Part II].

In the first of these discoveries it was possible to image a 5 M_J planet directly [Chauvin et al., 2004] with the use of adaptive optics. 2M1207 is a nearby young brown dwarf, located at approximately 70 pc from the Sun, and its companion orbits at around 55AU from the host star. Therefore, the combined inherent faintness of the host star, proximity, age and large separation between the two bodies has made this discovery possible. Figure 1.2a contains the obtained image for this system.

Other examples of direct imaging of planets include the case of Fomalhaut b, which was thought to exist prior to its discovery as the cause for the structure in the dust belt around its host star in 2005 [Kalas et al., 2005] and later directly imaged by Kalas et al. [2008] using a rectangular-mask coronagraph and angular differential imaging. This particular case has shown movement along its orbit at two occasions, which are depicted in Figure 1.2b. Fomalhaut b orbits the star at 115 AU and has an upper mass of 3 M_J . Doubts about the existence of the planet have been raised recently, and further observations are required to confirm these suspicions. Another interesting case is that of the HR 8799 system, located 39.4 pc from the Sun, which exhibits 4 planets. Figure 1.2c shows the discovery image of the first 3 [Marois et al., 2008], with projected separations of 24, 38 and 68 AU. The fourth planet was recently discovered [Marois et al., 2010] and Janson et al. [2010] announced spatially-resolved spectroscopy of HR 8799c using VLT-NACO at 4μm. This example shows that direct imaging is a powerful tool for understanding planet formation, since it is capable of detecting young planets on wide orbits. The focus of direct imaging observations is, however, still restricted to those cases where the chances of success are maximised. Burrows et al. [2004] have shown that young stars, with young, massive, warm and therefore self-luminous planets are more likely to be imaged. Also, the chances of detecting reflected light are increased for nearby stars

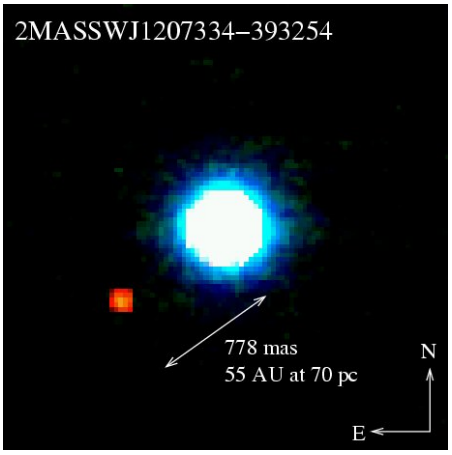

(a) Image of 2M1207b

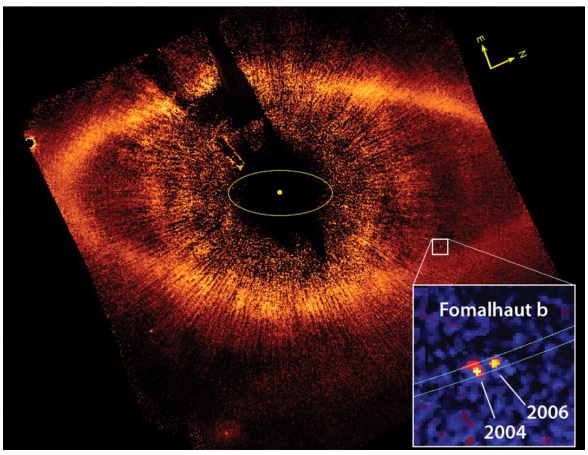

(b) Image of Fomahault b

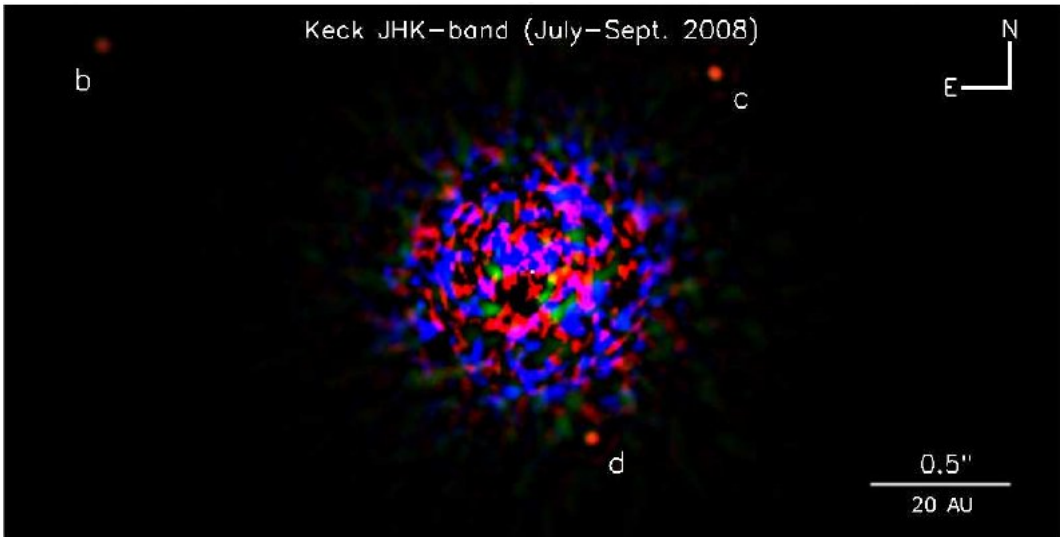

(c) Image of the HR8799 system

Figure 1.2: Top left panel: Image of the 2M1207b planet using the deep VLT/NACO infrared imager. From Chauvin et al. [2004] Top right panel: Image of Fomahault b using Coronagraphic observations with the HST. From Kalas et al. [2008]. Bottom panel: Image of the HR8799 system, obtained using high contrast images with the Keck and Gemini telescopes. From Marois et al. [2008]

($d < 5pc$). Hence, there is an observational bias towards imaging known planets, young stellar systems and nearby stars.

1.2.2 Reflex motion of the star

This subsection describes a series of methods that rely on the fact that a planet and its host star both orbit a common centre of mass. The relative position of any star with respect to an observer on Earth is mostly dictated by its motion within the galaxy, the orbit of the Solar System in the galaxy and the orbital speed of the Earth around the Sun. It is often the case that the orbits of stars in the galaxy are defined with respect to the Local Standard of Rest (LSR). This, in turn, is defined as the rotational velocity for a circular orbit in the galactic plane. The motion of the stars in the galaxy is, however, distinctly non-Keplerian due to the nonspherical mass distribution within the galaxy. Nevertheless, they are often stable and the Earth's orbit can be accounted for easily in the context of a heliocentric correction. Therefore, if any periodic perturbations to the motion of another star are detected it is possible to infer the presence of additional bodies in the system.

Astrometry

This technique consists of measuring the relative positions of a particular star and look for variations with respect to other objects in the sky. Specifically, it relies on a measurement of the second-order perturbation (wobble) of the position of the star with respect to background sources, only noticeable after other larger components, such as proper motion and parallax, have been accounted for. This method is therefore optimised for nearby stars and limited by the resolution of the telescopes used. The motion of a star orbiting the centre of mass of a star-planet system as an eclipse with angular semi-major axis α is given by

$$\alpha = \left(\frac{M_p}{M_*}\right)\left(\frac{a}{1AU}\right)\left(\frac{d}{1pc}\right)^{-1} arcsec, \tag{1.1}$$

assuming the mass of the planet M_p is much smaller than the mass of the star M_* [Perryman, 2011]. In this equation, d is the distance to the system and a is the semi-major axis of the orbit (assumed circular).

This technique has not yielded any planets due to both the inherent difficulty of detecting such changes in position, but also because it is not ideally suited for large surveys. An example of the expected astrometric signatures of known planets is shown in Figure 1.3. This Figure shows the *astrometric signature* α as a function of the period, and circles are proportional to M_p or $M_p \sin i$. It is clear that the majority

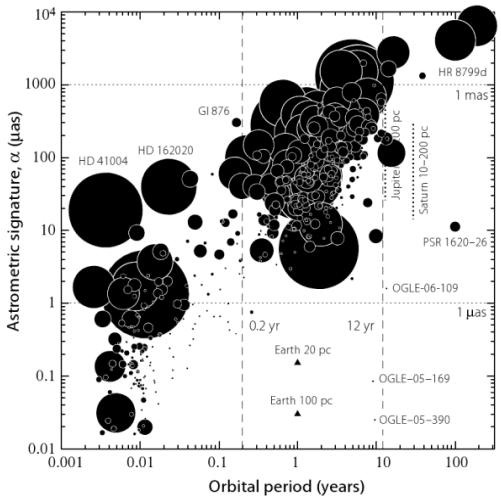

Figure 1.3: Astrometric signature, α, as a function of period calculated for known planetary systems using equation 1.1. The sizes of the circles correspond to M_p or $M_p \sin i$, depending on whether the degeneracy has been solved using several detection methods. Horizontal lines show the 1mas and 1μas levels. For comparison, the signatures of Solar System planets at relevant distances is also depicted. From Perryman [2011].

of known planets are expected to yield a signature of under 1mas in amplitude. An astrometric measurement was made with HST by Benedict et al. [2002] of previously known planet Gliese 876b and, despite the fact that a non-negligible number of false positives have been suggested in the past, the upcoming ESA mission GAIA [Perryman et al., 2001; Lindegren, 2009], launching in 2013, is expected to add a large number of planets to this list. Initial estimates of up to 30,000 planets discovered were made at the planning stages [e.g. Perryman et al., 2001; Quist, 2001], but more recent evaluations point towards around 2500 planets with semi-major axes of a = 3 − 4AU out to 200pc, assuming GAIA will reach a precision of 12μarcsec on single measurements [Casertano et al., 2008]. This is, however, highly dependent on the real achieved precision. This mission is designed to map out the galaxy in 3D over the space of 5 years, making accurate measurements of stellar positions and proper motions, which will reveal the presence of bodies disturbing the paths of stars as they orbit the centre of the galaxy.

Radial Velocity

Unlike the astrometry case, planets with orbital inclinations closer to 90 degrees will show variations in their radial velocity, defined as the velocity with which

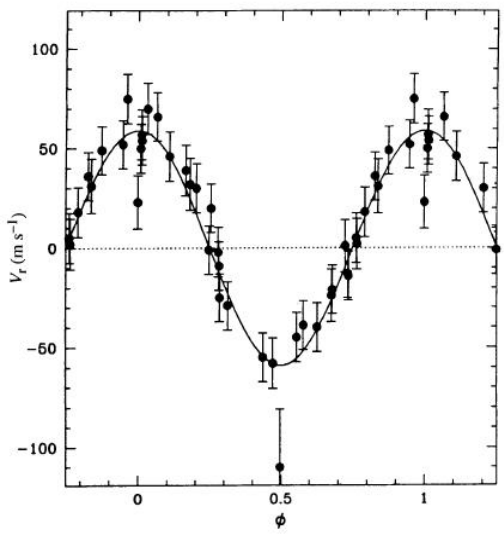

Figure 1.4: Radial velocity variations for the star 51 Peg due to the presence of a Jupiter mass planet orbiting it. From Mayor & Queloz [1995]

the star moves towards or away from an observer on Earth. Spectroscopic observations of systems with exoplanets can reveal this perturbation from Doppler shifts of the spectral lines in the form of periodic sinusoidal variations in the radial velocity. This technique is by far the most successful at finding exoplanets, and is often used to confirm candidates found by other methods. Indeed, the first ever planet discovered orbiting a main sequence star, 51 Peg b, was found via this procedure [Mayor & Queloz, 1995]. Figure 1.4 contains the radial velocity curve of this planet, in which variations of 60ms^{-1} are found to take place. This is a gas giant planet on a short 4.23 d period around its host star, an unexpected discovery since planet formation close to a star is not likely to take place [e.g. Bodenheimer et al., 2000; Ida & Lin, 2004]. This marked the start of a substantial acceleration in exoplanet research and modelling of planetary systems. Current models that explain the existence of hot jupiters tend towards a migratory evolution, where the planet is formed in the outer part of the system and migrates inwards [e.g. Michael et al., 2011].

The advantage of this method is that it allows the direct measurement of system parameters simply from the radial velocity curve. The shape of the curve can provide a measurement of the orbital eccentricity e of the planet and the argument of the pericentre ω. Figure 1.5 shows the phase-folded radial velocity curve and best Keplerian orbital solution of planet HD156846b observed with the CORALIE spectrograph [Tamuz et al., 2008]. This 359.5 day period planet is a clear example of

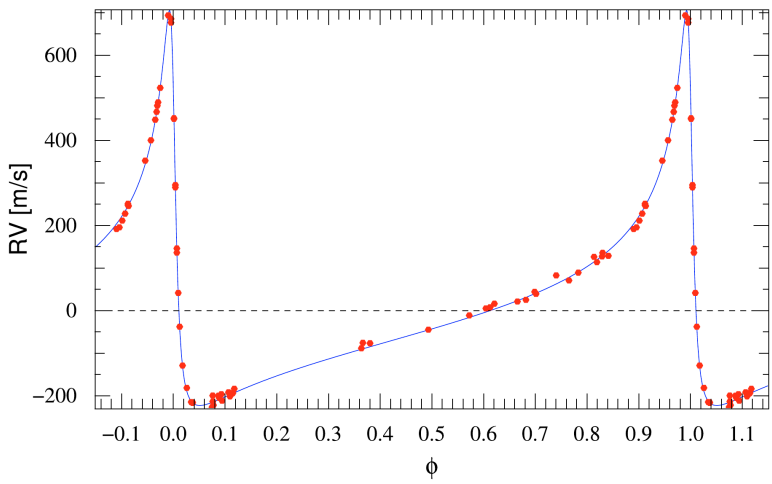

Figure 1.5: Radial velocity variations for the star HD156846 due to the presence of a Jupiter mass planet orbiting it. From Tamuz et al. [2008]

a highly eccentric exoplanet with measured parameters of $e \simeq 0.85$ and $\omega \simeq 52.23°$. A simple comparison with the radial velocity signature of 51 Peg b shown in Figure 1.4, which exhibits no measurable eccentricity, shows a clear contrast in the shapes of the curves due to the disparate eccentricities of the orbits of the planets.

The semi-amplitude of the radial velocity measurements equate to $M_p \sin i$ [Seager, 2010b], where i is the inclination of the system, defined as the angle of the orbital plane with respect to the line-of-sight of the system. Therefore, only a lower limit to the mass of the planet can be achieved with this method alone, but a combination of measurements with other methods can solve this degeneracy (see Section 1.3). This restriction is represented in Figure 1.1 by the shape of the markers for the radial velocity detections. They show the lower limit and a vertical range indicating that the planet mass is undefined. This method is also capable of detecting multiple planetary systems using dynamical fitting, since the gravitational interactions between several planets modifies the total radial velocity of the star [e.g. Laughlin & Chambers, 2001]. Various studies have been performed on the detectability using this method, which are dependent on the orbital period and signal amplitude [e.g. Cumming, 2004; Narayan et al., 2005]. Cumming [2004] offers analytic expressions for the detectability which is simply characterised as the semi-amplitude K of the oscillations if the duration of the observations T is larger than the orbital period P. However, for long period planets, the radial velocity signals are *sine-like* at the maximum and minimum stages and *cosine-like* at the zero crossings, and therefore the velocity variations are as given by

$$\Delta\nu = K \sin\left(\frac{2\pi T}{P}\right) \quad \text{or} \quad \Delta\nu = K \cos\left(\frac{2\pi T}{P}\right). \tag{1.2}$$

Naturally, this technique is more sensitive to high mass planets close to their parent stars. However, modern spectrographs are capable of achieving a precision of 1.5ms^{-1} because they have no moving parts and are vacuum sealed for ultimate stability [Pepe et al., 2000]. The High Accuracy Radial Velocity Planet Searcher (HARPS) instrument [Mayor et al., 2003], used primarily on the ESO's 3.6m telescope in La Silla, is an échelle spectrograph operating in the $378 - 691$nm range responsible for the discovery of a large number of planets, including 9 planets around M-dwarf stars showing that it is indeed possible to form planets around lower mass stars. However, stellar features, such as spots, pulsations and activity are becoming the ultimate limitation to the radial velocity method. It is now becoming necessary to obtain long baseline radial velocity measurements before the stellar activity is understood and any planetary signal becomes evident. Moreover, asteroseismology information of planet host stars is providing more accurate masses and ages, which can only be achieved through longer base line observations of both radial velocity and photometry [e.g. Borsa & Poretti, 2012; Gilliland et al., 2011].

Asteroseismology refers to the study of the internal structure of stars via the interpretation of the frequency of detected oscillations. For an early review on the matter, refer to Brown & Gilliland [1994]. Stars naturally exhibit radial pulsations due to hydrostatic equilibrium and to the fact that some layers are able to trap energy during the contraction of a star and release it during the expansion. The smallest frequency oscillation of this type is inversely proportional to the square root of the mean density of the star, thereby providing an accurate measurement of the bulk stellar structure. When combined with the stellar temperature easily determined from a single spectrum, the mass and radius can be determined without the need for stellar models. However, if transverse motions occur, non-radial pulsations take place, which can be caused by several phenomena. These include pressure modes, which are essentially acoustic waves that rely on pressure as the restoring force, and gravity modes, which are sustained due to buoyancy and density gradients across the various layers of the star. More importantly, gravity modes tend to penetrate deeper into the star, and hence an analysis and decomposition of all the pulsations of stars provides information regarding the density profile of such objects [Aerts et al., 2010]. This technique is particularly useful for stars in instability strips on the Hertzsprung-Russel diagram, in which radial velocity measurements for the purpose of planet detection are often contaminated by the signals from pulsations.

1.2.3 Gravitational Microlensing

Microlensing events occur when the light from a distant object (source) is observed as a foreground object (lens) passes close or in front of it. The gravitational field of the lensing object bends the light path from the distant source acting as a lens, thereby focussing its light. During this process, the lens star splits the source into two images with distorted shapes that follow curved trajectories around the lens star. These 2 images have separations of the order of the *Einstein radius*, which is the characteristic projected angle of gravitational lensing in general [Einstein, 1936], and are typically unresolved (1mas). Nevertheless, the total area of these 2 images is larger than the area of the source, causing it to appear brighter. Figure 1.6a shows the projected view of this event, where two images of a source (S) are produced by the gravitational field of a lens star (L). The dashed line shows the Einstein ring, with Einstein radius R_e. The presence of an additional body with projected separation close to the paths of these images in the lensing system acts as an extra lensing factor for a short period [Seager, 2010b]. The first suggestion that microlensing events could be used to detect planets was done by Paczynski [1991] and surveys of the galactic bulge such as the OGLE project [Szymański et al., 2000] have detected 15 of these examples[2].

In the case where the lens star contains another body orbiting it with projected separation a, the second lens introduces an extra lensing effect, similar to a perturbation on the original lens, providing extra magnification at those times when the object is aligned with either image of the background source. The duration of this extra magnification event depends upon the mass ratio of the two elements in the binary system, $q = M_p/M_*$. The larger the mass of the companion, the longer the event, and Earth-mass planets can have typical time scales of 3-5h [Perryman, 2011]. The projected orbital separation can be scaled with the Einstein radius as $d = a/R_e$, which is a crucial parameter in understanding the shape of the microlensing light curve. In optics, the envelope of reflected or refracted light by a curved surface is denominated as *critical lines*, and the point in the source plane where this envelope originates is called the *caustic*. In the case of the binary lens system, the companion to the lens star (in this case, a planet) causes a perturbation of the critical lines, generating one extra large diamond-shaped caustic if $d > 1$ and two small triangular-shaped caustics close together on the opposite side of the lens if $d < 1$ [Wambsganss, 1997]. As the source moves across the lens system, it will come close to these caustics and lensing events will occurs for each. The large caustic $d > 1$

[2] exoplanet.eu

configuration is more sensitive to planets, since the chance of the source crossing this region is greater, and the magnification is also larger.

Figure 1.6b shows the light curve of a planetary microlensing event [Bond et al., 2004]. In a typical case the light of the source star is enhanced for a period of time as the lensing object crosses the path of the light. However, the presence of a planet is inferred from the short peaks in the early part of the light curve when the additional body causes a further magnification to occur. The large magnification implies a $d > 1$ configuration, and indeed the best fit gives $d = 1.120$.

Note that the flux of the source star is increased by a factor of 8 at its maximum (without considering the perturbation of the planet), and that the duration of the event spanned 60 days. Microlensing events are now often observed by several different instruments around the globe, since such occurrences can be identified in the early stages and follow-up can be triggered immediately.

The remarkable advantage of this technique is that the magnification is higher for planets outside the Einstein radius than those at close separations from their host star. Hence microlensing is more sensitive to planets in long orbits, but a confirmation of these is extremely hard, especially since microlensing events are unique and not repeatable. Nevertheless, lensing events due to Earth-like planets have typical time scales of hours, and longer for larger values of q (Jupiter-like planets), making this a prime technique for probing planets at large separations, irrespective of their mass, that are not easy to image directly. This is a region of parameter space where most other methods are not sensitive.

1.3 Transiting exoplanets

For any multiple body system there is a chance that the orbital inclination is close to 90°and that periodically the two bodies will appear to cross in front of each other. This is the case for transiting planets, which are the main focus of this thesis. If the projected disk of the planet is large enough, a significant portion of the stellar light is blocked during transit and a characteristic dip in the luminosity can be detected. This effect is small, with the typical transit depths around 1% or 0.01mag for Jupiter-sized planets orbiting a Solar-like star. Naturally, planets with radii similar to the Earth exhibit shallower eclipses with depths under 1×10^{-4}, but depths up to 7% can occur around M dwarfs and more for planets orbiting white dwarfs [e.g. Faedi et al., 2011].

In the years that followed the first discovery of the planet orbiting 51Peg by Mayor & Queloz [1995], photometric observations were taken to look for transits

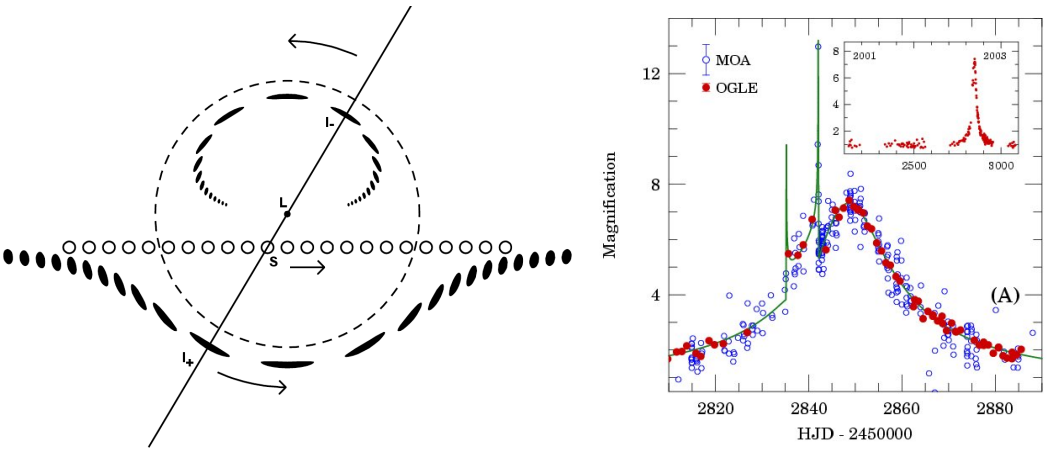

(a) Microlensing event projected view

(b) Light curve of microlensing event

Figure 1.6: Left panel: Schematic view of the projected view of a microlensing event. This is plotted in the lens' rest frame, so the background source (S) moves behind the system, and the images I_- and I_+ produced by the gravitational field of the lens star (L) are shown. The two images remain colinear along the line visible. The dashed line represents the Einstein ring. Modified From Paczynski [1996]. Right panel: Microlensing event light curve of OGLE 2003-BLG-235. The inset Figure shows the data for this target spanning the 2001-2003 period. From Bond et al. [2004]

of known exoplanets discovered by radial velocity observations. The first result of such efforts was the detection of the planetary transit of HD209458b. Henry et al. [2000] and Charbonneau et al. [2000] independently detected the characteristic dip of this event, the latter one presenting two transits spanning 2.5 hours at a depth of $\approx 1.5\%$ separated by 3.5 days, a period consistent with the radial velocity measurements taken previously. Figure 1.7 shows the published light curve with the best fit. This is a $0.714\mathrm{M_J}$ planet that orbits its host star at a separation of 0.046AU [Southworth, 2009] and is one of the most important exoplanets found to date due to the high brightness of the host star and proximity to the system. It orbits a $V = 7.65$ magnitude star at a distance of $47pc$. The close-by nature of this system is particularly useful since the distance can be measured through parallax and therefore a more precise measurement of the intrinsic brightness is possible. This, combined with the high brightness of the target and the relatively deep transit make it a perfect case for detailed studies. Thus, it is not surprising that this planet has the largest number of associated scientific publications of any known exoplanet.

Other bright known planets from radial velocity measurements have been

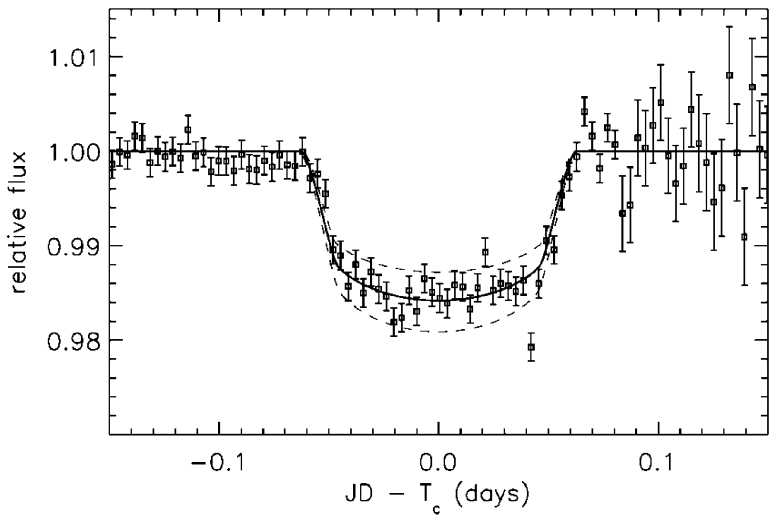

Figure 1.7: Transit light curve of the first ever detected transiting exoplanet, HD209458b. It shows the relative flux of the host star as a function of time, with the best fit. From Charbonneau et al. [2000]

found to transit through photometric follow-up at predicted times based on the radial velocity curves [e.g. Kane, 2007; Kane et al., 2009]. However, the vast majority of discoveries of currently known transiting exoplanets come from dedicated wide-field surveys scanning the entire sky in search for the tale-tell signs of eclipses (see Section 1.4). Ground-based searches such as the HATNet project [Bakos et al., 2002] and the SuperWASP project [Pollacco et al., 2006] use small aperture wide-field telescopes to systematically survey the whole sky in search of transits. These instruments can detect transit depths of $\approx 1\%$, making them sensitive to hot Jupiters on short orbits around bright stars. This explains the clear bias towards short period high-mass planets found via the transit method in Figure 1.1, which is very useful in terms of follow-up studies.

Transit light curves

Figure 1.8 shows schematic views of what occurs during a planetary transit. As the planet crosses in front of the disk of the star, some of the light is blocked and therefore a decrease in flux is observed. Furthermore, careful analysis of the light curves of such events can yield direct measurements of the system parameters. The model presented by Seager & Mallén-Ornelas [2003] describes the shape of a transiting light curve under the assumption that the orbital eccentricity is null and that multiple transits have been observed. There are four principle observables that

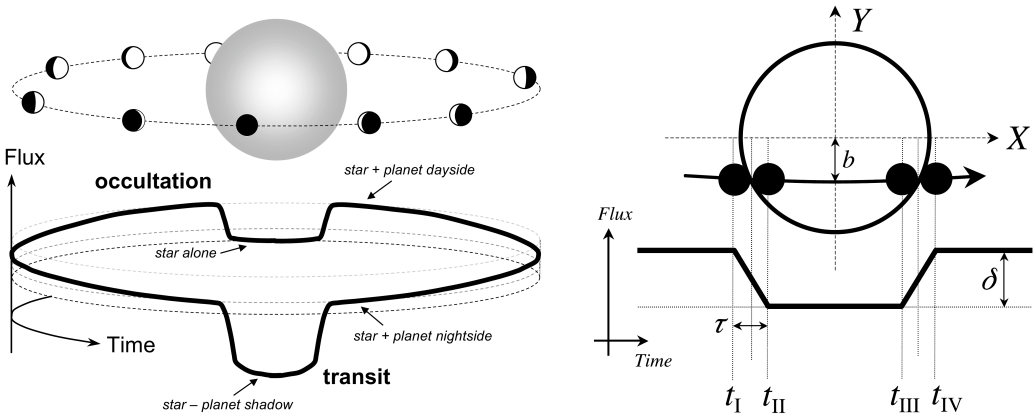

(a) Schematic of the orbit of a transiting planet

(b) Schematic of a planetary transit

Figure 1.8: Left panel: Schematic view of the orbit of a transiting planet. This Figure shows the illustration of the primary (transit) and secondary (occultation) eclipses with some emphasis on the visible phases of the planet. The effect of the difference between the day and night sides of the planet is negligible in most cases. Right panel: Schematic projected view of a planetary transit, indicating the important points of contact (t_I, t_{II}, t_{III} and t_{IV}) and the impact parameter b, as well as the transit depth δ. From Seager [2010b]

characterise the light curve: the period P; the transit depth δ; the transit duration t_T, defined as the difference between the first (t_I) and fourth (t_{IV}) contacts; and the time difference between the second (t_{II}) and third (t_{III}) contact, essentially the duration of the flat part of the transit t_F. The period of the orbit is simply calculated from the separations of the observed eclipses. The analytic solutions for the depth δ and duration of the transit t_T are given by

$$\delta = \left(\frac{R_p}{R_*}\right)^2 \tag{1.3}$$

and

$$\sin(t_T\pi/P) = \frac{R_*}{a}\left\{\frac{[1+(R_P/R_*)]^2 - [(a/R_*)\cos i]^2}{1-\cos^2 i}\right\}^{1/2}. \tag{1.4}$$

The duration of the middle contacts t_F is scaled to the total duration of the transit according to

$$\frac{\sin(t_F\pi/P)}{\sin(t_T\pi/P)} = \frac{\{1-(R_P/R_*)]^2 - [(a/R_*)\cos i]^2\}^{1/2}}{\{1+(R_P/R_*)]^2 - [(a/R_*)\cos i]^2\}^{1/2}}. \tag{1.5}$$

The simultaneous solution of these equations assumes prior knowledge of the stellar

radius R_* from stellar models, and therefore measurements of the planetary radius R_P, orbital separation a and system inclination i can be performed. It is important to note that the accuracy of these is highly dependent on the prior knowledge of stellar parameters, typically using a similar approach to that of Mandel & Agol [2002]. This method relies on determining the stellar mean density from measurements of the orbital period, R_*/a and Kepler's Third Law and using stellar models to infer the remaining parameters using evolution models that reproduce the mass-luminosity-radius-composition relations followed by real stars. A comparison of the results of this method with more accurate measurements from asteroseismology or eclipsing binaries by Brown [2010] shows that up to 4% discrepancies can arise. Therefore, care must be taken to consider the effects of such model dependence.

The shape of the light curve is further affected by a phenomenon associated with a combination of optical depth and variations of stellar density and temperature at different altitudes. This effect, known as *limb darkening*, causes the transit to appear shallower than δ when the planet crosses the edge (limb) of the stellar disk and deeper in the middle [Milne, 1921]. Naturally, this darkening is also wavelength dependent, larger for shorter wavelengths (higher temperatures), and was first accurately modelled by Deeg et al. [2001] for a single main sequence star other than the Sun. This effect is very significant for planetary transits, however, as it is clear from Figure 1.9. This Figure shows a collection of observations of the transit of HD209458b using the Hubble Space Telescope at wavelengths ranging from 0.32μm to 0.97μm [Knutson et al., 2007]. The impact of this phenomenon is typically approximated by the fourth order Taylor series as

$$I(r) = 1 - \sum_{n=1}^{4} c_n (1 - \mu^{n/2}) \tag{1.6}$$

provided the transit observations are sufficiently precise [Claret, 2000]. In this equation, $\mu = \cos\theta$, where θ is the angle between the normal to the stellar surface and the line of sight to the observer and c_n are a set of coefficients that can either be calculated from stellar atmosphere models or directly fitted using the transit light curve. The result is a function that describes the further fractional decrease in flux as a function of what part of the stellar disk the planet is crossing in front of.

The limb darkening solution is often also simplified to the lower order cases ($n \leq 3$) depending on the choice of model, as discussed by Southworth [2008]. It is also important to note that, in a more complete case, the transit light curve results from attenuation of the stellar and the *planetary* atmospheres (which has an associated limb darkening). However, the effect of the planetary atmosphere limb

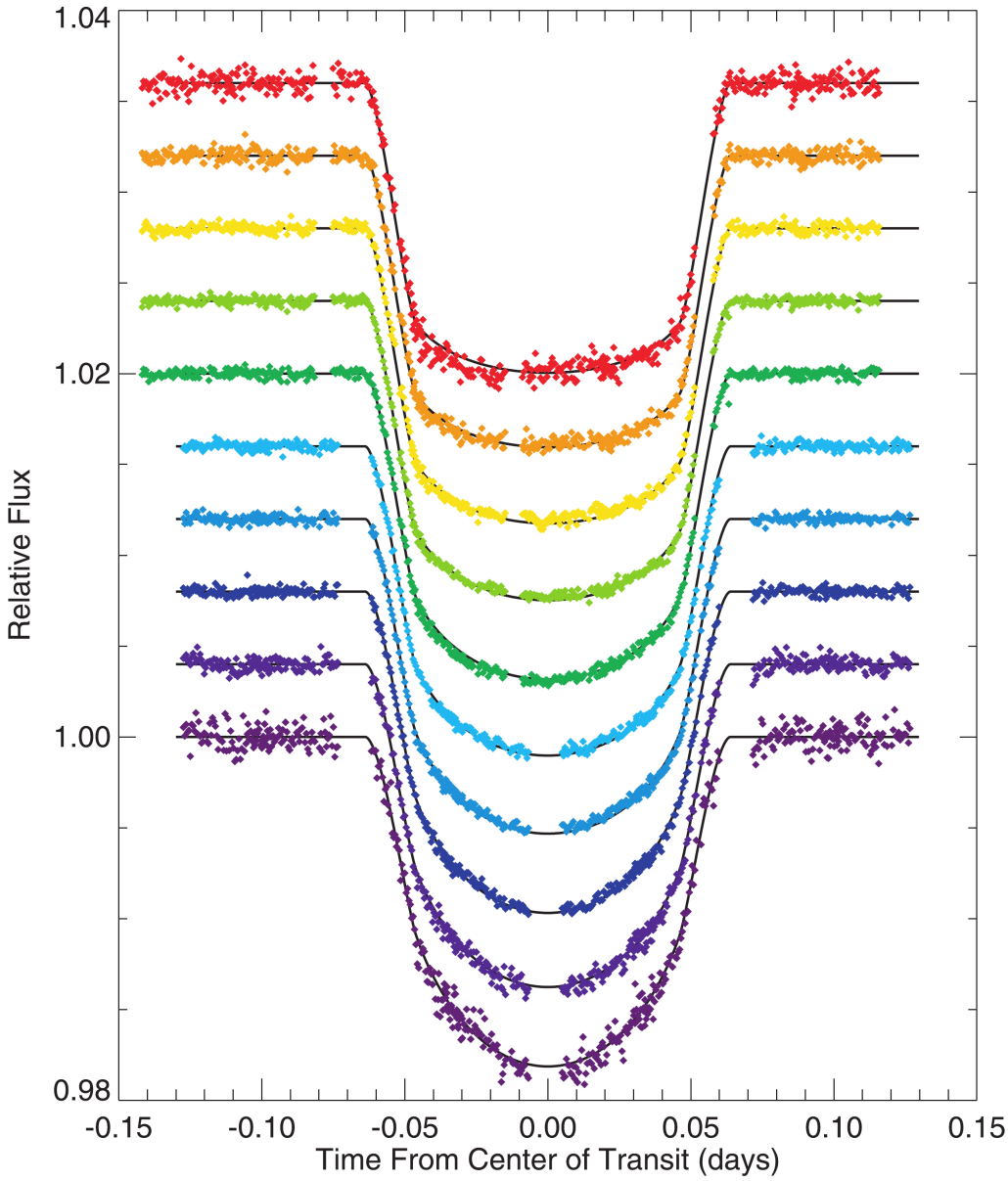

Figure 1.9: Transit light curves of the transits of HD209458b using the Hubble Space Telescope. The multiple light curves are shown with constant offsets for clarity and represent observations in the $0.32\mu m$ (bottom) to $0.97\mu m$ (top) wavelength range. The wavelengths shown are: 0.32μm, 0.38μm, 0.43μm, 0.49μm, 0.54μm, 0.58μm, 0.68μm, 0.78μm, 0.87μm and 0.97μm. This shows the effect of limb darkening especially at shorter wavelengths. From Knutson et al. [2007]

darkening is usually ignored.

Light curve fitting for planetary transits is often done simultaneously with radial velocity measurements, since both can provide constrains to the orbital period and, together, solve certain degeneracies. An important factor, as mentioned in Section 1.2.2, is the fact that radial velocity measurements alone provide only a lower limit to the mass of the planet, due to the $M_P \sin i$ degeneracy. Using the transit light curves, the inclination of the system is uniquely determined, and therefore the mass of the planet can be calculated. Moreover, equations 1.3 to 1.5 assume a non-eccentric system, which is frequently an oversimplification. Despite the fact that a recent study by Pont et al. [2011] suggests that, for a number of systems, their non-zero eccentricities in the literature can be attributed to statistical biases and that a circular orbit is a compatible solution, planets in eccentric orbits are clearly present in the sample.

The duration of a planetary transit suffers from a degeneracy with the eccentricity of the orbit. Kipping [2008] have developed a model that describes the transit light curve shape including the eccentricity [Ford et al., 2008], and the analytic solution is given by

$$t_T \simeq \frac{PR_*}{\pi a\sqrt{1-e^2}} \left\{ \left(1 + \frac{R_P}{R_*}\right)^2 - b^2 \right\}^{1/2} \left(\frac{r_t}{a}\right), \tag{1.7}$$

assuming $R_P \ll R_* \ll a$. In this equation b is the impact parameter and r_t is the planet-star separation at the time of mid-transit, given by

$$r_t = \frac{a(1-e^2)}{1 + e\cos\omega}. \tag{1.8}$$

The impact parameter is defined simply as $b \equiv a\cos i/R_*$ and is used often in the fitting process to represent the optimised value of the inclination. This equation simplifies back to the expression shown in equation 1.4 for $e = 0$. Luckily, the shape of the radial velocity curve provides a direct measurement of this eccentricity, as well as the argument of the pericentre (see Section 1.2.2), and when combined with transit observations, a unique solution can be found.

Therefore, if a planet is found to transit and radial velocity measurements have been taken, the mass and radius of an exoplanet can be determined, and hence the overall density of the planet calculated [Perryman, 2011]. This is extremely important for understanding the structures and properties of these planets, and it is no coincidence that the vast majority of known planets that have been studied beyond the discovery status happen to transit.

1.4 Transiting exoplanet surveys

Modern astronomical surveys are often robotic in nature and are designed to observe whenever possible. Ground-based exoplanet surveys in general have been responsible for the majority of discoveries of known transiting planets to date. The typical principle of these surveys, since there is no *a priori* knowledge of which stars will contain planets in well aligned orbits for transits to be detected, is to frequently monitor the brightness of a large number of stars in search for periodic drops in flux. In the early days of the development of these surveys the predicted yield of such projects was very optimistic [Horne, 2001; Gillon et al., 2005], but as the surveys begun to operate, the stringent requirements necessary to consistently detect planetary transits became obvious.

It quickly became clear that detections of this type of planets require dedicated telescopes and are subjected to optimizing several factors. The telescope aperture, exposure times, wavelength range and stellar distribution are among the most important, as these affect the number of stars monitored of any stellar type. Larger apertures (wide-field surveys) and longer exposures generally increase the numbers of monitored stars, but increasing both these factors contributes to decreasing spatial resolution and possible over-crowding, depending on the choice of observed fields. These problems have been approached in recent studies aimed at predicting the yield of transit surveys [e.g. Beatty & Gaudi, 2008; Heller et al., 2009], and the advantages of combining several surveys have been considered by Fleming et al. [2008]. The next Sections describe examples of such surveys. The SuperWASP project is the world leading *ground-based* transiting exoplanet survey, whilst the Kepler space telescope is the leading *space-based* project. We also describe a new ground-based survey, the Next Generation Transit Survey (NGTS), which builds from the experience of the SuperWASP enterprise to search for smaller planets.

1.4.1 SuperWASP

The Wide-Angle Search for Planets (WASP) project is a UK-led initiative that operates two fully robotic observatories in the northern (La Palma, Canary Islands, Spain) and southern (Sutherland, South Africa) hemispheres in search of planetary transits [Pollacco et al., 2006; Collier Cameron et al., 2009]. This particular survey was motivated by observations of the transit of HD209458b by Charbonneau et al. [2000] using a small and relatively inexpensive telescope and CCD setup, at a time when using such instruments was providing positive results [e.g.

Cremonese et al., 1997; Akerlof et al., 1999]. The consortium used commercially available hardware to limit the development work and begin observing as soon as possible. The prototype instrument for the WASP project, designated *WASP0*, monitored 35,000 stars in the Draco constellation for around 2 months as well as observing transits of HD209458b [Kane et al., 2004, 2005], which tested and demonstrated the principle under typical observing conditions. It used a Nikon 200mm, f2.8 telephoto lens attached to an Apogee AP10 CCD camera and operated during 2000 in La Palma and during 2001 in Kryoneri (Greece).

Science goals

The project was designed to search for bright transiting exoplanets suitable for spectroscopic and photometric follow-up studies orbiting mainly Main-Sequence stars. It is capable of achieving better than 1% photometric precision for stars in the $V \approx 7 - 11.5$ magnitude range whilst observing stars down to a limiting magnitude of V=15 [Pollacco et al., 2006]. Despite being able to survey the entire visible sky in just 40 minutes, the project was designed to observe a choice of fields per night in relatively high cadence, visiting each field at an average of 7 minutes [Smith et al., 2006] in a cyclic fashion for approximately 100-150 days each year. This strategy is sensitive to large planets in close-in orbits, which exhibit transits of approximately 1% depth every few days. It is currently the most successful ground-based transiting exoplanet survey in history, having discovered over 60 confirmed planets to date[3].

Observatories and hardware

Each facility comprises of a two-roomed enclosure incorporating a roll-off roof design housing a single telescope mount and the computer hardware systems to control the instrument. The telescope mount, capable of a pointing accuracy of 30 arc second rms over the whole sky and yet providing a slewing rate of 10 degrees per second, is constructed by Optical Mechanics Inc. (Iowa, USA) and contains 8 2kx2k Andor Technology (Belfast, UK) CCD cameras with 13.5μm pixels. These are back illuminated chips with QE peaking at over 90%, operating at a temperature of $-50°$C, through a five stage thermoelectric cooler where the dark currently has been measured to be negligible ($\approx$ 11e/pix/h). Figure 1.10 shows a picture of the SuperWASP South facility. Canon 200mm, f1.8 telephoto lenses are used for each camera, providing a field of view of $\approx$ 64 square degrees for all 8 cameras arranged in a 2x4 disposition [Pollacco et al., 2006].

[3]Information from exoplanets.eu

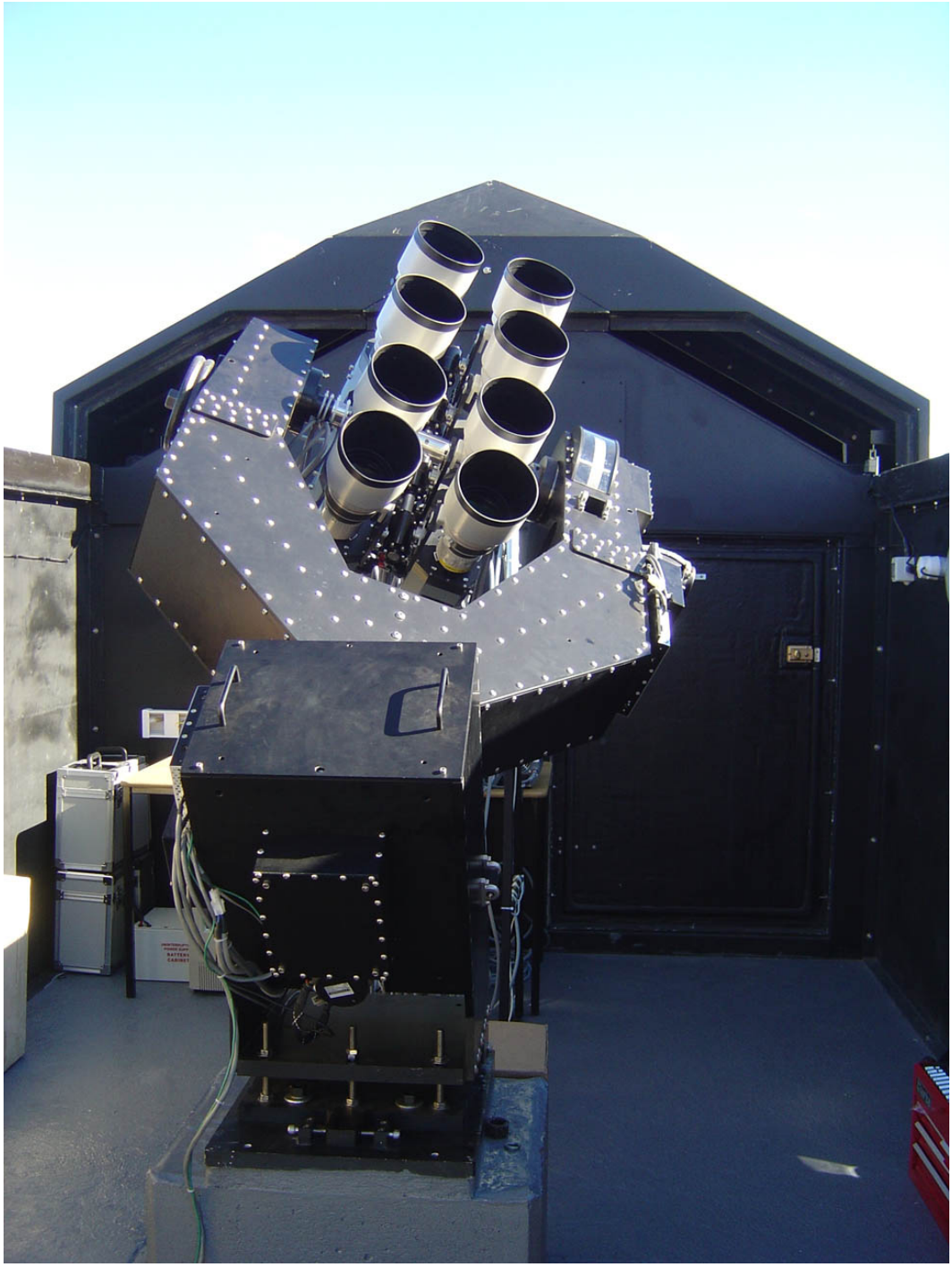

Figure 1.10: Picture of the SuperWASP South instrument. From Pollacco et al. [2006]

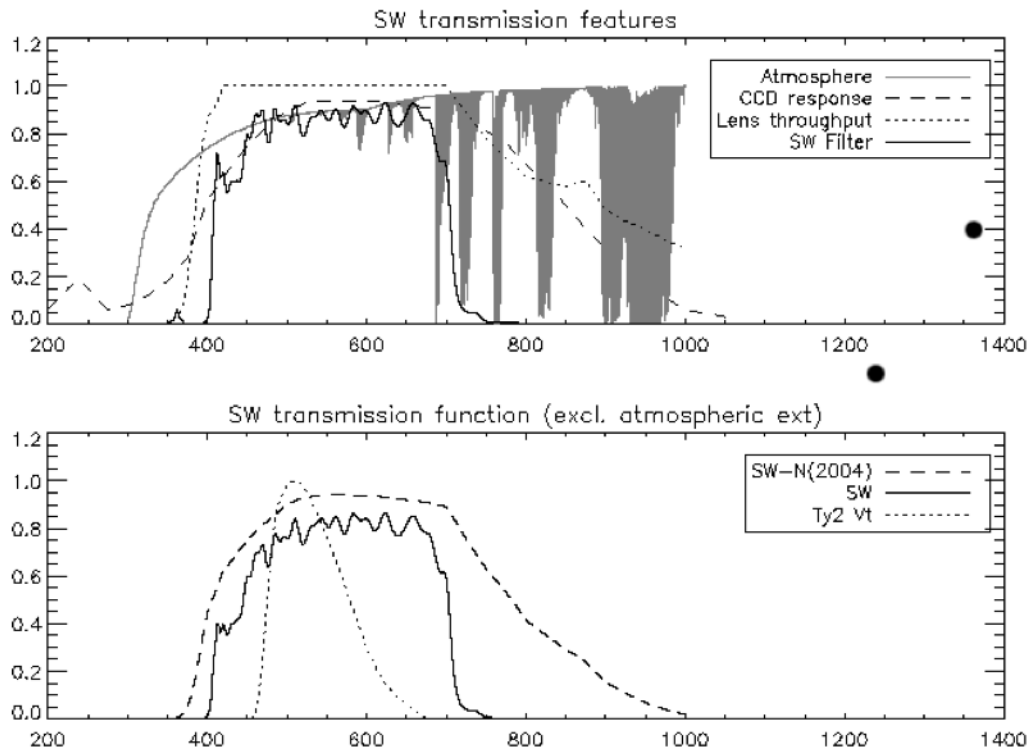

Figure 1.11: Wavelength response of the SuperWASP instrument. The top panel shows the passband of the SuperWASP filter alongside the atmospheric and optics transmission and the CCD QE curve. The bottom panel shows the original unfiltered system alongside the Tycho 2 V filter response for comparison. From Pollacco et al. [2006]

The telescopes use a broad passband filter at the 400 - 700 nm wavelength range which, when combined with the atmospheric and optics transmission functions, provides an instrument response as presented in Figure 1.11. This broadband approach has the advantage of maximising the collected flux at optical wavelengths, thereby maximising the number of available targets. However, color differences are likely to be an issue that requires calibration.

The data are collected by a *Data acquisition computing cluster*, responsible for the control of each individual CCD camera and the telescope mount. This is a cluster present inside the enclosure, which collects images of the sky into a repository. The data are analysed by a dedicated software pipeline described by Pollacco et al. [2006] and also broadly in Section 2.2 and eventually ingested into an archive system that serves as a database repository of the several Terabytes of measurements collected to date. The first 6 months of operation the SuperWASP

North facility observed 6.7 million stars and collected 12.9 billion data points [e.g. Christian et al., 2006; Lister et al., 2007] and the archive has been publicly released to the scientific community [Butters et al., 2010].

Once the data has been reduced, the process of looking for planetary transits takes place. In most surveys this is done using a modified box-least squares (BLS) algorithm such as that presented by Kovács et al. [2002]. This algorithm folds the light curve over a set of periods of interest and attempts to fit a rectangular shaped function to the data. This fit can then be refined using transit profile models at a later stage [Protopapas et al., 2005]. Other authors have proposed and analysed alternative search methods in order to maximise the scientific output of these surveys [Aigrain & Favata, 2002; Aigrain et al., 2004; Tingley & Sackett, 2005; Moutou et al., 2005; Collier Cameron et al., 2006; Ford et al., 2008]. This identification is complicated by the presence of a number of other astrophysical events that mimic planetary transits. Star spots on the surface of stars can produce periodic dips in the light curves, as well as eclipses from binary systems and ellipsoidal variations [Willems et al., 2006]. The selection of planetary candidates is, therefore, simply a selection of targets that then require further follow-up with larger telescopes in order to disentangle scenarios such as those mentioned.

Only the most promising candidates are chosen for follow-up. Photometric follow-up can identify any cases where aperture blending has taken place and the period dips coming from eclipsing binaries whose flux has been contaminated by another nearby star. Double-lined eclipsing binaries can be normally identified by a single spectrum and a set of radial velocity measurements are required to indeed confirm the sub-stellar nature of exoplanets.

History and discoveries

The various planets found by this survey have challenged our understanding of the structure and formation of such exotic bodies. Because SuperWASP is sensitive to close-in large planets it has found examples of bodies under extreme conditions of temperature, irradiation and density. Moreover, the sheer number of planets found has contributed to a rich and diverse sample of exoplanets.

WASP-3b [Pollacco et al., 2008] is a highly irradiated 2.06M_J planet found to exhibit transit timing variations over the period of 2 years consistent with the presence of a $\approx 15M_\oplus$ planet in a 2:1 mean motion resonance orbit around the host star [Maciejewski et al., 2010]. The example of WASP-8b, a 2.25M_J planet, revolves around its host star on a highly eccentric ($e = 0.31$) 8.16 day orbit in a retrograde fashion. This is the case when the planet orbits in a contrary direction to

the rotational spin of the star. This is also the SuperWASP planet with the longest period found to date. Due to the short baseline of coverage of each field (around 4 months) and the stringent requirements for a convincing detection of transits, the instrument is not sensitive to planets on orbital periods over 10 days and this is the highest trial period of the transit searching algorithm.

The case of WASP-12b [Hebb et al., 2009] is of particular importance. At the time of its announcement it was the exoplanet exhibiting the largest radius ($1.79R_J$) and shortest period, completing an orbit around the host star in just over one day. This made it the most heavily irradiated exoplanet known to date, with a predicted surface temperature of 2516 K and triggered a series of follow-up studies to determine its atmospheric properties. The presence of an extended exosphere around the planet with absorption from Na and Mg II has been suggested by Fossati et al. [2010], where enhanced transit depths are detected in near-UV observations. Secondary eclipse observations of this planet using both space and ground-based telescopes have revealed a high brightness temperature of around 3000 K, which initially suggests a low albedo and poor redistribution of the heat around the planet [López-Morales et al., 2010; Campo et al., 2010; Croll et al., 2011; Zhao et al., 2012]. However, recent observations by Crossfield et al. [2012] using the low-resolution prism on IRTF/SpeX suggest otherwise, showing that a 200-1000 K day/night effective temperature contrast is possible, and that therefore an efficient heat redistribution around the planet is probable. The low density of this planet makes it a good candidate for transmission studies (see Section 1.5.4) and this example has demonstrated that ground-based telescopes are capable of achieving enough quality for such studies.

The discovery of WASP-17b [Anderson et al., 2010b] had an immediate impact. This is the lowest density planet known to date, with a mass of $0.49M_J$ but a radius of $\approx 2R_J$ and therefore a prime candidate for studies of planetary atmospheres. Transmission spectroscopy of this planet has been performed from the ground [Wood et al., 2011], where the authors detect a depletion of sodium compared to the expected levels from a cloud-free atmosphere with solar sodium abundance. Moreover, secondary eclipse observations using the Spitzer space telescope at IR wavelengths have found the brightness temperature to be around 1500K and suggest a low albedo with efficient heat redistribution around the planet.

On the opposite end of the scale to WASP-17b in terms of density, the massive and extremely dense exoplanet WASP-18b ($10M_J$ but $1.16R_J$) orbits its host star in just under one day [Hellier et al., 2009]. These two particular examples reveal the wide range of possibilities in terms of exoplanet composition and structure and show

that further study of exoplanet atmospheres is crucial towards understanding these bodies. Moreover, the shortest orbital period exoplanet known to date, WASP-19b [Hebb et al., 2010], which circles the host star in 0.79 days, has challenged models of planetary orbital stability [Hellier et al., 2011] and has triggered several observations of its secondary eclipse. The thermal emission detections of this planet [Anderson et al., 2010a; Gibson et al., 2010] suggest a brightness temperature of over 2500K and a zero albedo and poor heat redistribution model just manages to explain such high levels. The authors suggest that the model used is potentially too simplistic and advise that further measurements are required to better constrain the parameters.

Other examples of particularly interesting SuperWASP planets include WASP-29b [Hellier et al., 2010]. This is currently the lowest mass planet found by this survey. With a mass of $0.24M_J$, it is a Saturn-mass planet orbiting a K4 dwarf star. This planet is given as an example of the potential of the project to push towards smaller planets (see Section 1.5.3). WASP-34b is also a sub-Jupiter mass planet that has been found to orbit a hierarchical triple system. The planet orbits the main star every 4.31 days in a slightly eccentric orbit, but a linear trend in the radial velocity curve of 55ms^{-1} suggests the presence of an additional body in the system, thought to be either a long period star or an extra planet [Smalley et al., 2011].

A final example of an outstanding discovery is the case of WASP-33b [Collier Cameron et al., 2010]. This planet orbits a hot, fast-rotating A5 star and is the first ever known planet to orbit a δ Scu host star [Herrero et al., 2011]. It is also the hottest known planet found to date, with an estimated surface temperature that exceeds 2700K. The authors find evidence of non-radial pulsations present in the radial velocity measurements distinct from the planet signal, which suggest tides created by the planet on the surface of the star. Moreover, a secondary eclipse detection of this object points towards a brightness temperature in the z-band of $\approx 3600K$, suggesting zero-albedo and inefficient heat redistribution from the day to the night side of the planet. However, due to the presence of stellar pulsations, the detection of the secondary eclipse required those to be modelled and removed. Since the baseline of the observation was relatively short, the remaining light curve shows large residual effects of this decorrelation, and further observations are required.

1.4.2 Kepler

Ground-based surveys are ultimately limited by the effects of atmospheric extinction and scintillation, which impose limits at around 0.01%. Therefore, extending the efforts to space is particularly important, where long uninterrupted

observations are possible. In this context, NASA's Kepler satellite was launched into a heliocentric orbit trailing the Earth's path [Borucki et al., 2010b; Koch et al., 2010]. The 0.95m modified Schmidt telescope houses 42 2Kx1K CCDs simultaneously monitoring the brightness of 150,000 main sequence stars in its 105 square degree field of view. 4 fine guidance sensors provide accurate pointing and the telescope is deliberately defocused to 10 arcsec to improve photometric precision over the 30 second integrations taken. The mission was launched in March 2009 and the first results have been announced recently.

Science goals

The space craft is capable of achieving a 4σ detection of an Earth-mass planet orbiting a 12th magnitude G2 dwarf star (Sun-like) over 6.5 hours [Borucki et al., 2010b]. The objectives of this mission are varied but are mainly oriented towards exploring the structure and diversity of extrasolar planetary systems. It achieves this by detecting planetary transits around a large sample of stars, which will help determine the frequency of terrestrial and larger planets within the habitable zones of their parent stars. This will also aid in providing an insight into the distribution of planet radii and orbital separations for exoplanets in order to understand if the particular case of the Solar System is an exception in these terms.

The high precision photometric measurements and long baseline of observations will also allow the discovery of multiple planet systems which can be used as case studies of the orbital stability and frequency of such systems. Moreover, this is the first project capable of detecting the variations in reflected light from close-in highly irradiated planets as they orbit the host stars. Results of such observations will provide a direct measurement of the albedo of these planets, a critical parameter to understand the optical properties of the atmosphere of exoplanets.

Finally, any measurement of the properties of transiting exoplanets is dependent on a good understanding of the physical characteristics of the host stars. The intense coverage provided by the space telescope has motivated enterprises to further enhance the knowledge of the properties of stars within its field [Howard et al., 2010, 2012; Everett et al., 2012; Greiss et al., 2012; Oshagh et al., 2011]. This information will provide the opportunity to explore the properties of planet-host stars, such as the spectral class, luminosity and metallicity using ground-based facilities.

Important discoveries

As of 30th August 2012, the Kepler team has announced the discovery of 77 confirmed planets[4]. The following examples highlight some of the most important cases in the context of exoplanet exploration.

The first new planet detected, Kepler-4b [Borucki et al., 2010a], is a Neptune-sized planet on a 3.2 day orbit around a late G0 star. The designations 1-3b are reserved for previously known planets in the Kepler field (TrES-2b [O'Donovan et al., 2006], HAT-P-7b [Pál et al., 2008] and HAT-p-11b [Bakos et al., 2010] respectively). This is a typical example of a hot-Neptune but demonstrates the photometric precision of the Kepler instrument. Figure 1.12 shows the Kepler light curve for this planet. Note the depth of the transit is 1mmag, which is an order of magnitude smaller than the typical depth of a Hot-Jupiter.

The first planetary system found with multiple transiting planets was that of Kepler-9 [Holman et al., 2010]. This system contains two planets that transit the disk of the host star every 19.2 and 38.9 days for Kepler-9b and Kepler-9c respectively. These show detectable transit timing variations of 4 and 39 minutes due to each other's presence, consistent with a 2:1 resonance motion, but once these trends are removed evidence of a third planet is presented, corresponding to a super-Earth-sized planet on a 1.6 day period orbit, later confirmed by Torres et al. [2011].

The case of the Kepler-11 has, however, revolutionised the field of exoplanets [Lissauer et al., 2011]. At the time of its announcement, this star system showed the largest number of transiting exoplanets orbiting the same star to date. 6 planets were found to transit this star, Kepler-11 b-f showing orbital periods between 10 and 47 days and Kepler-11g at $\approx$ 118 days. This system is an excellent case for studies of the stability of orbits of multiplanetary systems [Migaszewski et al., 2012]. Moreover, the masses of planets in multiple systems can be measured from the timing variations caused on the others. The Kepler team have recently confirmed the discovery of another system with 6 planets orbiting it, Kepler-33 [Lissauer et al., 2012]. Using this system as a test case, the authors argue that systems showing transits of multiple planets are unlikely to be false positives, and that validation is possible without resorting to radial velocity measurements.

Kepler-10b represents the first ever rocky planet found by the Kepler instrument [Batalha et al., 2011]. This $4.56M_{\oplus}$ and $1.42R_{\oplus}$ planet orbits it's host star in just over 45 days and represented a significant result, as it was the smallest planet ever found at the time via the transit method. The subsequent discovery of the

[4]Information from kepler.nasa.gov

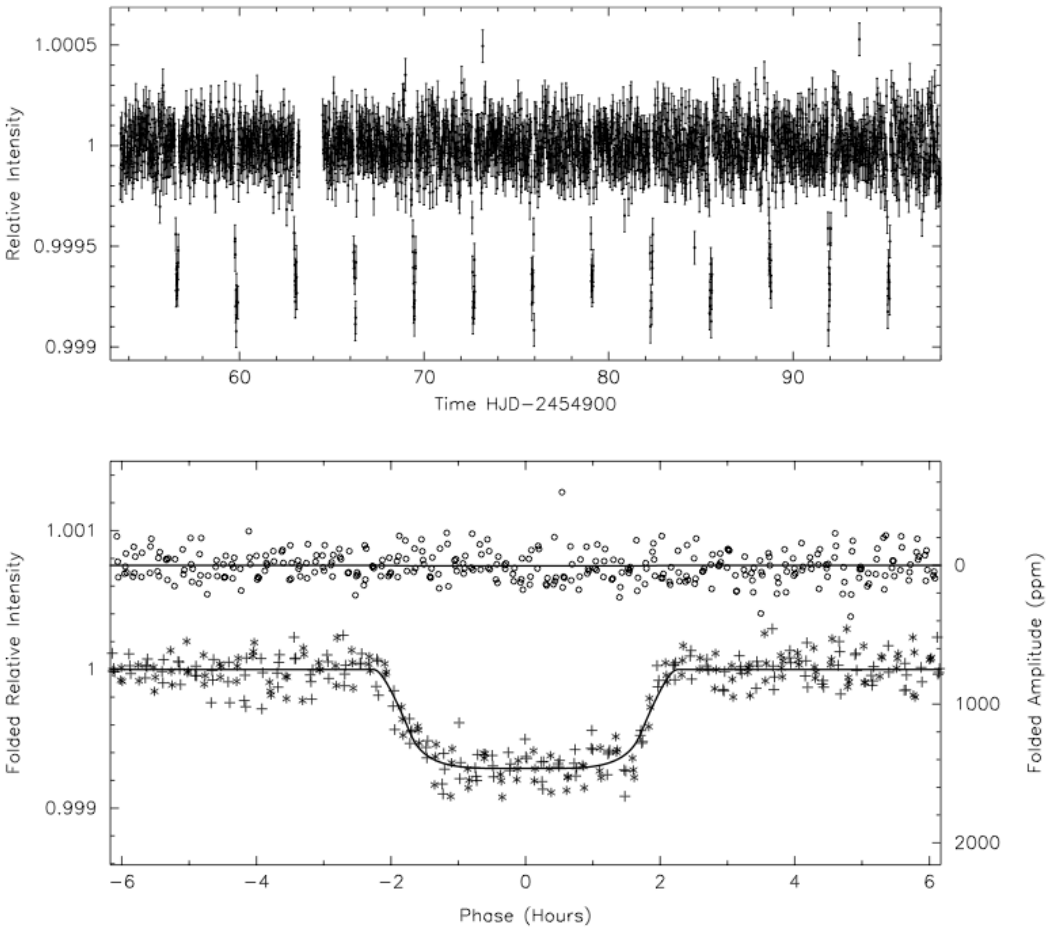

Figure 1.12: Kepler light curve of 13 transits of planet Kepler-4b. The top panel shows the unfolded light curve for 44 days after detrending. The bottom panel shows the folded light curve, where different symbols denote even and odd-numbered transits (Bottom curve). The above time series shows the folded light curve at the expected phase of secondary eclipse, where no evidence of a detection is seen. From Borucki et al. [2012a].

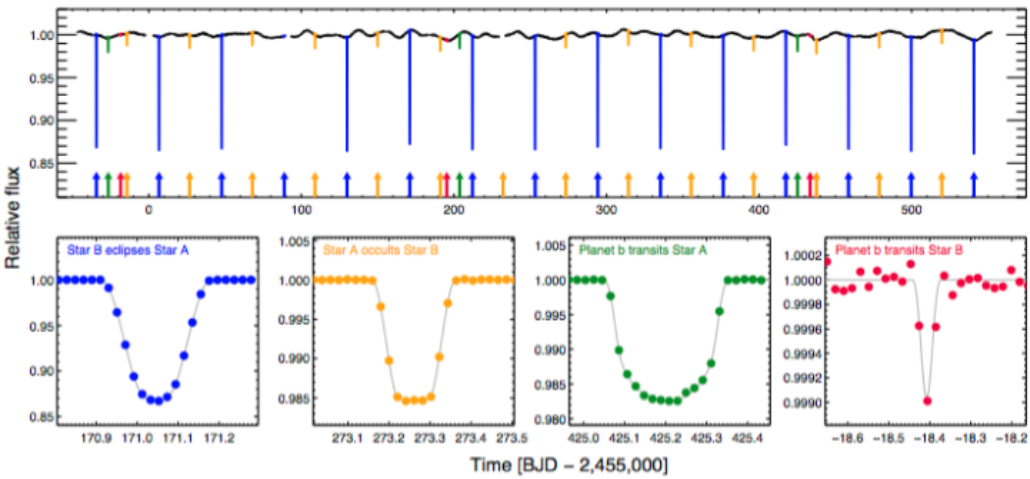

Figure 1.13: Kepler light curve of planet Kepler-16b. The top panel shows the unfolded detrended light curve with each of the eclipses color coded, corresponding to the cases shown in the bottom panels. The blue eclipses are those where star B eclipses star A (the larger star) and the yellow eclipses show the reciprocal event. The green eclipses correspond to the transit of the planet across star A, and the red the transits across star B. From Doyle et al. [2011].

Kepler-20 system was another milestone, containing 5 planets in total, 2 of which are smaller than Kepler-10b [Gautier et al., 2012; Fressin et al., 2012]. Kepler-20e ($1.08R_\oplus$) and Kepler-20f ($0.87R_\oplus$) represent some of the smallest planets ever found. A recent analysis of the Kepler Object of Interest (KOI) 961, also known as Kepler-42, suggest the presence of 3 planets orbiting an M dwarf star with radii smaller than the Earth, Kepler-42d being Mars-sized ($0.57R_\oplus$). These cases show the power of this mission and the particular advantage of intensive coverage of a single field from space.

Perhaps the most impressive result from this mission is the discovery of the first ever circumbinary planet by Doyle et al. [2011]. Kepler-16b orbits a pair of low-mass stars (Kepler-16A and Kepler-16B) over the period of 229 days. The stellar binary's 41 day orbit is eccentric but the motions of the three bodies are confined to within 0.5° of a single plane, consistent with a disk formation scenario. The light curve for this particular system contains the transits of the planet as it travels across the disks of both stars, as well as the deep stellar eclipses, as shown in Figure 1.13. The top panel shows the detrended light curve, with the several eclipses color coded according to the corresponding cases outlined in the bottom panels.

The recent announcements of another two circumbinary planets, Kepler-34b and Kepler-35b [Welsh et al., 2012] add to the list of these cases which, in conjunction

with the multi planetary transiting systems mentioned earlier, seem to suggest a disk formation scenario is likely to be the viable solution for these cases. Indeed, these discoveries have motivated the question of whether this is indeed the case at all times [e.g. Meschiari, 2012; Paardekooper et al., 2012]. However, since Kepler is not sensitive to multi planetary systems that are non-coplanar, this question remains unanswered.

Despite the generous number of confirmed planets by this mission, perhaps the most useful and remarkable science output of the Kepler instrument has been the announced of over 2,300 planetary candidates that are yet unconfirmed. Gautier & Kepler Science Team [2010] describe several methods to reject false positives, such as careful analysis of the light curves in search of features common to eclipsing binaries, spectroscopic follow-up and multi-band photometry such as that performed by Colón et al. [2012] in which signs of eclipsing binary behaviour can be detected.

The large number of candidates provides an opportunity to perform reliable statistics even if only a fraction of those are indeed later shown to be real planets. An example of such study is that performed by Kane et al. [2012]. Lissauer et al. [2012] argue that most of the planetary candidates are true on the basis that there are around one hundred times more candidates in multi-planetary systems then what would be expected from a random distribution of candidates. This conclusion is supported by the empirical analysis of Morton & Johnson [2011], where the authors conclude that over 90% of Kepler candidates have a probability of being a false positive of less than 10%.

Finally, the discovery of the first Earth-like planet in the habitable zone of its host star [Borucki et al., 2012b] marks the ultimate accomplishment of this mission. Kepler-22b is a $2.38R_{\oplus}$ planet on a 290 day orbit around a G5 dwarf star. The radiative equilibrium temperature for a planet on this orbit is of 262K and, despite the fact that only an upper limit to the mass of this planet of $124M_{\oplus}$ (with a 3σ confidence) from radial velocity measurements is available, this is the closest to an Earth analogue of any exoplanet known to date.

1.4.3 The Next Generation Transit Survey

The Next Generation Transit Survey (NGTS) is a new project designed to discover Neptune-sized planets around bright (V $<$ 13) and nearby stars. NGTS will deploy an array of fully-robotic small telescopes on independent mounts operating in approximately the 600-900nm band, thereby maximizing sensitivity to bright but relatively small host stars (K and early-M spectral type). This project builds from hardware and software heritage from the world-leading SuperWASP project

[Pollacco et al., 2006], and has recently secured full funding and authorisation to be commissioned early 2013 at ESO's Paranal Observatory in order to benefit from one of the world's premier sites.

NGTS has the potential to find Earth-like planets around smaller stars and, because the covered area is larger than that of Kepler [Koch, 2010] ($> 1500\text{deg}^2$), it will find transiting planets around bright stars, which are those where atmospheric follow-up studies are possible with facilities such as the Hubble Space Telescope, the Very Large Telescope (Chile) and all the planned large telescope facilities (ESO's E-ELT, ESA's ECHO mission and NASA's concept FINESSE). It will achieve this by monitoring the brightness of all the visible targets within its field-of-view in search of periodic dips, which are the tell-tale signs of the existence of transiting planets. Contrary to the SuperWASP project (see section 1.4.1), which is an *almost all-sky survey* that samples several pointings every night, NGTS will employ a *staring* strategy in which it will observe one field for as long as possible (typically around 4 months) before changing. This has the added advantage of increased precision in the time-scales of single transits (around 1-3 hours) but also, crucially, brings the potential to discover planets on longer orbits. The vast majority of transiting planets found to date orbit their host stars in typically less than 10 days (based on exoplanet.eu) mostly due to an observational bias, and only recent surveys, such as the Kepler mission, have observed a single location for a long enough time-scale to be sensitive to longer period planets [e.g. Borucki, 2012].

As with any transiting planet survey, careful follow-up studies are required to confirm the planetary candidates. As discussed by Evans & Sackett [2010], there are many astronomical events that can mimic the transit signature, such as grazing eclipsing binaries, blended objects with deep eclipses, low-mass eclipsing binaries or simply systematic effects, and further observations are necessary to disentangle these scenarios and filter the real planets. In those cases where either there is doubt that a transit was observed or that the signature could be caused by a background source contaminating the flux inside the typically large apertures used on low resolution wide-field imaging surveys, photometric follow-up on 1-2m class telescopes is often sufficient. The location of the NGTS facility is advantageous in this context, since there is a whole host of nearby telescopes such as the TRAPPIST telescope at the La Silla Observatory and the Henrietta Swope telescopes at the Las Campanas Observatory for these follow-up procedures. Spectroscopic follow-up helps identify binary systems rapidly, and is invaluable for this kind of research. Moreover, if a planet is confirmed, radial velocity measurements are necessary to measure the mass and instruments such as the HARPS spectrograph [e.g. Dumusque et al., 2011;

Ségransan et al., 2011; Pepe et al., 2004] currently mounted on ESO's 3.6m telescope in La Silla have proven to be extremely successful in these enterprises.

The final NGTS facility will be composed of 12 fully-robotic wide-field 20cm telescopes, equipped with deep-depleted CCDs developed to the project's specifications by industrial partners (Andor Technology plc, Belfast and e2v, Chelmsford, UK). The CCD model, now available at Andor's general range, is capable of achieving high precision photometric measurements within the desired wavelength range of the instrument (600-900nm). The facility is housed in a custom designed building with a rolling roof, that will comprise of an inner chamber containing the telescopes and two side rooms for the computer servers required to control the facility and communicate with the UK. Each telescope is assembled on an individual mount, in order to achieve precise guiding and maximise the flexibility of the experiment in terms of observing strategy.

Science goals

The main objective of the survey is to search for transiting planets of Neptune-size and below around bright stars. The many recent discoveries of planetary systems harbouring Neptune-mass planets and super-Earths clearly indicate that low-mass planets around solar-type stars must be very common [Traub, 2012; Wittenmyer et al., 2011; Mordasini et al., 2009a,b]. However, very little information is available regarding the structure and composition of these planets. Moreover, planetary systems such as the Kepler-11 case show that, as is the case for gas giants, there is likely to be a large diversity of earth-sized planets [Lissauer et al., 2011]. Figure 1.14 shows the optimal sensitivity range of the facility. It shows that this project is designed to explore a region of parameter space that is relatively unpopulated.

As described in Section 1.3, the geometry of transiting exoplanets places tight constrains on the orbital inclination of these systems, thereby providing the opportunity to accurately measure their radii and masses. Moreover, multi-wavelength observations of the transits provide the chance to probe the atmospheres of exoplanets (see Section 1.5.4), and secondary eclipse observations can give an indication of the brightness temperatures and overall atmospheric circulation. NGTS aims at providing a set of bright targets for follow-up studies with facilities such as the Spitzer and HST, and also from the ground with large telescopes like the VLT using FORS or HAWK-I.

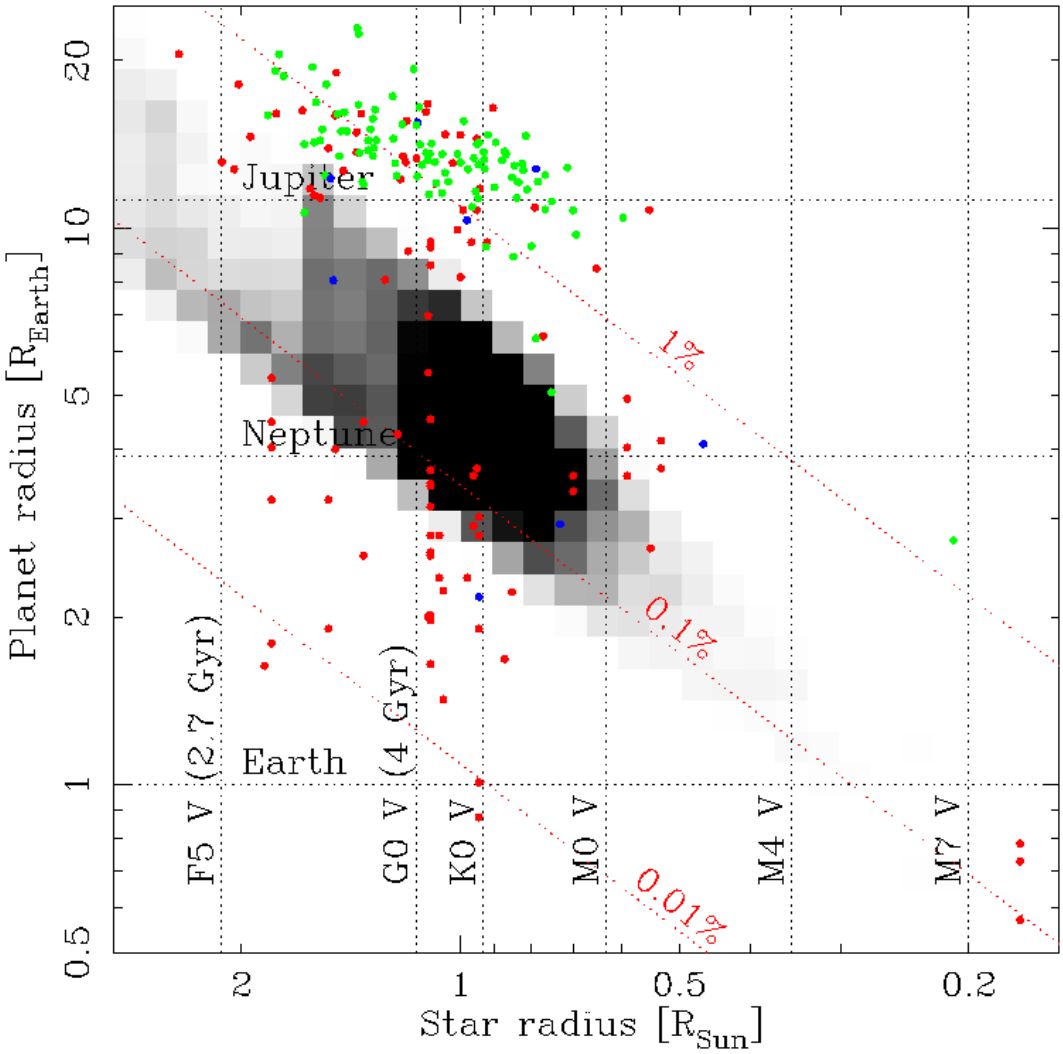

Figure 1.14: Parameter space for transit detection with the shaded region indicating the optimal parameter space of the NGTS facility in terms of the smallest planets that can be found for each stellar type. This Figure shows the transit depth as a function of planet and star radius. Known transiting systems are shown in cases where they were discovered in ground-based surveys (green), from space (red) and those in blue represent planets detected through radial velocity measurements and later found to transit. Approximate spectral types of stars are also indicated, as well as the radii of representative Solar System planets.

The Prototype

The ability to achieve 0.1% precision across the wide-field of view is very demanding and was demonstrated using a prototype system operated on the La Palma Observatory (Spain) during the 2009-2010 season. A smaller version of the e2v CCD (1k×1k) was deployed on an 8 inch Takahashi telescope and tests were performed to determine if the desired sub-mmag precision was possible to be achieved. This puts this facility in a superb position to explore a region of parameter space that is currently relatively unpopulated, as shown in Figure 1.14. This Figure also contains information on the typical stellar types associated with each radius as well as radii of representative Solar System planets for reference. The analysis of the data taken by the prototype instrument have shown that 1mmag precision is indeed achieved, as presented in Figure 1.15. This plot displays the fractional RMS for stars in a field observed for one night with the prototype instrument as well as the expected noise based on the model to be described in Section 2.3. Transits of the Hot-Neptune GJ436b were easily recovered and a precision of 0.5 mmag is reached in one hour time scales for a star of magnitude I=10.5, which corresponds to V=12, fulfilling the science requirement.

Other tests were performed on the prototype instrument, such as the guiding capability of the telescope and flat-fielding, and results have shaped the design of the project, with the majority of telescope components already purchased. A testing system will be assembled in the Summer of 2012 by a team at the Geneva Observatory for software and operations testing before the complete system is integrated on the mountain in early 2013. Other elements crucial to the project, such as data storage and mining, analysis software and knowledge of infrastructure are largely based on those developed for the SuperWASP project, making this facility science ready as soon as it is commissioned.

1.5 High-precision photometry for exoplanet research

Photometry in astronomy is a technique concerned with measuring the flux or luminous intensity of a celestial source [Martinez & Klotz, 1998]. This principle dates back to times when important astronomical events such as supernova explosions were detected with the human eye. Since light is the main source of information upon which knowledge of celestial objects is drawn from, photometry, together with spectroscopy, form the basis of the vast majority of all that we know of the Universe outside the Earth. In particular, time-resolved photometric measurements can be extremely useful to study the temporal evolution of any given target. Observations

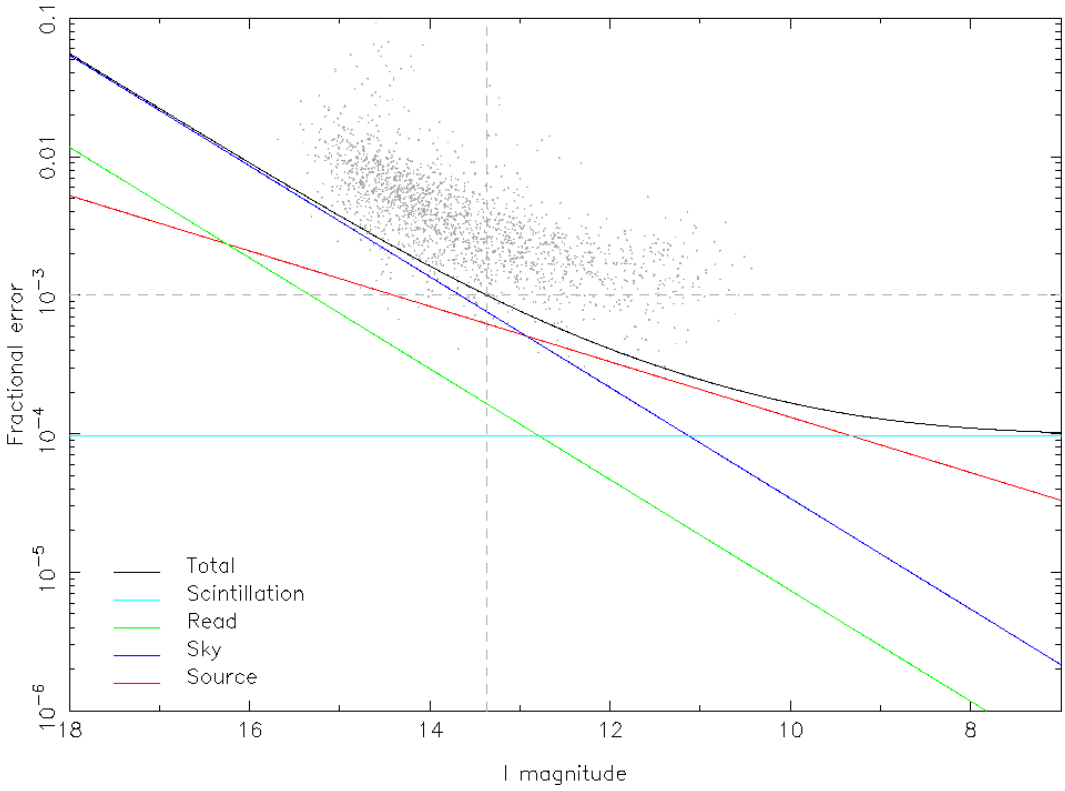

Figure 1.15: Fractional RMS as a function of I magnitude for one night of the NGTS prototype. The data are averaged into one hour bins and a noise model based on the method described in Section 2.3 is presented along with the contributions from the several sources. The dashed horizontal line is a measurement of the precision achieved for bright stars. Courtesy of Simon Walker.

are typically done in a specific wavelength range usually restricted with the use of filters, which leads naturally to *spectrophotometry*. This process simply involves making measurements with multiple filters to obtain a spectral profile of a given event/target.

Time series photometry is a very powerful method, not only because it can be done on many stars simultaneously (see Section 1.4) but also because of the valuable information that can be derived from it. Planetary transits (see Section 1.3) are observed through this method and hence this is the only type of photometry featuring in this thesis.

The time resolution that can be achieved is only dependent on the read-out time of the photometer used and the brightness of the target[5]. The use of CCDs has revolutionised the field, not only because of the relatively short read-out time but mostly because of the precision that can be obtained in terms of photon counting with respect to other options such as image sensors and photodiode cells. It does, however, have some drawbacks that have to be understood if high-precision photometry is to be achieved. Section 1.5.1 introduces these devices in detail and outlines the standard processes used to minimise these drawbacks.

1.5.1 Astronomical photometry using CCDs

Charge Coupled Devices (CCDs) have revolutionised modern astronomy. The knowledge brought by the arrival of these instruments can be paralleled with the advances due to the invention of the telescope [Howell, 2000]. In the short time since CCDs were employed in astronomy in the early 1980s, our understanding of the Universe has changed dramatically. The accuracy with which it is possible to make measurements with CCDs in contrast to photographic plates (which have a non-linear response) has brought a new era in astronomical findings. The linear response of such devices has allowed precise photometric all sky surveys to take place, as well as unprecedented accuracy and consistency in photometric measurements, leading to the discovery of exoplanets and better understanding of astronomical phenomena such as Gamma-ray Bursts, Stellar flares and Supernova explosions.

A CCD chip is generally based around a slightly p doped layer of semi-conducting silicon formed of arrays of *picture elements*, typically abbreviated to pixels. The major advantages of these devices are the relatively low noise, high quantum efficiency (QE) and good wavelength response in the visible range of the spectrum (typically 3,000 to 10,000 Å) [Martinez & Klotz, 1998] . QE is defined as

[5]If the target is very faint, it is necessary to collect photons for a long enough period of time (exposure) to image the object at all

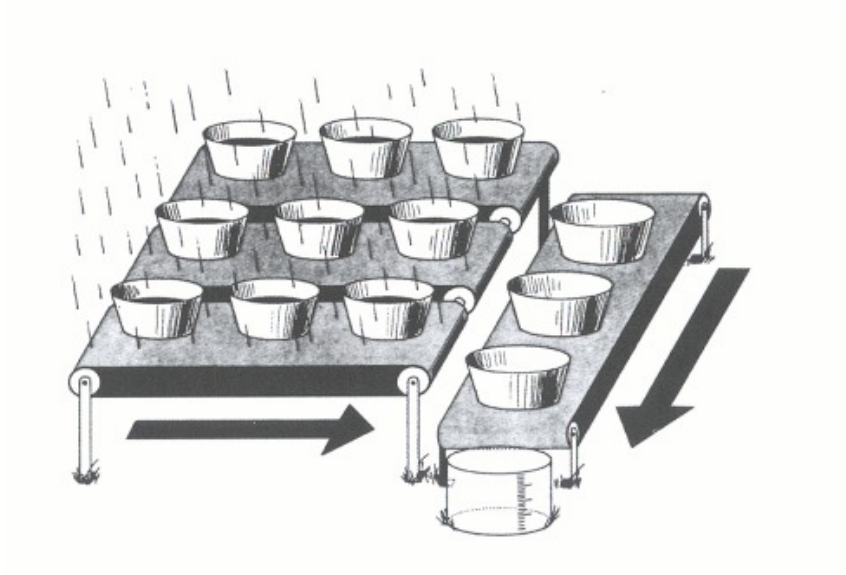

Figure 1.16: Analogy of a CCD readout to a series of buckets. This image demonstrates the horizontal and vertical readout process. From Janesick & Blouke [1987]

the fraction of the incoming photons the CCD is able to convert into electrons, which is wavelength dependent. More importantly, obtaining an image from a CCD camera takes only a few seconds (readout time) and therefore testing, acquisition, inspection and analysis of the data is quick. Each pixel converts photons into electrons which can then be converted to numeric values, also known as ADUs, through analogue-to-digital converters.

The readout stage of a CCD chip follows a principle similar to that depicted in Figure 1.16. The charge in all rows is shifted to the row below via a generation of an electric potential that forces the electrons to move to the adjacent pixel. The charge in the lowest row is transferred to an additional readout row which is then horizontally shifted. The charge in each pixel is then sent onto the analog-to-digital converter where the change in voltage caused by this charge is detected by the on-chip amplifier. This process is not completely noise free, as the amplifier's noise performance is typically a simple relation of 1/f at low sampling frequencies but displaying a white noise level at higher frequencies. This is commonly known as the readout noise. The sampling frequency is the rate at which each individual pixel is read by the CCD electronics (the readout speed). This information can then be used to reconstruct the image digitally and proceed to the calibration and analysis stages.

The capacity for holding charge on a given pixel is not unlimited. Once the

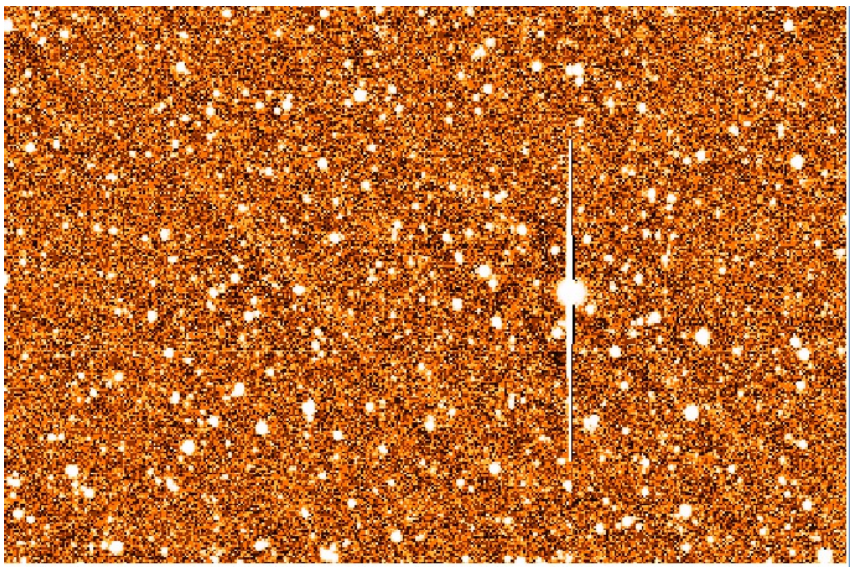

Figure 1.17: An example of a saturated star that exhibits charge spillage. Taken from the SuperWASP project archive [Butters et al., 2010]

amount of light hitting a pixel is high enough the number of generated electrons reaches its full well depth and saturates. At this point the charge from this pixel will spill to neighbouring pixels, typically of the same column. Figure 1.17 contains an example of an image in which a bright star has saturated. This image is taken from the SuperWASP archive [Butters et al., 2010].

Modern CCDs can vary in size, depending on the requirements of any given experiment. The dimensions of each pixel are also variable, typically 10-15 microns. This, combined with the diffraction limit[6] of the optics sets the ultimate limit on the spatial resolution of an instrument. There are several experiments, however, where resolution is not a priority, and where a defocussed image is preferable. If the objective of an instrument is to make accurate measurements of the luminosity of bright stars, then defocussing and spreading the light over many pixels can be convenient to avoid saturation and to minimise other sources of noise (see Section 1.5.2).

The actual process of measuring the number of photons from a given source can be done in several ways. However, the most widely used is the method of aperture photometry, which can be applied to a large number of stars on a single image [Newberry, 1992]. This method consists of considering a circular aperture centred on each star and counting the number of photons each pixel inside that

[6]Which depends on the wavelength of the incident light and the telescope aperture diameters

aperture is contributing. It is common to attribute a weight to the flux of each pixel, depending on how much of it lies inside the circular aperture. This provides a measure of the flux from the source of interest and the background light. The latter can be estimated using a *sky annulus* also centred on the source of interest but outside the source aperture. The background flux per pixel can be estimated using a statistical measure (median or average) and subtracted from the aperture flux, to give the uncontaminated source flux.

Bias and Dark frames

A characteristic of all CCDs used for any purpose is the presence of an electronic bias level applied during the readout stage to avoid negative values because of statistical noise [Howell, 2000]. This level is usually high enough to guarantee that, even under extremely unlikely random fluctuations, the number of ADU counts is positive but is kept relatively low to minimise the reduction in measuring range. This level can be measured using bias frames, which are simply a readout of the unilluminated CCD with zero exposure time and are typically characterised by a homogeneous Gaussian distribution of values centred around the mean bias level [Martinez & Klotz, 1998]. This level can fluctuate slightly between frames and this change can be monitored on other frames using an overscan region of the CCD. This region can either be a physical unexposed area of the chip or simply a result of electronically extracting values from an extra set of rows/columns during the readout stage.

Most photometric data reduction involves producing a master nightly bias frame, which is the result of a median combination of several individual bias frames taken as close as possible from the time of observations[7].

Dark current in CCDs is a result of thermal effects that generate additional electron/hole pairs on individual pixels. In order to minimise this process, astronomical CCDs are kept at low temperatures ($\approx 230 - 270K$) [e.g. Dhillon et al., 2002; Pollacco et al., 2006]. The choice of operating temperature depends on the specific characteristic of the CCD and its application, but is normally set to reduce the average dark current to negligible levels. It is, however, not uncommon for dark frames to be ignored if the CCD used is found to have negligible dark current, or for the bias level to be corrected simultaneously with the dark current, by taking dark frames with the same exposure as the science frames.

Similarly to the method applied to calibrate the bias level, dark frames consist of long unilluminated exposures, in which dark current is allowed to accumulate.

[7] Typically at either the beginning or end of an observing night or run

These can be scaled to the science frame exposure times and (much like bias frames) combined to produce a master dark frame.

1.5.2 Flat field frames

Flat-fielding is crucial in most applications of CCDs. It deals with the variations in QE between different pixels, both inherently or due to non-uniform transmission of the optics. This can be the case in situations where there is dust on the optics or a non-homogeneous coating of the silicon layer, among others. Considerations of these effects in the literature include the work of Manfroid [1996] and Moehler et al. [2010].

In order to calibrate these factors the chip needs to be uniformly illuminated. The variations in the QE between different pixels will result in a non-uniform image, which can be used to scale their relative responses. However, achieving a sufficiently uniform illumination of the chip is very challenging. Methods commonly used in astronomy involve the use of light sources with diffusers or imaging relatively uniform parts of the inside of the telescope dome but by far the most widely used method consists of observing a region of the sky without bright stars during twilight. The twilight sky is generally considered to be quite uniform, and small offsets to the telescope between exposures guarantee that any bright star on the field is removed during the median combination of the frames. A set of these *twilight flats*, when corrected for bias and dark levels as described in Sections 1.5.1, can be combined to account for the inter-pixel QE variations of the chip.

It is however important to note that flat fielding should only be done if there is indeed need for it. In photometric applications, it is often the case that the telescope used has *guiding* capabilities. This consists of attempting to keep the stars of interest fixed in CCD coordinates during an observing run, thereby making sure the *same pixels* are always used to make the measurements. This can sometimes bypass the need for a flat fielding correction, provided the QE of all the pixels involved is not anomalous. Moreover, the flat-field frame used for this calibration stage is limited by the photon noise of the set of individual frames used to produce it. Therefore, the calibration itself will suffer from the introduction of this extra source of noise and its consequence must be considered before the decision to flat-field is taken. Examples of studies where flat fielding is used as a form of diagnostics are found in almost every application of CCDs in astronomy [e.g. Ford et al., 2010; Evans et al., 2005; Ferguson et al., 1995; Southworth, 2009].

CCDs will often show a fraction of pixels that produce anomalous results, depending on the illumination levels. Bad pixels are specific examples of pixels whose

response is either non-linear, show extraordinarily high dark current or particularly low QE. It is also often possible to see one particular pixel affecting the counts of an entire column or row of the chip. Figure 2.6 shows several of these cases, which are a result of issues in the charge transfers during the readout stage.

Since typically the fraction of the CCD chip that contains bad pixels is relatively low, it is common to produce *bad pixel masks*, which are simply static frames that contain information on which pixels to ignore during data reduction. These masks are produced based on visual inspection of images by members of any team responsible for the operation of CCD cameras, and should be updated regularly.

1.5.3 Limiting factors towards finding smaller planets

While the majority of stars observed in surveys are faint and therefore dominated by photon noise, which is random (white) in nature, the stars of interest, where the highest photometric precision is possible in principle, are often dominated by systematic (red) noise sources. This type of noise consists of trends in the data at significantly lower frequencies than white noise. Hence, the power spectrum of white noise is characterised by a flat spectrum across all frequencies whereas red noise will exhibit higher power at lower frequencies. Furthermore, a sub-set of red noise, denominated *correlated noise*, is present in cases where the obtained data show trends that correlate with an observable or system parameter, such as airmass, pixel position, seeing or instrument set-up related options. As mentioned by Pont et al. [2006], the presence of red noise can explain the lower numbers of planets found when compared with initial estimates and has consequently the effect of increasing the detection threshold, limiting the ultimate precision of ground-based surveys to $\approx 3mmag$ [Pont et al., 2007]. The advantage of red noise is that it is often correlated with an observable parameter, and therefore correctable in principle, but it is often not trivial to do so. An example of such a source that is well understood and that is present on any ground-based survey is the effect of atmospheric refraction (airmass dependent) [Kristensen, 1998]. However, since this effect is wavelength dependent, surveys that observe in a broad wavelength have to compensate for color differences between all targets.

The presence of bad/non-linear/hot pixels can introduce systematic effects if a PSF moves across any of these. However, the use of bad pixel masks is sufficient to avoid this problem. Refer to Section 1.5.1 for more details.

Flat-fielding errors are also a common limitation to stable long-term photometric quality. This is typically compensated for using *flat-field frames* but this calibration often only results in an attenuation of the inter-pixel variations. Tech-

niques such as telescope guiding can be used to minimise these errors, but achieving sub-pixel guiding precision over the duration of a typical survey (several years) is technically challenging. Other techniques such as deliberate telescope defocus can be applied to reduce the weighting on each pixel and thereby reduce the effect of such inter-pixel variations [Southworth, 2009; Southworth et al., 2009; Southworth, 2010].

Other sources of systematic noise include seeing/focus changes and results of instrument maintenance. Compensating for any non-Gaussian effects is paramount to the detection of planetary transits, especially if the typical drop in flux is of the order of a few mmag. At the end of each observing season, most surveys will attempt to remove correlated noise using de-trending algorithms such as that proposed by Tamuz et al. [2005] and/or the trend-fitting algorithm presented by Kovács et al. [2005]. These algorithms are designed to work on data sets where the flux of many (usually thousands) of stars are measured simultaneously for long periods of time. Weights are assigned to each star and the trends fitted simultaneously, thereby reducing the effect of correlated noise in the light curves.

Nevertheless, extending the sensitivity of ground-based telescopes to the regimes where smaller planets can be found and studied requires a better understanding of the systematic sources of noise any instrument is subjected to. Chapter 2 explores this topic in the context of understanding the sources of noise present in the SuperWASP light curves, whilst Chapter 3 describes an enterprise to push the limits of ground-based photometry for the purpose of measuring properties of the atmospheres of exoplanets.

1.5.4 Planetary atmosphere studies

The growing sample of transiting planets is proving to be the key towards understanding the structure, composition and formation of exoplanets through analysis of the mass-radius relation [e.g. Pollacco et al., 2008]. The extreme densities of WASP-17b and WASP-18b (see Section 1.4.1) represent examples of cases that are challenging the current models of planetary formation and bulk structure and it is clear that further observations are needed to understand the atmospheres of these planets.

Planet transits allow the unique opportunity to sample the absorption profile of the atmosphere of an exoplanet, i.e., essentially, the radius of the planet to be determined as a function of wavelength. In wavebands where the opacity of the atmosphere is enhanced due to the presence of a specific absorber, the planet will appear a little larger, and so by making very precise measurements of transits we

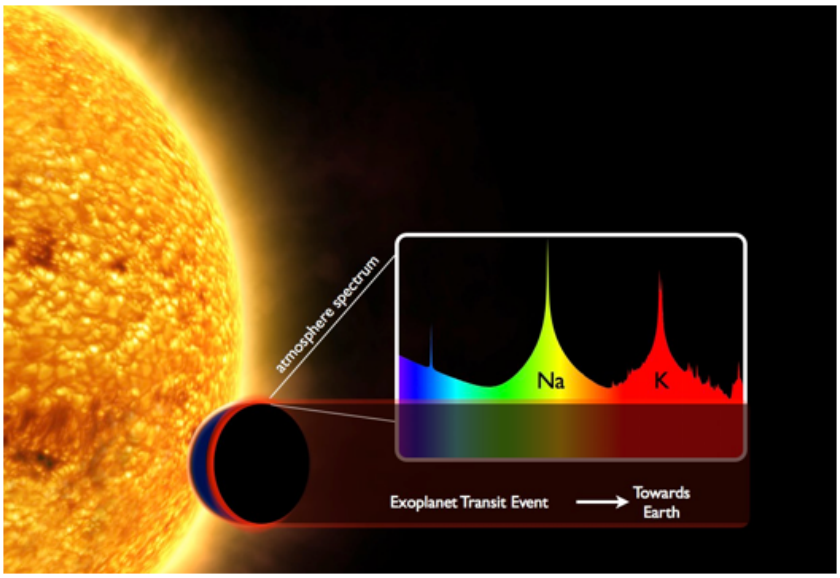

Figure 1.18: Pictorial representation of the method of transmission spectroscopy. As the light from the star passes through the exoplanetary atmosphere during transit, an absorption spectrum can be obtained. Original image credit ESA, additional illustrations by D. K. Sing.

can probe the atmospheric composition and chemistry of the planet (a technique known as *transmission spectroscopy*). This is demonstrated in Figure 1.18.

Transmission studies

The first detection of the wavelength dependence on the planet radius of an exoplanet was achieved in a narrow band containing the NaI doublet. This observation of the transit of HD 209458b using the Hubble Space Telescope (HST) [Charbonneau et al., 2002] shows an enhanced planet radius in this band, implying a higher opacity of its atmosphere in this wavelength range due to the presence of atomic sodium. The detection of sodium had been predicted because alkali metals remain in the atomic state at low temperatures, when other abundant elements have formed molecules [Seager & Sasselov, 2000; Hubbard et al., 2001]. The atmosphere of HD 209458b has also been explored at low-spectral resolution across the optical waveband, also using HST [Sing et al., 2008; Lecavelier Des Etangs et al., 2008b]. The resulting transmission spectrum is dominated by a short wavelength broadband opacity source (around 300-500nm), interpreted as Rayleigh scattering by H_2. Moreover, the sharp NaI feature appears to be superimposed upon a broad Na absorption thought to be a Stark-broadened component of the NaI line. A low-resolution HST

transmission spectrum of the other very bright hot Jupiter, HD 189733b, also shows evidence for a broadband scattering continuum [Pont et al., 2008; Sing et al., 2011] (plotted in Fig. 1.19). However, in this case the scattering particles are larger, perhaps silicate condensates [Lecavelier Des Etangs et al., 2008a]. There is also no evidence for a broad component to the sodium line.

The difference between the broadband transmission spectra of HD 209458b and HD 189733b demonstrates the need to study a sample of transiting exoplanets in order to probe atmospheric chemistry under a wide range of physical conditions. Detections from the ground are extremely challenging, and so far have been achieved only in the narrow bands around the cores of the NaI lines [e.g. Snellen et al., 2008; Redfield et al., 2008]. Other attempts at repeating the results from HST have so far been reported to be consistent with previous observations but dominated by systematic effects [e.g. Narita et al., 2005]. In part, this is because spectrographs are not designed to be photometrically stable, and it is necessary to decorrelate data against a large number of parameters to remove these systematics [e.g. Pont et al., 2008; Snellen et al., 2008]. Fortunately, however, the main features revealed by HST spectroscopy are broadband components and so broadband observations from the ground, both in low-resolution spectroscopy and photometry, can provide further constraints for the composition of these bodies.

In addition to detections of these atmospheric features in absorption, planetary atmospheres have also been detected in emission using secondary eclipse measurements. An example of such measurement is shown in Figure 1.20. Observations in the IR using the Spitzer space telescope have been done for a large number of planets [e.g. Deming et al., 2005; Todorov et al., 2010; Nymeyer et al., 2011; Beerer et al., 2011; Deming et al., 2011]. Moreover, observations from the ground have now been performed of this phenomenon for several very hot exoplanets, mostly centred in the K-band [e.g. Sing & López-Morales, 2009; de Mooij & Snellen, 2009; Croll et al., 2011; de Mooij et al., 2011; Burton et al., 2012]. A surprisingly wide range of brightness temperatures have been measured, and this is thought to result from temperature inversions in the atmospheres driving emission at low pressures [Fortney et al., 2008].

The presence of a temperature inversion is thought to be determined by the high irradiation of the upper atmosphere, where TiO and VO absorption starts to take place and is probed directly by transmission spectroscopy. Fortney et al. make a clear prediction that the transmission spectra of highly-irradiated planets should be dominated by TiO opacity, which can be distinguished from Rayleigh scattering because the opacity decreases in the u band. Specifically, hot planets (class

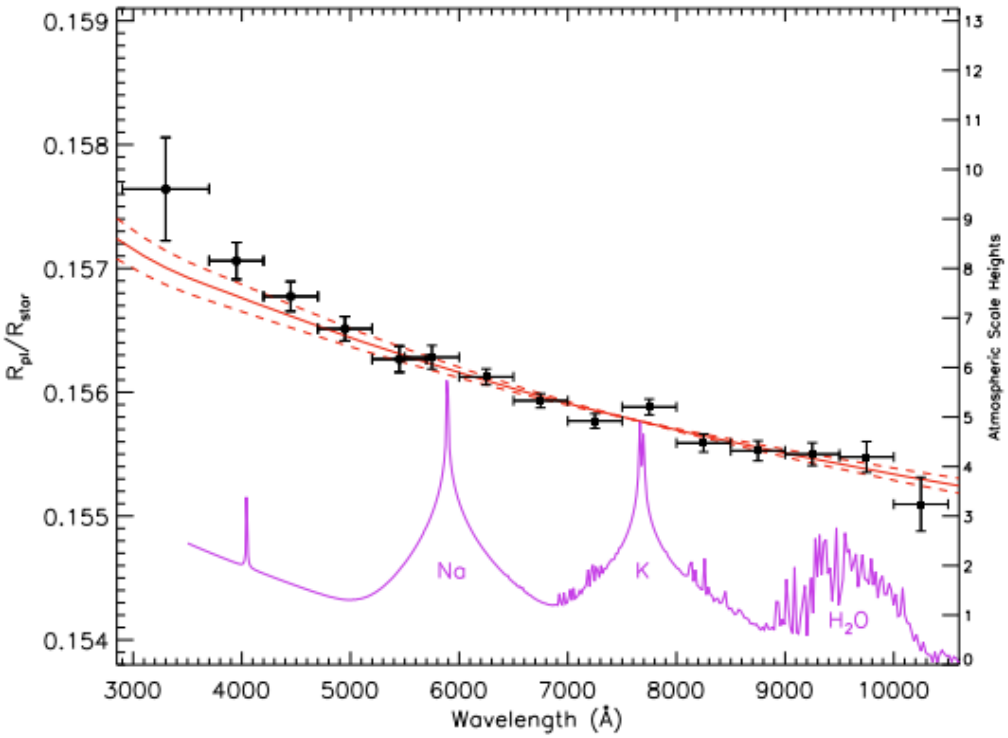

Figure 1.19: STIS and ACS transmission spectra for HD189733b. (From Sing et al. [2011]). The wavelength bins are indicated by the X-axis error bars and the 1- error is indicated by the Y-axis error bars. The prediction from ACS Rayleigh scattering (solid and dashed lines) is also shown, as is a haze-free model atmosphere for HD 189733b from Fortney et al. [2010] which uses a planet-wide average T-P profile, and is normalized to the radii at infra-red wavelengths.

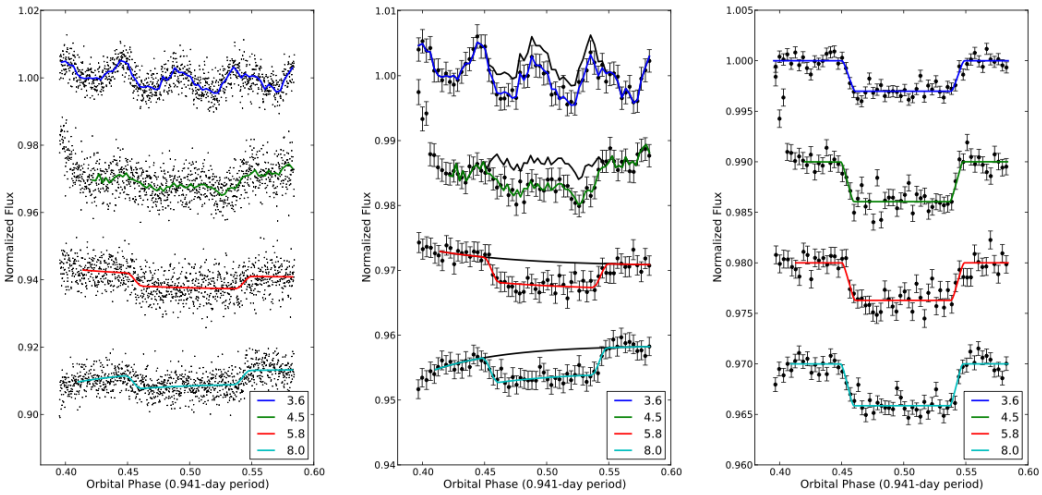

Figure 1.20: . Secondary eclipse observations of WASP-18b using the Spitzer space telescope. The panels show the raw Spitzer fluxes (left), the detrending applied based on known intra-pixel dependencies of the detectors (middle) and the resulting light curves with the corresponding fits (right) for all 4 bands available ($3.6\mu m$, $4.5\mu m$, $5.8\mu m$ and $8.0\mu m$). From Nymeyer et al. [2011]

pM) are predicted to have optical opacities dominated by TiO molecular bands, while in cool planets (class pL) the TiO should have condensed out of the atmospheres. The strong optical TiO opacity results in a temperature inversion in the upper atmosphere of the planet, driving infra-red molecular bands into emission and explaining the high brightness temperatures measured with Spitzer. They predict this transition to occur for irradiation levels higher than $\approx 1 \times 10^9 \mathrm{ergs}^{-1}\mathrm{cm}^{-2}$. However, recent measurements suggest that this threshold may not be accurate. Observations of the secondary eclipse of WASP-4b by Beerer et al. [2011] suggest this highly-irradiated planet has a weak temperature inversion or no inversion at all, contrary to expectations. Moreover, recent discussions on this topic seem to show a change in opinion with regard to the existence of any sharp features in the atmosphere profile of exoplanets.

Further measurements are required to determine the bulk characteristics of the atmospheres of exoplanets. Specifically, it is often the case that measurements in a small number of wavelengths are insufficient to distinguish between models with reasonably different parameters [Knutson et al., 2007; de Mooij et al., 2011] and therefore secondary eclipse depths at other wavelengths are required for a complete picture of the atmosphere of a given planet. Additionally, other high precision measurements are starting to reveal other features, such as the suggested presence

of water in the atmosphere of HD209458b [Swain et al., 2009; Beaulieu et al., 2010].

Observations of this nature mark the beginning of a new era in exoplanetary research, in which the properties of exoplanets are being measured and the emphasis is being placed on characterising planetary systems as much as possible with the current facilities.

Chapter 2

Understanding systematic effects in SuperWASP light curves

2.1 The importance of understanding systematic noise

Wide-field ground-based surveys are a prime example of astronomical instruments that can be limited by both random and systematic sources alike. Improving the photometric precision is strongly dependent on the compensation for any systematic effects which, by definition, can be understood and potentially corrected. Examples include the effects of atmospheric extinction, inter-pixel dependencies as the stars move across the chip, clouds, and focus variations, among others. Moreover, an analysis of correlated sources of noise almost certainly leads to better understanding of the instrument in question and brings the potential of the implementation of upgrades and improvements. This Chapter describes a study of the noise sources present in the SuperWASP project but many of its conclusions apply to any optical survey.

2.2 Reduction pipeline

The automated nature of the SuperWASP project is not limited to the observatory control itself. It extends to the software reduction pipeline that it employs. Data are collected by the instruments, transferred to the UK, where the reduction is triggered, and eventually ingested into an archive. The many steps of this reduction are largely described by Kane et al. [2004] in their description of the pipeline used

for the WASP prototype camera. The outline of this pipeline is briefly described below as it has a direct impact on the understanding of the sources of systematic noise present in the final light curves.

The processing of individual images follows a few steps before photometry is performed. Each image is statistically analysed and classified as either bias, dark, flat, science or unknown. Nightly master bias, dark and twilight flat-field frames are produced as described in Section 1.5 and applied to science images. The nightly flat-fields in particular use frames from previous nights with exponentially reduced weighting. This is done to improve the photon noise on the flat-field calibration frame, since it would be a dominant source of noise if only the night flats were used. Whenever the weather did not permit flat-field frames to be taken, flats from the nearest night are used. A bad-pixel mask previously generated is applied and an astrometric fit is found [Pollacco et al., 2006]. The pipeline then uses SExtractor [Bertin & Arnouts, 1996] to create an object list of all detected stars in every image and the coordinates of the field are used to extract sources from the USNO-B1.0 catalogue [Monet et al., 2003] as the photometric input catalogue. An aperture is placed at all positions of stars brighter than a limiting magnitude (r2 $\leq$ 15) and aperture photometry is performed using 3 different sized apertures (2.5, 3.5 and 4.5 pixels in radius) selected from visual inspection of typical images. This ensures that the photometry is always done on known objects and that it is centred in a consistent position. The r2 magnitude information refers to the filter used with the second epoch Schmidt photographic plates from by the UCAC3 (U.S. Naval Observatory CCD Astrograph Catalog) image archive, and is therefore not as reliable as modern all-sky surveys. However, due to the relatively low efficiency of photographic plates when compared to CCDs, this archive contains information on bright stars which correspond to the targets of interest for the SuperWASP instrument. Moreover, the r2 filter (579-642 nm) is located between the Johnson V and R magnitudes and, hence, within the SuperWASP filter wavelength range. The final SuperWASP photometry uses the 3.5 pixel radius aperture and the flux ratio between measurements from the other aperture sizes are used for assessments of blending from nearby objects. The photons from the pixels inside the aperture are counted and the estimated background flux from an annulus around the apertures is subtracted, providing the flux from the source only.

The post-calibration stage computes and corrects for the four main trends in the photometry: primary and secondary extinction, instrumental color response and zero-point [Pollacco et al., 2006]. This process ensures that, once all measurements for a given star (often from multiple cameras) are combined, the inconsistencies in

flux levels are minimised. This is followed by the implementation of de-trending algorithms, such as that developed by Tamuz et al. [2005]. We will refer to this algorithm as *Sysrem*. Sysrem analyses all light curves from a given field simultaneously with no prior knowledge of the existing systematic effects and fits a basis function to all stars with different weights in order to minimise the presence of any trends. This code is very powerful in removing systematic noise due to detector efficiency, PSF changes with time, seeing and focus evolutions and even airmass. In other words, any time-dependent trend that is present in a large number of stars simultaneously can be efficiently removed. This step is crucial in achieving high-precision photometry of many stars in a given field, as it is somewhat equivalent to using every star in the field as the comparison star for every other star in the same image. Indeed, a large number of wide-field photometric surveys deploy this procedure to de-trend their light curves.

The final stage of the pipeline process consists of the transit searching procedure. This step is done after the data have been ingested into the SuperWASP archive. It uses a searching code based on the Box-fitting Least Squares algorithm [Kovács et al., 2002]. Stellar light curves with planetary transits can be approximated by flat lines periodically disturbed by a decrease in flux. Since surveys like SuperWASP do not achieve good enough precision to resolve the ingress and egress well, a periodic box shaped transit is fitted for all periods within the range of interest. This is the final stage of the automated processing and is followed by visual eye-balling made by the SuperWASP team, which selects candidates for photometric and radial-velocity follow-up.

The design of the SuperWASP project is aimed at finding transiting planets orbiting bright ($V < 12$) stars. This is mainly because these stars are the easier sample to perform follow-up on and are generally optimal for other studies. A simple consequence of this is the fact that correlated noise tends to dominate as photon noise becomes negligible when the data are binned up in time.

Typical sources of systematic noise often come from changing weather conditions and degradation of the instrument. Clouds and changes in the focus across the field of view can introduce features in the light curves that are not easy to remove. If the same trends are present in a large number of stars, Sysrem is generally capable of minimising these effects. However, inconsistencies in the pointing of the telescope causes the stars to drift in CCD coordinates over time. This is a large source of systematic noise that is not common to large numbers of stars, but fixed in CCD space. Section 2.5 contains a diagnostics study of what factors can be the source of such noise.

2.3 Noise model

In order to understand the various sources of noise present in the SuperWASP light curves, it is important to consider the expected limiting precision the instrument can achieve. This is a theoretical low threshold of noise where several sources were considered in order to model the instrument's performance as a function of stellar magnitude. Since the depth of planetary transits is a measurement of the fraction of the stellar light blocked by the disk of the planet (see equation 1.3), it is most convenient to represent the noise amplitudes in fractional terms. For the inherent noise from the source counts and sky background counts respectively the photon noise was assumed and is therefore described in fractional terms by

$$\sigma_{target} = \frac{\sqrt{C_{target} t_{exp}}}{C_{target} t_{exp}} \tag{2.1}$$

and

$$\sigma_{sky} = \frac{\sqrt{C_{sky} n_{pix} t_{exp}}}{C_{target} t_{exp}}. \tag{2.2}$$

In these equations, t_{exp} is the exposure time used, which for the SuperWASP instruments is 30 seconds, C_{target} is the counts per second from the target, n_{pix} is the number of pixels inside the 3.5 pixel radius aperture and C_{sky} is the sky counts per second per pixel.

The readout noise contribution is calculated by determining the total contribution of the readout noise from all the pixels inside the aperture according to

$$\sigma_{read} = n_{read} \sqrt{n_{pix}}, \tag{2.3}$$

where n_{read} is the readout noise measured to be 3.3 electrons per pixel [Pollacco et al., 2006]. The contribution from the flat-fielding errors, σ_{flat}, is more difficult to estimate and is inherently inaccurate on the basis that it will depend on the location on the chip. Its estimation was done based on the photon noise present in a typical master flat field frame, produced from a set of 50 flat field frames per night. This noise, f_{flat}, expressed as a fraction of the electrons in a pixel, was found to be 0.001 (1mmag). The contribution from this source is estimated by

$$\sigma_{flat} = f_{flat} \left[\frac{C_{target} t_{exp}}{n_{pix}} + C_{sky} \right], \tag{2.4}$$

This model is based on the noise treatment of Southworth et al. [2009]. A similar approach is taken in Section 3.4 to determine the optimal defocus to use during a

transiting planet observation using a 3.6m telescope.

Finally, the contribution from astronomical scintillation is considered. This is characterised by an apparent change in brightness of an astronomical object as it travels through a medium, such as Earth's atmosphere. This variation in flux is caused by changes in local refractive indexes at several heights above sea level due to fluctuations in air density commonly related to temperature gradients. The component of the wind direction perpendicular to the line of sight of the observer moves these *air pockets* across the field of view of the telescope, causing these variations in flux. The contribution from scintillation is determined using the relation given by Young [1967], later used by Dravins et al. [1998] as

$$M_{scin} = 0.004 D^{-2/3} \chi^{7/4} e^{-h/H} (2t_{exp})^{-1/2}. \tag{2.5}$$

This relation gives the scintillation noise level as a fraction of the total electrons in magnitude units, M_{scin}, where D is the telescope aperture (m), H is the scale height of the atmosphere (8000m), χ is the airmass of the observation and h is the altitude of the telescope above sea level (m). For the SuperWASP instruments,the telescope aperture is 11cm and the altitude of the telescope is 2344m. This is the altitude of the northern facility, and all models presented are for cameras on this mount. The Southern facility is located at an altitude of 1798m and therefore the results would be similar. Naturally, the scintillation noise is dependent on the airmass of the observation, which is time-dependent for observations such as that from ground-based surveys. Hence, any calculations of the contribution from this source will be inaccurate and simply a estimate.

In order to convert the scintillation noise into a fractional contribution we reversed the error in magnitude units to a quantity comparable with the other sources:

$$\sigma_{scin} = 1 - (10^{-M_{scin}/2.5}). \tag{2.6}$$

Using these, a noise model for the SuperWASP cameras was determined. The magnitude range observed spans the range between V= 8 and V=16 and the theoretical determination of the count rate for a given magnitude requires knowledge of the zero point (ZP) of the camera. This is naturally dependent on which camera/telescope assembly is considered. Moreover, the SuperWASP pipeline determines the zero point for every image during the reduction process, by matching the fluxes of a set of standard stars to their catalogue magnitudes. A unique determination of the zero point for a given camera is hence not possible. A comparison

between the model and a specific data set is possible provided the measured average zero point for that night is used.

Figure 2.1 shows the theoretical noise contributions from each source as well as the combined noise (blue line) as a function of V magnitude. It can be seen that the flat fielding noise is negligible in single exposures and that the readout noise is not a dominant source at any point. The total noise is then dominated by the background sky for faint stars and stellar counts for bright targets. At the very bright end (V < 11) the contribution of the scintillation begins to have an impact, becoming the dominant factor at the very bright end (V < 9). This forms the basis of the models presented in Section 2.4, as a comparison with the SuperWASP light curves. For each case, the background sky level has to be adjusted to match the level present on each night, as well as the measured zero point and airmass. This is done from inspection of the images and from the relevant information from the SuperWASP archive.

2.4 Light curve quality

The quality of the photometry performed by the SuperWASP instruments is highly time dependent. Modifications and upgrades of the telescopes over the 8 year period of observations have changed the performance of the instrument, and an analysis of this evolution is possible. Generally, the root mean squared (RMS) is a good indicator of the inherent noise present in a light curve. This is a measure of the variance of the data points with respect to the average. The fact that it is independent of the number of measurements or their time sampling rate makes it an ideal indicator for comparison between many stars and data sets. The fractional RMS, RMS_{frac}, is defined as the ratio between the light curve RMS and the weighted average flux as

$$RMS_{frac} = \frac{\sqrt{\frac{\sum_{i=1}^{n}(x_n - \bar{x})^2}{n}}}{\bar{x}}. \tag{2.7}$$

Typically, fainter stars will have a larger fractional RMS, simply due to the Poissonian nature of the photon noise assuming no systematic sources of noise are present.

This parameter can be measured for each individual star's light curve over the course of one night as a measurement of the photometric precision achieved. Plotting this value as a function of stellar magnitude is a simple but efficient method to gauge the precision of each instrument. Figure 2.2 contains an example of such curve, where the blue and green data points refer to the data before and after the

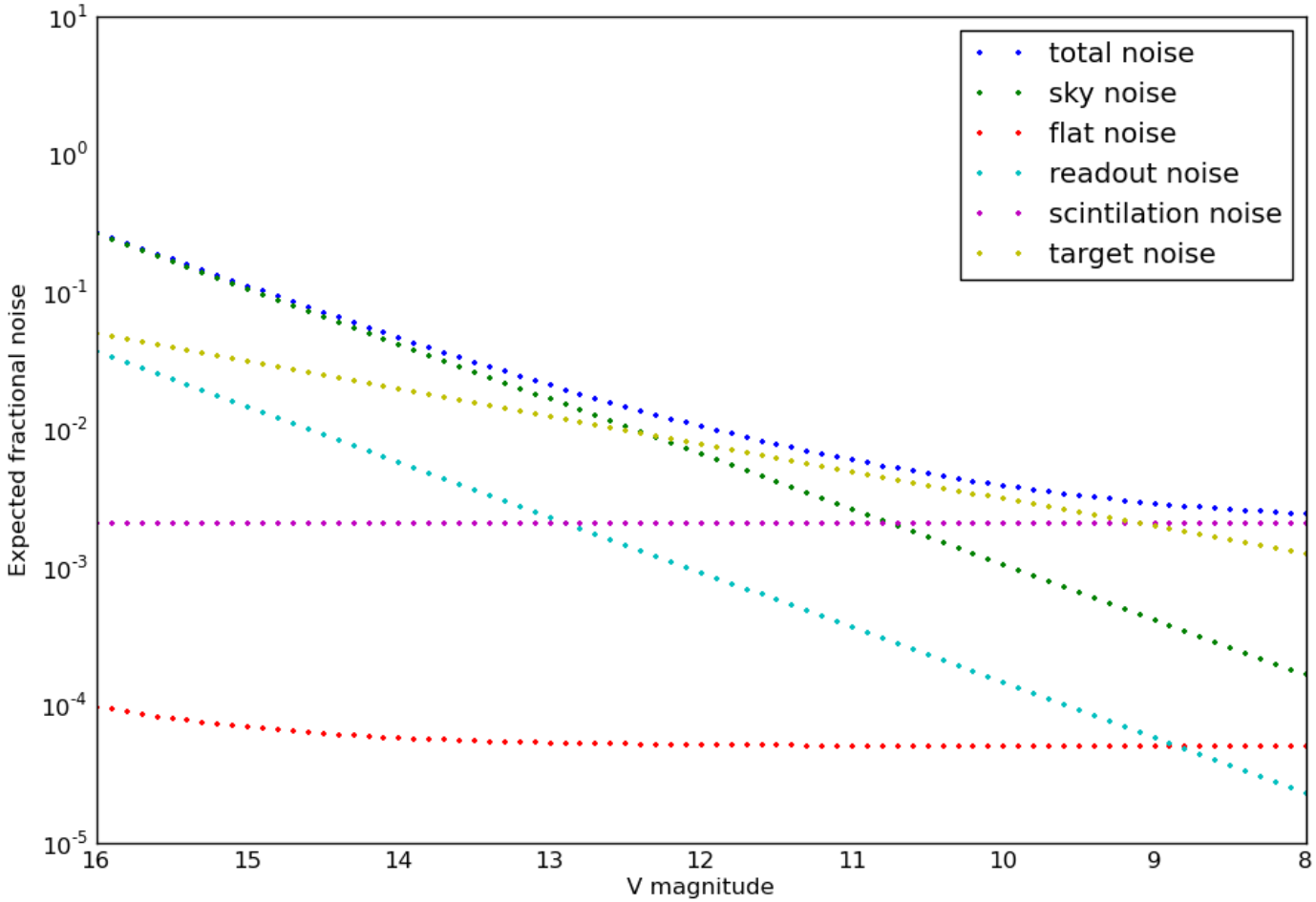

Figure 2.1: Noise model for the SuperWASP camera. The fractional contributions from all noise sources are shown as a function of stellar magnitude of a 30 second exposure during dark time.

implementation of Sysrem respectively. This data set refers to a typical cloudless night in early 2007 from camera 144 of the northern facility. A curve of the theoretical noise expected based on the model described in Section 2.3 is also included for comparison (black line). This line corresponds to the expected noise model for a star observed in the centre of the FOV, where maximum flux is obtained. However, since the SuperWASP lenses introduce a component of vignetting (approximately 40% drop in flux between the centre and the edges), a purple line is also included which corresponds to stars measured close to the edges of the FOV, showing the possible range of expected fractional RMS values for a given star. It is possible to conclude that these two lines contain the majority of the data sets and that vignetting is a major contributor to the spread of the RMS values. The large fractional RMS values of faint stars (those above the purple line) are likely to be due to the fact that stars close to the edge of the chip will drift in and out of the FOV due to the inaccurate tracking of the telescope and are sometimes not detected at all.

The green and blue data sets differ significantly from each other for bright stars, from which the presence of systematic noise is inferred. Sysrem appears to deal with this issue well. The primary source of noise is thought to be due to an issue with the telescope focus, found to be temperature dependent and non-uniform across the field-of-view (FOV). Since the aperture sizes are always fixed, as the focus degrades and the point spread function (PSF) size increases the photometry suffers from light loses and creates a large systematic effect. This issue was resolved during a large maintenance period in late 2008. The team responsible for the northern hemisphere instrument have used heating blankets to stabilise the temperature of the lenses, whilst the southern instrument employs an automated focusing system to stabilise the focus across the FOV.

Figure 2.2 also shows the resulting RMS from averaging data points in bins of one hour in length, which is closer to the typical time scales of planetary transits (red points) thereby representing the precision of interest, along with the corresponding theoretical noise curve. The model shown for the binned example (orange curve) was constructed under the assumption that all separate sources of noise, with the exception of the flat field case, are random (white) in nature and therefore propagate in a standard way when the data points are averaged. The flat field contribution was left unaltered since this source would potentially generate slow changing trends in the light curve. As described by Smith et al. [2006], a typical SuperWASP pointing is visited on average every 7 minutes, since the observing strategy has been chosen to cycle through a number of fields with 2 images taken for each visit to a single field. This leads to an average of 16 frames per hour, which was the number used

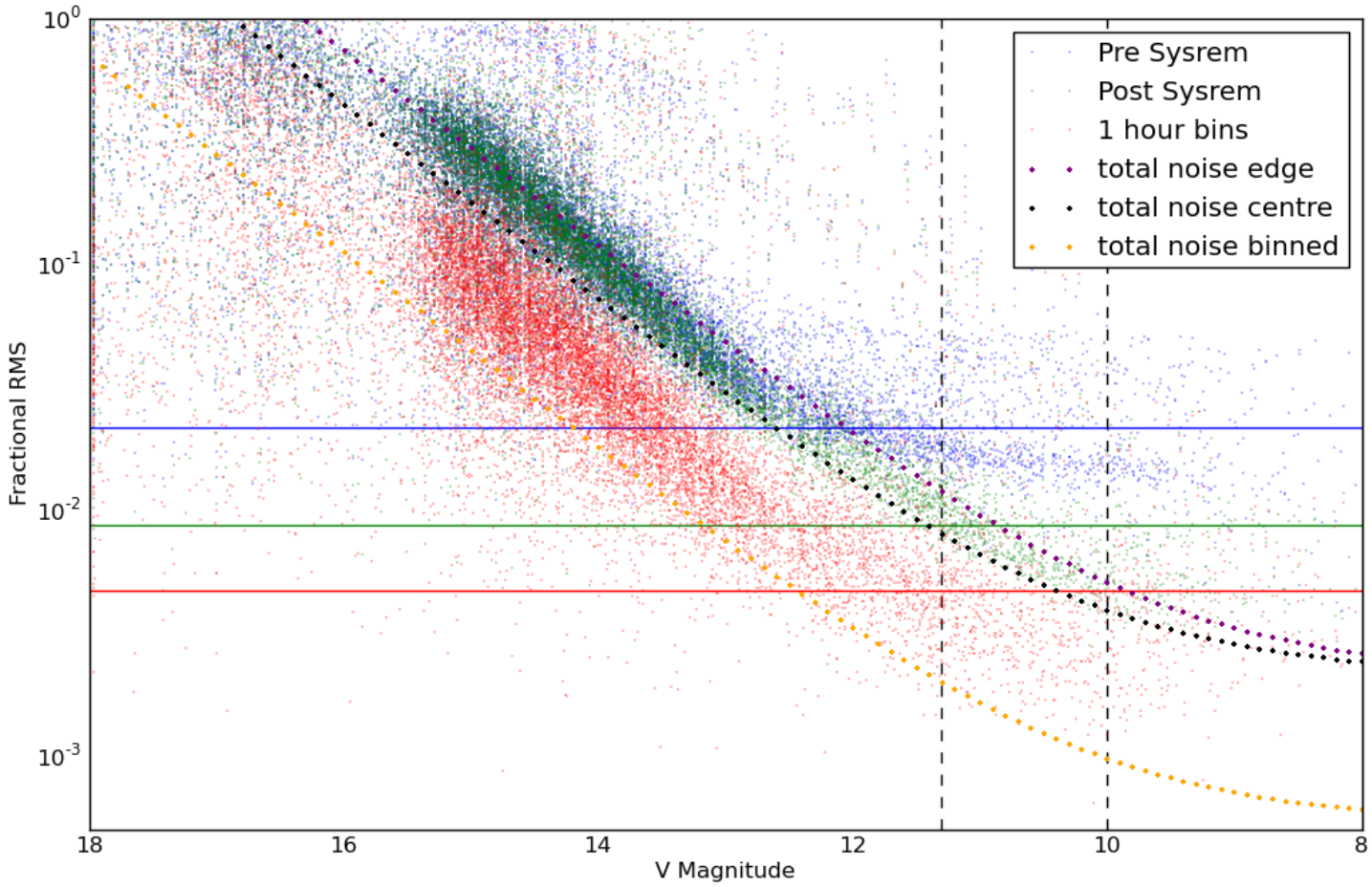

Figure 2.2: Fractional RMS as a function of stellar magnitude for stars belonging to field SW1522+3000, camera 144 on the night of 28/04/2007. The blue and green data sets represent the fractional RMS of the light curves before and after the application of Sysrem respectively. The red points refer to the results of averaging measurements into hourly time bins after Sysrem. The black and orange curves show the predicted noise models for un-binned and binned data respectively. Included is also the purple line, which represents the equivalent un-binned total noise model for stars observed at the edge of the chip and therefore suffering from the approximate 40% drop in flux caused by the vignetting of the SuperWASP lenses. The horizontal lines show the median of the fractional RMS of all the stars inside the region delimited by the vertical dashed lines.

for the model presented.

It is clear that the shape of the black curve agrees relatively well with the data after the application of the detrending algorithm. However, all noise models presented in this thesis fall below the bulk of the fractional RMS curves. A model in complete agreement with the data should, in principle, overlap the RMS curves. This is not the case for possibly a number of reasons. A single airmass value is used in the production of the model, as well as a single sky background level. Both these quantities vary through the night, making the light curves inherently heteroskedastic. Moreover, the background sky level is not uniform across the FOV due to the large vignetting visible in raw images, and the value used was obtained from images after the flat-fielding calibration. For stars of magnitude $V > 16$ the large spread is due to the fact that these are not always detected on every image, thereby making the RMS an unsuitable precision estimator. It is also possible to see that the model also underestimates the quality of the data for very bright targets, especially in the case where the data has been binned, suggesting the presence of an additional systematic effect remaining.

Another example of a similar plot is shown in Figure 2.3 referring to data from October 2009. These data were collected after the focus issue upgrade and it is possible to see that Sysrem has a much smaller impact, showing that the processed but still un-detrended data quality has improved.

We have implemented several diagnostic tests that have been applied to data after the ingestion into the archive. One of these consists of calculating a figure of merit that allows the assessment of the quality of a single night when compared to others. This is done to determine which nights contain deteriorating factors, such as clouds or especially poor seeing, and serves as a way to measure the performance of the instrument. The parameter in question is a measure of the median of the fractional RMS of a bright subset of stars over the length of the entire night for each observed field. A range of brightnesses between V=10 and V=11.3 was chosen for quality analysis, as this group is the brightest set observed that is found to never saturate the CCD. Figures 2.2 and 2.3 show vertical dashed lines that delimit this range where the median of the normalised RMS of the stars is indicated by the horizontal lines. The value represented by the blue line is stored in the archive. Therefore, each camera will have a value of this *median fractional RMS* for each field observed on any given night, providing a consistent data set for quality control. Several stars in this range show a large RMS, which bias the median measurement. These are likely to be stars that are not photometrically stable, but show variability, deep eclipses and/or flares. The Figures also show the

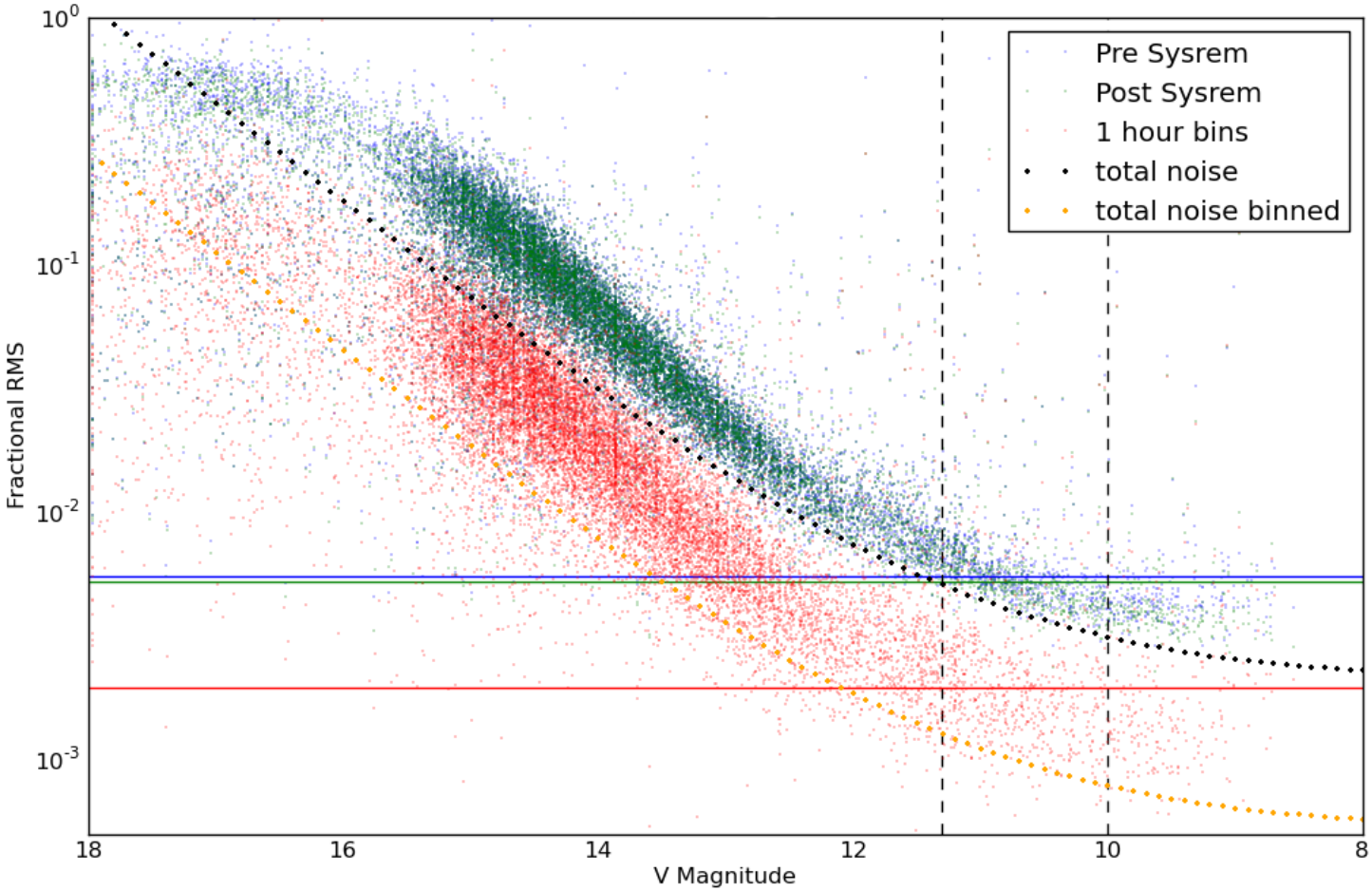

Figure 2.3: Fractional RMS as a function of stellar magnitude for stars belonging to field SW0118+0758, camera 144 on the night of 14/10/2009. The blue and green data sets represent the fractional RMS of the light curves before and after the application of Sysrem respectively. The red points refer to the results of averaging measurements into hourly time bins. The black and orange curves show the predicted noise models for un-binned and binned data respectively. The horizontal lines show the median of the fractional RMS of all the stars inside the region delimited by the vertical dashed lines.

equivalent value (red line) corresponding to the data after binning (these data are binned after the implementation of Sysrem), in which it is possible to see that it provides a measure of the quality of the data in time scales closer to the transit duration. This calculation is not yet implemented in the diagnostic step, but should perhaps be implemented, since the current calculation may be fundamentally limited by scintillation, as seen in Figure 2.1.

The median fractional RMS values are displayed in Figures 2.4 and 2.5, in which the results of all 16 cameras (8 cameras from the northern hemisphere facility, and 8 from the south facility) are shown as a function of time from the beginning of 2007. The vertical blue lines represent the beginning of each year and the data were available up to mid 2011. The red lines in Figure 2.4 show a period of inactivity due to a major hardware upgrade to solve the problem related to the temperature dependence of the focus of the telescopes. A clear improvement in the precision is visible on cameras 144, 147 and 148 after this upgrade and a consistency in the precision for the 3 years after shows that the upgrade was a successful enterprise.

A periodic variation in the minimum fractional RMS is present, attributed to the lunar influence on the photon noise from the background light (consistent with the values expected from the noise model), and the occasional sharp increases are due to the presence of clouds. It is nevertheless possible to conclude that the SuperWASP instrument delivers precision of under 1% on the brightest stars in its field on all telescopes, despite the fact that the maximum precision is not coherent between all telescopes. Nevertheless, a consistently good overall quality is key to finding planets, since any star observed to exhibit transits on different cameras is usually a good indicator of a real signal and a potential planet.

The data do not, however, fully reach the expected precision given by the noise model and, for bright stars, there is evidence of the presence of a source of systematic noise that the detrending algorithms are not able to fully correct for. This additional noise is likely to be related to flat-fielding errors, which were very simplistically estimated from the photon noise of the combined master flat in the case of the noise model. Section 2.5 describes a study to identify any residual errors from the flat-fielding stage that may be present in the light-curves.

2.5 Flat-fielding noise

One of the main strengths of astronomical surveys in general is the sheer volume of data available for diagnostic tests. In particular, some of SuperWASP's operational features make it possible for detailed studies of each camera's perfor-

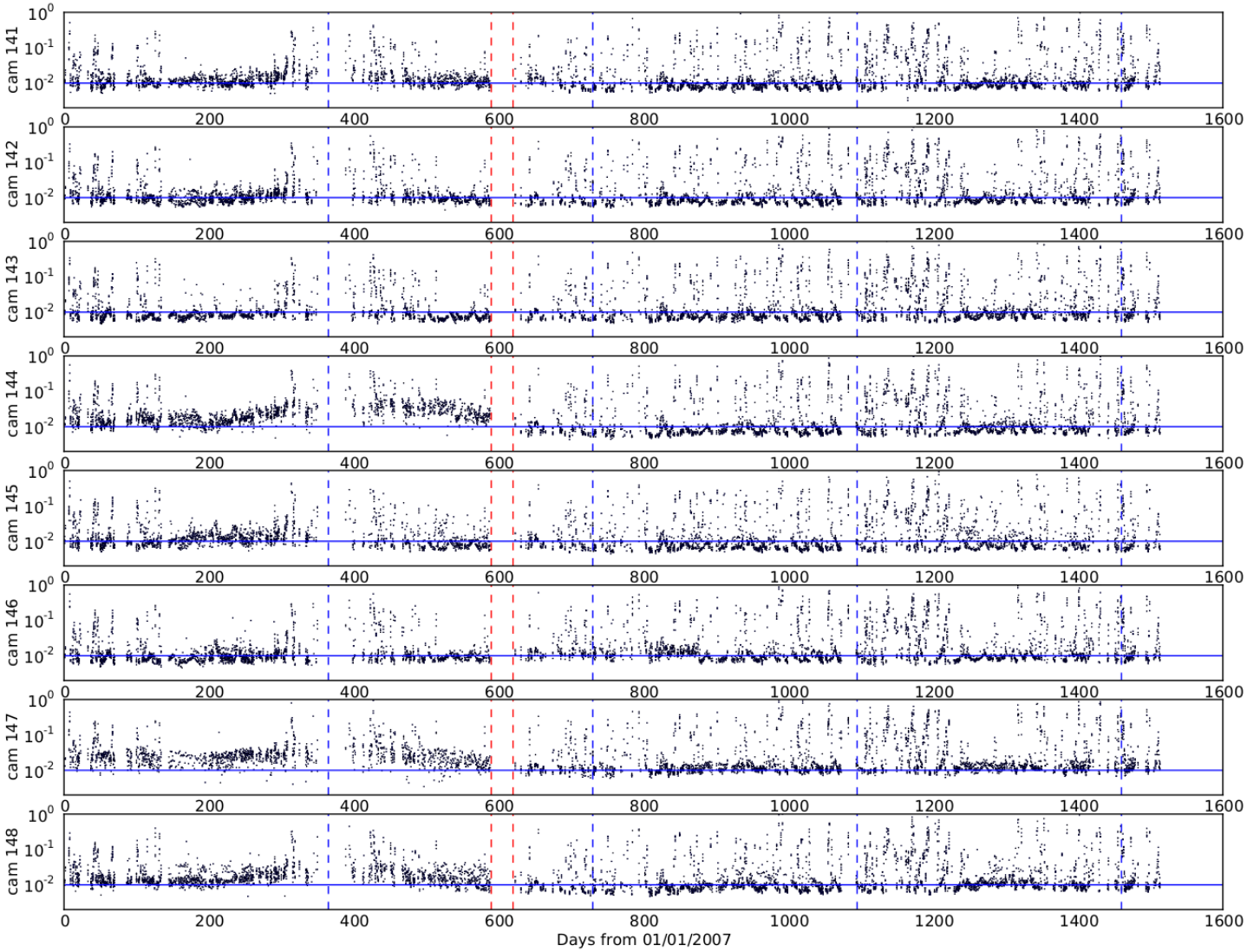

Figure 2.4: Median fractional RMS for all stars in the $11.3 > V > 10$ magnitude range as a function of time for all cameras of the SuperWASP North facility. The vertical blue lines represent the transition between each year, as the time axis represents the number of days from the start of 2007. The vertical dashed red lines show a portion of time where a major hardware update took place to solve a problem with a focal length temperature dependence. The horizontal blue line shows the 1% precision level.

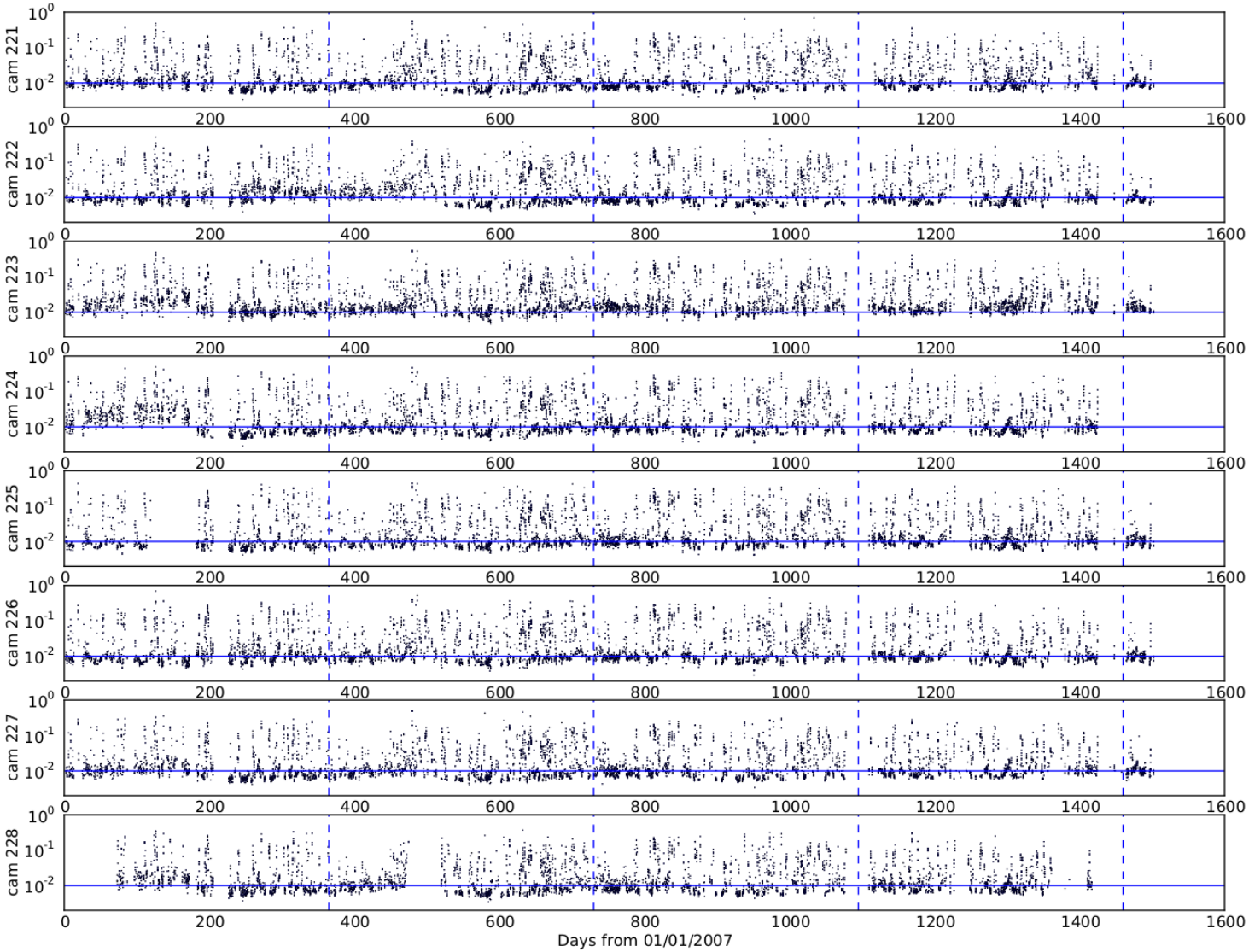

Figure 2.5: Median fractional RMS for all stars in the $11.3 > V > 10$ magnitude range as a function of time for all cameras of the SuperWASP South facility. The vertical blue lines represent the transition between each year, as the time axis represents the number of days from the start of 2007. The horizontal blue line shows the 1% precision level.

mance to take place once several years of data have been acquired. Flat-fielding errors are generally considered to be any multiplicative effects fixed in detector coordinates which, since the SuperWASP pointing accuracy provided by the telescope mount drifts by several pixels over the course of one night, can be a source of systematic noise.

We have used large data sets for each camera (typically all measurements of an observing season) to produce diagnostic plots of any feature fixed in the CCD chip. *Detector Maps* are the result of averaging the light curve residuals in detector space. This consists of gathering all photometric measurements centred on a given pixel and averaging the fractional deviations from the mean fluxes of each star. This process is then repeated for every pixel, and an image can be produced. Therefore, if a given pixel happens to have a higher sensitivity with respect to its neighbours, on average a flux measurement made using that pixel will have a slightly higher value and it will appear brighter on the detector map. The pointing drift of the telescope is indeed an advantage to this method, as it ensures that the whole CCD is sampled over time. It is however necessary to use data on time scales of one year or longer in order to obtain enough signal to noise to distinguish any features.

Detector maps show features that are present in the light curves and that are fixed in CCD coordinates at any stage of the processing. In fact, all detector maps presented in this thesis will have been produced using completely reduced data after the last stage of de-trending. These maps are therefore a good diagnostic of the presence of systematic effects fixed in detector coordinates and can provide useful insight into potential improvements to the system.

From private communication with Dr. Richard West we obtained a set of detector maps for the SuperWASP cameras. The top panel of Figure 2.6 shows an example of the detector map for camera 141 (SuperWasp-North), produced using data from the 2006 season and early 2007[1]. The study performed here focuses on data for this camera, but similar features are seen in all cameras. The results show that there is clear structure present in the data in the form of several distinct features whose strength is comparable to the typical transit signal depth and hence may compromise planet detection. These features are numbered in the Figure as follows:

1. Dark lines that run diagonally across the frame. Typically 0.7% depth.

2. Large dark blobs at localized places in the picture. Around 0.6% depth.

[1]Detector maps for all cameras produced with data from 2006 can be found at `http://isolde.star.le.ac.uk/detmaps/tam_dw_norm.html`, along with the corresponding downloadable FITS files.

3. Light wispy patches that appear at several places in the frame. About 0.6% higher than average.

4. Bright annuli around a patch of dark pixels. The depth and peaks of these features depend on the individual example, but can amount to up to 3% minimum/maximum.

5. One of five regions of the CCD where a dark strip is surrounded by a bright region. Dark patch contains a cluster of darker pixels. Up to 12% depth in the central cluster and typical peak of 7% in the surrounding zone. This feature looks like an extreme case of feature 4.

6. Dark line that represents a trail left above feature 5. Typically 4% below average.

7. Dark rows of pixels at the bottom of the frame, standing just above another series of bright rows.

8. Dark rows of pixels that run horizontally across the chip. Typically 0.8% depth. There are 2 more lines at other positions above this one, which are light instead of dark and are fainter and harder to see. These can be up to 5%

9. Bright spots located at various places on the image, some of them being clusters of NaN's (Not a Number; See section 2.5.1 for definition), corresponding to pixels flagged out by the pipeline using bad pixel masks. Others have values associated with them, typically around 1% above the average.

10. Dark spots with no rings around them. Most cases contain a small halo of bright pixels immediately surrounding them. Typically 0.8% depth. Figure 2.9 contains enlarged sections of the frame with examples of these.

2.5.1 Known Features

Several of the features described above are related to known characteristics of the WASP data/pipeline. The clusters of NaN's (Not a Number) in the detector maps (feature 9) are due to the normal running of the pipeline, rejecting measurements in which a known bad pixel falls in the source aperture. The We note, however, that these clusters often have immediately nearby individual pixels with deviations of up to 4%, both positive and negative. This may just be photon noise resulting from a lack of coverage in these pixels or could be due to not enough pixels being flagged as bad in the bad clusters.

The bright rings surrounding dark features (feature 4) are due to a bug in the masking of bad pixels in flat fields and in the background estimation that was only clipping positive outliers. The author's understanding is that these bugs have been fixed in the current version of the pipeline.

The dark cluster of pixels surrounded by bright halos that have a vertical trail (features 5 and 6) look like an extreme case of the dark spots with rings. However in this case the dark spot is caused by a CCD defect. The specific case of the highlighted patch contains 6 NaN pixels flagged out by the pipeline, indicating that it is directly associated with known defective/anomalous pixels. The fact that the dark trails (feature 7) are connected to the cluster of dark pixels suggests that these are a consequence of the way the pixels in the main cluster affect the values of others during the CCD readout stage.

The bright and dark rows at the bottom of the frame (feature 7) consist of a well defined structure. The bottom and top edges of the frame have 5 rows consisting of NaN's which must have been flagged out in the pipeline, but at the bottom end rows 6-17 (just above the 5 flagged out rows) are represented as a brighter region up to about 5% peak and are followed by the dark rows visible in the picture, which can have depths of 2%. This effect may be caused by the extra bright rows affecting the background fit calculation made by the pipeline and then biasing any stars that fall on this region. Hence, possibly a more severe cut is needed at the bottom of the frame, as it may still be affecting the light curves considerably.

The horizontal rows across the chip (feature 8) have been noted and seen on individual images before and thought to be related with the driver software, but their presence in the detector maps shows that they have a significant effect on the light curves.

2.5.2 Investigating the features on the detector maps

In order to determine the origin of the unknown features in the detector maps, we have attempted to use the background light in the science images to investigate any potential nightly evolution. All images analysed on this Chapter have been corrected for bias and dark current levels as described in Section 1.5. Bad pixel masks were ignored for this study, allowing any bad pixels to be visible in the results. The science images have not, however, been flat-fielded, where potential correlations with the features in the detector maps can be found.

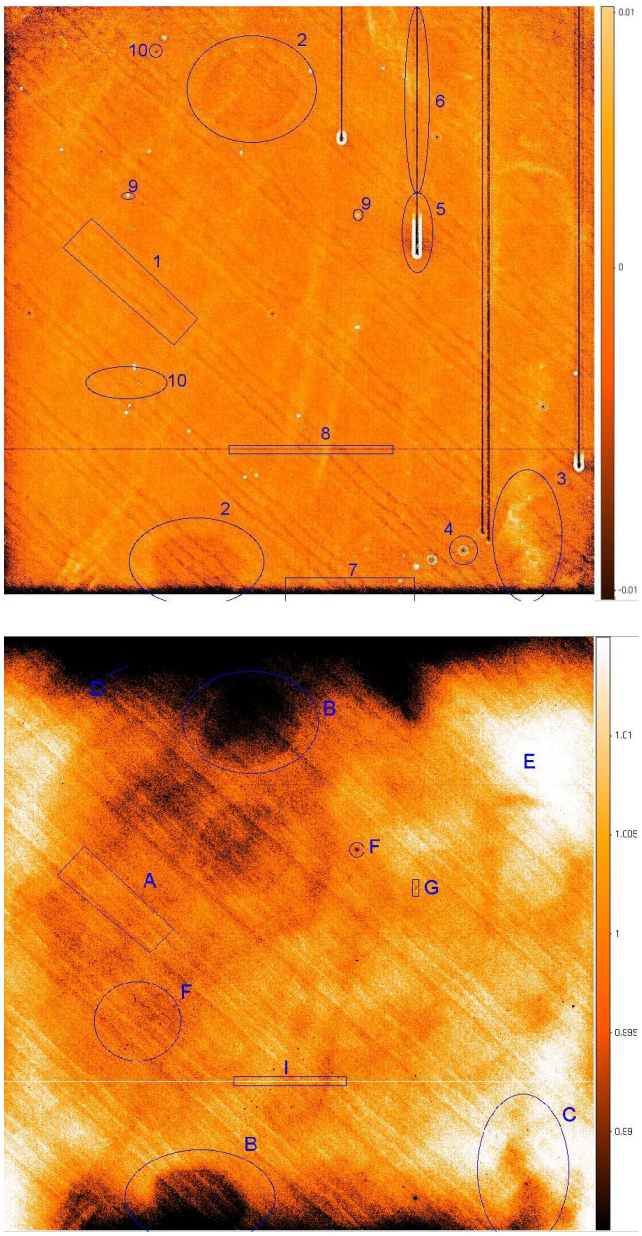

Figure 2.6: Top Panel: 2006 Detector Map for camera 141, produced with data from the 2006 and early 2007 seasons. Bottom Panel: Twilight flat obtained from the combination of all twilight frames for the night of 12th October 2006, camera 141

Initial attempt to view detector features

An initial test was performed to evaluate the feasibility of visualising these features on single images, which involved the use of a median filtering algorithm.

This uses a running box of a given size, replacing the pixel at its centre with the median of all the pixels within the box. This process acts as a blurring mechanism for single images and was used to remove their large scale background structure. The left panel of Figure 2.7 contains an example raw frame from the SuperWASP instrument in which the most clear feature is the strong vignetting. The particular median filtering algorithm used (from the IRAF[2] software package [Tody, 1986, 1993]) allows for sigma clipping inside the filtering box and rejection of any values above 15,000 counts (chosen to reject any pixels from very bright stars), as well as wrapping at the edges of the frame when insufficient pixels are available. This level was . The immediate result showed the presence of feature A (diagonal lines in Figure 2.6), thereby demonstrating that these features are present in the twilight flat fields. However, this method was found to be unusable for a detailed study because the median filter images still show residuals due to bright stars. In order to blur out the images without compromising the overall background structure determination a box of 50x50 pixels in size was chosen for the median filter. This was also found to blur out features that have lateral dimensions larger than the area covered by the averaging box (such as feature B) and therefore this method was abandoned.

The adopted procedure to study the origins of the features visible in the detector maps was based on measuring the large scale structures separately for each image and combining images after the correction to enhance the signal to noise and reject any outliers. The following Sections contain details regarding this method.

Gradient removal

Each image shows an overall gradient present. In the current WASP pipeline "Gradients in the sky brightness across each flat field are removed by rotating each image through 180 degrees about the center of the vignetting pattern, subtracting the rotated image, and performing a planar least-squares fit to the residuals . The gradient is then divided out from each flat field exposure." [Pollacco et al., 2006]. A similar method was used to remove the gradients from each frame (both twilight flat fields and object frames), using the median filter of each image to measure the values of such gradients.

To determine approximately the center of the vignetting, a horizontal strip of 200 pixels in width through the middle of the median filter frame was considered. The column values of that strip were summed and the maximum value used as the

[2]IRAF is distributed by the National Optical Astronomy Observatories, which are operated by the Association of Universities for Research in Astronomy, Inc., under cooperative agreement with the National Science Foundation.

central coordinate. The same principle was used for the vertical direction. Figure 2.8 shows the horizontal and vertical direction results of this sum in the top two panels. The clear vignetting shape dominates these curves. This method was found to yield a good estimate of the center of the vignetting pattern, but is nevertheless not immune to error if there is a bright star near the center which may not have been blurred out entirely. However, the measurement of the gradient was found to be quite insensitive to the centre of rotation, and so this estimate was used. Each median filter is then rotated 180 degrees about the estimated vignetting center, the original median filter is divided by the rotated version and collapsed in both directions. This process results in two linear profiles, one for each direction (shown in the bottom two panels of the figure). A linear fit was obtained for each case, where the gradient is twice the real image gradient in both directions. A 2D map was then produced using these gradient values, and subsequently used to correct the original image and its median filter.

Vignetting removal

Once all frames have been corrected for gradients, the vignetting profile had to be removed. Again, the median filter was used to measure this profile and a model was produced to correct the science frames.

At this point it is important to find the center of the vignetting pattern with better precision, since the gradient removal stage shifts the centre from its original position in the raw frame. To achieve this, we developed a method based on a center of mass approach to find the centroid of a distribution. Since all frames have been corrected for an overall gradient, the center of the vignetting profile was expected to be close to the center of the image, and hence an initial position guess at the exact center of the frame was used as the starting point. A circumference of 100 pixel radius was considered for the center of mass calculation and the estimation of the vignetting centroid position is done iteratively until the deviation between calculations is less than 0.2 pixels.

We estimated the shape of the vignetting by finding the polar profile of the image[3]. This process involves taking the average value of all the pixels equidistant to a reference point (the estimated centroid coordinates) and calculating what this average is for all distances from the center to the furthest corner. This profile was found to be sufficiently smooth to be used as a basis for modelling the vignetting, since it was measured using the median filter. Any random variations along the pro-

[3]Part of the software used for this process was based on a script written by Dr Richard West that used a previously existing centroiding procedure, part of the Q programming language.

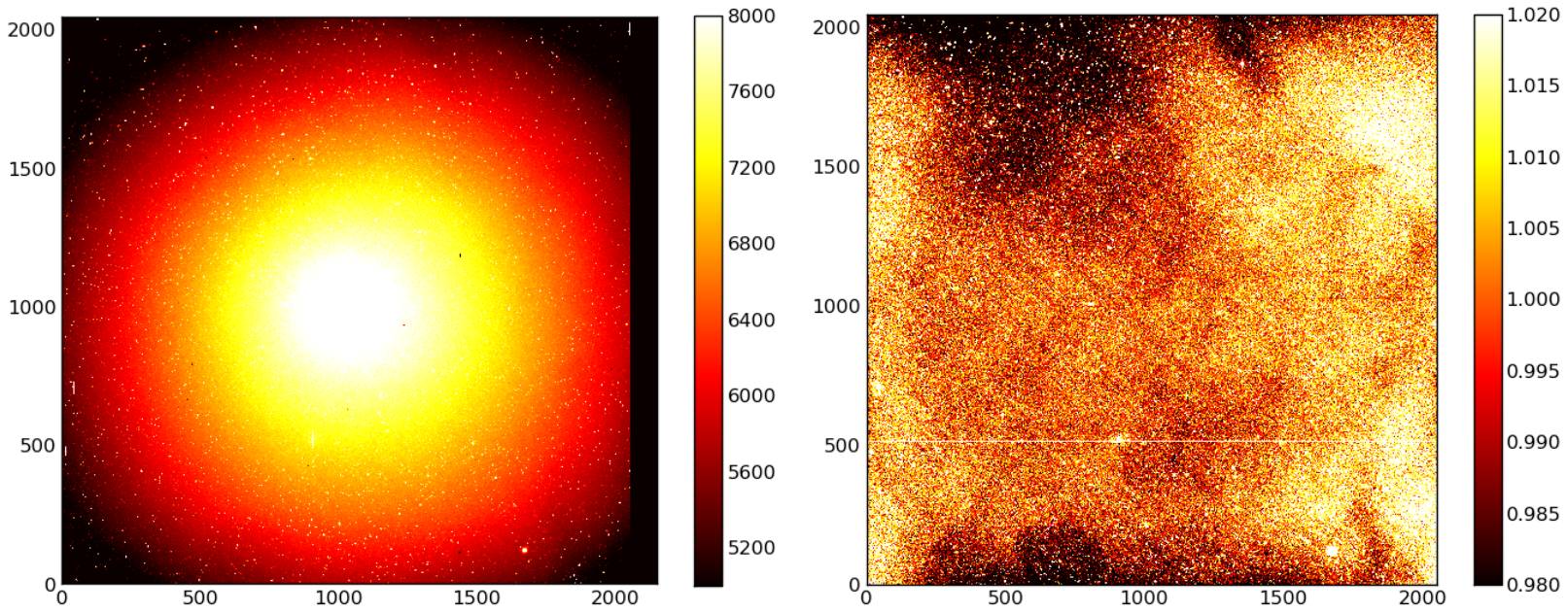

Figure 2.7: Example raw SuperWASP image (left panel) and the result of applying the method described in Section 2.5.2 (right panel). This image was taken on 24th July 2008 using camera 141 (La Palma).

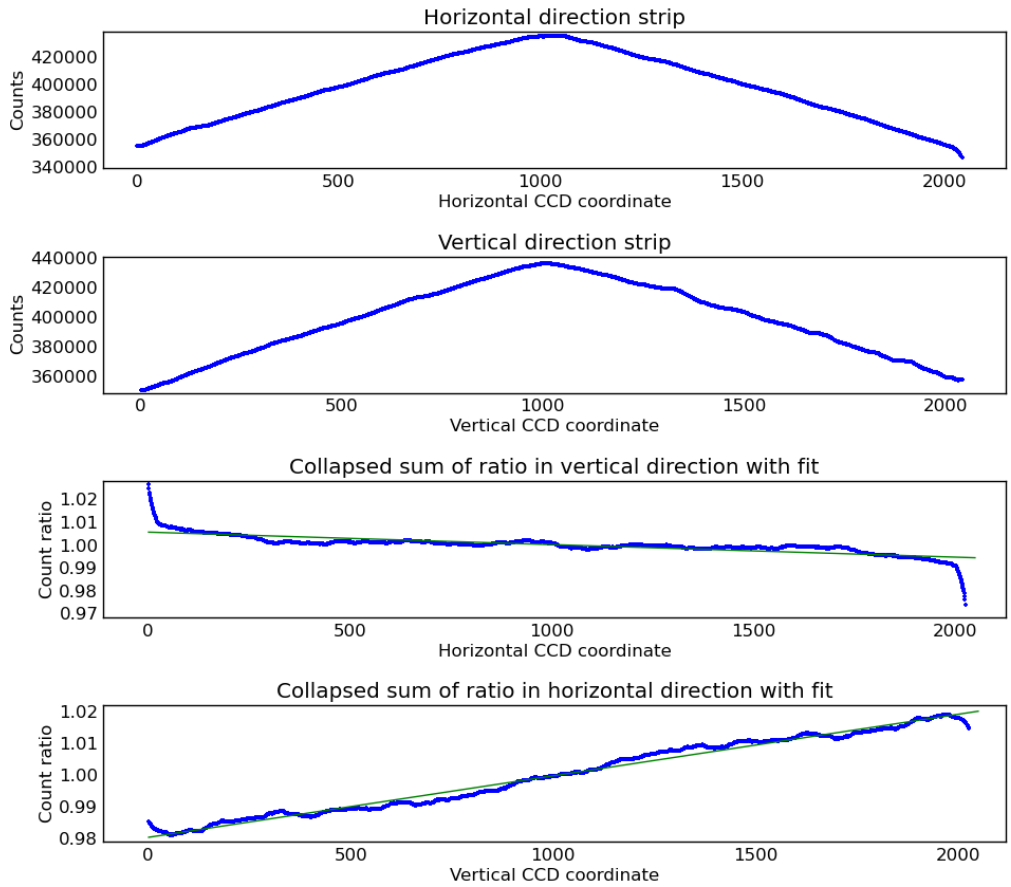

Figure 2.8: The top two panels show the summed values of columns/rows of strips of 200 pixels in width through the middle of the median filter frame in both directions. The bottom panels contain the result of rotating the image, dividing the result by the original image and collapsing all the values in both directions, along with the linear fits used to generate the 2D gradient map of the median filter.

file were considered negligible. The polar distribution was then linearly interpolated with a centered radial profile model, which produced the desired vignetting model.

Every image was then divided by this distribution, which not only corrects for the vignetting present, but also normalizes each individual frame to a common scale. An example of the result of this method is shown in the right panel of figure 2.7, which shows that there is no clear vignetting or gradient remaining, but still shows overall complex structure, as well as examples of the features also present in the detector maps.

Frame combination

The final removal of stars was achieved by median combining a set of images. The fact that for a given field observed by the WASP telescopes the positions of stars drift across the chip is also a major advantage to this approach. However, in the case of very crowded fields this method of stellar removal may not be entirely efficient, since a given pixel may contain light from a star in all observed fields on a given night. This problem was surpassed using some complementary techniques, such as pixel range rejection.

A full set of normalized gradient and vignetting corrected frames was available at this stage. The nightly frames were combined to generate a flat field frame based on science frames only (night sky flats). These frames were median combined with the additional option of constraining the range of considered values to a maximum of 10,000 counts, in order to avoid the contribution from bright stars. This option proved critical, since the presence of stars can bias the calculation of the median for each pixel. This introduces unwanted diagonal lines in the night sky flats since stars drift across the chip during the night due to inaccurate pointing of the telescope. Hence, a restricted range of accepted values of $\{0.97; 1.03\}(\pm 3\%)$ was applied. This is not only to remove any residual presence of stars, but also to eliminate any outlier frames that may not have been successfully normalized because of errors in the correction process, such as failure to find the correct vignetting center due to a bias from a bright star close to the image center. An image scaling factor was applied before combination, using the median of each frame for that purpose. This ensures that the frames can in fact be comparable before the combining process.

2.5.3 Wavelength dependent features in the twilight flat fields

We suspected that the presence of certain features on the detector maps (features 1, 3 and 8) could be associated with the fact that the color of the twilight

sky is significantly different to that of the objects being observed. With this in mind, one can make flat frames on night time images, as long as there are enough background photons to achieve an overall good sampling across the chip. The night sky light changes color with lunar phase and, since the moonlight is essentially reflected sun light, any bright time will have a color close to that of the twilight sky. On the other hand, dark time is mainly dominated by OH emission. Therefore, dark sky background is more red and potentially closer to the color of the stars observed.

Twilight flat fields

In order to determine if any of the detector map features are related to the flat fielding stage, we analysed the twilight frames in search of these features. Gradients and vignetting were removed from every frame individually, and all frames from each night were then median combined to remove stars (as described in Section 2.5.2). The second part of Figure 2.6 shows a result of such method applied to a series of all 50 twilight frames for the night of 12th October 2006 (chosen randomly after ensuring that a full set of twilight frames were available), again for camera 141. The features present are labelled as follows:

- A. Bright lines running diagonally across the Figure, coincident with feature 1 in the detector maps. Typically 0.5% amplitude.
- B. Dark blobs that correspond to feature 2. Varying from 0.4% to 1.2% depth.
- C. The dark wispy patches that appear at several places in the frame which anti-correlate with feature 3 in the detector maps. About 0.5% lower than average.
- D. The large, dark zones in some places. Typically 2% depth.
- E. The large, bright zones in some places. Typically 2% peak.
- F. Dark spots throughout the CCD, corresponding to examples of both features 9 and 10 in the detector maps.
- G. Dark pixels with a slight trail, at the same locations as features 5 and 6. Up to 8% depth.
- I. A bright row of pixels placed at the same coordinate as feature 8. Around 2.5% above surroundings. Two other dark faint lines appear at the same positions as in the detector map, but are very hard to see in Figure 2.6.

Many features in the twilight flats can also be seen in the detector maps. Interestingly, the major diagonal lines, the wispy patches, the horizontal rows and some examples of dark spots (features A, C, I and F) anti-correlate with features in the detector maps (features 1, 3, 8 and 9 respectively). It may be that these features are being overcorrected for during the flat field process (see Section 2.5.3). In contrast, the dark blobs (feature B) correlate with feature 2, albeit with smaller amplitude. Moreover, the large scale dark and light structures (features D and E) do not appear in the detector maps at all, suggesting that they do not have a significant effect on the light curves. Either they are successfully flat fielded, or their scale is sufficiently large to be removed by the detrending algorithms.

Figures 2.9 and 2.10 contain enlarged sections of detector maps and the corresponding regions in the twilight flats to show smaller features in further detail and to emphasise correspondences. As can be seen in Figure 2.9, the patches of NaN's correspond to dark pixels in the twilight flats, confirming that these are flagged out pixels. The dark pixels with bright halos (feature 10) also correspond with bad pixels and should also be flagged by the pipeline. However, other dark pixels in the twilight flats do not appear in the detector maps. These are presumably stable and have been flat fielded out correctly. This demonstrates how the detector maps can be used to identify which features significantly affect the light curves and should be rejected, and which should not.

The bright rows followed by dark ones at the bottom of the frame (feature 7) show no significant presence in the twilight flats. This indicates that the effect is either variable or introduced at some point in the processing stage. The dark rows could be introduced due a bad background fit biased by the bright pixels.

Moreover, in Figure 2.10 it should be noted that the dark spots with bright rings around them (feature 4) have no corresponding feature in the twilight flats, confirming that they are from bugs in the processing (Section 2.5.1).

There is clear correspondence between the dark patches with vertical trails (features 5 and 6) and a series of darker pixels with a slight trail (feature G) in the twilight flats, but feature G is much smaller in size, even if much stronger. The reason that such small feature in the twilight flats yields such a significant feature in the detector maps underlines the importance of producing detector maps as a form of diagnosis. It seems bad pixels behave differently at different illumination levels. We have looked at the particular case of the highlighted regions in the Figure to analyse the vertical profile of features 5 and 6. Figure 2.11 shows the pixel values of such features in the vertical direction from the origin of the feature for several example frames. We have plotted this profile for the cases of twilight, full moon night, 2 dark

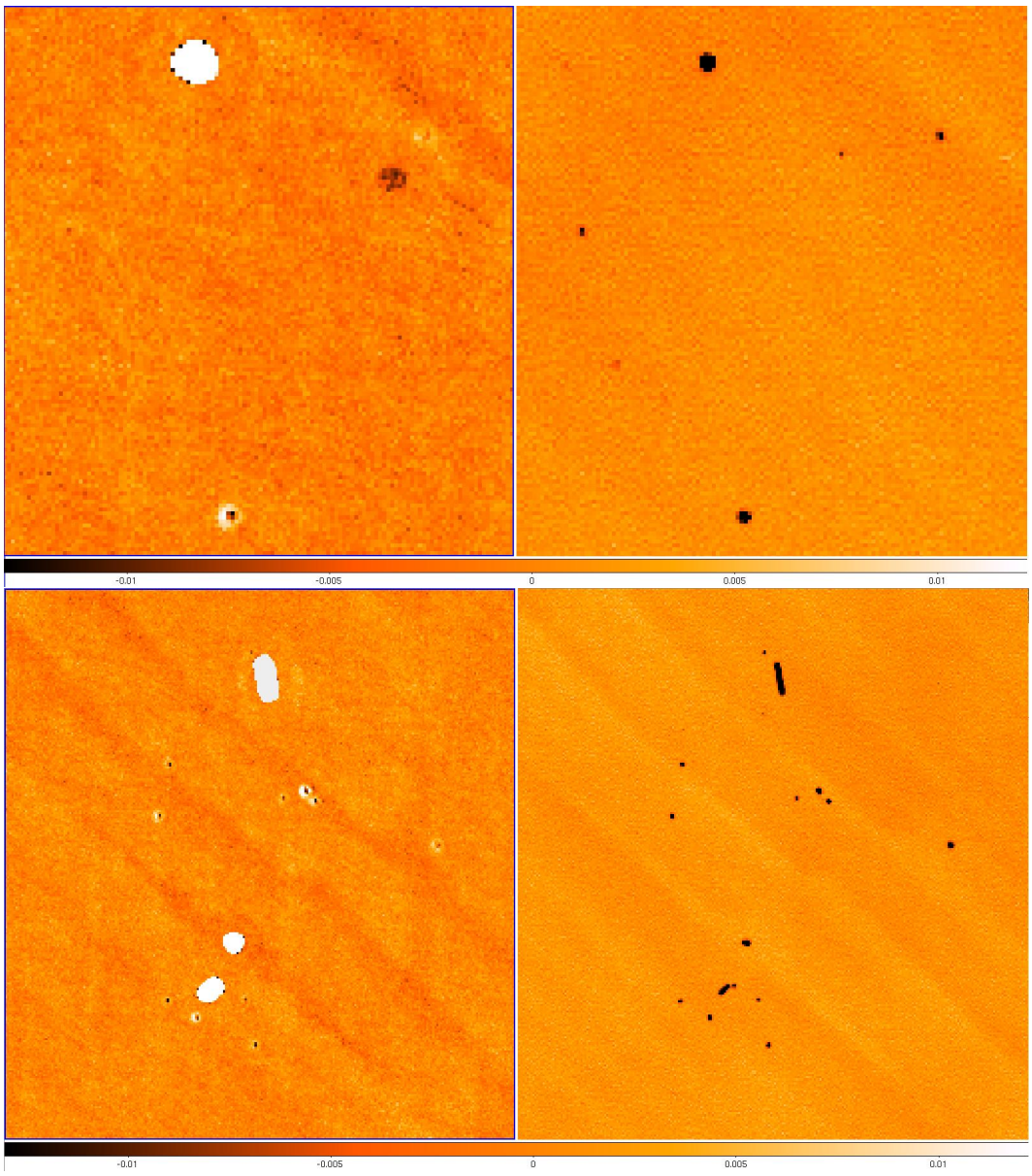

Figure 2.9: Selected enlarged regions of both detector maps (left) and twilight flats (right), showing examples from features 9 and 10

night examples and for the detector map. This provides a numerical view of how the bad pixels influence the values of their successors in the readout process. There is a relatively flat region before the values of the dark trail rise to match the background level. The length of trail depends highly on the illumination level, as does the initial value (the value being larger for higher number of background counts and the trail

being smaller for that case too). We have tested whether a fixed number of electrons is lost, but this is not the case. In fact, for two different example frames from a dark night separated by 2 hours, slightly different background levels have significantly different dark row lengths, which seems to suggest a non-linear effect taking place. The fact that the profile in the detector map appears constant (at about 5% depth) is puzzling. We conclude that the behaviour is not stable enough to be corrected and that the pixels contained in these features should be flagged out in the pipeline.

Raw frames

The method described in Section 2.5.2 was applied to a set of 12 nights between 18th July (full moon night) and 29th July 2008 (31st July being the new moon night) for camera 141 (SuperWASP North instrument), for both science and twilight frames separately. We describe this method in detail in the following Sections. Figure 2.12 shows a close up of the region that includes both the diagonal lines and one of the dark blobs (features A and B) for 12 successive nights taken from each twilight master flat. The numbers in the top left corner of each section refer to the date from which the data were taken. As expected, there is no variation on the strength of the features over the 12 day period. However, when the same principle is applied to generate night sky flats, the result is as shown in Figure 2.13. Features get weaker with fading moonlight, which suggests an overall CCD wavelength dependence. Also, the lunar light, being essentially reflected sunlight, should have a similar wavelength to the Sun's. This is consistent with the fact that for the full moon night case (18th July), the feature strengths between twilight and sky flats are similar.

2.5.4 Visual results from the sky flats

Feature A

Figures 2.12 and 2.13 provide only a visual inspection but it is possible to obtain numerical evidence of the wavelength dependence of selected features, by averaging pixels belonging to the same feature and producing one dimensional plots of pixel values running across the desired section. The case of feature A poses a problem, as one would like to combine pixels in a diagonal direction. This requires a process that enables an efficient comparison between pixels that fall on each diagonal structure. On the other hand it is desirable that the pixel values are conserved, and that no re-sampling is made. Hence, the method used implies a selection of a region of the image to be considered and, using one horizontal row as a reference,

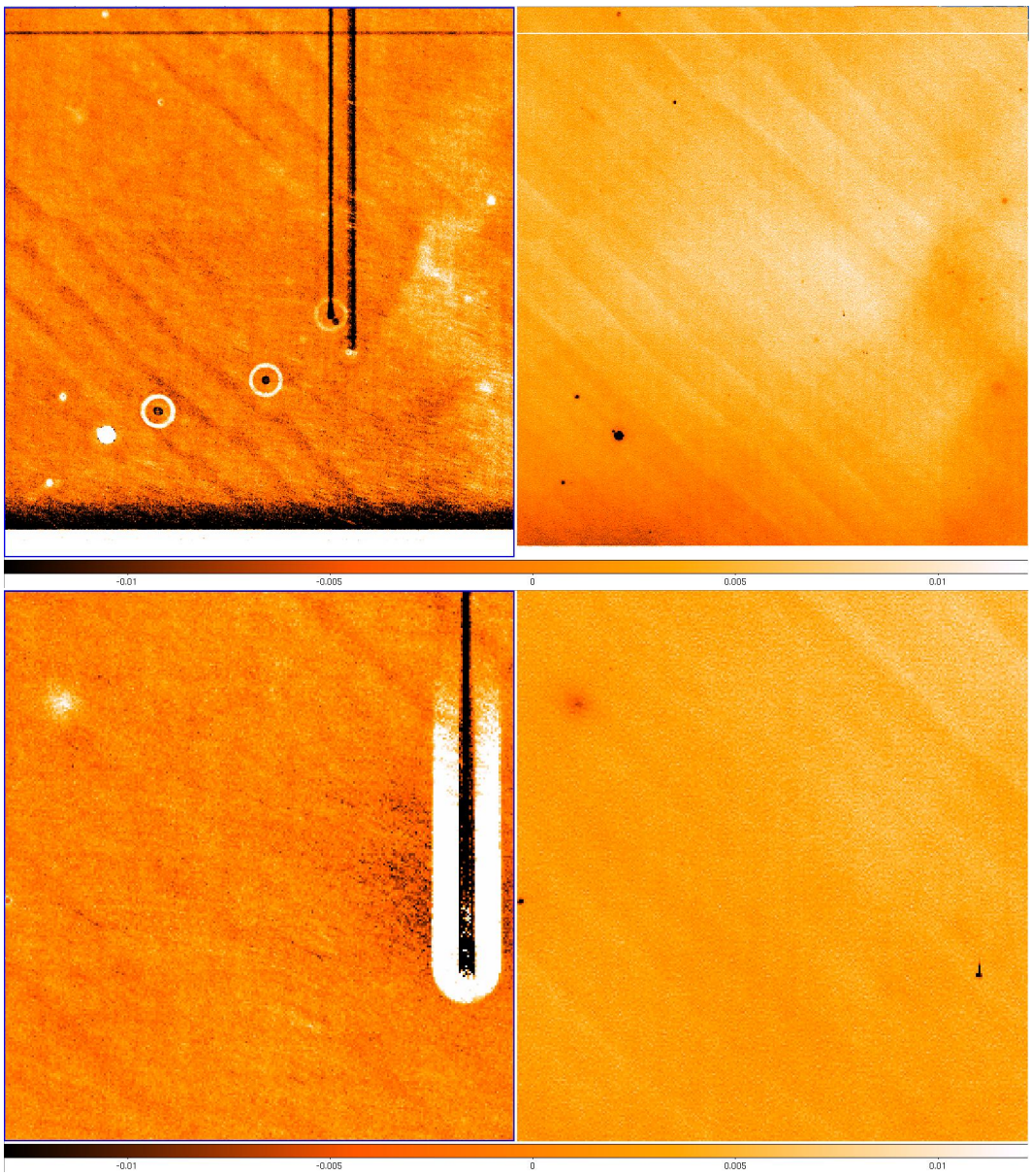

Figure 2.10: Selected enlarged regions of both detector maps (left) and twilight flats (right), showing examples from features 3, 4 and 5.

calculating what linear shift would be required from each other line such that it simulates the desired rotation, i.e, such that all pixels from feature A belonging to the same diagonal structure align vertically. After this, every line is shifted the nearest integer number of pixels to the calculated value, avoiding any re-sampling. This is a valid method because the spatial scale of the lines in feature A is larger

Figure 2.11: Vertical profile of features 5 and 6 for several example frames. Every case contains the signal inside the feature and the average of the surrounding columns for comparison.

than a single pixel and hence the signal will become more evident without the introduction of noise from re-sampling issues.

During the shifting process, a second order polynomial is fitted to each individual row and divided out, in order to separate feature A's signal from any local large overall structure that may be superimposed. The result will be the residuals to this fit, corresponding to the real feature strengths. Finally, a plot of the average of every column is produced, which should provide the intended one dimensional plot of pixels running across the feature.

Figure 2.14 shows a representation of a selected strip of a twilight flat containing feature A after the rotation. The top panel contains the column average of twilight flats for both full moon and new moon nights. They have identical feature strengths, as expected due the identical color of all twilights. The second panel shows the column average for the night sky flats of both full moon and dark nights. This now shows that the feature strength varies with lunar phase, where it can be seen that the S/N in the dark night case is still good enough to measure the strength of feature A, if only much weaker.

In order to simulate what the result of flat fielding the night sky data with twilight flats would be, one can divide the results from the night sky flat by the equivalent twilight flat values for the same night, which is shown in the 3rd panel of Figure 2.14. This immediately shows that the full moon night case is mostly featureless, due to the close nature of the wavelength incident on the CCD, but the dark night case now correlates with the detector map (bottom panel), suggesting that the feature presence is indeed due to overcorrection in the flat fielding process. Note that the detector map is made from star light and that the signal strength is slightly different, but it is clear that the dark night sky flat is a better representation of the flats needed for star light than the twilight flat.

This wavelength dependence also applies to feature 3, as well as some examples of feature 10 where the strength of the bright small regions is similar to that of feature 3. Also, the morphology of those examples seems to suggest a common origin to that of feature 3 (see bottom panel of Figure 2.10 for an example).

Feature B

A similar method was applied to feature B, differing only in the fact that no rotation was necessary. So, a straightforward column average was done to a strip 80 pixels in height that runs across this feature and the results of the same type are shown in Figure 2.15. This feature appears on the twilight and sky flats to be of higher strength in comparison to feature A, amounting to just under 2% peak-

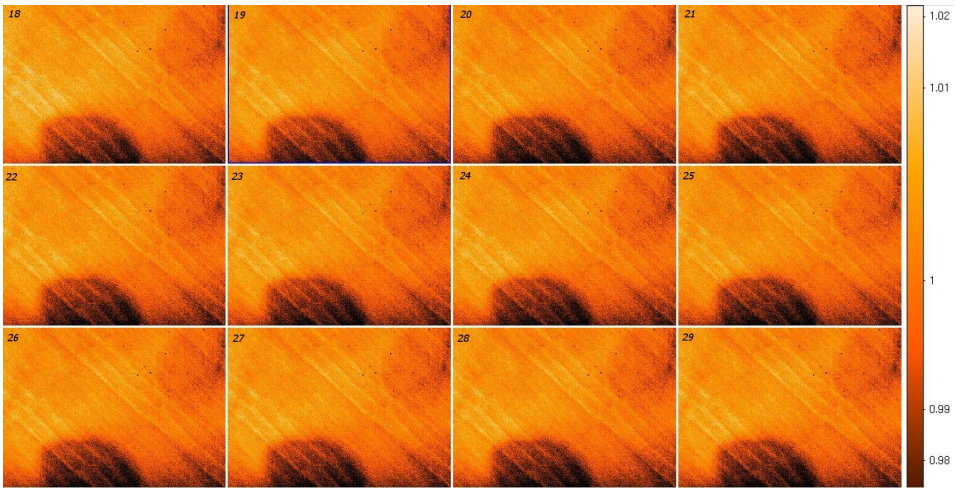

Figure 2.12: Feature evolution for all twilight flats generated for the nights between 18th July and 29th July 2008. Dates are indicated by numbers on the top left corner of each image. The scale range is ±2%.

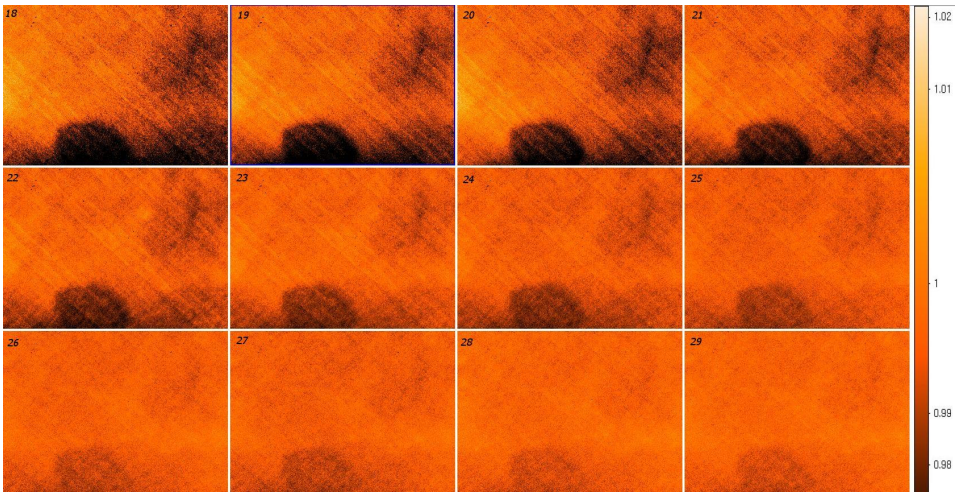

Figure 2.13: Feature evolution for all sky flats generated for the nights between 18th July and 29th July 2008. Dates are indicated by numbers on the top left corner of each image. The scale range is the same as Figure 2.12. The various panels also correspond to a changing lunar phase.

to-peak variations on the data that falls within this set of pixels. The results show a similar relation to the diagonal lines (feature A) with the strength of the feature decreasing towards the new moon. This again hints towards a dependence with the feature happening to be weaker in red light than blue. However, this analysis suggests that the feature should be overcorrected by the twilight flats, and so should appear as a bright feature in the detector maps. Instead, it is seen as a dark feature (feature 2). This is puzzling, and suggests a different wavelength dependence to features 1,3 and 10. It is weaker in OH emission lines that in twilight lines, but it is stronger in average star light than in twilight light. Perhaps this might arise from a narrow band absorption feature. We also investigated the possibility that this feature is not present in all images, which might explain a different average strength in the detector map, but we found this particular example to be present in images at the beginning and end of the season. In contrast, other similar features on other cameras seem to appear at particular times during observing seasons, and we traced the time of first occurrence of a particular example to a specific image taken during a night. This particular blob appeared during the night, in which there were no logged hardware maintenance, no interruptions due to hardware faults or deteriorating weather conditions. This feature requires further investigation.

This study reveals that the wavelength dependence of the detectors is responsible for the effects present in the light curves and that the current flat field strategy is introducing systematic errors into the data. Therefore, a different approach might provide better results. A possible solution may be to obtain laboratory flats at several wavelengths or to use narrow band filters on sky and use those in conjunction with the daily twilight flats as scaling factors, as even a lab flat of only similar color to the targets would be sufficiently good to apply the flat field correction without the introduction of unwanted effects due to wavelength dependent nature of the detectors.

2.5.5 Comparison with Sky flats

As a visual representation of what the current pipeline does at the flat field stage, we divided the night sky flats from two nights by their corresponding twilight flats[4] (Figure 2.16). This is comparable to the normal flat field process in the sense that these flats differ from the pipeline's master flat field and object frames only in the fact that vignetting has been removed and all frames normalised. It is possible to see that for the full moon case, the result is essentially flat, with the exception

[4]This is a visual representation of the operation performed in the third panel of Figures 2.14 and 2.15

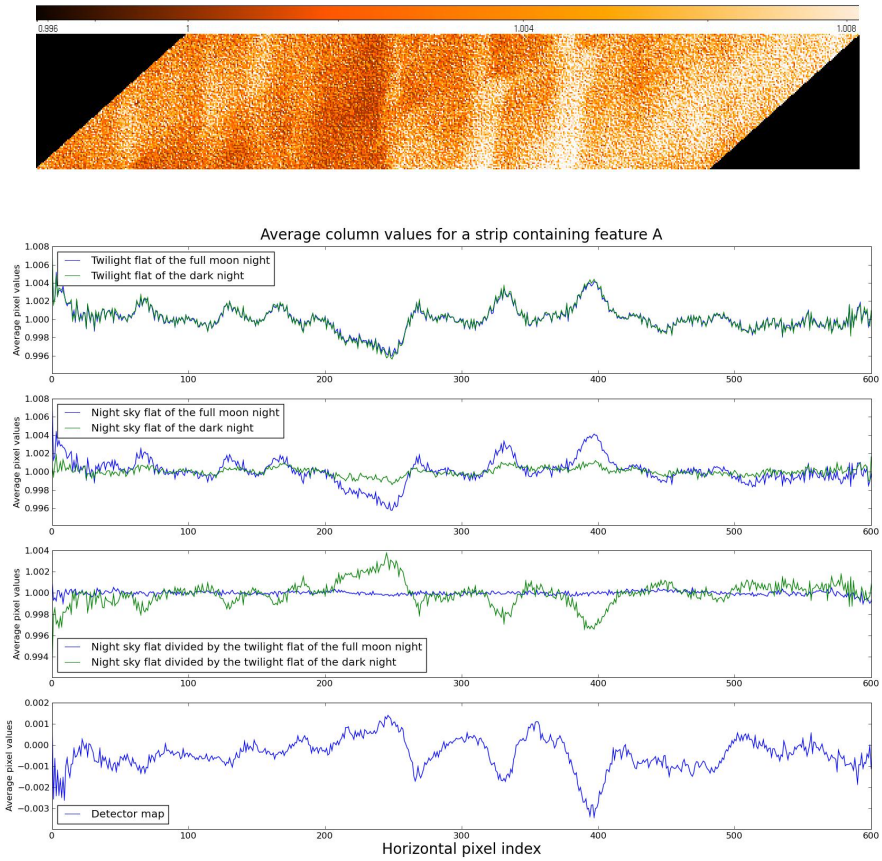

Figure 2.14: Representation of a selected strip containing feature A after rotation. Plots of the average of every column for twilight, night sky, division between night sky and twilight flats and detector maps, for both full moon and new moon nights. All horizontal axes represent the pixel index from the left.

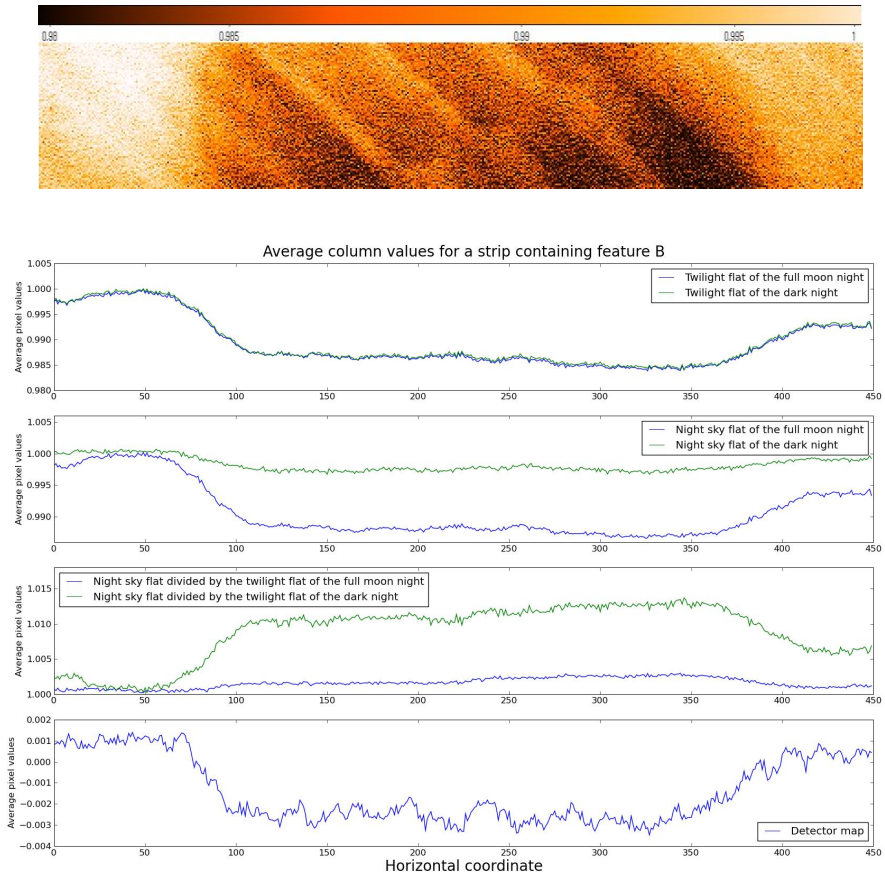

Figure 2.15: Representation of a selected strip containing feature B. Plots of the average of every column for twilight, night sky, division between night sky and twilight and detector maps, for both full moon and new moon nights.

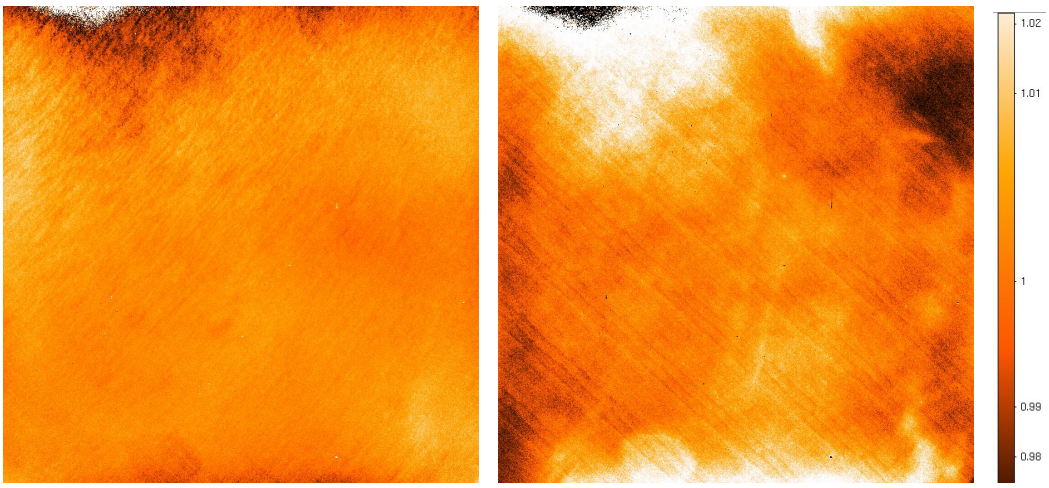

(a) 18th July 2008 (Full Moon Night) (b) 30th July 2008 (Dark Night Calibrated)

Figure 2.16: Results of a division between the night sky flat and corresponding twilight flat for both full moon and dark nights.

of the dark blob at the bottom of the frame still visible. On the other hand, when this simple division is applied to the dark night case, the diagonal lines and wispy patches now correlate with the detector maps, visually showing that their presence is indeed due to overcorrection during the flat fielding stage. This is not the case of feature B, as it shows as a bright patch.

It is now interesting to note the effect of this division on some additional features. Figure 2.17 shows another enlarged area of the frame, but now contains the comparison between the twilight and dark night sky flats, the detector map and the resulting division between the dark night sky and twilight flats. The dark pixels with surrounding bright ones (feature 10) that were referred to before in section 2.5.1 now appear in this frame. This feature appears as dark pixels in both the twilight and night sky flats, but their division shows the bright halo seen on the detector maps too, suggesting that this is due to the non-linearity of these pixels at different illumination levels. Note that the general strength of the dark pixels and surrounding bright pixels is comparable between the detector map and the result of the division referred above. Moreover, the trail left above the dark pixels numbered as features 5 and 6 is more noticeable in the division of dark night sky and twilight flats as would be expected from the results shown in Figure 2.11. This again confirms the non-linearity in these regions.

A closer inspection of the strongest horizontal line (feature 8) for different frames shows that the strength of this feature is non-linear, being approximately +28% in the twilight flat fields, +25% in the full moon night flats and around

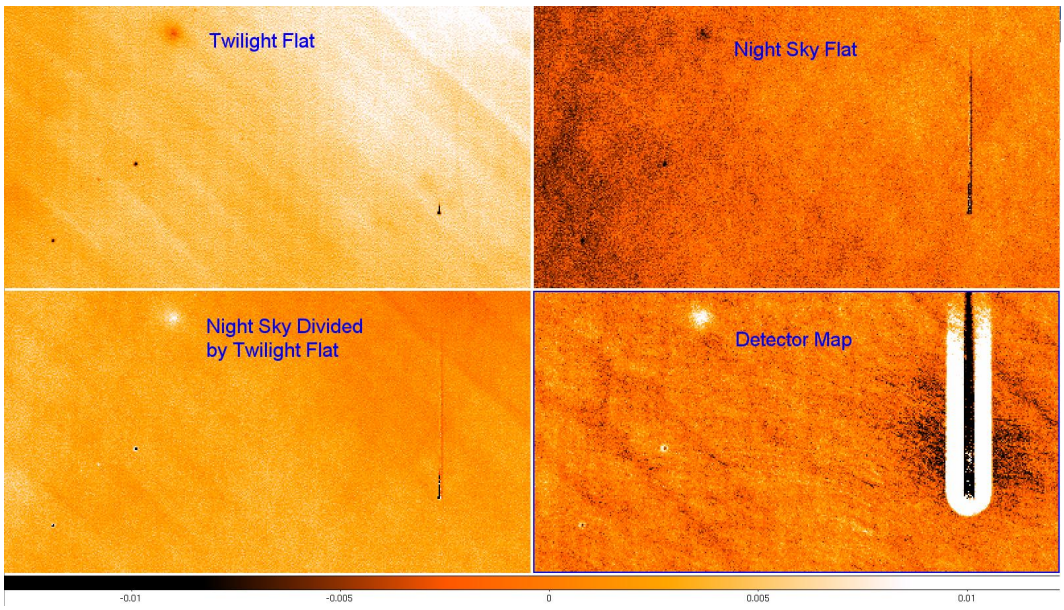

Figure 2.17: Selected enlarged section of the twilight flat, night sky flat, detector map and night sky flat divided by the twilight flat from a dark night (30th July 2008)

+11% in the dark night flats. This explains their presence in the detector maps as dark rows and is consistent with the relative strengths of this feature on the results of the division between the flats for both nights.

Potential improvements

Here we summarise the actions suggested to mitigate the effects of the features identified in the detector maps, based on the conclusions of our analysis.

1. A different flat fielding strategy could be adopted. We suggest 3 possible solutions: A set of lab flats at different wavelengths to be combined with the twilight flats; A set of sky flats with narrow band filters to be applied to different objects; or using the night sky frames to generate night sky flats, as these will be made from light closer to that of the observed targets. This should apply to features 1, 3 and some examples of feature 10.

2. A set of sky frames with narrow band filters can be used to further investigate feature 2, which is particularly serious, as it is potentially source of false transits.

3. A further 10 rows of pixels must be flagged out at the bottom of every frame on this camera (corresponding to bright rows above the standard 5 rows flagged out already), since these still seem to affect the light curves considerably (feature 7). Alternatively, making the background fit insensitive to these lines could be a solution.

4. The detector maps allow us to identify bad pixels that are not currently flagged out but which show non-linear behaviour. This will improve features 5, 6, 8 and 10

5. It is important to revise how the flagging out of bad pixels is done at present. Feature 9 shows that this rejection may not be taking place correctly at the edges of the flagged regions.

Temporal variability of the detector maps

The software used to produce the detector map shown in Figure 2.6 was then used to make detector maps for each observing season, for each camera. All the fields observed with a particular camera over the length of a season were used as an input of this code in order to achieve this result. This allows for a visual assessment of the temporal evolution of the features visible in the maps as the instrument is subjected to maintenance and operations. Naturally, the features present on each detector map depend on the amount of data collected and any possible modifications to the hardware. At the time of production of these maps, the 2011 season data was only available between January and August, and this results in inherently noisier maps for this year. Figure 2.18 contains the detector maps for camera 141, where the yearly evolution can be seen. It is possible to see the presence of features 1/A and 3/C throughout, as well as all the non-linear pixels. However, feature 2/B suffers from a change in morphology between the years 2007 and 2009 (either side of the major upgrade), and the particular example on the bottom seems to shift its position on the chip in 2011. Figure 2.19 shows the detector maps for camera 147 where the later years seem to be dominated by examples of this feature. The change in morphology of this feature from a dark blob into an elliptical shape more prominent in the edges is due to the improvement in the telescope pointing during the major upgrade. Since the production of the detector maps uses the residuals of each light curve with respect to the average, only stars that drift across boundaries of features will show deviations with respect to the average. Any star that always falls inside one of these blobs will have a lower average flux but no significant residuals due to detector features. Ultimately, in principle, a sub-pixel accurate pointing

would completely remove the features seen in the detector maps. However, effects such as differential refraction would still introduce a large enough deviation of pixel position for a subset of stars to introduce such effects. Differential refraction is a phenomenon related to the wavelength dependence of the refractive index of the Earth's atmosphere, such that stars of different colors will appear to change their positions by different amounts with respect to other stars in the FOV as observations are undertaken at different airmass. For the case of SuperWASP, this deviation can be as high as 3 pixels.

In summary, these maps show any features fixed in detector space that remain on average in the light curves at the stage where they are analysed in search for planetary transits. As shown in Section 2.5.3, there is the potential for systematic noise of the order of a few mmag to be introduced in a light curve if a star drifts over certain features on a nightly basis. The question then remains on whether these maps can be used not only as a diagnostic but also as the basis for an extra step in the software pipeline, where they are used to de-correlate the data. In principle, this would improve the rate of false positives, as this would potentially remove cases where the transit search algorithm used often finds events on periods of integer days. At the moment, any periods close to integer days are automatically rejected on the basis that they are highly likely to be false positives and, therefore, genuine cases of planetary transits in this window are lost. Section 2.6 discusses the possibility of using the detector maps as a de-trending step in the data processing stage.

2.6 Attempting to correct for flat-fielding noise

As mentioned in Section 2.5.5 the existence of features fixed in detector space have the potential to introduce systematic noise into the light curve of a star that drifts across them. In order to gauge the effect of the detector map features in the light curves and the potential to correct them the fractional RMS as a measurement of the inherent error has once again been used. The detector map values represent the average residual of all the measurements made where the aperture was centred on a given pixel. Naturally, each pixel in the detector map contains a value that represents the sensitivity of not just the central pixel but also the neighbouring pixels within the aperture size chosen. However, in terms of determining what the potential correction for this effect is, only the central pixel needs to be used, since it already includes the contributions of its neighbours. In this context, it is possible to produce a *detector map time series*. This is the result of producing a time series of detector map values corresponding to the pixel where each measurement was

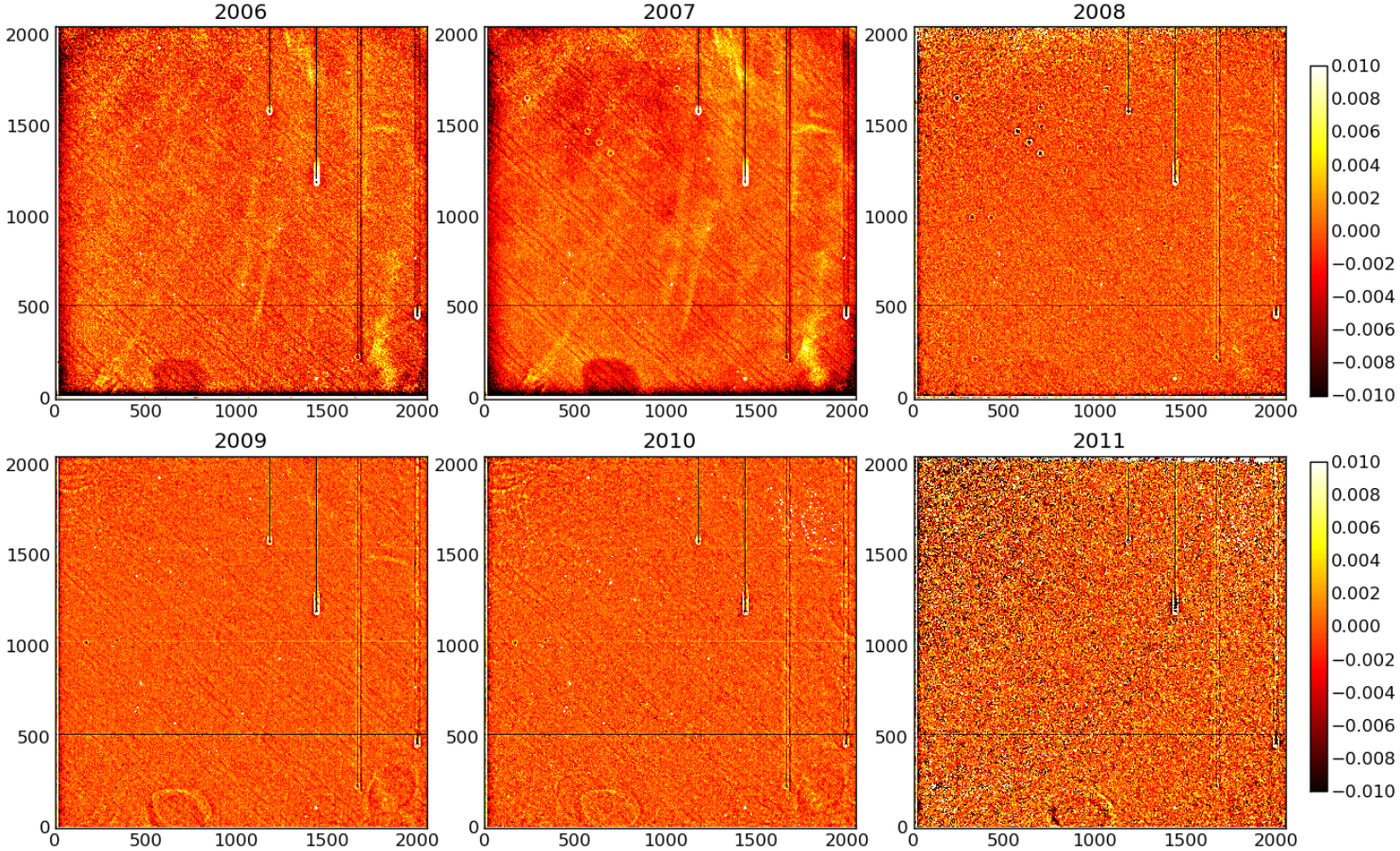

Figure 2.18: Detector map yearly evolution for camera 141. All the plots share the same scale as shown in the panels on the right hand side.

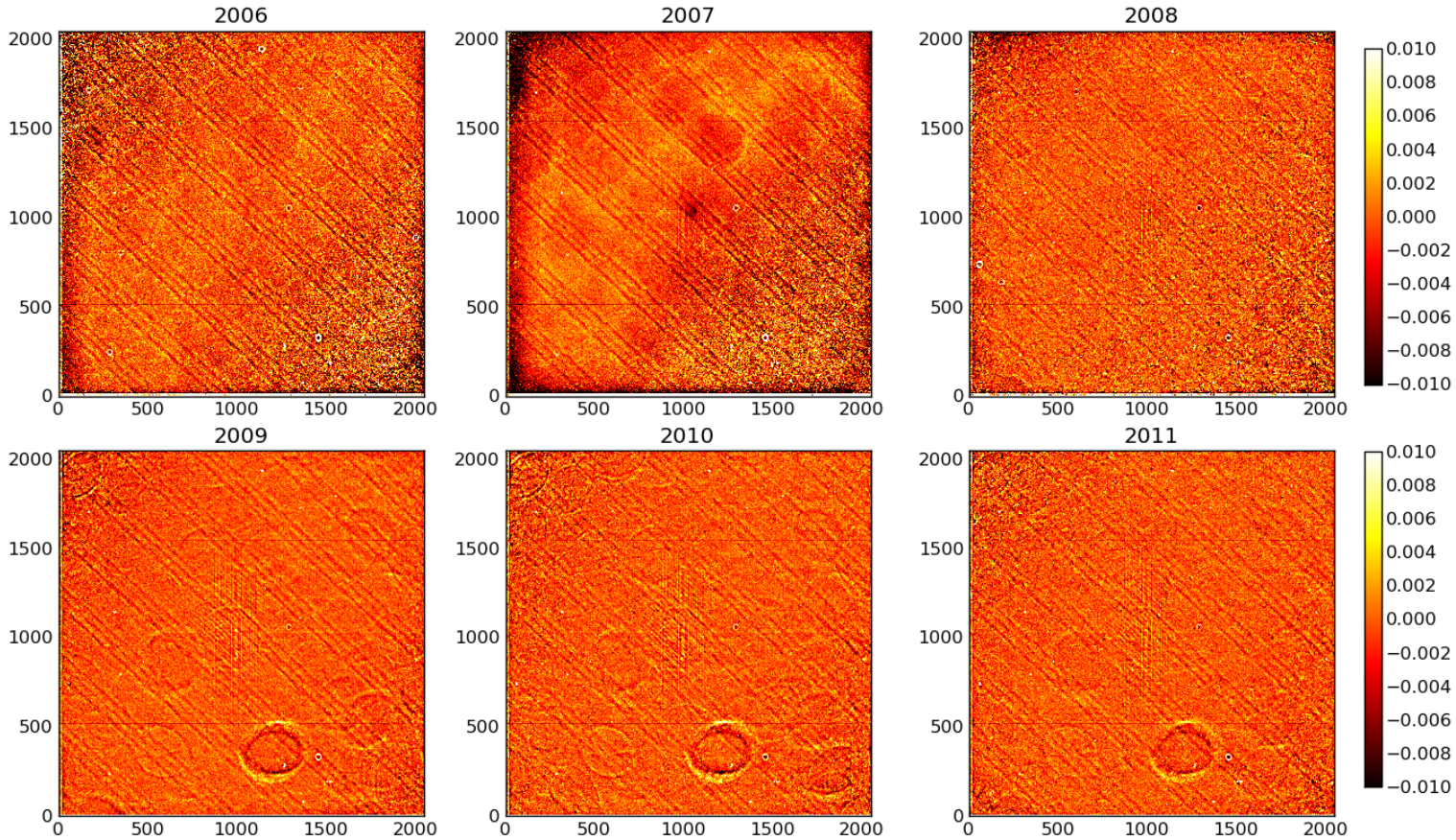

Figure 2.19: Detector map yearly evolution for camera 147. All the plots share the same scale as shown in the panels on the right hand side.

made, scaled to the brightness of each star. A measure of the fractional RMS of this time series provides an indicator of the expected photometric precision level these features have an impact upon. Since detector maps were produced for each separate year of data, each light curve's detector map series used the corresponding map.

Similarly to the plots shown in Section 2.4, Figure 2.20 contains the fractional RMS of each star as a function of magnitude, as well as the corresponding points for the data averaged into hourly bins. This plot, however, contains two extra sets of points representing the fractional RMS of the detector map series, before (purple) and after (black) binning the signal to hourly time scales. This demonstrates that the detector map features have, on average, a negligible effect on the bulk of the un-binned light curves, and only a few bright stars achieve a precision similar to the level where the detector map could have an impact once binned. It is clear that using the detector map to decorrelate the light curves will not make a significant improvement to the overall sample of targets. However, a small set of stars that drift across particularly serious features seen on the detector maps are still likely to exhibit periodic flux variations and show an improvement after this correction.

For the period between March and September 2011 the SuperWASP North facility operated under a different observing strategy. A single field was chosen and the telescope was set to observe that field only for as long as it was possible. The choice of field is discussed in Section 4.4. The increased sampling rate of this *staring* strategy has the advantage of increasing the photometric precision achieved on time scales comparable to the transit duration. This decision was implemented at a time when the facility had already surveyed the available sky using its typical strategy and motivated by a desire to improve the photometry in order to test whether it is possible to search for shallower transits. This method will also improve the instrument's sensitivity to longer period planets, increasing the precision achieved over multiple transits of planets that exhibit these less often.

At the time of writing this document, the only available data on this strategy refers to fields observed between March and June 2011. However, a similar approach for data quality assessment as that used in Section 2.4 was applied. A cloudless night was chosen and a fractional RMS plot for camera 144 was plotted along with the binned data (Figure 2.21). The model curve was generated using the same principle described in Section 2.3 using 90 exposures per hour. This number assumes 30 second exposures and an average of 10 seconds between exposures for the readout process and initial acquisition.

This Figure once again reveals that the overall quality of the photometry prior to the implementation of detrending algorithms is consistent with the data

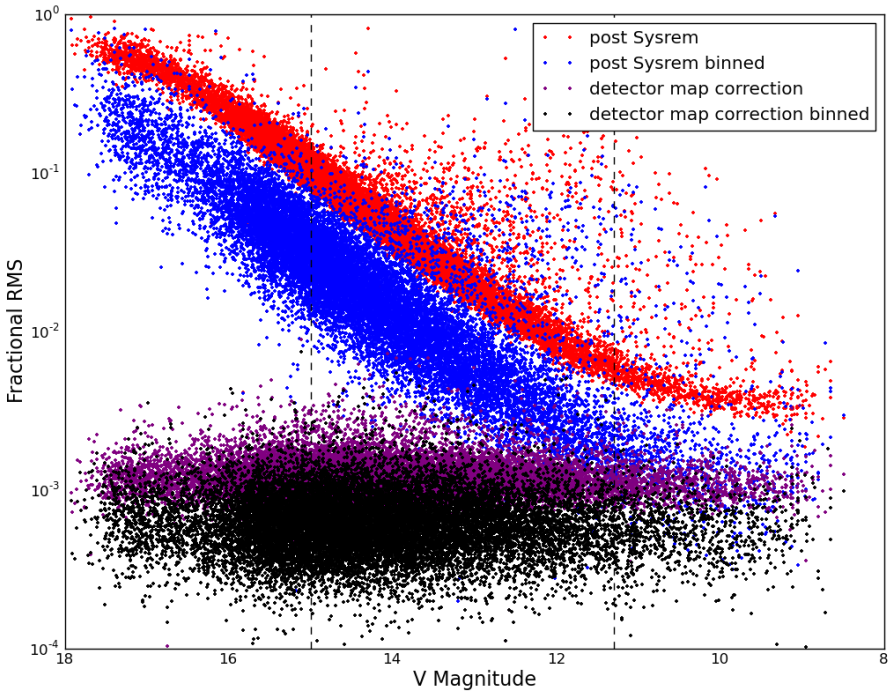

Figure 2.20: Fractional RMS as a function of stellar magnitude for stars belonging to field SW0118+0758, camera 144 on the night of 14/10/2009, after the implementation of Sysrem. The red and blue data sets represent the fractional RMS of the light curves before and after averaging the data points into 1 hour bins respectively. The purple points refer to the RMS of the detector map series, whilst the black points show the resulting RMS of this series also averaged into 1 hour bins.

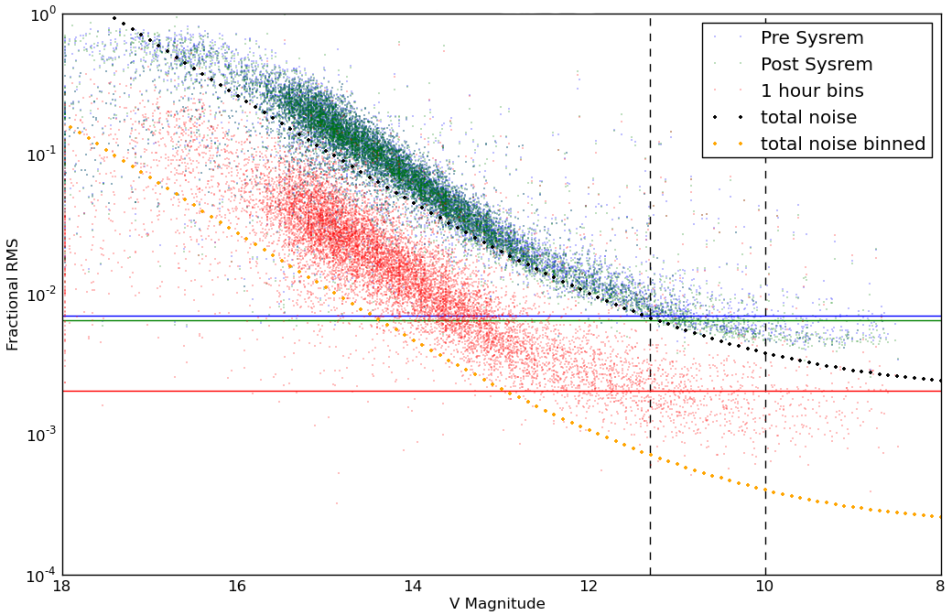

Figure 2.21: Fractional RMS as a function of stellar magnitude for stars belonging to field SW1254+4249, camera 144 on the night of 24/04/2011. The blue and green data sets represent the fractional RMS of the light curves before and after the application of Sysrem respectively. The red points refer to the results of averaging measurements into hourly time bins. The horizontal lines show the median of the fractional RMS of all the stars inside the region delimited by the vertical dashed lines. The black and orange curves represent the expected fractional error from the model described in Section 2.3.

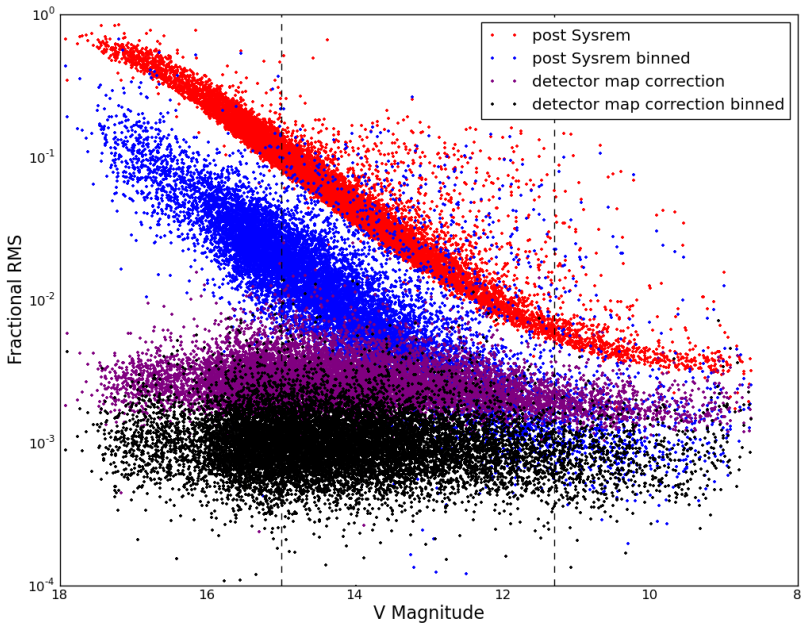

Figure 2.22: Fractional RMS as a function of stellar magnitude for stars belonging to field SW1254+4249, camera 144 on the night of 24/04/2011, after the implementation of Sysrem. The red and blue data sets represent the fractional RMS of the light curves before and after averaging the data points into 1 hour bins, respectively. The purple points refer to the RMS of the detector map series, whilst the black points show the resulting RMS of this series also averaged into 1 hour bins. The black and orange curves represent the expected fractional error from the model described in Section 2.3.

shown in Figure 2.3, and that, once again, Sysrem has a relatively small impact. On the other hand, the fractional RMS of the data once averaged into one hour bins now shows a discrepancy with the expected model for bright stars. The fractional RMS of stars brighter than V=12 seems to be constant, suggesting the presence of a source of systematic at the 2mmag level. This is not only a very small improvement with respect to non-staring data quality, but is also consistent with the typical RMS from the detector map series shown in Figure 2.20. A similar Figure can be generated for the case of a night under a staring strategy (Figure 2.22). It is possible to see that the fractional RMS of the binned data for stars brighter than V=12 seems to overlap with the expected RMS from the detector map contribution, suggesting that this could indeed be the source of systematic noise causing a degradation in the photometric precision at this level.

In order to test this hypotheses, the detector map series were used as a correction factor for the light curves and the fractional RMS re-calculated. This set of points is not plotted since it visually overlaps with the existing binned series. The difference between the fractional RMS values before and after this step were used to assess whether an improvement (negative difference) or a degradation (positive difference) of the data quality took place. This evolution can be compared with either the result when applied to non-staring data sets or to faint stars, where the impact of the detector map correction is expected to be negligible. The top left plot in Figure 2.23 once again shows the fractional RMS of the binned light curves and also the RMS of the detector map series once also binned for clarity. Two separate vertical dashed lines delimit three regions of considered magnitude ranges (bright, medium and faint) are also shown. These distinguish the regions where the fractional RMS observed agrees well with the noise model ($15 > V > 12$; designated as *medium* brightness), the range of stars which are too faint to be detected at all times ($V > 15$; *faint*) and the *bright* end ($V < 12$) which seems to show the presence of a systematic source of noise limiting the data quality. The three other panels of the Figure present histograms of the fractional RMS difference values (as described earlier) for all three separate brightness ranges.

Despite the clear overlap of the two distributions at the bright end displayed in the top left panel, the corresponding histogram (top right corner) exhibits a relatively uniform distribution that is centred very close to zero, similar to the histograms corresponding to the other two regimes. The smaller range of difference values at the bright end is related to the fact that a much smaller number of stars is detected in this brightness range with comparison to the other two. This suggests that the detector map correction has not improved the overall data quality. Since the features in the detector map are a multiplicative effect, the results shown are consistent with using a random function to correct each light curve of RMS smaller or equal to the light curve's initial level. This method was applied to all nights available from several fields and the results show a similar outcome, with just over 50% of stars of any regime displaying an improvement. The distribution is slightly skewed towards negative values, implying that on average a larger number of stars show this improvement. However, this is not a significant effect as a large fraction exhibit a degradation of the quality once the detector map series is applied as a correction, suggesting that this step is currently not viable as a form of quality improvement.

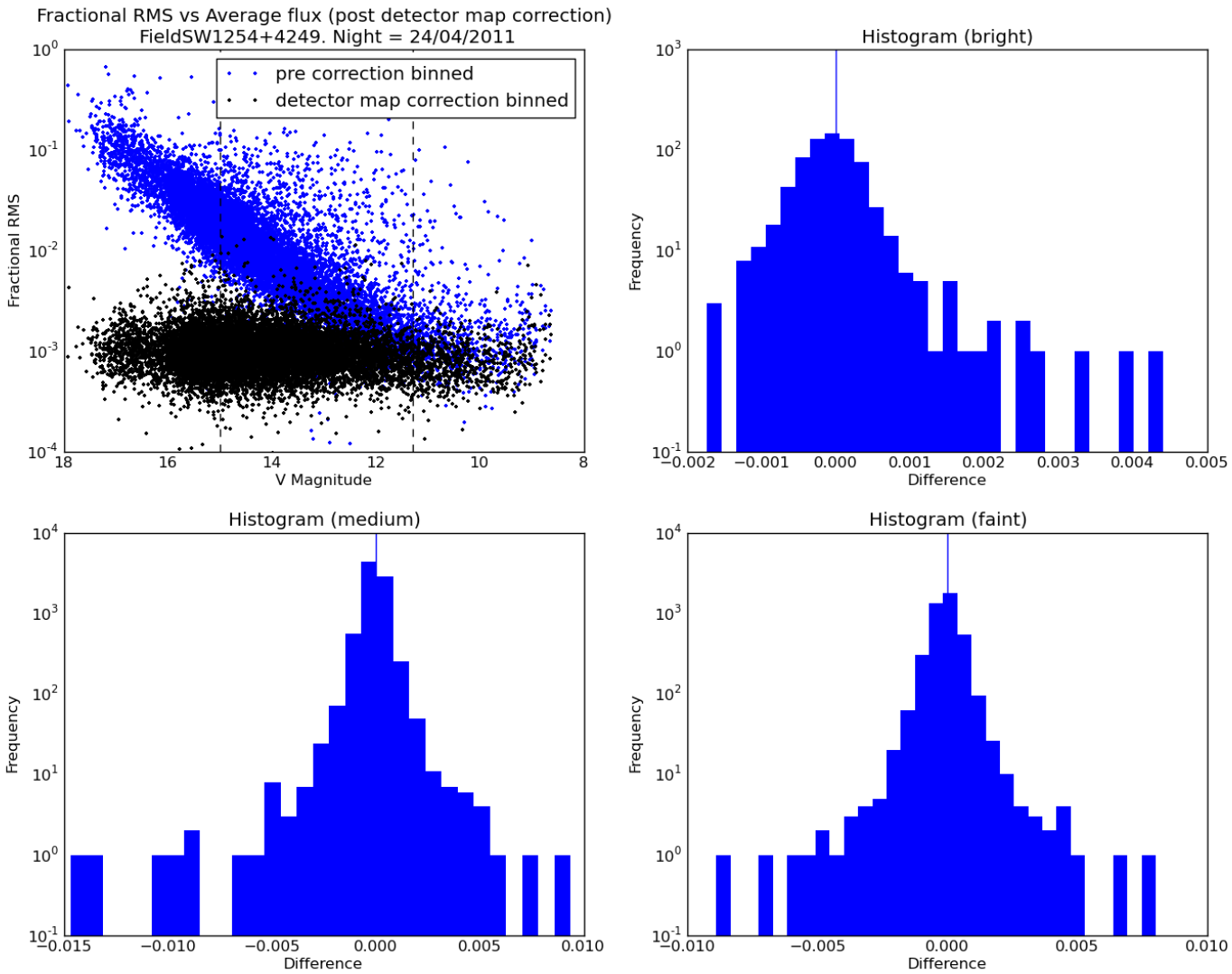

Figure 2.23: Fractional RMS as a function of stellar magnitude for stars belonging to field SW1254+4249, camera 144 on the night of 24/04/2011, after the implementation of Sysrem and averaging to one hour bins. The plot in the top left corner represents the fractional RMS of the light curves after averaging the data points into 1 hour bins and the corresponding detector map series. The vertical dashed lines separate three regions designating the faint, medium and bright star regimes, which form the basis of the histograms shown in the other panels of the Figure. The distribution of the difference between the fractional RMS after and before the correction with the detector map series is applied for each subset of stars. The vertical blue lines indicate the location of the zero rms difference.

2.7 Discussion

The SuperWASP instrument is currently achieving levels of precision very close to it's optimal performance over the entire magnitude range of sensitivity. The hardware upgrades and implementation of detrending algorithms has reduced the effects of systematic errors on single exposures to a negligible level. This is also partly true on time scales comparable to the duration of planetary transits where for faint and moderately bright stars the sky background and photon noise from the targets dominates. However, the stars of interest for this survey are the brightest, where follow up studies are more likely to be successful. The bulk of these targets are reaching precisions of around 4 mmag on hourly time scales and at this level of precision there is evidence of a small fraction of residual systematic noise.

The current flat fielding strategy employed in the SuperWASP instruments is introducing unwanted systematic effects into the light curves due to the wavelength dependence of the CCD chips. The broadband filter used in the telescopes makes them susceptible to effects of this kind and the wavelength difference between the twilight light and the stellar light is an example of a possible source of noise. An analysis of the SuperWASP detector maps has not only revealed this problem but also served as a diagnostic study for the performance of the CCD chips in terms of non-linear pixels and issues with the pipeline software. It can be used as a basis for selection of further pixels to reject from the software reduction and has revealed the presence of features of unknown origin that affect large portions of the chip and that warrant further study.

The amplitude of the systematic effects these features could introduce in the light curves has been found to be negligible under the typical observing strategy of the instrument, where on average 16 exposures are taken every hour for a given field. However, a recent staring observing strategy employed in the northern facility has increased this number to over 90 exposures per hour in order to increase the chances of finding longer period planets, as well as improving the photometric precision on time scales comparable to the planetary transit duration. This has generated a data set with the potential to reach photometric precision similar to the typical amplitude of the noise generated by the detector map features on time scales of one hour. However, the use of a fractional RMS plot as a function of magnitude shows a clear photometric limit inconsistent with the expected modelled noise, suggesting the existence of systematic noise sources at the 1mmag level. Using the detector maps as a decorrelating step has revealed no significant improvement on the brightest targets in the field and was therefore deemed unsuitable at this time. The results show a

distribution that is consistent with the implementation of a random multiplicative function of negligible amplitude compared with the existing noise levels. This can be explained by a number of scenarios:

- It is possible that an unknown source of systematic error is limiting the precision at the 1mmag level, thereby causing the detector map to be an ineffective means of compensation.
- The typical fractional RMS of the detector map series shown in Figure 2.22 for a staring field appears to be larger than that of Figure 2.20. This is likely to be related to the fact that the non-staring data was taken in 2009 whilst the staring fields are all observed in 2011, where only half a year of data were used for the creation of the detector map. The detector maps require a very large number of measurements to achieve the S/N necessary to visualise the features seen, typically entire seasons. The noise present in the 2011 detector maps is likely larger that any other previous year, which leads to a larger fractional RMS of the detector map series generated from it. It is possible that a map created with the full data set for 2011 (not yet processed completely) would provide a more accurate measurement of these features and would potentially serve as the basis for an improvement in the photometry of bright stars.
- Using the detector map as a basis for decorrelating every star may be unsuitable in principle, since this would be compensating for a feature resulting from a wavelength dependence, whose amplitude is likely to be different for every star. A more profound understanding may be required in order to scale the detector map series to the color of every star and make this decorrelation a viable step.

Despite the fact that at this time systematic effects visible on the detector maps appear to be negligible in the bulk of SuperWASP light curves, this analysis is relevant to any survey using CCDs for optical astronomy. Knowledge of such noise sources has had an impact in the design and operation strategy of the Next Generation Transit Survey (see 1.4.3). They have motivated the need for precise guiding to take place and the choice of 600nm as the low wavelength cut-off for the instrument filter in order to reduce the effects of wavelength dependent flat-field noise. These results are also applicable to any project aiming to reach sub mmag photometric precision.

Chapter 3

Transmission Photometry of WASP-15b and WASP-17b

3.1 Transmission photometry as a test for two classes of exoplanets

Transiting planets, in addition to the mass-radius relation, provide the means to measure a host of other physical properties of exoplanets. As referred in Section 1.5.4, one example is the detection of atomic sodium in the atmosphere of HD 209458b using the technique of transmission spectroscopy [Charbonneau et al., 2002]. This technique relies on opacity sources in the planetary atmosphere raising the altitude of the photosphere at certain wavelengths. Spectrophotometric observations during transit can measure the increased planet radius at these wavelengths, and thereby determine the chemical composition of the planetary atmosphere.

In addition to detections of atmospheric features in absorption, planetary atmospheres have also been detected in emission using secondary eclipse measurements with the Spitzer Space Telescope [e.g. Deming et al., 2005]. A surprisingly wide range of brightness temperatures have been measured, when compared with expected equilibrium temperatures [Harrington et al., 2007], and this has been interpreted by Fortney et al. [2008] as resulting from two classes of exoplanet atmospheres. Specifically, hot planets (class pM) are predicted to have optical opacities dominated by TiO molecular bands, while in cool planets (class pL) the TiO should have condensed out of the atmospheres. The strong optical TiO opacity results in a temperature inversion in the upper atmosphere of the planet, driving infrared molecular bands into emission and explaining the high brightness temperatures measured with Spitzer. The model of Fortney et al. makes a clear prediction that

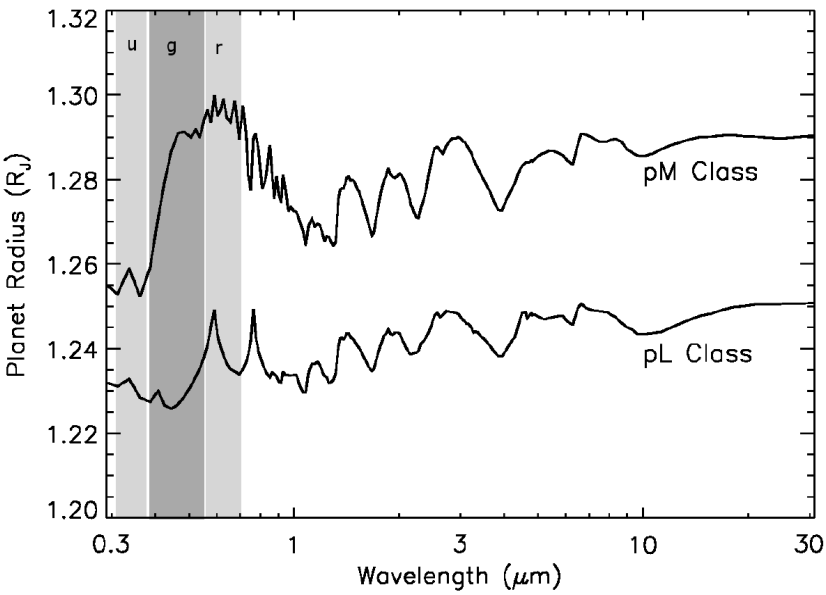

Figure 3.1: Predicted planet radius as a function of wavelength for a pL and a pM class planet with a surface gravity of $15\,\mathrm{m\,s^{-1}}$ and a radius of $1.20\,\mathrm{R_{Jup}}$ at a pressure of 1 bar (taken from [Fortney et al., 2008, Fig. 11]). We have indicated the ULTRACAM u, g and r passbands with shaded rectangles. It can be seen that the planet radius varies by over 3% between u and r for the pM planet. The radius variation for the pL planet is dominated by NaI absorption (in the r band).

the optical opacity of hot exoplanets should be dominated by TiO absorption bands. Their predictions for planet radius as a function of wavelength are reproduced in Figure 3.1, showing that the radius of the planet is expected to increase by 3 per cent in the TiO bands. In contrast, the optical opacity of cool planets (class pL) is expected to be dominated by broad lines of sodium and potassium (also shown in Figure 3.1).

The observed transmission spectra of the cool (expected pL-class) planet, HD189733b, are fairly consistent with this picture [Redfield et al., 2008]. However, observations of the hotter planet HD209458b, predicted to fall at the border between the pL and pM classes, suggested features from both scenarios [Sing et al., 2008; Knutson et al., 2008; Lecavelier Des Etangs et al., 2008b]. In order to test the two-class model predicted by Fortney et al. [2008] it is necessary to sample planetary atmospheres beyond the systems studied to date.

As mentioned in Section 1.5.4, transmission spectroscopy is particularly challenging since spectrographs are not usually designed to be photometrically stable. A similar technique that does not suffer from this, transmission *photometry*, uses

multiband photometry during transit to the same end. Using a combination of narrow and broad-band filters, such as those shown in Figure 3.1, we aim to test for the presence of TiO opacity, Rayleigh scattering, and broad NaI absorption in the atmospheres of transiting exoplanets. We chose to use the multiband photometer ULTRACAM on the NTT for a number of reasons outlined in Section 3.2.

3.2 ULTRACAM

ULTRACAM is a multi-band fast photometer resulting from a collaboration between the universities of Sheffield, Southampton and Warwick with the purpose of studying any fast astrophysical phenomenon. The design of this camera arose from the need to study systems that show changes in time-scales of miliseconds to seconds. Such systems are mostly compact objects (white dwarfs, neutron stars and blackholes) but it is also useful to increase the time resolution of eclipses and occultations. This has the consequence of increasing the spatial resolution, both in terms of resolving the ingress and egress but also since it provides the possibility of measuring transit timing variations from which the presence of additional bodies in the system can be inferred [Dhillon et al., 2007]. This instrument consists of a set of 3 frame-transfer CCD cameras that image a field simultaneously using different filters. Figure 3.2a shows a photo of the instrument mounted on the 4.2m William Herschel Telescope located in the Isaac Newton Group of telescopes in the Spanish island of La Palma. The right panel of Figure 3.2 contains a schematic view of the camera, in which the path of the incoming beam is depicted. The light from the telescope is split into separate wavelengths/cameras using dichroic beamsplitters [Dhillon et al., 2007].

Figure 3.3 contains the filter response of all available filters for ULTRACAM. The three panels show which filters can be used in each arm, thereby specifying which filter combinations are possible.

The frame transfer CCDs allow for a faster readout than standard CCDs. This specific type of chip contains two regions: the image area and the storage section. Since the vertical shift of a row on a CCD is done much faster than the horizontal readout of the same row, frame transfer CCDs shift the entire data from the image area onto the storage section before the horizontal readout takes place. This image shift takes approximately 24 ms. Therefore, the image can be extracted from the storage area whilst the top part of the CCD is being illuminated. Moreover, the ULTRACAM CCDs contain two separate readout channels, each reading out the right and left side of the chip simultaneously, thereby reducing the total readout

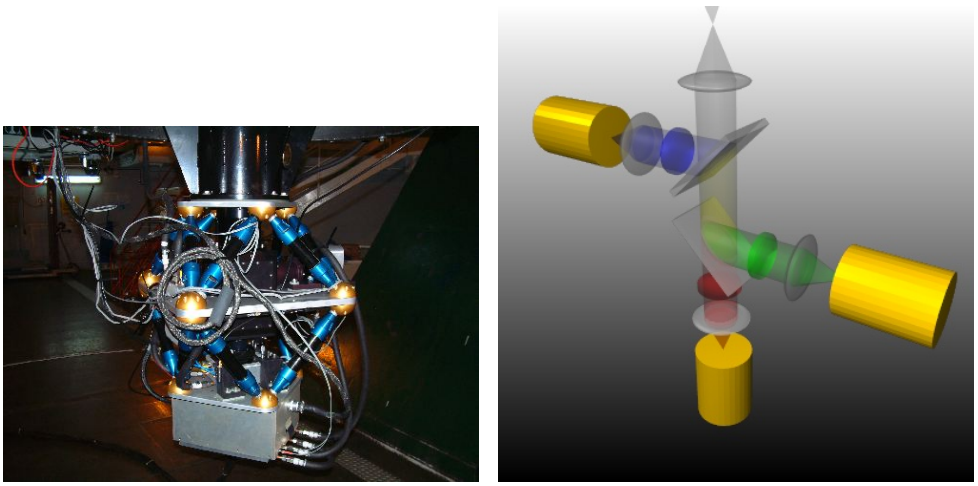

Figure 3.2: Left panel: The ULTRACAM instrument mounted on the WHT. Right panel: A schematic view of the instrument. This shows the disposition of the cameras and how the incoming beam from the telescope is split into the three arms by dichroic filters. These are designed to reflect light of a particular wavelength range whilst being transparent to all other wavelengths. (Courtesy of Thomas Marsh)

time by a factor of 2. The readout speed can be further enhanced by binning or using windowing modes and options for faster readouts with extra read noise are also possible. A combination of these factors makes ULTRACAM capable of performing photometry at rates of up to 500Hz [Dhillon et al., 2007].

ULTRACAM has been used to study a wide range of objects, from white and brown dwarfs to pulsars, gamma-ray bursts and occultations by Solar System objects. The flexibility of this instrument makes it ideal for studies of exoplanets. The fast readout makes it possible to image bright targets without defocussing excessively and hardly any dead time. The simultaneous multi-wavelength capability of the instrument provides the opportunity to perform transmission photometry without the need for multiple observations of the same system to obtain measurements of the transit depth in several bands. We use a combination of filters that can test the presence of TiO opacity, Rayleigh scattering and NaI absorption in the atmosphere of our selected targets. Using the SDDS u, g and r filters tests both the presence of a temperature inversion or a Rayleigh scattering dominated atmosphere from the transit depth differences between the filters (see Figure 3.1). Moreover, the ULTRACAM Sodium filter in the red arm can be used to test the presence of the NaI absorption feature predicted in pL class planets. Section 3.3 describes the method used to select planets for these observations, based on their scale height and irradiation levels.

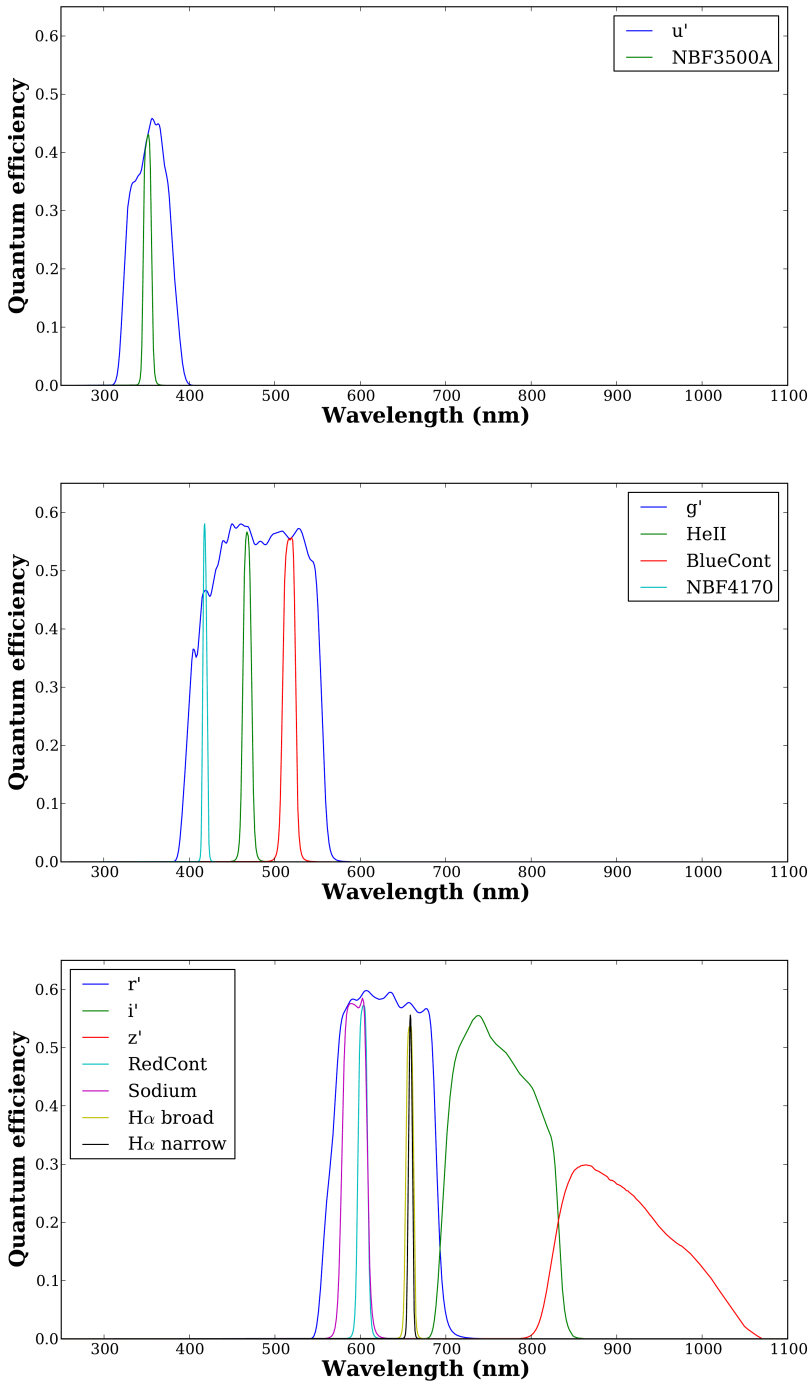

Figure 3.3: Ultracam system response for all available filters. Top: Blue arm, Middle: Green arm, Bottom: Red arm. Courtesy of Richard Hickman.

3.3 Candidate selection

The selection of candidates for observations of atmospheric transmission has been done in terms of their pressure scale height. This parameter is the characteristic length scale for a planetary atmosphere, and can be used to measure its height. It is also defined as the altitude above which the pressure drops by a factor of e, and is derived from first principles based on hydrostatic equilibrium [Seager, 2010a]. The scale height h as a function of the equilibrium temperature T and surface gravity g, where μ is the mean molecular mass of the particles in the atmosphere and k is Boltzmann's constant is given by

$$h = \frac{kT}{\mu g}. \tag{3.1}$$

We assume the mean molecular mass of the atmospheres of inflated Hot-Jupiters from Jupiter's Hydrogen-Helium mixing ratio. In terms of candidate selection, typically a low mass highly irradiated planet is a good candidate for observations of this kind. However, since the depth of planetary transits only provide the ratio between the stellar and planetary disk areas, our choice of targets should also take this fact into account. Indeed, regardless of the scale height of a planet's atmosphere, if this object orbits a large star its transit will be shallow and the signal due to opacity sources in the atmosphere will be small.

Figure 3.4 shows a pictorial representation of the system. In this Figure R_p is the planet's radius, R_s is the stellar radius and h is a representation of the scale height of the atmosphere. In reality, measuring the difference in transit depths at multiple wavelengths is a measure of the opacity of the partially thick atmosphere of exoplanets, which can be several scale heights. In the case of HD209458b, Vidal-Madjar et al. [2011] have found the NaI absorption feature to probe a section of the atmosphere corresponding to 14 scale heights, whereas observations of HD189733b using STIS on the HST have triggered the development of models that apply to portions of the atmosphere of 5.5 scale heights [Huitson et al., 2012].

In terms of selecting targets for observation, however, it is optimal to choose a planet that maximises the ratio between the area of the annulus formed by atmosphere around the planet and the stellar disk. If this annulus is chosen to be one scale height for comparison between all known planets, it is possible to rank them in order to select those with higher signal. The numerical expression of the difference in the depth of a planetary transit between multiple wavelengths due to one the extra opacity of one pressure scale height D_{sh} is given by

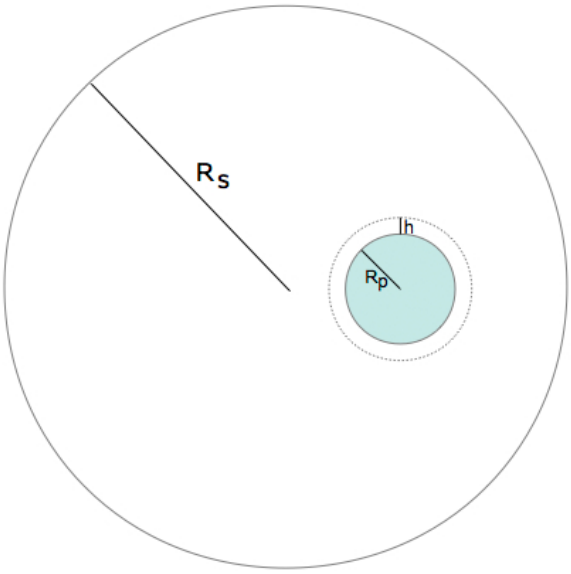

Figure 3.4: Graphical representation of a planet's scale height.

$$D_{sh} = \frac{\pi(R_p + h)^2 - \pi R_p^2}{\pi R_s^2} = \frac{2R_p h + h^2}{R_s^2}. \tag{3.2}$$

This parameter is a dimensionless measure of the fraction of the stellar light blocked by the section of the planet's atmosphere responsible for this difference. This equation shows the ratio between the area formed by the scale height annulus and the stellar disk. Assuming that $R_p \gg h$, and using equation 3.1 for h, the result is simply

$$D_{sh} = \frac{2R_p kT}{\mu g R_s^2} \propto \frac{R_p T}{g R_s^2}. \tag{3.3}$$

It then becomes evident that the stellar radius has a large impact on the detectability of the signal from a planetary atmosphere and that simply selecting targets based on their scale height is too simplistic. This criterion was used to select targets for observations with ULTRACAM, thereby favouring large scale height planets with deep transits. Table 3.1 contains a list of planets ranked in terms of the D_{sh} to date, excluding the Kepler unconfirmed candidates. This parameter is shown in the last column. Also shown are the planet's surface temperature due to irradiation from the host star, the pressure scale height and the value of the corresponding depth difference D_{sh}. It is important to note that a number of planets found on this Table

had not been announced or discovered at the date of candidate selection (September 2009) and therefore could not have been selected. This is the case of the highest ranked planet, WASP-39b [Faedi et al., 2011], for which telescope time on the WHT with ULTRACAM has been recently awarded to the Warwick team but observations in order to perform transmission photometry have not yet taken place. Since the telescope used is located in the southern hemisphere and observations of this kind require typically entire nights, only targets with negative declination that transit close to the middle of a night can be selected. Using these criterion, the planets selected for observations with the NTT were WASP-15b [West et al., 2009] (ranked 21st) and WASP-17b [Anderson et al., 2010b] (ranked 9th). Both these targets rank higher in the list than the two most studied planets to date, HD209458b and HD189733b, with WASP-17b displaying a predicted D_{sh} 50% higher than that of HD209458b and more than twice the amplitude of that of HD189733b. The final criterion for candidate selection was based on the apparent magnitude of the host stars. This was chosen such that the total photon noise over the duration of the transit in the u band would be small enough to allow a detection of the order of the expected signal. Initial calculations of the expected photon noise over the duration of the planetary transits for WASP-17b (V = 11.6 for the host star) in the u (due to CCD quantum efficiency and filter profiles, this is the least sensitive band) are of the order of 2×10^{-5} and 7×10^{-5}, which are below the expected signal from one scale heigh difference in the signal (see Table 3.1). WASP-15b orbits a V = 11.0 magnitude star, corresponding to a better photon noise. As mentioned before, however, it is likely this signal corresponds to several scale heights. Therefore, this instrument used on the NTT is capable of collecting enough photons to perform this measurement.

When considering ground-based observations of planetary transits the relatively long duration of the eclipse proves to be a difficulty. These transits typically tend to last a few hours ($\approx 2 - 5$) and since the depth is measured with respect to the out-of-transit level it is often necessary to collect data for an entire night. In order to avoid the transit depth being dominated by the out-of-eclipse data, at least as much time out of transit as the eclipse duration needs to be observed. Moreover, systematic effects on time-scales of hours are common in ground-based photometry and it is possible that these will be the dominant error source.

Rank	Planet Name	Surface Temperature (K)	Scale Height (m)	Depth Difference (D_{sh} in text)
50	XO-1 b	1095	2.8907e+05	1.2184e-04
49	HD 189733 b	1096	2.0740e+05	1.2280e-04
48	WASP-22 b	1301	4.8657e+05	1.2528e-04
.	.	.	.	.
.	.	.	.	.
.	.	.	.	.
31	WASP-13 b	1387	9.3361e+05	1.5626e-04
30	WASP-1 b	1665	7.7072e+05	1.5939e-04
29	HAT-P-1 b	1195	5.7845e+05	1.6368e-04
28	Kepler-8 b	1523	8.7728e+05	1.6477e-04
27	WASP-40 b	1080	4.1588e+05	1.6898e-04
26	HAT-P-30 b	1498	6.3429e+05	1.6958e-04
25	CoRoT-12 b	1320	4.9792e+05	1.6965e-04
24	HD 209458 b	1326	5.9290e+05	1.7635e-04
23	WASP-35 b	1328	5.3787e+05	1.7673e-04
22	WASP-4 b	1550	3.9683e+05	1.8179e-04
21	WASP-15 b	1513	9.4936e+05	1.8264e-04
20	WASP-34 b	1060	4.5219e+05	1.9014e-04
19	WASP-12 b	2303	9.1130e+05	2.0123e-04
18	WASP-25 b	1119	4.8017e+05	2.0315e-04
17	WASP-21 b	1156	7.3447e+05	2.0506e-04
16	HAT-P-33 b	1680	1.2216e+06	2.0777e-04
15	HAT-P-26 b	909	8.2530e+05	2.2087e-04
14	CoRoT-1 b	1736	6.2586e+05	2.2444e-04
13	WASP-19 b	1878	5.3952e+05	2.3113e-04
12	WASP-6 b	1083	5.1906e+05	2.4711e-04
11	Kepler-18 b	1189	2.1988e+06	2.5214e-04
10	CoRoT-5 b	1318	9.1735e+05	2.6475e-04
9	WASP-17 b	1517	1.1688e+06	2.7465e-04
8	HAT-P-19 b	923	6.7482e+05	3.3477e-04
7	HAT-P-18 b	776	6.4951e+05	3.3798e-04
6	Kepler-12 b	1356	1.5028e+06	3.4051e-04
5	WASP-31 b	1436	1.1845e+06	3.4725e-04
4	HAT-P-12 b	877	6.3789e+05	3.6621e-04
3	HAT-P-32 b	1684	1.2251e+06	3.7934e-04
2	GJ 1214 b	510	2.3865e+05	3.8254e-04
1	WASP-39 b	1023	9.6741e+05	4.5186e-04

Table 3.1: Table containing a selection of the planets with the largest transit depth difference due to one scale height ordered by this parameter. The columns shown for each planet are the surface temperature from stellar irradiation, scale height and depth difference, as well as the rank order in terms of this last parameter. Kepler candidate planets have not been included. Information from exoplanet.eu and exoplanets.org.

3.4 Observing Strategy

High precision photometry requires a large S/N ratio and a detailed planning of the observations is required in order to minimise the sources of systematic error. The majority of known planet hosting stars are relatively bright objects. This is an observational bias but it is certainly in the bright sample that studies of exoplanets can be performed. When using telescopes with a large collecting area a deliberate defocus is usually applied to avoid saturation. There are, however, additional advantages to defocusing a telescope. Since the light from a single target is spread over a larger number of pixels the weighting on each pixel is reduced, thereby reducing the flat-fielding noise.

Noise sources

We followed a method used by Southworth et al. [2009] to determine the contributions from several noise sources for the observations, in a similar way as that used in Section 2.3 to model the expected noise from the SuperWASP instruments. In chapter 2 the analysis was done to estimate the expected noise as a function of stellar magnitude for a fixed aperture size. In the case of planning the observations of planetary transits with the NTT+ULTRACAM, the stellar magnitude is known and the analysis is done as a function of aperture size, in order to determine the optimal amount of defocus of the telescope. Several sources of noise contribute to the aperture, and they do so differently depending on how many pixels are being used for the photometric measurements. The contributions are then combined to achieve a final error.

We again use the Poisson noise for the target and sky counts (S_{target} and S_{sky} respectively). We then calculate the noise due to the target and sky as $N_{target} = \sqrt{t_{exp}C_{target}}$ and $N_{sky} = \sqrt{t_{exp}n_{pix}C_{sky}}$. The contribution from the read noise is also estimated as $N_{read} = n_{read}\sqrt{n_{pix}}$, where n_{read} is the readout noise per pixel. This value was taken to be 3.5 electrons per pixel [Dhillon et al., 2002]. The estimation of the contribution from the flat field, N_{flat} is again non-trivial and is inherently inaccurate on the basis that the flat fielding noise will depend on the location on the chip. Its estimation was done from visual inspection of the flat field frames of ULTRACAM. In this case we estimate the flat fielding noise per pixel, f_{flat}, expressed as a fraction of the electrons in a pixel and scale it to the levels of the source and sky according to equation 2.4, where the nomenclature σ_{flat} is now N_{flat}. We have used the value 0.001 (1mmag) for this flat fielding per pixel fraction as this is the average photon noise in the combined set of useful flat fields taken at twilight.

On average we find that 60 useful frames are taken per night with illumination levels ranging from 28,000 to 15,000 counts for all three arms of ULTRACAM.

It is also important to note that equation 2.4 assumes uniform distribution of light inside the aperture. This is, however, not true, as the PSF will have a shape that puts different weighting on each pixel, depending on the true seeing on the night of observation. A larger defocus will reduce this weight, but it will nevertheless be non-uniform. Any drifts in the central position of the PSF have the potential to introduce systematic effects into the light curve and the presence of any bad pixels in the aperture needs to be minimised. This is, however, also true in the case of a uniformly distributed PSF. Tests of correlations between the flux acquired and pixel position can be done to assess the extent of any effects of this kind during data reduction.

The final source of noise considered is astronomical scintillation. The estimation of the contribution of atmospheric scintillation is the same as that used in Section 2.3 from the relation given by Young [1967] later used by Dravins et al. [1998]. This relation gives the scintillation noise level as a fraction of the total electrons in magnitude units, σ_{scint}, where the nomenclature M_{scin} is now σ_{scin}.

It is therefore now necessary to convert all the previously calculated error contributions into magnitudes to make them comparable with scintillation. The following equations contain these conversions:

$$\sigma_{target} = -2.5 \log_{10} \left(\frac{S_{target} - N_{target}}{S_{target}} \right) \tag{3.4}$$

$$\sigma_{sky} = -2.5 \log_{10} \left(\frac{S_{target} - N_{sky}}{S_{target}} \right) \tag{3.5}$$

$$\sigma_{read} = -2.5 \log_{10} \left(\frac{S_{target} - N_{read}}{S_{target}} \right) \tag{3.6}$$

$$\sigma_{flat} = -2.5 \log_{10} \left(\frac{S_{target} - N_{flat}}{S_{target}} \right) \tag{3.7}$$

And now we simply add all the contributions in quadrature to obtain the final error;

$$\sigma_{total} = \sqrt{\sigma_{target}^2 + \sigma_{sky}^2 + \sigma_{read}^2 + \sigma_{flat}^2 + \sigma_{scint}^2} \tag{3.8}$$

In planetary transit observations it is often the case that the time scales of interest are much larger than that of single exposures, and so a slightly modified version of this equation must be considered. When the data points are averaged

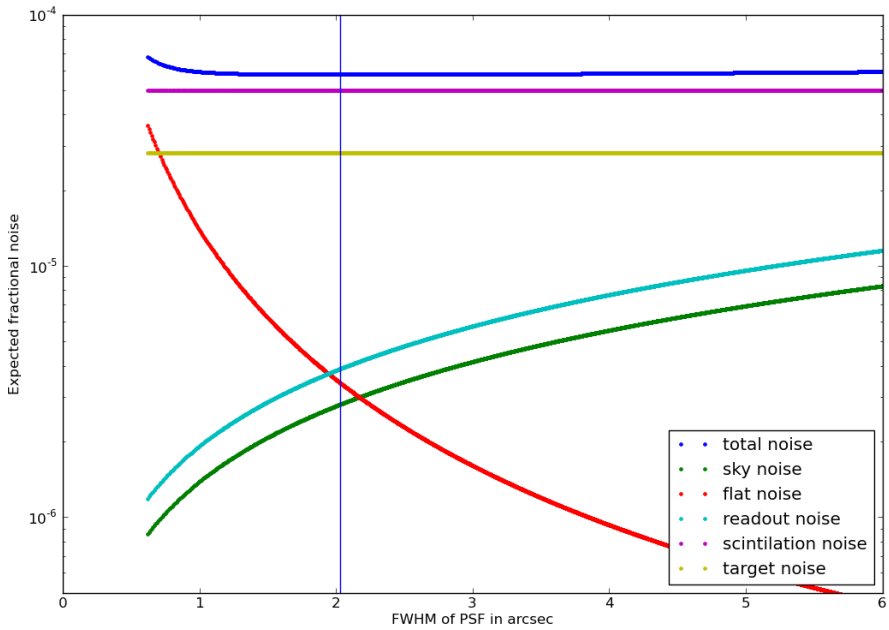

Figure 3.5: Total and individual noise contributions from several sources for a defocussed image observation. This has been done for a time scale comparable to the **typical transit duration (1 hour)**, on observations at **airmass 2**, for WASP-15 (V=11.0). The simulation is for a 3.6m telescope (as is the case of the NTT), for the g band in dark time (sky level of 12 counts/pixel/second)

in time bins (binned), all sources of noise that are random (white) in nature will evolve through simple error propagation. This is the case for all components with the exception of the flat fielding noise, which is a systematic effect (red noise) and will not be reduced from averaging of data points. It is, however, reduced by increasing the defocus, but this will introduce extra noise from the sky flux. An optimal trade-off between these two parameters has to be found.

Optimal defocus

Using the principle outlined it is possible to find the individual and total noise contributions from all sources over time scales of interest for a range of aperture FWHMs. A simulation was developed, which can be used to decide the optimal defocus of any observation, and sample results are shown in Figures 3.5 and 3.6. These represent results for the NTT in the g band in dark time.

The only differences between the two examples is that the airmass of the

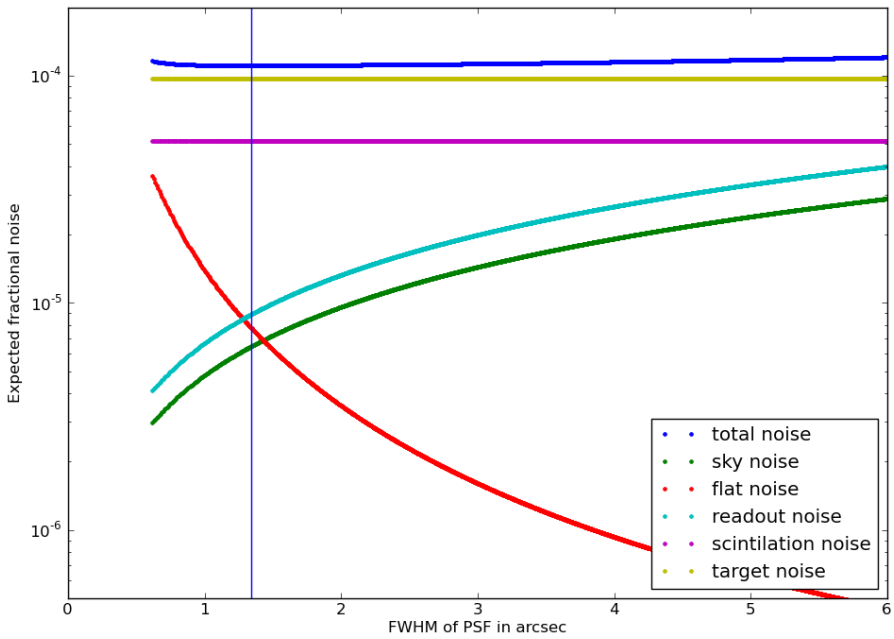

Figure 3.6: Total and individual noise contributions from several sources for a defocussed image observation. This has been done for a time scale of **5 minutes** on observations at **airmass 1** for WASP-15 (V=11.0). The simulation is for a 3.6m telescope (as is the case of the NTT), for the g band in dark time (sky level of 12 counts/pixel/second)

observation is not the same (1.0 and 2.0), which ultimately affects mostly the scintillation noise level and the time scales of interest vary from a few hours to a few minutes (the examples are for time bins of 2.5 hours and 5 minutes). Both Figures contain a vertical line that shows the lowest point on the total noise curve (blue), at $\approx$ 2.0 arcsec FWHM for the long time scale and lower for the shorter. This shows that the optimal defocus depends on a series of factors, one of them being what the time scale of interest is, since this affects the trade-off point between the flat fielding noise and the sky/read noise after binning. It also demonstrates the power of this study, showing that for any given star it is possible to predict which optimal defocus should be used, given a time scale of interest. The simulation also shows that, for the particular case of WASP-15, the noise in the data collected will be dominated by the photon noise of the target at low airmass, but by scintillation at high airmass. It also shows that, for long time scales of interest, the expected fractional noise is very similar in the FWHM range $[1.5, 5.0]$ arcsec. Therefore, as long as the telescope is defocused beyond the limit at which the flat-fielding noise is negligible ($\approx$ FWHM $>$ 1.5arcsec) the results are comparatively insensitive to extra degradation of focus, and therefore to changes in seeing, provided this does not improve dramatically.

This study does not take into account the fact that defocussing increases the chances of there being bad pixels/columns inside the aperture, but it is down to the observer to avoid this situation if possible. In the observations with ULTRACAM this was achieved by inspecting flat field frames at the locations of the apertures for any signs of bad pixels. Therefore, the optimal choice is to defocus beyond the point where the flat-field noise is important whilst trying to keep the PSF FWHM small enough to ensure no bad pixels in the aperture.

The simulation was also used to estimate the impact of the sky background level when observations take place in bright time. Figure 3.7 shows the result, which assumes a sky brightness of 200 counts/pixel/second, estimated to be the extreme level seen in previous observations with ULTRACAM in the g band. It demonstrates that the sky level can be a dominant source of noise under extreme defocus conditions during bright time. This is a motivation to keep the defocus to a minimum in nights with high sky brightness, which is the case in the majority of the nights where observations took place (see Table 3.2).

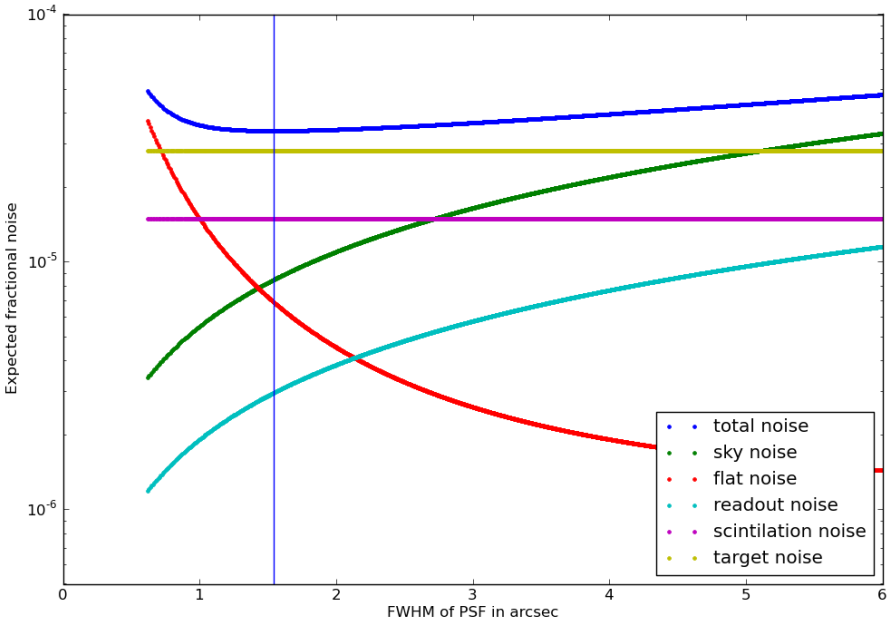

Figure 3.7: Total and individual noise contributions from several sources for a defocussed image observation. This has been done for a time scale of **1 hour** on observations at **airmass 1** for WASP-15 (V=11.0). The simulation is for a 3.6m telescope (as is the case of the NTT), for the g band in bright time (sky level of 200 counts/pixel/second)

3.5 Observations

6 nights were awarded to observe 3 transits each of WASP-15b and WASP-17b using ULTRACAM on the NTT. The log of the observations is depicted in Table 3.2 with comments regarding the weather conditions and any noteworthy features in the light curves. These notes regard a series of systematic features whose origin will form the basis of the analysis described in this Chapter. The final awarded night was that of 2010-05-26 but observations did not take place due to adverse weather conditions.

An inspection of this Table reveals that during 3 full nights observations were carried under mostly photometric conditions, and this analysis focuses on data from those nights. These are the WASP-15b observations on the 25th April and 10th May and the WASP-17b observation on the 26th April.

Figures 3.8a and 3.8b contain the finding charts for the observations of WASP-15 and WASP-17 respectively. The shown area corresponds to the ULTRACAM field of view when observing with the NTT. The target is indicated with a red circle and the label T whilst all comparison stars used are circled in blue and numbered. This order and numbering corresponds to that used throughout this Chapter.

In order to reduce the exposure time and avoid saturation on the brightest stars in the field of view ULTRACAM offers the possibility to window regions of the CCD. Table 3.2 indicates which nights required this to take place. This ensures that, due to the frame transfer nature of the CCDs, the total readout time is still under 24ms but only a selection of the CCD is acquired. The images shown in Figure 3.9 display example ULTRACAM frames from the observations. The particular case of WASP-15 shows an example of a situation where windowing was used to reduce the exposure time.

Information regarding the magnitudes and colors of all the stars shown in Figure 3.8 are presented in Table 3.3. Information from the NOMAD catalogue [Zacharias et al., 2005] was used to obtain the stellar magnitudes in the Johnson R and B bands and hence the B-R colors of all the stars. This information is potentially useful to understand any correlations with brightness and/or color in any aspect of data reduction. The selection of these magnitudes was based on the availability of such information in the online *Vizier resource* [Ochsenbein et al., 2000], which are simply originated from the TYCHO-2 catalog [Høg et al., 2000] and on the fact that the Johnson B and R bands are broadly equivalent to the SDDS g and r filter responses. This catalog is the result of ESA's Hipparcos satellite's second phase,

Target	Date	Filters	Moon phase (%)	Moon distance (deg)	Windowing	Zenith stop	Weather	Comments
WASP-15b	25th April	u' g' r'	93	35	Yes	No	Good throughout	Dip in flux before meridian, all stars, all bands
WASP-15b	10th May	u' HeII NaI	9	153	Yes	Yes	Some clouds at around third quarter of night	Systematic effect present near the meridian
WASP-15b	25th May	u' HeII NaI	96	14	Yes	Yes	Clouds present at several times during the night	Systematic effects at the beginning of night and during the meridian transition too
WASP-17b	26th April	u' g' r'	98	42	Yes	Yes	Good throughout	Increase of flux before stop on all stars, all bands
WASP-17b	11th May	u' HeII NaI	4	145	No	Yes	Clouds present through most of the night	Any systematic effect present hard to assess due to clouds
WASP-17b	25th May	u' HeII NaI	96	14	No	Yes	Cloudy	Clouds make the data unusable

Table 3.2: Description of ULTRACAM observations in 2010 with noteworthy comments. The available columns indicate the date of each observation, the filter combination used, the Moon phase and average distance during the runs, whether windowing was applied during the readout, whether the observation was paused during the zenith approach, the weather conditions and any comments regarding the data sets.

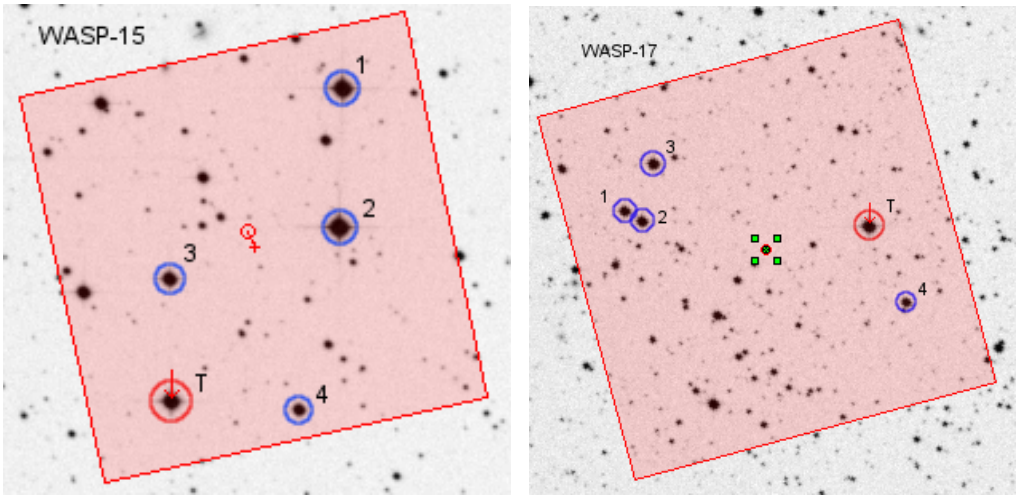

(a) Finding chart for WASP-15 (b) Finding chart for WASP-17

Figure 3.8: Finding charts for WASP-15 (left) and WASP-17 (right). The area shown corresponds to the ULTRACAM field-of-view when commissioned on the NTT. The targets are circled in red and labelled T while the comparison stars are circled in blue and numbered.

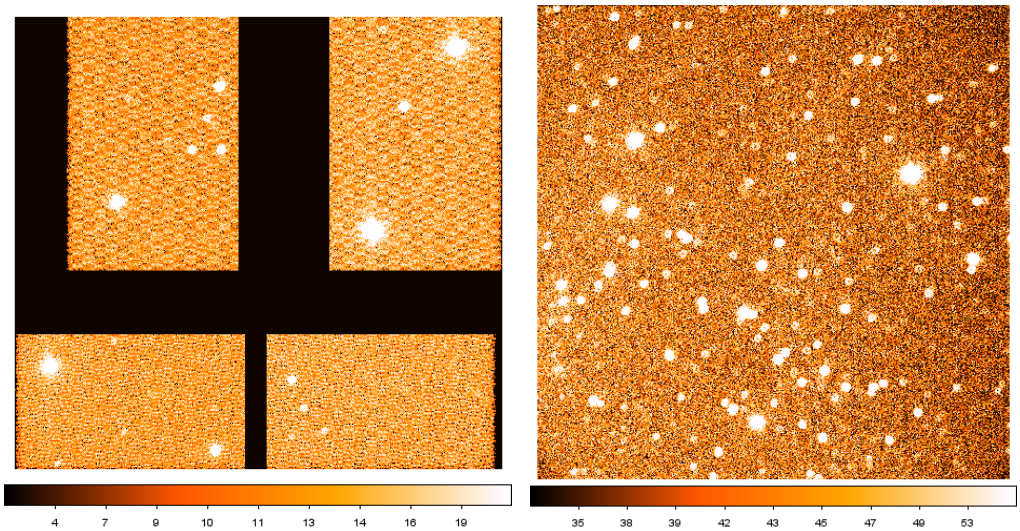

(a) Example ULTRACAM frame for WASP-15 (b) Example ULTRACAM frame for WASP-17

Figure 3.9: Example ULTRACAM frames for WASP-15 (left) and WASP-17 (right) using the NaI and r band filters filters respectively. The case of WASP-15 shows an example of the windowing used in those cases where the exposure time for a full frame readout would saturate the CCD. The horizontal structure visible in the top windows is simply an effect of image sampling and is not real.

	WASP-15		WASP-17	
	R mag	B-R	R mag	B-R
Target	11.0	0.2	11.4	0.6
Comparison 1	10.0	0.9	12.6	0.9
Comparison 2	10.2	1.1	12.0	3.2
Comparison 3	11.5	0.5	11.9	0.9
Comparison 4	12.3	1.6	13.1	0.3

Table 3.3: Table containing the R magnitude and B-R colors for the targets (WASP-15 and WASP-17) and comparison stars indicated in Figure 3.8. These are based in information from the NOMAD catalogue [Zacharias et al., 2005].

which is slightly more precise due to the improvements on the reduction pipeline from the TYCHO-1 phase.

3.6 Data reduction

The calibration and photometry of these planetary transits were carried out using ULTRACAM's dedicated software pipeline [Dhillon et al., 2007]. This is a powerful software suite designed specifically to reduce data from this instrument with a wide flexibility of options.

Every observing night the ULTRACAM team takes twilight flat fields and biases to suit each observation mode. As mentioned in Section 3.2, ULTRACAM is capable of several readout speeds and windowing, so suitable bias frames have to be taken and used. The software creates nightly master bias and flat field frames based on knowledge of the instrument characteristics and applies the bias and flat fielding in the standard way. The ULTRACAM CCDs suffer from an effect that has been named *peppering*, which is characterised by a non-linear charge spill typically observed at illumination levels just before the onset of saturation. This level has been measured to be over 53,000 counts for the blue arm CCD and over 30,000 counts for the other two arms on a given pixel. The pipeline can be configured to ignore measurements in the regime where this takes place and observations were planned specifically to avoid this occurring in the science images. Dark frames have not been used since the ULTRACAM team have measured the dark current to be negligible [Dhillon et al., 2007].

At this stage the ULTRACAM pipeline contains a routine that allows the user to place apertures over the stars of interest, with the option to mask regions

where nearby stars could potentially contaminate the results. A PSF profile for every star is displayed, which allows for both a visual inspection of the actual size of the aperture required to contain the entire stellar flux and the shape of the PSF. This depends on how much defocus was applied to the telescope and what the seeing conditions were during the observation. A simple Gaussian fit to the PSF is often a bad indicator of the FWHM when observing out of focus. The pipeline has the ability to adjust the aperture size to keep a constant ratio of the FWHM and to centroid each aperture on each star for every image according to set criteria. The option to link apertures together is also available. With this option enabled, a specific aperture will be placed at a constant offset from another reference aperture. This is useful for both total eclipses[1] or for diagnostic tests (see Section 3.6.2).

Each image is analysed and aperture photometry is performed on every star of interest, after calibration and centroiding have been applied, as described in Section 1.5.1. For the exoplanet observations described in this Chapter, a fixed sized aperture was used throughout the night, large enough to ensure that most of the stellar flux was contained inside the aperture but chosen to minimise the noise from the background contribution. The final used aperture radius was 40 pixels (equivalent to 14"), with the sky annuli between 60 and 85 pixels in radius. Results were found to be insensitive to variations in the aperture size over a minimum threshold (35 pixel radius) where a non-negligible amount of flux from the star would fall outside the aperture at low airmass. As seen in Section 3.4, for bright targets scintillation is expected to be the dominant source of noise and therefore an increase in aperture size has a negligible effect on the resulting light curve.

A typical result from the photometry procedure can be seen in Figure 3.10, where the raw flux of a comparison star is presented. The most evident feature is the *n-shaped* atmospheric extinction effect which is addressed in Section 3.6.1. The relatively long transit duration of WASP-15b (2.71 hours [West et al., 2009]) and WASP-17b (4.37 hours [Anderson et al., 2010b]) makes these observations particularly long, and therefore the targets were observed for as long as possible with a minimum altitude of 30°, corresponding to airmass 2.0. An additional feature close to the maximum flux point (which coincides with the approach to the local meridian and also zenith) is addressed in Section 3.6.2. The vertical line indicates the meridian crossing moment.

[1]Where the star of interest effectively disappears but one would still want an aperture to be placed

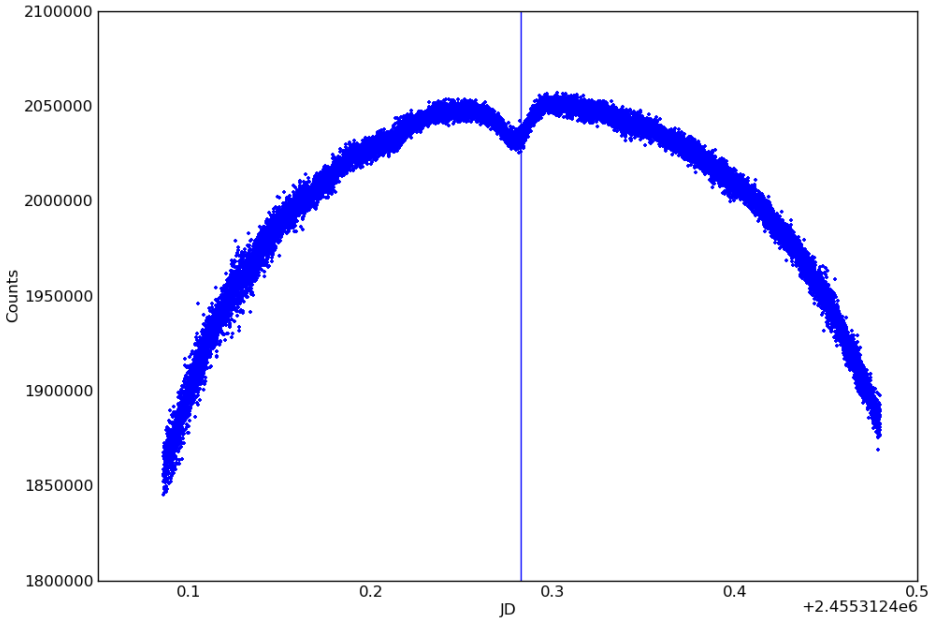

Figure 3.10: ULTRACAM r' band raw flux photometry of comparison star 2 during the WASP-15b transit observation of 2010-04-25. The vertical line indicates the meridian transition point.

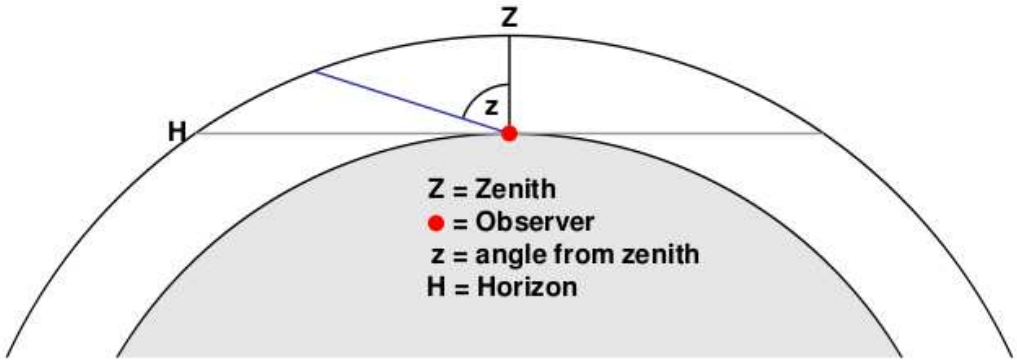

Figure 3.11: Graphical representation of airmass as a function of zenith distance. [Lynch & Livingston, 2001]

3.6.1 Airmass correction

Ground-based astronomy is always subject to atmospheric extinction [Smart, 1933]. The Earth's atmosphere is not completely transparent and this transparency is wavelength dependent [Birney et al., 2006]. Therefore, during photometric measurements, the total flux from a given star depends on its color and, more importantly, on the amount of atmosphere is it being imaged through. Figure 3.10 contains an example of the consequences of such property. The flux will decrease depending on *airmass*, which is the path length of the light originating from the star as it travels through the atmosphere of the Earth. The airmass χ of a star is given by $\sec z$, where z is the angle between zenith and the target, as shown in Figure 3.11. This relation, however, assumes a flat Earth and therefore cannot be used for values of z close to 90°.

Assuming a constant atmospheric composition in all directions, the magnitude of a star can be modelled as a function of airmass using

$$m_\lambda = m_{\lambda 0} + k_\lambda \chi, \tag{3.9}$$

where $m_{\lambda 0}$ is the stellar magnitude if observed above the atmosphere and k_λ is the extinction coefficient. This parameter can be measured from each location and it typically relatively constant.

It is therefore possible to use the data plotted in Figure 3.10 and apply an *airmass correction*. This process involves plotting the magnitude (or simply $\log flux$) as a function of the airmass each point was taken under. A simple linear fit to the result will yield the extinction coefficient as the gradient and $m_{\lambda 0}$ as the

intercept. Using a fitted extinction coefficient accounts for the color differences between the stars. Figure 3.12 contains a series of panels of log $flux$ as a function of airmass and the result of the airmass corrections under them. The left pair shows the result of using a fit with constant extinction coefficient (equation 3.9). This is clearly unsuitable as there is a remaining trend on the corrected data, and a close inspection of the top panel shows two data sets, before and after the meridian crossing.

A more complex approach was used, which considered a linearly changing extinction coefficient with time t. The expression for this case is given by

$$m_\lambda = m_{\lambda 0} + (k_\lambda t + k_{\lambda 0})\chi, \tag{3.10}$$

which also corresponds to the middle panels in Figure 3.12. This is now a suitable correction. An attempt to use a quadratically changing extinction coefficient was done (right panels) and this shows no clear improvement with respect to the amplitude of the systematic effect being studied, so the linear approach was used throughout. The data points clearly within the feature visible close to the middle of the night were not considered for the airmass fit.

Due to the wavelength dependent nature of the observations and the fact that broadband filters will yield different airmass profiles for different stellar types, the standard use of comparison stars simply by taking the ratio of the fluxes results in a data set which contains an overall trend, commonly called the *color term*. An airmass correction prior to taking the ratio of fluxes typically takes this factor into account, as the color term is now included in the variations on the value of the extinction coefficient for different stars. The airmass correction also helps with investigating the *meridian feature* as this now becomes the dominant residual effect. Section 3.6.2 addresses this issue.

3.6.2 The 'meridian problem'

The results from the airmass correction described in Section 3.6.1 for both the target and all available comparison stars can be found in Figures 3.13, 3.14 and 3.15. These refer to the observations taken during the photometric nights, and the data are averaged into one minute time bins. Both targets' declinations are relatively close to the local latitude and therefore they cross the meridian at close proximity to zenith (WASP-15 at angular zenith distance of 3.1° and WASP-17 at 1.2°). Alt/Az telescopes cannot observe at locations close to zenith due to the inability of the rotator assembly and motors to turn the telescope and instrument

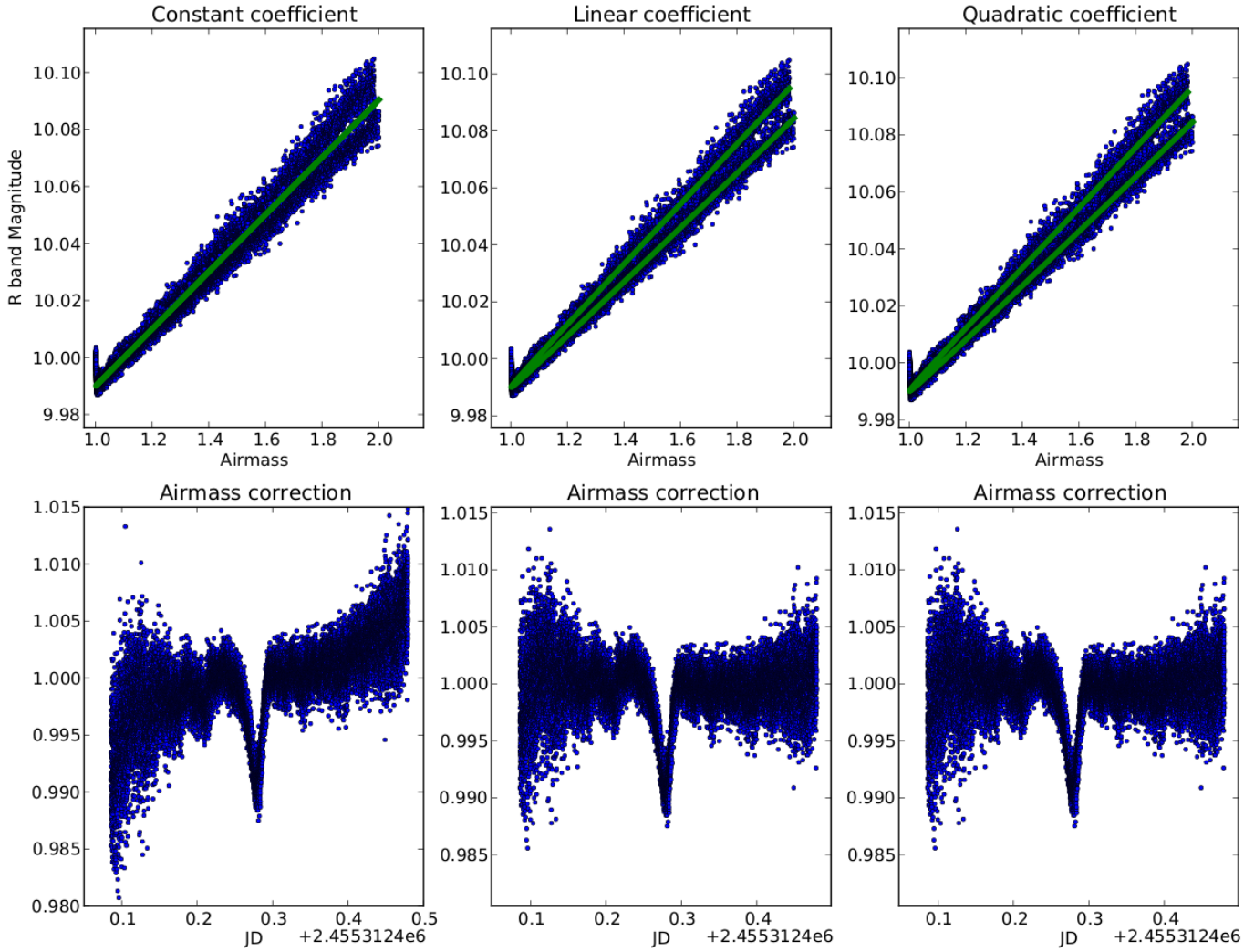

Figure 3.12: Airmass corrections for the WASP-15b transit observation of 2010-04-25 in the r band. The three examples show the correction to a comparison star using a constant (left), linearly (middle) and quadratically (right) time varying extinction coefficient. The data sets are plotted as a function of airmass (top panels) and the results of the airmass correction (bottom panels) are shown.

quickly enough. Due to this fact observing had to be halted and restarted before and after the zenith passage. However, an attempt to guide through zenith was made on the night of 25th April 2010 and, despite the fact that it is possible to see that all nights contain obvious features close to the lowest airmass point, this night in particular is better suited to study the cause of this feature in detail.

The airmass corrected raw fluxes firstly show evidence of the influence of the increased background light due to the Moon on the nights taken during April 2010, in the form a higher noise for these light curves. This is particularly severe considering the fact that the green and red arms contained broadband filters whilst the WASP-15b observation in May 2010 used narrower filters at these wavelengths. Additionally, a direct comparison between the light curves in the u band for both observations of this planet's transit are a clear example of the influence of the Moon. These Figures also show that the model presented in Figure 3.7 for bright time correctly predicts that the influence of the background sky light can be an important contribution to the overall noise budget, particularly for fainter stars. Comparison star 4 in Figure 3.13 is an example of this.

More importantly, however, the raw fluxes presented show that each light curve contains examples of red noise of amplitudes of up to 2% which happen simultaneously for all stars but show different amplitudes. Generally, the morphology of these features is common between stars on the same CCD, but a differential magnitude approach is incapable of removing them completely. (see Figure 3.27 for examples).

A detailed inspection of all the data sets shows that this *meridian feature* is typically similar in shape between all stars in the same arm, but there is a clear difference between the 3 arms of ULTRACAM for any given star. It is also significantly different over the several nights covered by these observations. Indeed, the only common characteristic of this feature between all nights, arms and stars is that it is consistently more noticeable close to or approaching zenith. Nevertheless, the general nightly trends seen in the g and u bands in Figure 3.14 also suggest that this effect may be affecting the entire data set. Furthermore, Tables 3.4 and 3.5 show the colors and fitted extinction coefficients k_λ for each star in the process of producing the results displayed in Figures 3.13 and 3.15. The coefficients presented are the nightly time average for each star which, as can be seen, do not correlate well with the stellar colors. The particular case of the extinction coefficient for the u band on comparison star 2 for the WASP-17 observation is a clear outlier related to the poor quality of the light curve. This non-correlation can be attributed to the possibility that the airmass correction using a linearly time varying extinction coef-

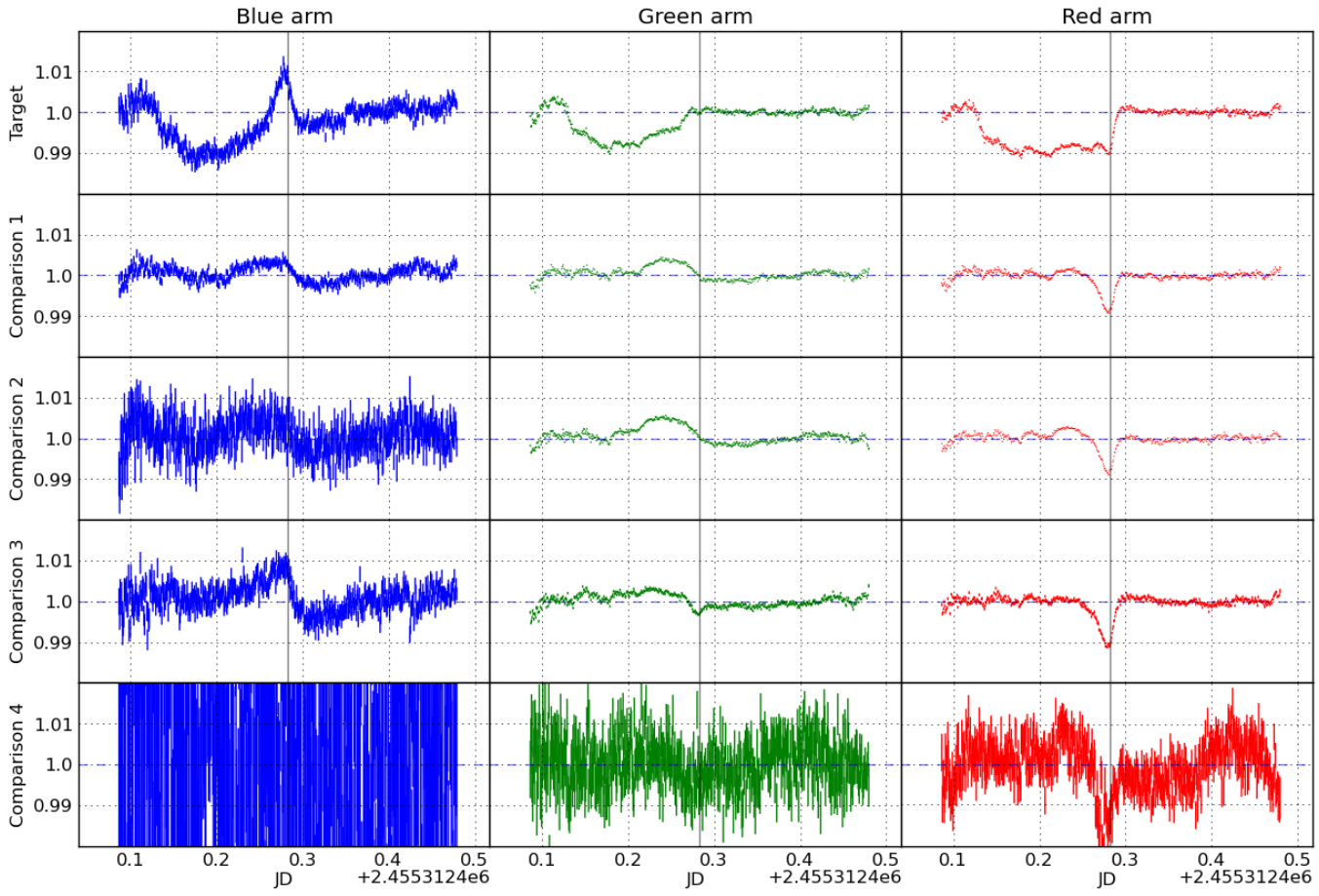

Figure 3.13: Airmass corrected raw fluxes for the target and 4 comparison stars. These data refer to the observation of the transit of **WASP-15b** on the night of **2010-04-25** in the u, g, and r bands (Blue, Green and Red arms respectively). All fluxes are normalised and plotted to a common scale for comparison. The vertical black lines indicate the meridian transition time. The data have been averaged into one minute time bins.

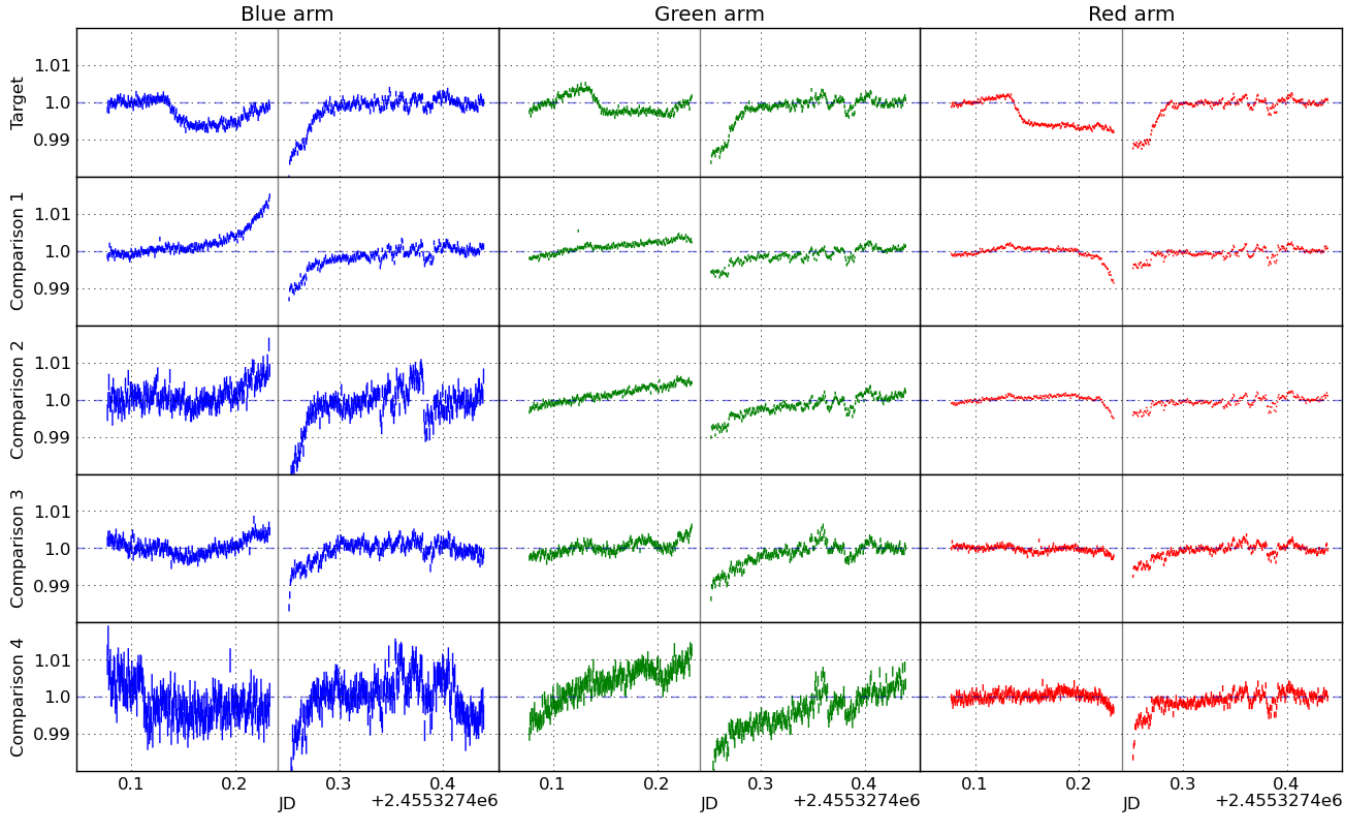

Figure 3.14: Airmass corrected raw fluxes for the target and 4 comparison stars. These data refer to the observation of the transit of **WASP-15b** on the night of **2010-05-10** in the u, HeII, and NaI bands (Blue, Green and Red arms respectively). All fluxes are normalised and plotted to a common scale for comparison. The vertical black lines indicate the meridian transition time. The data have been averaged into one minute time bins.

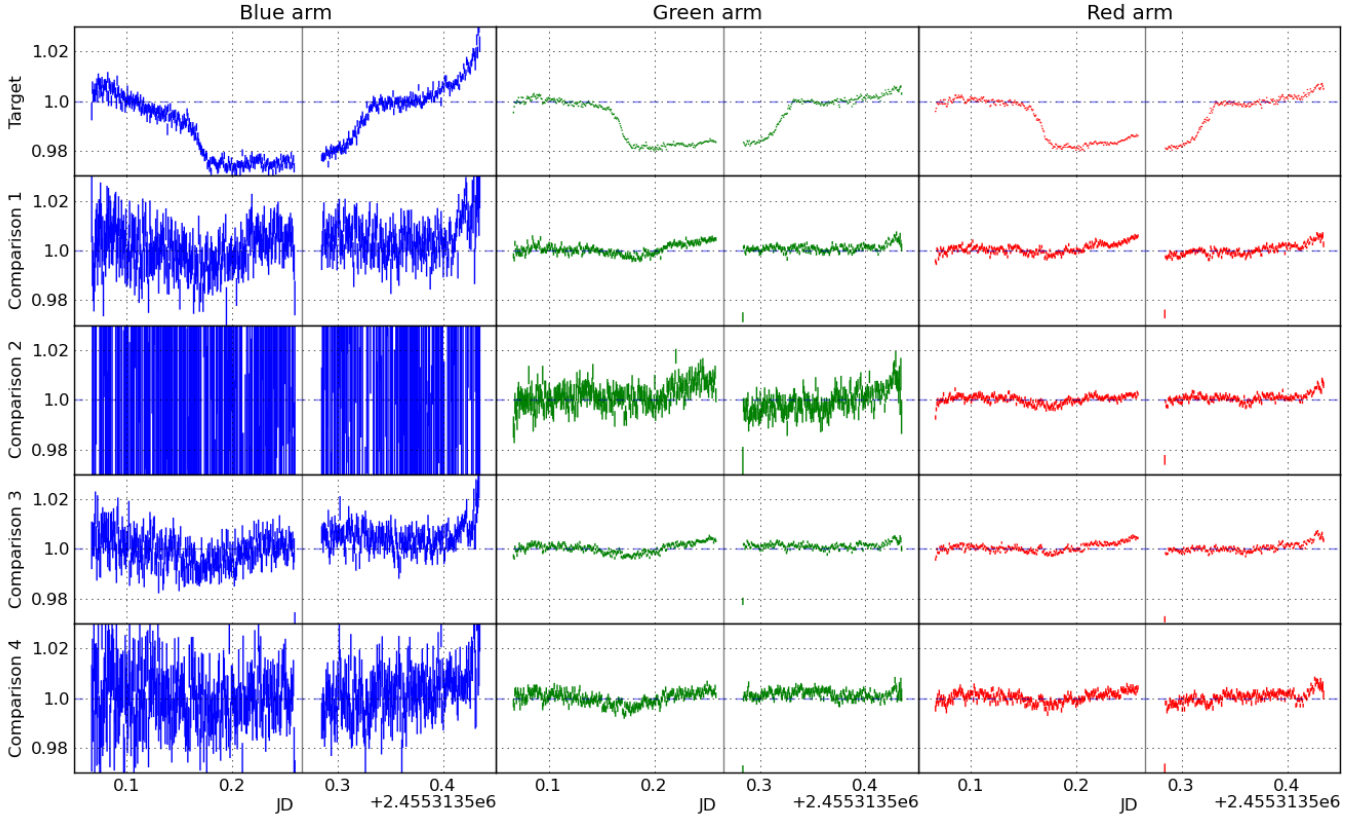

Figure 3.15: Airmass corrected raw fluxes for the target and 4 comparison stars. These data refer to the observation of the transit of **WASP-17b** on the night of **2010-04-26** in the u, g, and r bands (Blue, Green and Red arms respectively). All fluxes are normalised and plotted to a common scale for comparison. The vertical black lines indicate the meridian transition time. The data have been averaged into one minute time bins.

	WASP-15 2010-04-25			
	b-r	k_λ r	k_λ g	k_λ u
Target	0.2	0.0984	0.1798	0.4857
Comparison 1	0.9	0.1003	0.1811	0.4691
Comparison 2	1.1	0.0975	0.1668	0.4717
Comparison 3	0.5	0.0978	0.1829	0.4779
Comparison 4	1.6	0.0998	0.1835	0.5034

Table 3.4: Table containing the b-r colors for the target (WASP-15) and comparison stars indicated in Figure 3.8 and the fitted average extinction coefficients for all 3 bands on the night of 25th April 2010. The colors are based on information from the NOMAD catalogue [Zacharias et al., 2005] and the coefficients refer to the airmass correction described in Section 3.6.1 performed to the data set.

	WASP-17 2010-04-26			
	b-r	k_λ r	k_λ g	k_λ u
Target	0.6	0.0919	0.1707	0.4780
Comparison 1	0.9	0.0850	0.1661	0.4778
Comparison 2	3.2	0.0789	0.1537	0.6709
Comparison 3	0.9	0.0868	0.1636	0.4737
Comparison 4	0.3	0.0933	0.1690	0.4707

Table 3.5: Table containing the b-r colors for the target (WASP-17) and comparison stars indicated in Figure 3.8 and the fitted average extinction coefficients for all 3 bands on the night of 26th April 2010. The colors are based on information from the NOMAD catalogue [Zacharias et al., 2005] and the coefficients refer to the airmass correction described in Section 3.6.1 performed to the data set.

ficient is partially also compensating for an additional linear trend that is unrelated to atmospheric extinction.

Before any accurate measurement of the transit depths in the various wavelengths can be done, the source of these systematic effects must be understood. The following subsections describe experiments done to identify the potential causes of the meridian feature and exclude those that are not.

Cosmetic defects

The meridian feature in the majority of data sets seems to show a loss of flux at the zenith approach, therefore the possibility of loss of light inside the aperture was considered. It is unlikely that this could be due degradation of seeing as the feature is visible on every night, but saturation taking place on a selection of pixels could produce a resulting decrease of the total flux, and the number of saturated pixels could vary depending on airmass. Individual images were inspected and the

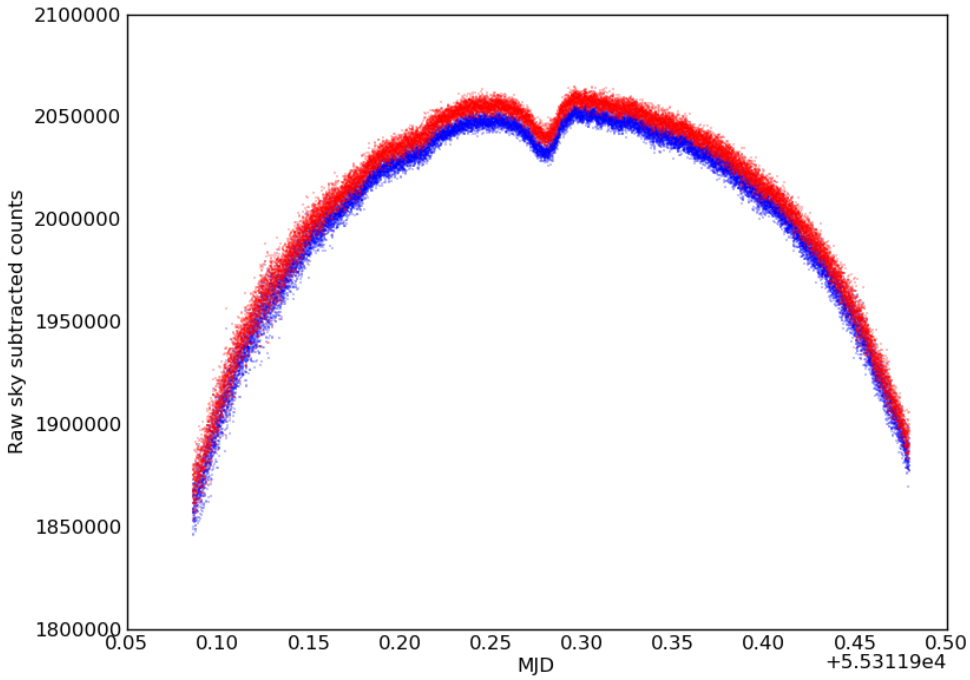

Figure 3.16: Raw fluxes of comparison star 1 of WASP-15 observed on the 25th April 2010. This Figure shows the result of reducing the data using an oversized aperture in red (60 pixels in radius) compared with the final chosen size for this observation (40 pixels) represented by the blue curve. It shows that the meridian feature is not caused by light falling outside of the aperture.

peak counts measured during the zenith approach and saturation was found not to take place. Moreover, the reduction pipeline flags any data points that contain pixels with count levels higher than the peppering level, and this did not take place in the observations. A reduction using an oversized aperture still contains the same feature, therefore the possibility of light spilling out of the aperture is definitely rejected. Figure 3.16 shows the result of this experiment. The difference in flux between the two curves is explained by the fact that when observing significantly out of focus it is inevitable that some small portion of the light from the star will fall significantly far from the centre of the stellar position, but within regions where the sky noise will dominate. Our choice of optimal aperture size was based both on visual inspection of the extent of PSF wings and to minimise the RMS of portions of the airmass corrected raw flux of the brightest star.

Individual images and flat field frames were inspected for the presence of

bad or non-linear pixels around the locations where stars were observed on the chip. As mentioned in Section 3.4 defocussing will reduce the flat fielding noise and the consequence of the presence of a bad pixel inside the aperture is reduced. However, if a significantly bad pixel is encountered (whose likelihood is increased by defocussing as the light is spread over more pixels) there might still be residual errors from it. No evidence of bad pixels was found in the inspection of the individual images. Moreover, since all stars suffer from a similar feature on the same CCD it is not possible that the feature of interest could be caused by bad pixels.

Background subtraction

The possibility that problems with the background subtraction stage could be causing this feature was considered. Moreover, the sky brightness in the observations done on 25th and 26th April 2010, as well as that which took place on 25th May 2010 all have high levels of background light due to the full Moon presence. Indeed, the background annulus is relatively large and structure in the background could cause systematic noise to be present. Reductions were performed with both a median and sigma clipped mean as estimators for the background and found to generate essentially identical results.

Figure 3.17 contains plots of the background levels as measured by the ULTRACAM pipeline for the target and comparison stars 1, 2 and 3 for the g band. These are the number of sky counts per pixel per second as a function of time for the target and the first 3 comparison stars. It is evident that the moon has a profound impact on the background curves, not only on the overall level of the background, but also on the structure visible in the background curves. This is mainly thought to be due to how much of the moon light enters the telescope dome at any given time and any abrupt changes close to the meridian transition will be due to the fact that the dome is moving rapidly and turning a full 180°. This experiment was done in order to understand if any correlations between changes in the background correlate with the effects visible in the light curves. A relation between the background levels of different stars (mainly the target and the comparisons) enables an extra degree of detail to be examined, since changes in the ratios indicate structural variations in the spatial distribution of the background light.

The results show that there are a large number of variations both in the background levels and the ratios that do not clearly affect the differential photometry light curves, and that most features visible close to the meridian passage are likely due to rapid changes in the illumination inside the dome by the moon, which also causes gradients across the field of view. Therefore, the features visible in the ratios

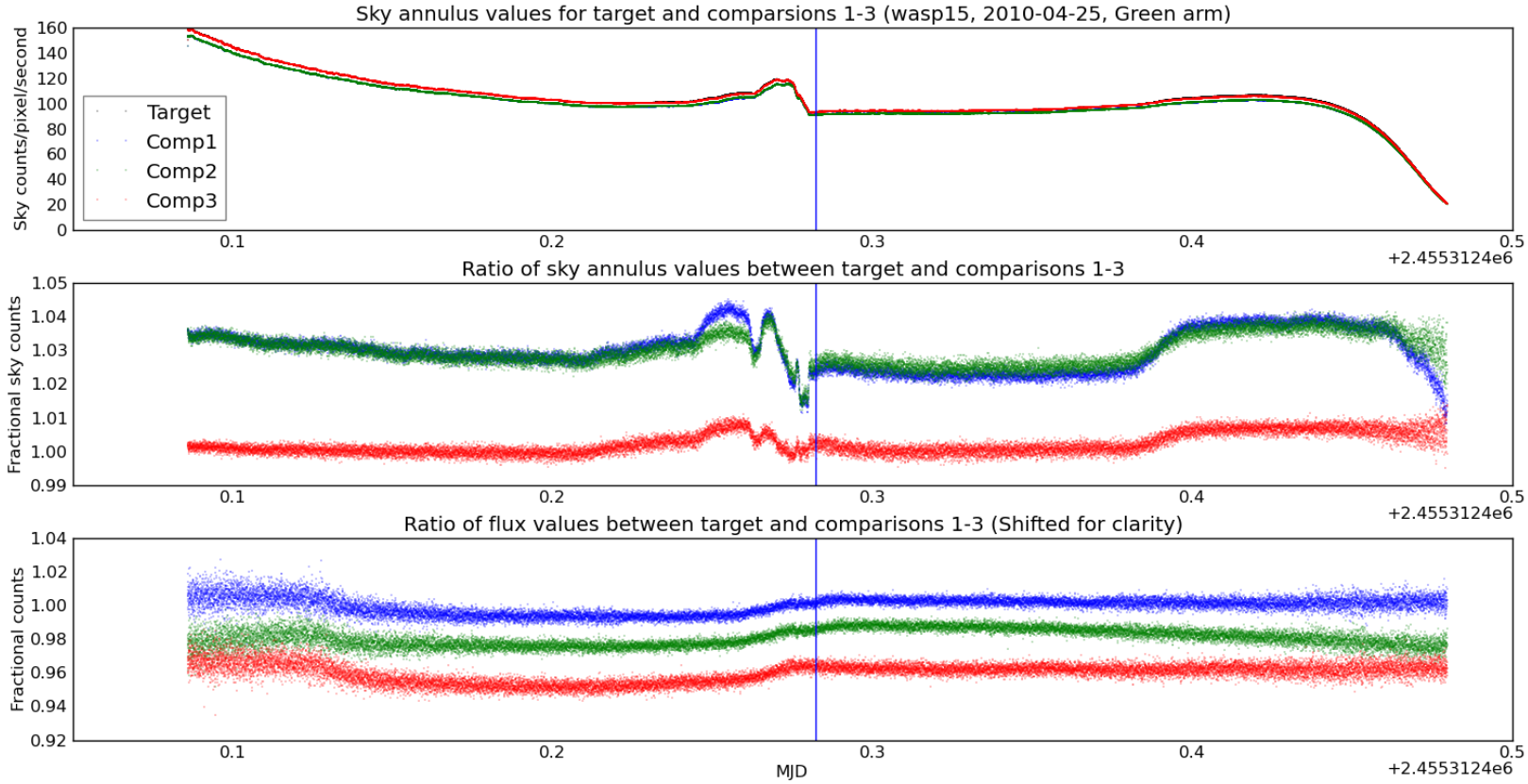

Figure 3.17: Background levels of the target and 3 comparison stars. These data refer to the observation of the transit of **WASP-15b** on the night of **2010-04-25** in the g band. The top panel contains the measured background level for the target and 3 comparison stars. The middle panel shows the ratio between the target's background levels and each comparison star, whilst the bottom panel contains the ratio between the fluxes. The blue vertical line indicates the point of the meridian passage.

of the background levels can be associated with these gradients. It does not, however, imply that any features would be visible in the background subtracted flux. Indeed, ideally this would not be the case.

As a final test, a reduction was done with three apertures placed where no stars were visible and linked (see Section 3.6) to a reference star, so as to move accordingly during the night. The expectation is that the background subtracted fluxes from these apertures would be completely flat, thereby indicating that the background subtraction is working well. Figure 3.18 contains the results of this test. The top panel shows the airmass corrected flux of comparison star 1 in the three observed bands (r,g, and u). The other panels show the background subtracted flux of the apertures placed elsewhere on the CCD chip. It is immediately clear that the sky apertures are flat and featureless.

Despite the high variation of the background level during the observation (see Figure 3.17) this experiment rejects the possibility that unsuitable background estimation is the cause for the meridian feature.

Flat fielding

Flat fielding errors typically arise from motion of the PSF in detector coordinates during a single run or due to multiplicative (as opposed to additive changes, such as increases in the background levels or gradients due to lunar presence, which can easily be decorrelated with the simple background subtraction) changes in the overall structure of the background light through the night. Exoplanet transit observations in particular can suffer from both, due to the relatively long time scale nature of these events. In Alt/Az telescopes, as is the case of the NTT, the instrument is mounted in a rotating assembly that compensates for the changing orientation of the sky with respect to the telescope as the celestial sphere moves. However, the telescope itself and, subsequently, it's vignetting pattern, remains fixed.

Shifts in the position of the stars in the CCD lead to changes in the overall QE of the pixels inside the aperture. Flat fielding minimises this source of error but at the sub mmag photometric level residual effects can still take place. ULTRACAM's pipeline centroids each aperture on the stars for each measurement, therefore it is possible to plot the path of the stars on the chip during the night. Figure 3.19 shows the pixel position evolution of the PSF of WASP-15 during the observation of 25th April 2010. The two panels show the X and Y positions of the aperture respectively. It is possible to see that during the meridian crossing the aperture moves rapidly by ≈ 10 pixels in the vertical direction while showing an associated shift in the horizontal direction. This is thought to be related to inaccuracies in the

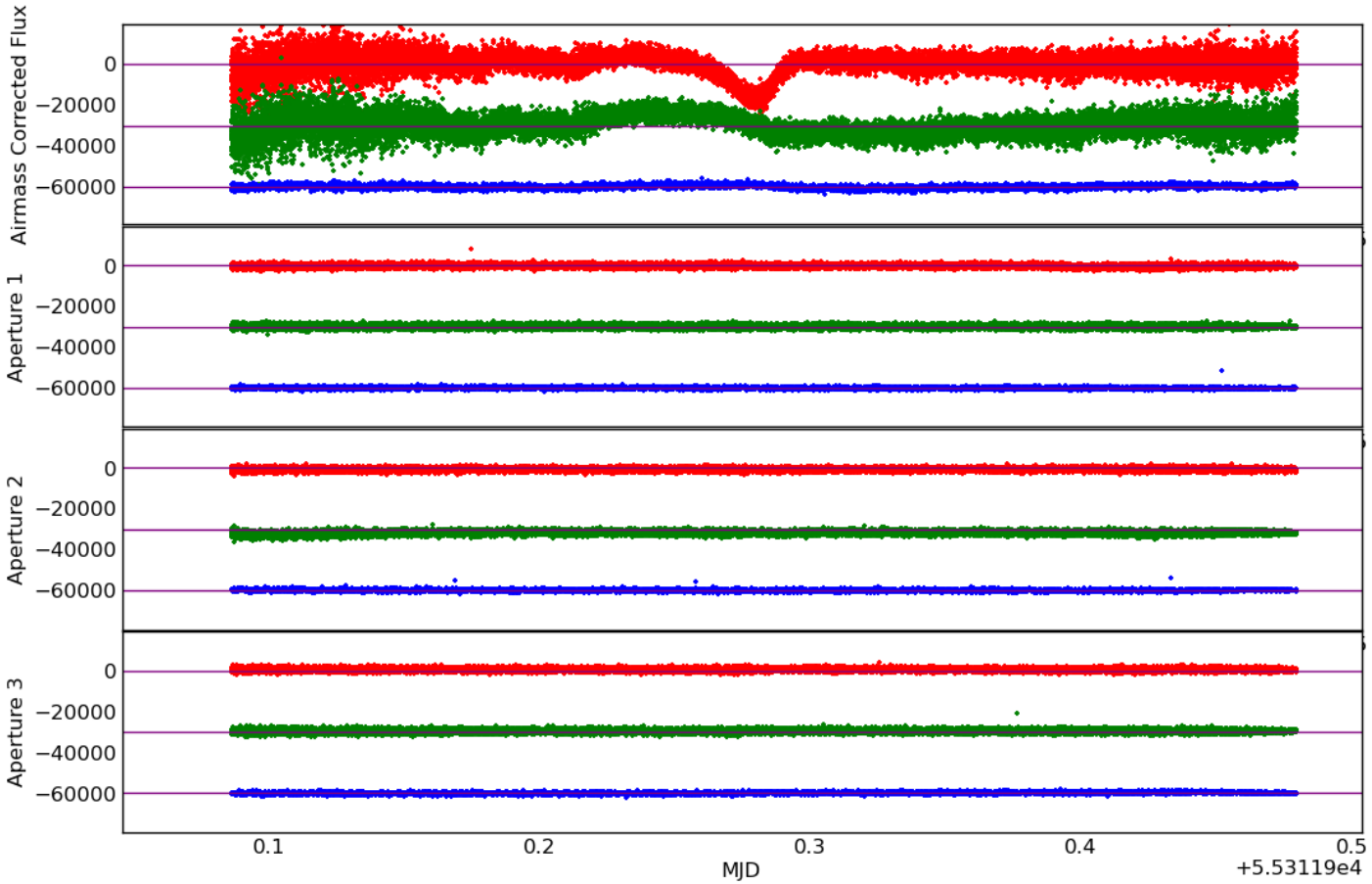

Figure 3.18: Background subtraction test, in order to determine if the correction is working correctly. This refers to the observation of the transit of WASP-15b done on 25th April 2010 with ULTRACAM on the NTT. The top panel shows the airmass corrected flux of comparison 1 on all bands: u (blue); g (green); and r (red). The other panels show the background corrected flux from 3 apertures place where no stars were visible. This Figure shows that the background subtraction is working well, despite this being a full moon night.

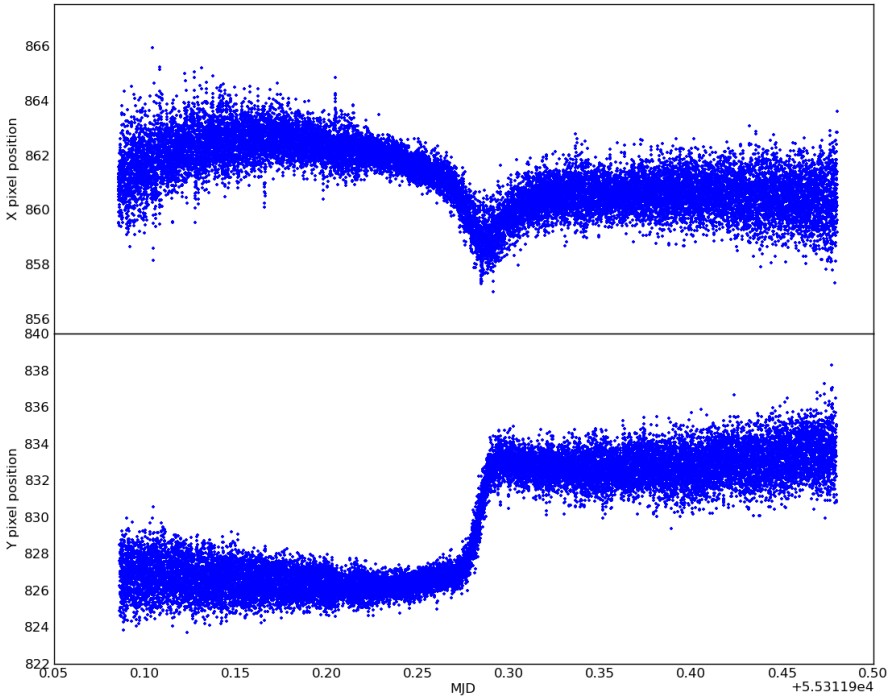

Figure 3.19: Measured pixel positions for the aperture placed on WASP-15 during the night of 25th April 2010. The top panel shows the horizontal (X) position and the bottom the vertical (Y) position evolution during the night.

telescope guiding as it approaches zenith, where both the telescope assembly, dome and the rotator are moving at maximum speed to match the orientation of the field with respect to the optical axis.

The shape of the horizontal position curve does seem to correspond with the airmass corrected fluxes in the r band shown in Figure 3.13 and attempts were made to decorrelate the systematic effect with pixel position. However, these attempts were unsuccessful, partly because the shape of the systematic does not match precisely that of the horizontal position curve, but also because the stellar positional drifts must be the same for all stars and all arms of the instrument, but the stars would drift over different pixels. Since the shape of the systematic noise is not common between all arms, positional drifts are unlikely to be the cause of such effects. Moreover, any drifts would most likely cause variations on the stellar fluxes that would be significantly different between all stars on the same CCD as they would

be associated with the QE of specific pixels. Indeed, the similarity in shape of the systematic effect clearly points to an overall and relatively uniform modulation that affects the entire chip at once whilst containing some structure which causes the flux variations between the stars to be slightly but sufficiently different not to be negligible.

Vignetting changes

The vignetting visible in flat field frames from any Alt/Az telescope is a combination of the vignetting from the telescope and that from the instrument being used. During twilight, typically the rotator angle is set to zero while a suitable field is chosen for twilight flats. However, during the observing run, the telescope vignetting is rotating with respect to the instrument, and thus there is a chance that a rotating pattern which is not correctly flat fielded might cause the effect being investigated.

Initial attempts to visualise this potential pattern by dividing frames taken in the middle of the night by those before the systematic effect is clear have yielded no results, since changes in the spatial structure of the background level dominate this ratio, especially on those nights where the Moon was present. An alternative solution attempted was to plot the values of the flat field frame starting at the position where the star was initially observed and trace its path in rotator space. In order words, during the meridian transition, for objects that do so close to zenith, the telescope and rotator have to essentially flip 180°. So, a plot of the flat field values in a path from the stellar initial position to its final location based on changes of the rotator angle was generated. This will also sample the instrument vignetting and any other flat fielding features present. Figure 3.20 shows the path of the star in rotator coordinates as it samples the telescope vignetting, as well as the resulting time series (bottom left panel). The majority of the data on this plot refers to the initial (top right) and final (bottom left) ends of the path shown. It is possible to see a sharp change, clearly associated with the transition of the dividing line between the 2 sides of the CCD. This is a result of the simultaneous readout of the chip in both directions, mentioned in Section 3.2. Other features are likely to be due to the overall vignetting present, whose components (i.e., from the telescope and instrument) can not be distinguished with this approach. The vignetting from the instrument is likely to be fixed with respect to the orientation of the CCDs, but the telescope vignetting will rotate through the night. However, the spatial position of the stars in the WASP-15 field, as seen in Figure 3.8a, shows that the target and comparison star 1 are place in opposite corners of the chip during the observation.

Therefore, the signals from the rotating telescope vignetting would be expected to be different and perhaps reversed between the two. Since the positions of stars occupy a wide range of locations on the chip and the signal is similar between them, it is unlikely that this could cause such an effect. For comparison, the same procedure for comparison star 3 was performed and the results are shown in Figure 3.21. This star is placed on the opposite side of the CCD chip with respect comparison star 1 and therefore shows a reciprocal shape in the flat field path. However, in contrast, the shape of the meridian feature is similar between the two stars.

Even though the possibility that a rotating telescope vignetting pattern is a source of systematic noise can not be completely excluded, we concluded that it could not be responsible for the systematic effect in question.

Rotator angle correlation: Vignetting by the guiding probe

The only common characteristic between the systematic flux variations in all stars, arms and nights is the fact that it is consistently more prominent when the telescope is close to zenith. At these times, many variables are changing more rapidly than they do at other times of observation, such as the dome position, telescope azimuthal pointing and the rotator angle. As discussed earlier, these lead to rapid changes in the background light, positional drift and other factors, including the parallactic angle. This angle is defined as "...the angle formed at a point on the sky between a great circle between the point and zenith and a great circle between the point and the celestial pole."[Birney et al., 2006]. In essence, the parallactic angle is a measure of the orientation of a stellar field with respect to the local meridian. For any field that crosses the meridian at the zenith point, the parallactic angle would not change apart from an instant 180° rotation at zenith. The relation between the stellar flux of comparison star 1 as a function of this angle is shown in Figure 3.22, where it is possible to see that the vast majority of the data are taken at either end of the systematic feature, where the parallactic angle is not changing rapidly. It is also possible to see that the feature is a smooth function of parallactic angle, showing that there is a strong correlation with the rotation of the field with respect to the telescope.

In summary, the systematic effect seen in the light curves is significantly different in shape between all three arms of ULTRACAM, and different between different nights. It is similar in shape between stars on the same chip, but sufficiently different in amplitude such that a differential photometry approach is unsuccessful at removing it. Therefore, it is a relatively uniform effect across the CCD but containing some structure. It is also a multiplicative effect, thereby implying that it

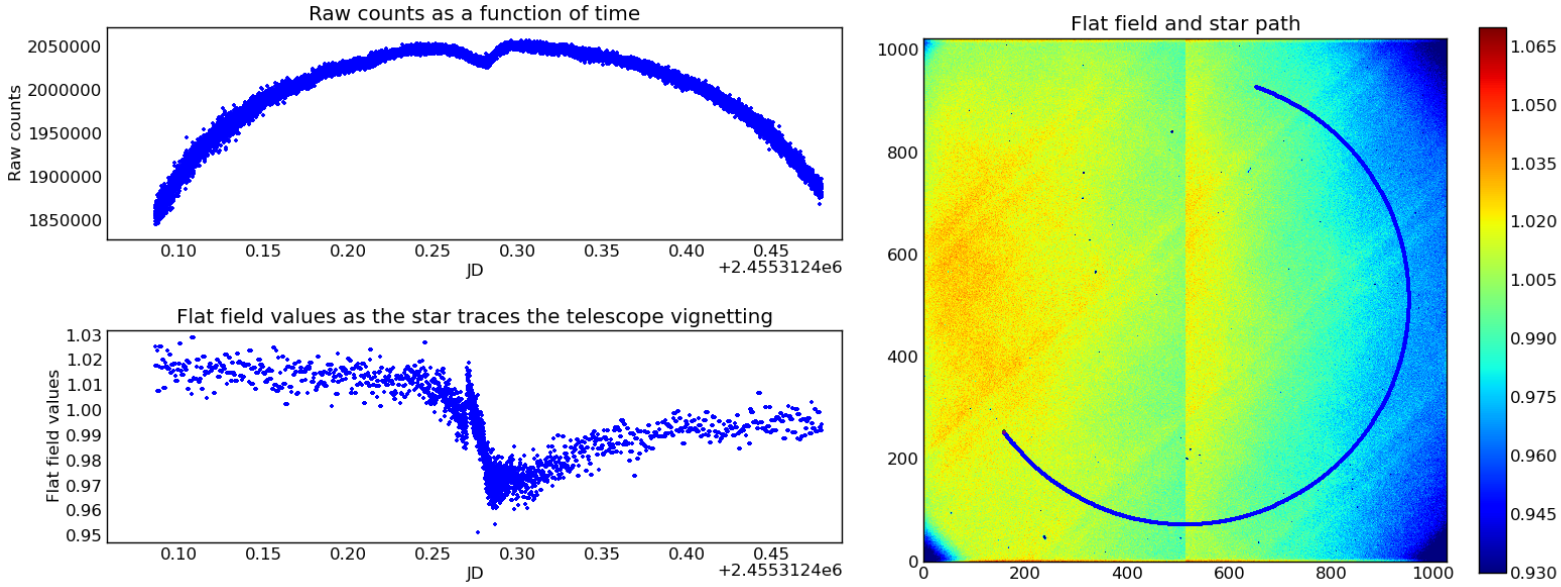

Figure 3.20: Sampling the flat field frame at positions where the telescope vignetting would be incident on a star of interest. The top left panel contains the raw flux of the star of interest (comparison 1) in the r band for the observation of WASP-15b on 2010-04-25 and the right panel shows the r band flat field frame with the path of the star in rotator coordinates. The bottom left panel shows the time series of the flat field values at the rotator angles corresponding to the positions adopted during the observing run.

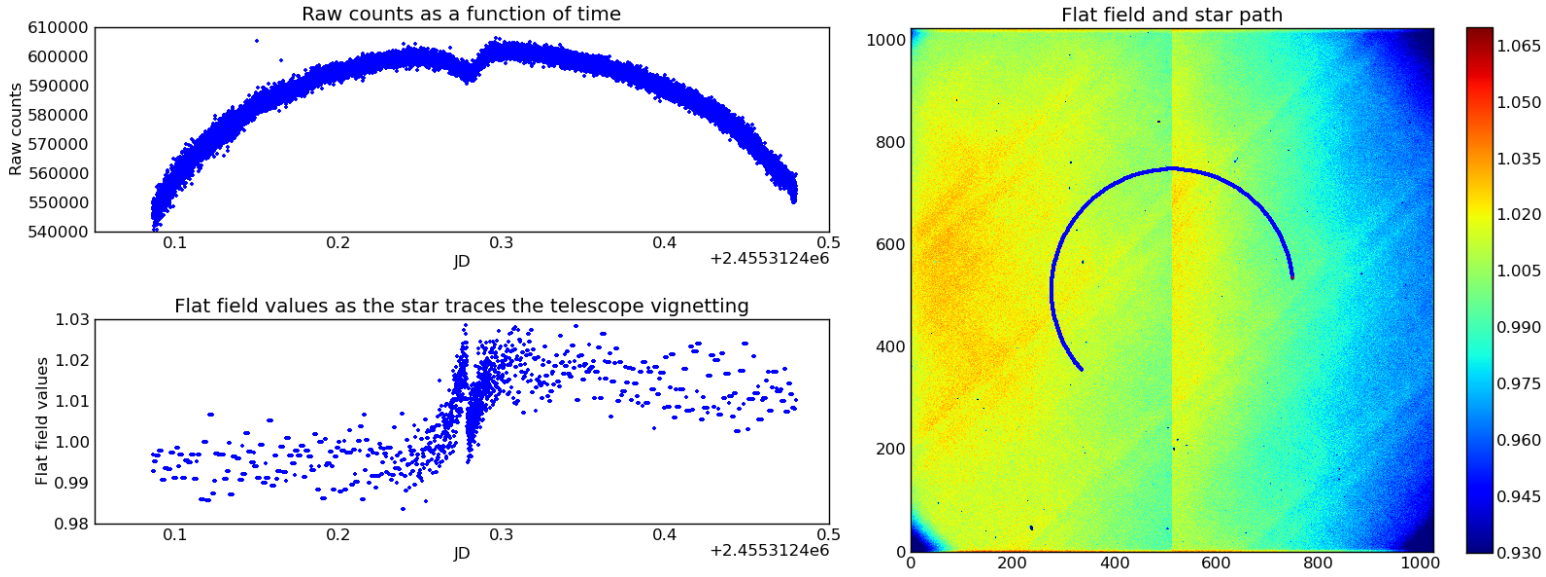

Figure 3.21: Sampling the flat field frame at positions where the telescope vignetting would be incident on a star of interest. The top left panel contains the raw flux of the star of interest (comparison 3) in the r band for the observation of WASP-15b on 2010-04-25 and the right panel shows the r band flat field frame with the path of the star in rotator coordinates. The bottom left panel shows the time series of the flat field values at the rotator angles corresponding to the positions adopted during the observing run.

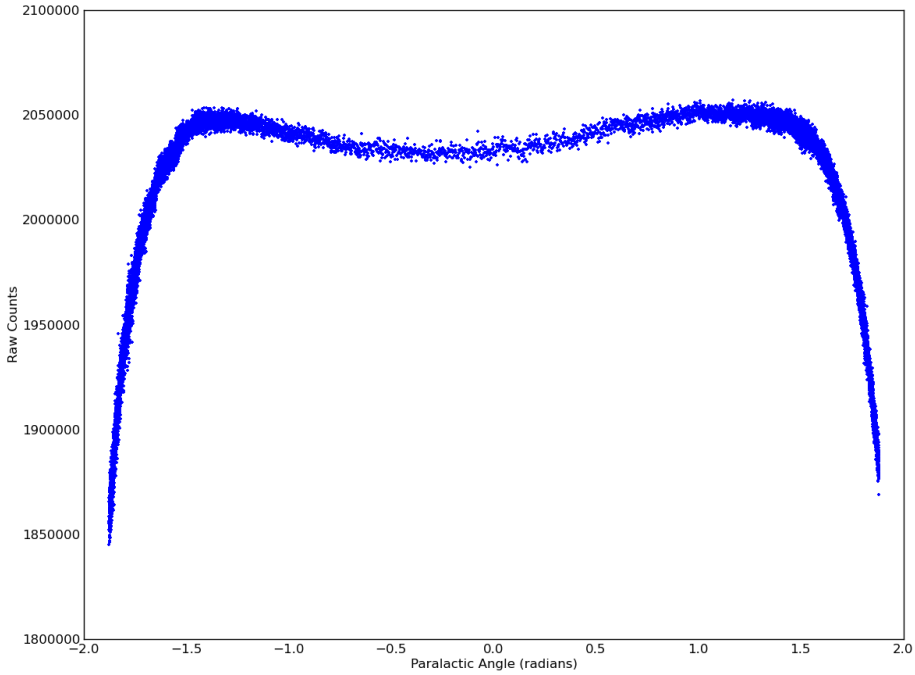

Figure 3.22: Raw flux of comparison star 1 as a function of parallactic angle for the observation of WASP-15 on the night of 25th April 2010 in the r band. The dip in the middle section of this plot corresponds to the $\approx 1\%$ seen in the airmass corrected light curve of comparison star 1 displayed in Figure 3.13.

is of a vignetting-like origin and not due to non-uniform variations in the background light. And finally, it is a smooth function of the parallactic angle, showing that it is naturally more likely to be evident at occasions where the telescope rotator is moving rapidly.

Through private communication with Professor Vik Dhillon, a series of test images were obtained. These refer to a test done by the ULTRACAM team to gauge the impact of the NTT's guide probe on the ULTRACAM FOV. This probe is used to ensure that every star remains on the same pixel during an observation, by observing another star outside the field of view and instructing the telescope to perform small offsets to keep this guide star in the same position. The guide probe is placed in the focal plane. The downside of this approach is that the probe is inserted into the telescope beam and can, if the guide star is chosen to be too close to the stars in the field of view of the instrument, introduce an extra vignetting component.

The ULTRACAM team used a dome lamp to illuminate the CCD and compared the resulting flat when the probe was parked with the probe at several places with respect to the FOV. A visual representation of the results of this experiment in the r band are visible in Figure 3.23, where the red square represents the ULTRACAM FOV while the yellow rectangle is the standard avoidance region for the guiding probe for use with the resident photometer of the NTT. Multiple positions for the guide probe were tested and the ratios between the flat at each and the flat with the probe parked are displayed. The g and u band filters were used in the other arms. It is immediately possible to see that at positions close to the limit of the avoidance region the probe introduces a component of vignetting at the edge of the FOV, which was measured to be as significant as 30%. This is perhaps not surprising, since the standard avoidance angle shown by the yellow box was set for the FOV of the resident camera (EFOSC), which has a field size of 4.1 arcmin x 4.1 arcmin. ULTRACAM's field size on the NTT is 6.0 arcmin x 6.0 arcmin, which would require a larger avoidance region.

In the interest of investigating the possibility that this could be the cause of the meridian feature, the results of the test performed by the ULTRACAM team were analysed in more detail. The approach of taking the ratio between the flats at the various positions and the flat when the probe is in *park* position was once again used. It is clear from Figure 3.23 that the shape of the vignetting pattern changes with the position of the probe with respect to the FOV. It is important to note that the probe assembly does not rotate with the instrument, but instead moves in horizontal/vertical translation to compensate the rotation of the field and,

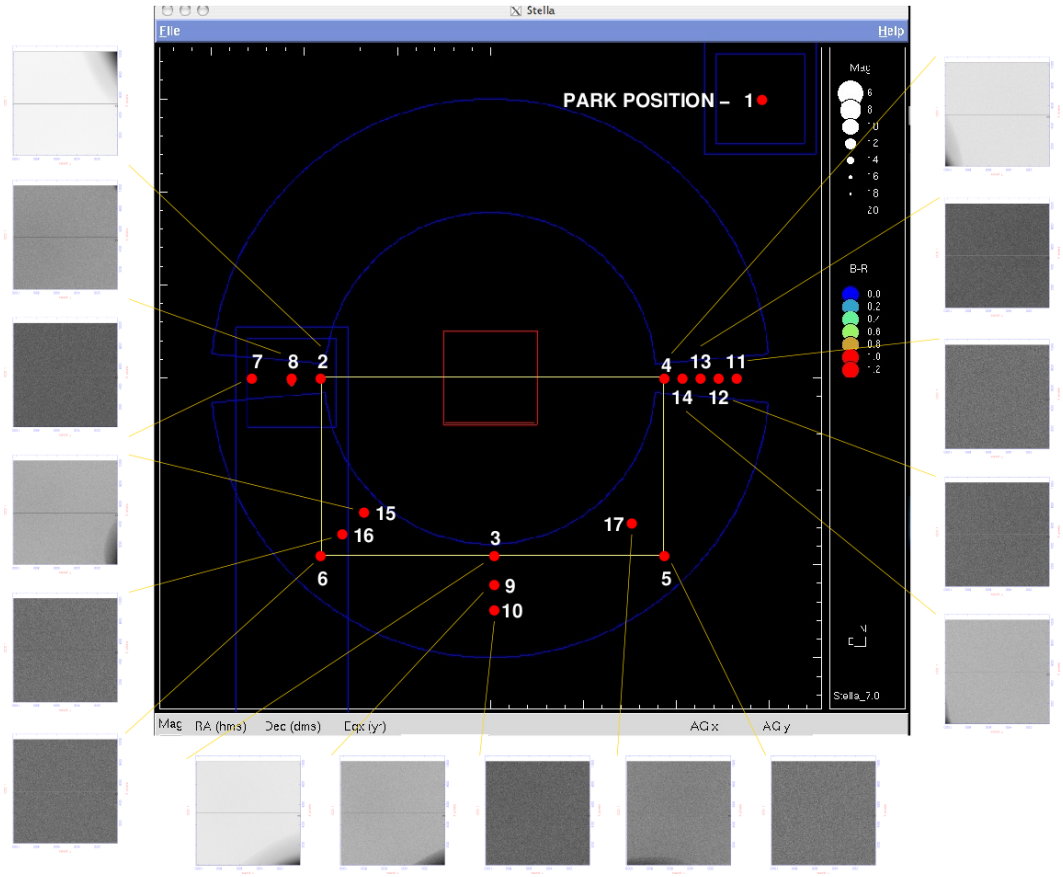

Figure 3.23: Visual result of a test performed by the ULTRACAM team on the effect of the NTT guide probe upon the field of view of ULTRACAM. The red square represents the ULTRACAM FOV while the yellow rectangle is the standard avoidance region for the guiding probe. The CCD was illuminated using a dome lamp and the images show the result between the division of the dome flat with the probe parked (position 1) and at all other shown positions. This test only show results for the r band filter. Courtesy of Vik Dhillon.

hence, during a zenith passage such as the one that took place on the nights under discussion the probe will move in a circular fashion across the zone of avoidance continually changing the vignetting properties.

Position 3 (see Figure 3.23) was used as an example to study this effect in more detail. The ratio between the dome flat at that position and the dome flat with the guide probe in "park" shows a vignetting feature at the corner of the CCD of up to 12% in amplitude in the r bands and 6% in the g band. The u band appears to show no visible structure. However, the results of the test performed by the ULTRACAM team in the u band show negligible flux, suggesting that either the lamp used exhibits no flux in the u band or that the path to the blue arm was blocked. A visual representation of the resulting pattern from the guide probe can be seen in Figure 3.24, where the ratios of the flats for all 3 bands are shown. The scales used for these images are identical in all arms for comparison. The plot in the top right panel of the Figure contains curves that show the pixel values of the diagonal starting in the (0,0) corner for each arm. It is possible to see the extent of the guide probe's influence in the corner of the chip for this particular position in the r and g bands and that the overall level of the fractional flux onto the chip has been reduced by just over 1% (see values quoted in the Figure legend). This level was measured by taking the median of all the values from the centre of the CCD to the top right corner, indicated by the horizontal lines on the plot. The u band case is essentially flat because of the absence of any counts present in this arm during the test. It is therefore impossible to judge the impact of the guide probe in the u band photometry.

The results of this test suggest that the guide probe can have a significant impact on any star that falls close to the edge of the chip. They also suggest that this extra vignetting component can reduce the overall fractional level of the flux in the remainder of the CCD chip, causing a similar fractional decrease in flux in all stars as that seen in the raw fluxes shown in Figure 3.13. The overall level is also found to be time-dependent. The same analysis applied to position 3 was repeated for other positions available from the test performed by the ULTRACAM team. The particular example of position 6 is shown in Figure 3.25, where no visible sharp feature is seen on any corner of the chip for any arm but a decrease in the fraction of light for the r and g bands is still visible. The available frames from the test do not provide a high S/N for a firm conclusion but the results suggest a change in the vignetting strength as a function of the relative position of the guide probe with respect to the field of view orientation. Therefore, a smooth variation in the fractional flux of stars at any position on the chip is expected as the parallactic

angle changes. The initial results of this test, however, imply that this variation would disappear with the use of differential magnitude provided stars are not close to the edge of the chip.

A closer analysis reveals that this may not be the case. Figure 3.26 shows two curves that represent the column average of all the pixels belonging to rows 800 to 1000 in CCD coordinates for the images shown in Figure 3.24. The two curves show the r and g band cases (the absence of any counts in the u band makes this particular test irrelevant regarding the blue arm of the instrument). It is possible to see that an additional spatial variation of the order of 0.5 mmag is present in both bands along the horizontal direction, which would introduce additional differences in the flux of stars located at several parts of the chip.

Despite the low S/N available from the guide probe test, this experiment shows that the characteristics of its vignetting correlate with most of the properties of the meridian feature discussed thus far. This is a multiplicative effect, which is capable of introducing a similar shape on any star in the field and shows evidence of further spatial dependent variations at a smaller amplitude. It is also different in amplitude between each arm, as indicated by the difference in the levels between the r and g bands on the guide probe vignetting test as well as the shape of the vignetting pattern. This is still puzzling, as any vignetting that would be introduced before the camera would be expected to correlate well between each arm. Figure 3.23 also shows that the shape of the vignetting changes depending on the position of the probe, thereby explaining why the systematic effect changes smoothly as a function of rotator angle.

It is therefore possible to conclude that extra time-varying vignetting from the guiding probe is likely to be a contributor to the presence of the meridian feature. This effect is perturbing the stellar fluxes in such a way as to make it impossible to correct for, firstly because there is no way to measure the extra vignetting component from the accumulated data of the test depicted in Figure 3.23, but also because there is no available information on the guide probe's position during the observations. ULTRACAM, as a visitor instrument on the NTT, does not collect any information regarding the telescope pointing, guide star choice, rotator angle, etc, thereby making any corrections impossible. Moreover, flat fielding cannot be used to correct for this feature, since the guide probe is likely to be parked during twilight and the rotator is fixed. In the next Section a short evaluation of the feasibility of performing any measurements is discussed.

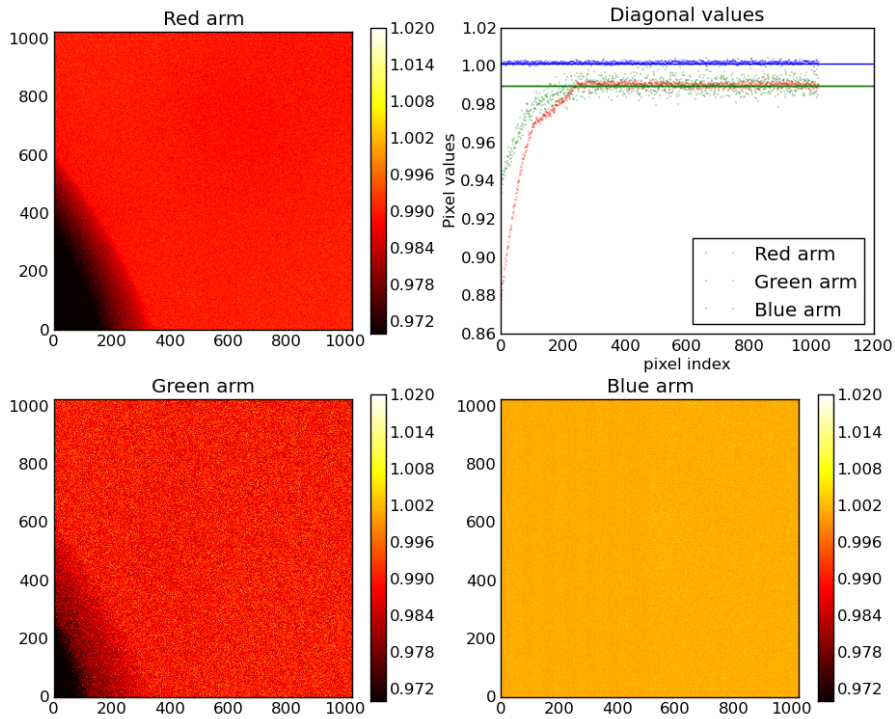

Figure 3.24: Result of the test performed by the ULTRACAM team on the effects of the NTT guide probe upon the field of view of ULTRACAM. The images show the ratio between the dome flat on position 3 (see Figure 3.23) and the dome flat with the probe parked for all 3 arms. The plot on the top right corner refers to the pixel values of a diagonal running from pixel (0,0) to pixel (1024,1024) taken from the images shown (the colors indicate the corresponding arm), where horizontal lines indicate the median of the values from the centre of the image to the final corner. These values are a measure of the overall fractional decrease in flux from the influence of the guiding probe, excluding the excess effect close to a particular corner (depending on the position of the guide probe). The values are as follows: red arm = 0.989; green arm = 0.989; blue arm = 1.001

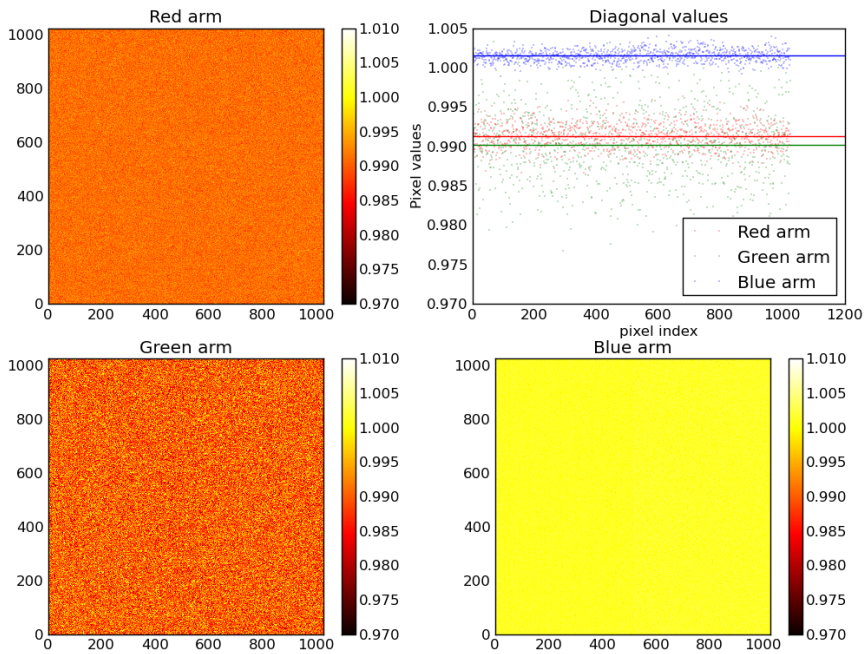

Figure 3.25: Result of the test performed by the ULTRACAM team on the effects of the NTT guide probe upon the field of view of ULTRACAM. The images show the ratio between the dome flat on position 6 (see Figure 3.23) and the dome flat with the probe parked for all 3 arms. The plot on the top right corner refers to the pixel values of a diagonal running from pixel (0,0) to pixel (1024,1024) taken from the images shown (the colors indicate the corresponding arm), where horizontal lines indicate the median of the values from the centre of the image to the final corner. These values are a measure of the overall fractional decrease in flux from the influence of the guiding probe, excluding the excess effect close to a particular corner (depending on the position of the guide probe). The values are as follows: red arm = 0.991; green arm = 0.990; blue arm = 1.001

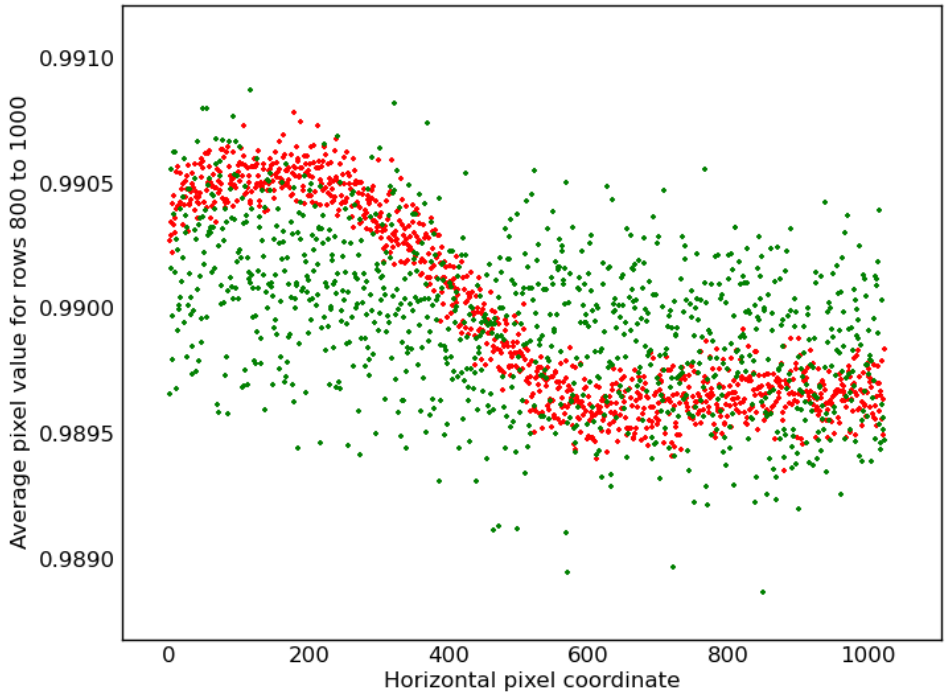

Figure 3.26: This plot shows the column average of the values between rows 800 and 1000 in pixel coordinates for the r band (red) and g band (green) in the results of the guide probe test in position 3 (see Figure 3.24). These averages are taken directly from the images shown in Figure 3.24 and show an additional structure in the horizontal direction for pixels away from the corner where the guide probe has a larger impact.

3.7 Discussion

The analysis presented in Section 3.6.2 describes the attempt to characterise the source of a systematic effect present in the light curves and ultimately limiting the photometric precision achieved. The effect of the guide probe in the field of view is thought to be the major cause of this feature, due to the fact that it generates a quasi-uniform fractional decrease in flux as a function of the relative position of the probe with respect to the centre of the FOV. Furthermore, evidence of additional spatial structure at the sub-mmag level is shown which would ultimately limit the precision of any measurement. This analysis does not, however, exclude the possibility that a rotating vignetting pattern of the telescope can cause additional systematic errors. Moreover, the dramatic changes in the shape of the meridian feature between each arm of the instrument are yet to be explained fully. At this stage it is impossible to determine whether this is due to any wavelength dependent nature of the issue or related to any disturbance in the path of the light to each CCD inside ULTRACAM.

In light of the findings described in Section 3.6.2 it is important to gauge whether a meaningful measurement can be obtained. The data from the night of 26th April 2010 on WASP-17b's transit was used to decide, based on the fact that this night was photometric and the meridian feature seems of smaller amplitude on a differential photometry context. There are several potential reasons for this, i.e. the possibility that the chosen guide star was relatively far from the centre of the field of view.

After the application of the airmass correction described in Section 3.6.1, Figure 3.27 contains the differential photometry results of using comparison stars 1, 3 and 4. Comparison star 2 was not shown on the basis of the poor signal to noise it shows in the u band (see Figure 3.15) due to the extreme color of this star (see Table 3.3). The fitting algorithm used for this test was a simplex routine as part of an eclipse fitting package developed by Professor Tom Marsh. The minimisation uses the simplex method via the Numerical Recipes routine 'amoeba' which works with a group of N+1 points in N dimensional space and moves the points around to move downhill in chi**2. It is used in order to visually gauge the impact of the guide probe on the data rather than for the purposes of obtaining a measurement. Using an MCMC routine to estimate the errors on any of the parameters is irrelevant since the measurements cannot be considered to be independent. The model light curve shown is produced using the previously known values by Anderson et al. [2011] and the limb-darkening coefficients for each band are estimated based on the calculations

Table 3.6: Initial system parameters for WASP-17

Parameter	Symbol	Value	Unit
Transit epoch (BJD)	T_{C}	2454577.85806±0.00027	d
Orbital period	P	3.7354380±0.0000068	d
Transit duration	T_{14}	0.1830±0.0017	d
Planet/star area ratio	$R_{\mathrm{P}}^2/\mathrm{R}_*^2$	0.01696±0.00026	
Impact parameter	b	$0.401^{+0.059}_{-0.077}$	R_*
Orbital separation	a	0.05150±0.00034	AU
Orbital inclination	i	$86.83^{+0.68}_{-0.56}$	degs
Stellar mass	M_*	1.306±0.026	$\mathrm{M}_\odot$
Stellar radius	R_*	1.572±0.056	$\mathrm{R}_\odot$
Stellar surface gravity	$\log g_*$	4.161±0.026	(cgs)
Stellar density	ρ_*	0.336±0.030	$\rho_\odot$
Limb Darkening Coefficient 1	ldc_1	0.0881±0.02	
Limb Darkening Coefficient 2	ldc_2	0.0967±0.03	
Planet mass	M_{P}	0.486±0.032	$\mathrm{M_J}$
Planet radius	R_{P}	1.991±0.081	$\mathrm{R_J}$
Planet surface gravity	$\log g_{\mathrm{P}}$	2.448±0.042	(cgs)
Planet density	ρ_{P}	0.0616±0.0080	ρ_{J}
Planet equil. temp. (A=0)	T_{P}	1662^{+24}_{-26}	K

by Claret & Bloemen [2011]. A simple fit was done to adjust the mid-time of the eclipse only in order to match the data set. The parameters used are shown in table 3.6.

The simple airmass correction curves for all 3 bands (Figure 3.15) show that there is temporal variability that requires a differential photometry stage. However, the results shown in Figure 3.27 indicate that the shape and amplitude of the meridian feature depend heavily on which comparison star is chosen. There are also examples of remaining overall trends still visible on several curves, i.e. the g band differential photometry curve using comparison star 4, which are either a residual effect of the airmass correction of the comparison star or an example of a particularly strong influence by the guide probe.

This suggests that the systematic effect is present throughout the entire night, despite the fact that a clear change is only typically noticeable close to zenith in the airmass corrected curves. The typical amplitude of the systematic signal in the raw light curves is larger than the effect seen in the differential photometry curves, thereby explaining why an overall trend may not be obvious in the raw light curves. This is likely to be a result of the fact that the parallactic angle remains relatively constant and only changes rapidly close to zenith. Despite this, any vignetting present must be different on either side of the meridian, which may explain numerous discrepancies between the stellar fluxes before and after the zenith stop seen in several cases. Since all transits observed contain out-of-eclipse data on either side of this boundary, a measurement of the transit depth is naturally inaccurate due to the inability to determine the out-of-eclipse level to enough precision.

Comparison star 3 appears to perform better at removing the meridian feature, in terms of the amplitude of the residuals to the fit. Nevertheless, clear systematic noise is still present and choosing this star simply on the basis of the fact that it *visually* seems to be the most suitable comparison is not possible, especially in the knowledge that the guide probe is potentially continuously having an impact on the data.

This data set is therefore deemed unsuitable for measurements in the context of performing transmission photometry of planets WASP-15b and WASP-17b, due to the presence of red noise, thought to be related to time-varying vignetting by the telescope's guiding probe. Despite the fact that any differences between the previously published results and the presented data are likely due to systematic noise, the consistency between the deviations between the data and the model light curve for each band have motivated another experiment.

The light curves were fitted using the same Simplex routine, but allowing the planet radius to vary as well as the transit timing. Once again, all other parameters were fixed at the previously known values. The results are shown in Figure 3.28, where it is possible to notice a significant improvement in the residuals with

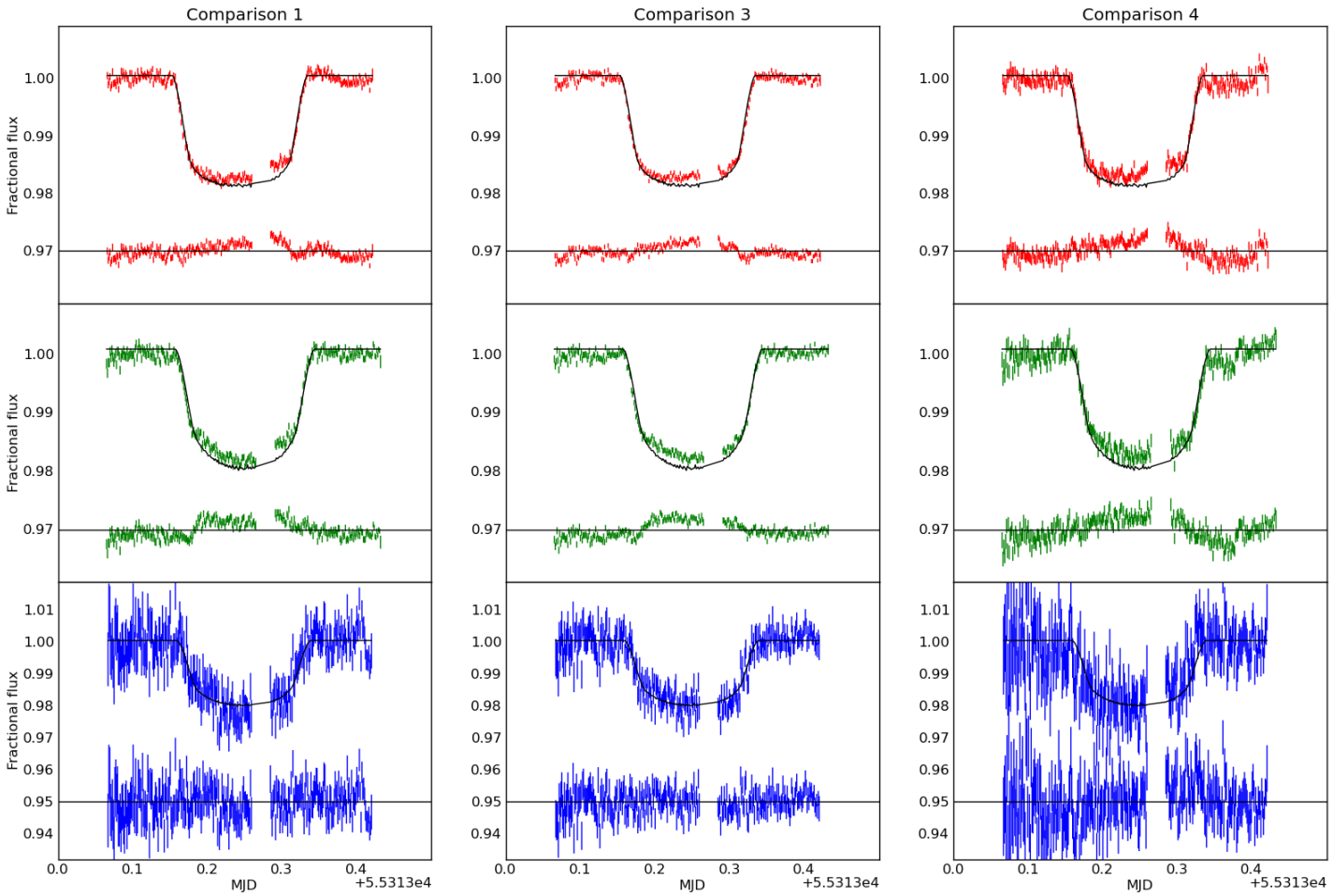

Figure 3.27: Transit light curves for the observation of the primary transit of WASP-17b on the 26th April 2010 in the u, g and r bands. The differential photometry curves using comparison stars 1, 3 and 4 are shown. Overlaid on each transit is the transit light curve model produced from the previous known values by Anderson et al. [2011], adjusted with the limb darkening coefficients given by Claret & Bloemen [2011] for the host star. Each panel also shows the residuals to the each fit.

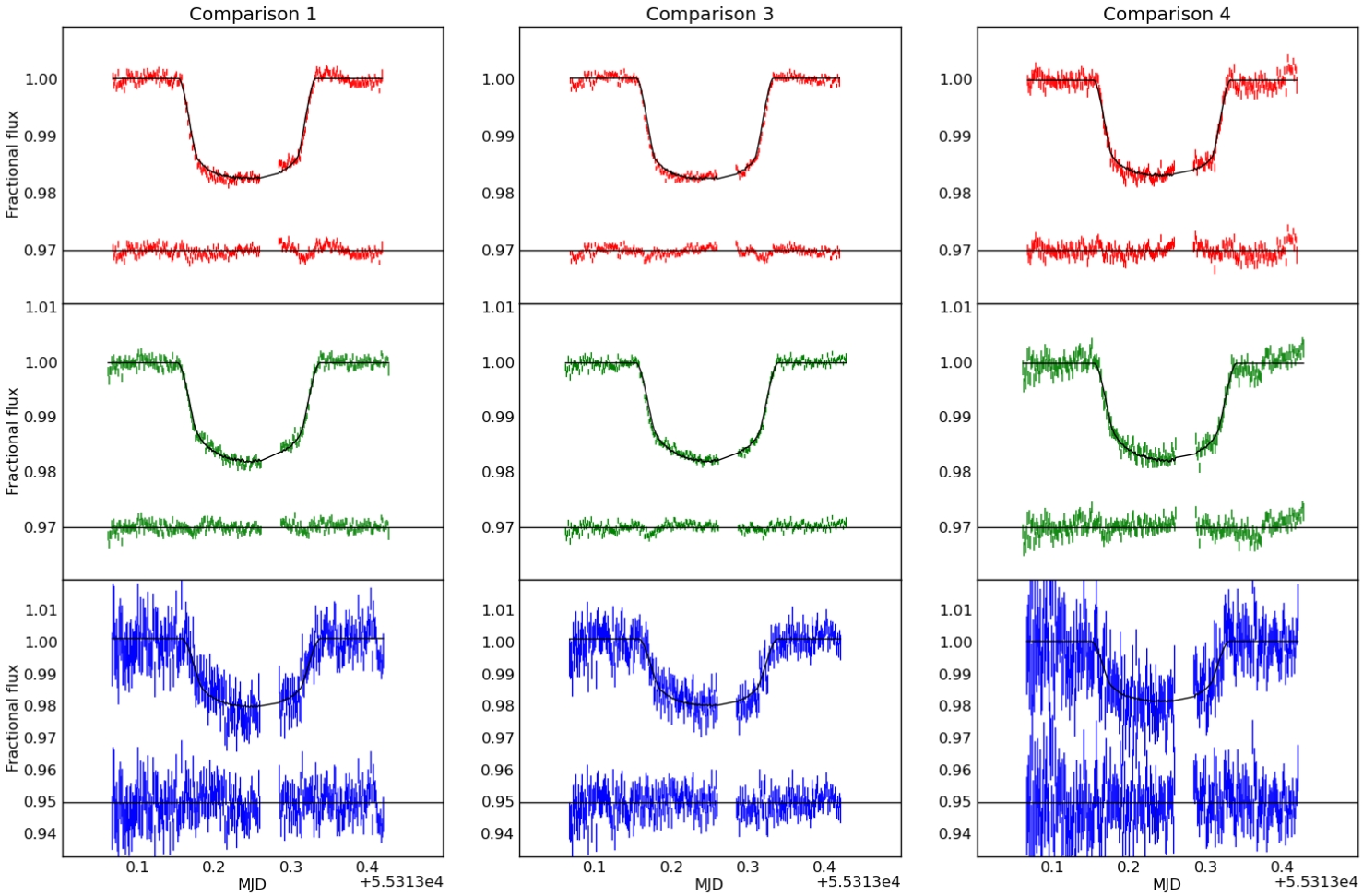

Figure 3.28: Transit light curves for the observation of the primary transit of WASP-17b on the 26th April 2010 in the u, g and r bands. The differential photometry curves using comparison stars 1, 3 and 4 are shown. Overlaid on each transit is the fitted transit light curve model where only the transit mid-time and planet radius were fitted. All other parameters were fixed as the previous known values by Anderson et al. [2011], adjusted with the limb darkening coefficients given by Claret & Bloemen [2011] for the host star . Each panel also shows the residuals to the each fit.

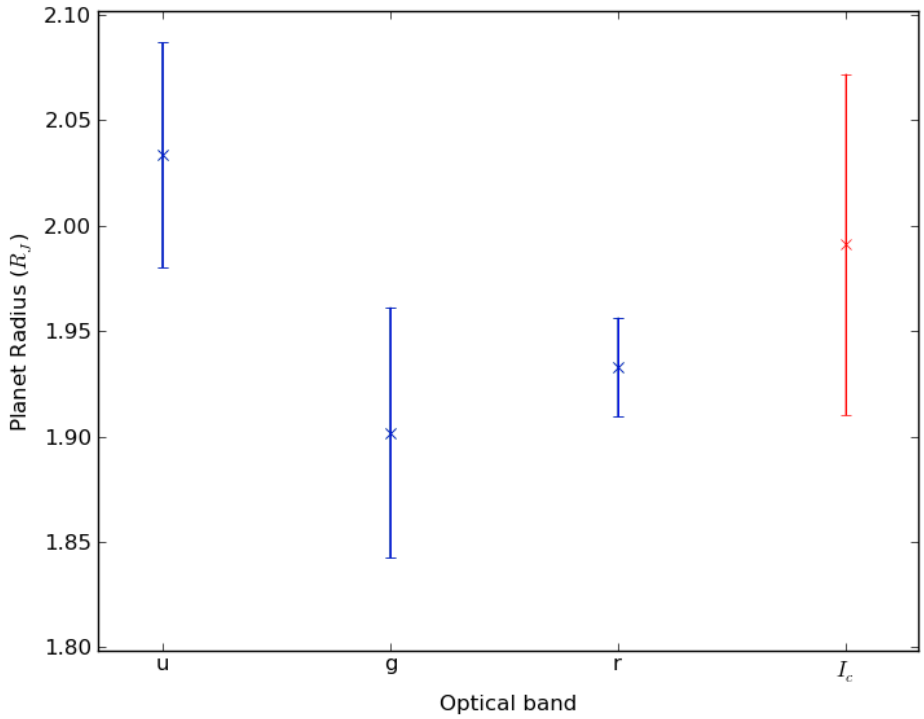

Figure 3.29: Average planet radius as a function of observed band (wavelength). The blue points refer to the average radius obtained from the differential magnitude light curves from Figure 3.28 for all 3 comparison stars for each band. The error bars correspond to the standard deviation of the set. The red point corresponds to the previous measurement in the I_c band by Anderson et al. [2011].

respect to those shown in Figure 3.27. We have plotted the average planet radius in each band, using the standard deviation of the three measurements (with the 3 comparison stars) as an estimate for the error. This is presented in Figure 3.29 for all 3 bands, where the previous measurement in the I band by Anderson et al. [2011] is also shown for comparison. The three measured radii and the previous value are consistent between them within the quoted errors. However, the distribution of the measured radii suggests a Rayleigh scattering dominated atmosphere, where the u band depth is higher than both g and r (c.f. Figure 3.1). The difference in planetary radius between the u and g bands corresponds to over 15 times the predicted scale height of the atmosphere, which seems to agree with previous results for similar measurements of planets HD209458b and HD189733b [Vidal-Madjar et al., 2011; Huitson et al., 2012] in terms of the idea that these variations can correspond to several scale heights. Moreover, the slightly higher radius in the r band with respect to the g band is also consistent with the broad sodium absorption detected in these planets. This evidence can potentially motivate another observation of this planet's transit using ULTRACAM.

The possibility that these data can be used to contribute to transit timing variation measurements is still to be assessed, provided care is taken to ensure that the shapes of the ingress and egress are not significantly affected by the systematic effects discussed.

Chapter 4

Optimising observing strategies of ground based transit surveys

4.1 Motivation

During the design and planning stages of any astronomical survey, an estimate of the expected scientific yield of the project is a key question. All design decisions are typically aimed at maximising this yield within the associated limitations (financial and physical). Exoplanet surveys are not an exception, and early examples of attempts to predict the number of planets each survey is likely to find include that of Horne [2003]. The author derived empirical scaling laws for the discovery potential of approximately a dozen transiting exoplanet surveys taking place at the time based on survey volume, star density, the orbit alignment probability and the number of planets per star. Naturally the latter can only be estimated, but information from planetary detections from radial velocity surveys was used. The results suggested generous numbers of planets that were later found to be an overestimate, but the author correctly predicted a high number of hot-Jupiters being found within the years that followed. A more recent attempt by Beatty & Gaudi [2008] comprises of a more complex approach which includes detector characteristics, observing conditions and assumptions on the underlying planet distribution to simulate the yield future projects and compare the results with existing ones. However, this simulation assumes a given location on sky is randomly sampled over a fixed average amount of time during the night, which is unrealistic. Moreover, despite using a S/N approach to determine the planetary detection probability, this simulation does not take into account the effects of atmospheric extinction, lunar presence or red noise.

This Chapter concerns the development of a simulation software with similar aims to that presented by [Beatty & Gaudi, 2008] but designed to aid in the planning of ground-based transiting surveys. This code is not designed to predict the number of planets found by a given survey, but to test what the effect of particular observing strategies have on the probability of detecting any planet. Examples of such observing strategy decisions include whether or not to limit the maximum airmass for any observation, whether multiple fields should be observed on any night or what the effect of the lunar presence has on the sampling of a location on sky. Moreover, it is also designed to aid in the choice of locations to observe in order to maximise the amount of useful time on sky.

Ground based surveys are designed to maximise the science return by employing an efficient field selection method. SuperWASP's observing strategy for the majority of the mission's duration has been to perform an essentially all-sky survey collecting measurements from several fields every night. The project has been designed to avoid fields close to the galactic plane and at extreme declinations due to excessive crowding and high airmass observations. Figure 4.1 shows the average number of points per star as a function of its location on the celestial sphere. This Figure shows that any field with declination over 65° and below −70° have not been observed, as well as those close to the galactic plane. The declination restriction in the northern hemisphere is, however, related to restrictions due to the design of the telescope enclosure.

Every night the scheduler selects a collection of fields which the telescope observes in a cyclic fashion. As mentioned in Section 2.4, each field is visited on average every 7 minutes [Smith et al., 2006]. A specific area of the sky is observed for a period of approximately 3-4 months. A planetary detection requires multiple transits observed over this period, ideally with multiple cameras, with enough measurements inside the transit to achieve enough signal to noise. The consequence of this is that SuperWASP is sensitive to short period (up to 10 days) close-in large planets (Hot Jupiters).

The probability of observing multiple transits is lower for planets exhibiting long periods. In order to maximise the number of observed transits, large orbital period planets require long baseline coverage to be detected. Moreover, intensive coverage increases the total exposure time in transit, thereby increasing the S/N of any detection. In order to achieve this goal, several projects have adopted a *staring* strategy, where a given field is observed for as long as possible before moving on to another. This is the case for the Kepler Mission [Borucki et al., 2006] (see Section 1.4.2), which has observed a single location in search of Earth-sized planets in the

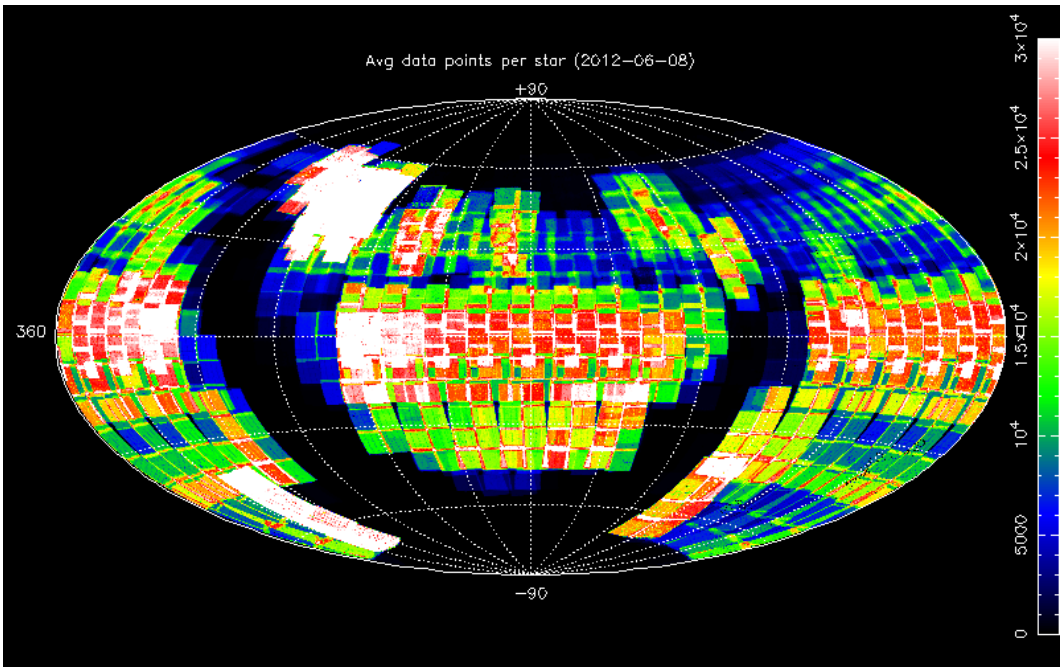

Figure 4.1: Average number of measurements made by the SuperWASP instrument (North and South facilities) as of 15th March 2012 as a function of location on sky. This Figure shows the deliberate avoidance of the galactic plane and extreme declinations.

habitable zone of their host stars as its primary goal. It has detected 72 planets to date with some showing periods of hundreds of days (Kepler-16b [Doyle et al., 2011] and Kepler-22b [Borucki et al., 2012a]). Similarly, the Next Generation Transit Survey (NGTS) (see Section 1.4.3) is a new wide-field survey that has recently secured funding and authorization to be commissioned at ESO's Paranal Observatory to search primarily for Neptune-sized planets around K and M dwarf stars. This project builds from the experience of SuperWASP (see Section 1.4.1) to improve the photometric precision to 1mmag on time scales comparable to the duration of a typical transit whilst also employing a staring strategy. This is thought to be necessary since Neptune-sized planets will exhibit shallower transits than the corresponding Jupiter-sized bodies and the mass-period distribution of close-in exoplanets shown in Figure 4.2 suggests that sub Jupiter-mass planets are typically not found in orbital periods shorter than 2.5 days, consistent with the inner edge of the protoplanetary disk for Solar type stars [Benítez-Llambay et al., 2011]. The explanation for this suggested by the authors is that small planets that migrate inwards of this edge are tidally disrupted and absorbed by the star. The cases of CoRoT-7b, GJ1214b and GJ876d are exceptions, possibly requiring further explanation for their current state.

A staring strategy poses the problem of selecting which locations on sky NGTS and SuperWASP should observe in order to maximise the performance of the instrument. This choice is not trivial and should address many factors, such as the lunar presence, galactic plane proximity and others. Moreover, fields should be chosen to maximise the time they can be observed, such that at any time the telescope will always have one of the selected fields available for data gathering.

Additionally, it is possible to estimate the planet discovery probability as a function of orbital period based on the number and timing of observations during one season. This can be a useful tool to compare the predicted performance of the instrument for several design options, such as the location of the telescope, airmass restrictions, sampling rate, etc.

This Chapter describes the development of a simulation software designed to provide solutions to such questions as well as a set of results that have had an impact on the design of the NGTS project and improvements to the observing strategy of SuperWASP. We describe the development of two separate software simulations with several common features written using the Python programming language[1]. The first deals with calculating the amount of time it is possible to observe any point on sky in one year given a particular location on Earth. This *Sky coverage simulation*

[1]Available at www.python.org

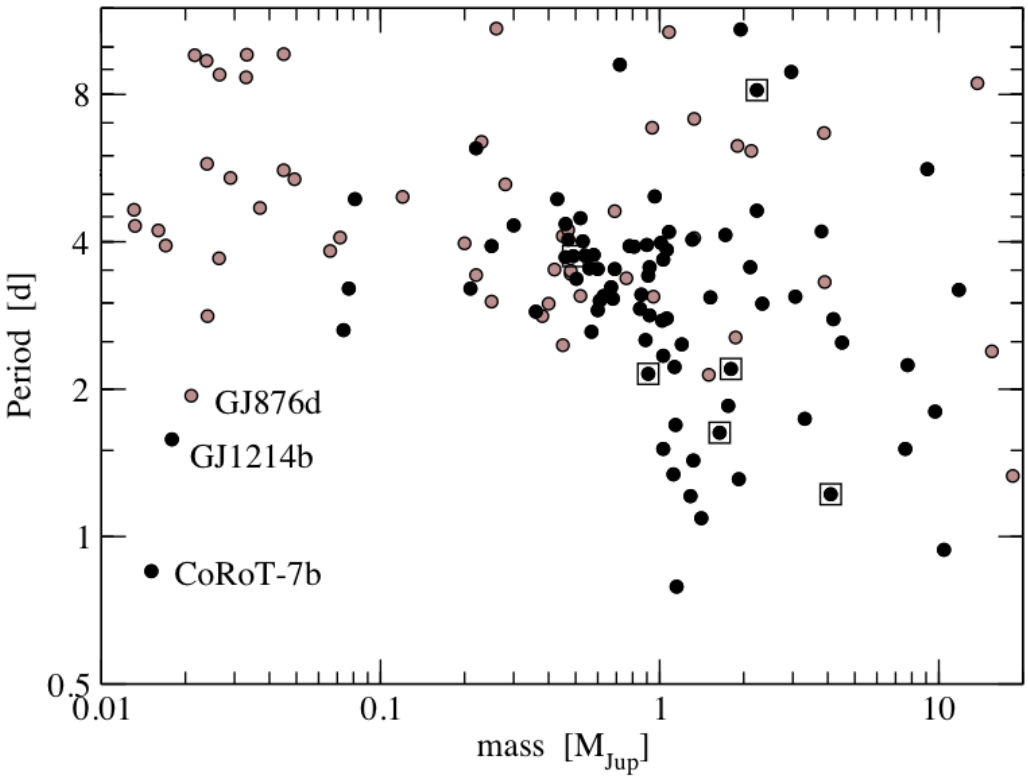

Figure 4.2: Distribution of planetary masses and orbital periods of planets with $P <$ 12 days. Black circles show the planets with radial velocity and transit observations, whilst the grey circles mark those with just Doppler measurements. The planets with square markers orbit their host stars in a retrograde fashion. From Benítez-Llambay et al. [2011].

(see section 4.2) is designed to be used as the basis for the choice of which fields the instrument should observe in order to maximise the number of measurements taken over one season.

The second simulation is designed to calculate the probability of detecting a planet orbiting a star belonging to a particular field as a function of its orbital period for a given set of parameters (the *window function*). These parameters can be adjusted to test several observing strategies and this *planet detection probability* simulation can be used to compare the expected outcome for each case. Section 4.5 (see section 4.5) contains a description of this second software, which implements many aspects of the code described in the following Section.

4.2 Sky coverage simulations

In order to determine the amount of time any particular location on sky can be observed, a list of factors has been considered. The approach taken in the development of this simulation was to generate an array with all possible times the telescope can take an exposure given a starting and finishing date of the simulation and an exposure time. These parameters are inputs to the software. In this particular simulation, the exposure time is a measure of the sampling rate at which a photometric measurement is made. It is a natural measure of the accumulated time in transit and accounts for the possibility that, for storage space restriction reasons, several exposures may be co-added and that the temporal resolution of the photometric measurements may not be identical to the real exposure time of the telescope.

Once this *time array* is generated, elements can be rejected from it for each location on sky, based on the several restrictions considered, and the product of the number of remaining elements and the exposure time will give the total observable time for the duration of the simulation. The following Sections describe in detail the criteria considered for rejecting elements from the time array.

Daytime

In order to reject any array elements that occur during the day it is necessary to have information regarding the timing of the Sunrises and Sunsets and remove any measurements that would happen between the dawn and dusk twilights. Information was gathered using the Jet Propulsion Laboratory HORIZONS on-line system [Giorgini et al., 1997] of the Sun's altitude between the year 2012 and 2016 in hourly resolution. This system is designed to compute a number of parameters for

a given Solar System object based on a set of inputs, such as the location on Earth and the desired coordinate system. For the case of this simulation, sets of these parameters for the La Palma Observatory (where the SuperWASP North facility is located) and ESO's La Silla and Paranal Observatories were obtained.

A linear interpolation of this set of altitude values to the time resolution of the simulation is performed and any elements of the time array that correspond to Solar altitudes of $> -18°$ (defined as the lower limit of the astronomical twilight) are rejected.

Weather

Weather is an important factor to consider. Depending on the site location and climate, a large number of nights may be unsuitable for observations to take place. However, since it is impossible to predict what the weather conditions will be, information from previous years has been used.

For La Palma, information from the SuperWASP weather station logs was acquired. Typically, every night contains information on whether the telescope performed any observations. One year of data were selected and used as the basis for the simulation. The year selected (2009) did not contain any major hardware upgrades. In essence, every element in the time array was matched to the SuperWASP weather indicator of the corresponding date and rejected if the telescope had not observed.

The weather information for La Silla and Paranal was based on the plot shown in Figure 4.3. This plot shows the monthly average fraction of nights where observations took place at the two locations over the years between 1983 and 2001 (Courtesy of Didier Queloz, from private communication with ESO). It is possible to see the difference in weather conditions at Paranal compared with La Silla. Despite the fact that during the Summer months the fraction of nights is comparable, the Winter months show a significant decrease in the available nights at La Silla.

This information was used to generate a weather log for both sites. For every month a fraction of nights corresponding to the values given by Figure 4.3 were randomly selected to have suitable weather, and all others rejected. This process generates a log similar to that taken from the SuperWASP instrument, which was then applied to the time array in the same fashion. This is not a realistic restriction since weather doesn't necessarily change only during the day. Short spells of good/bad weather do occur during the night. Additionally, it is often the case that particularly bad weather will last for a series of days and that periods of inactivity of several days are more likely than randomly selected nights. Furthermore, it is

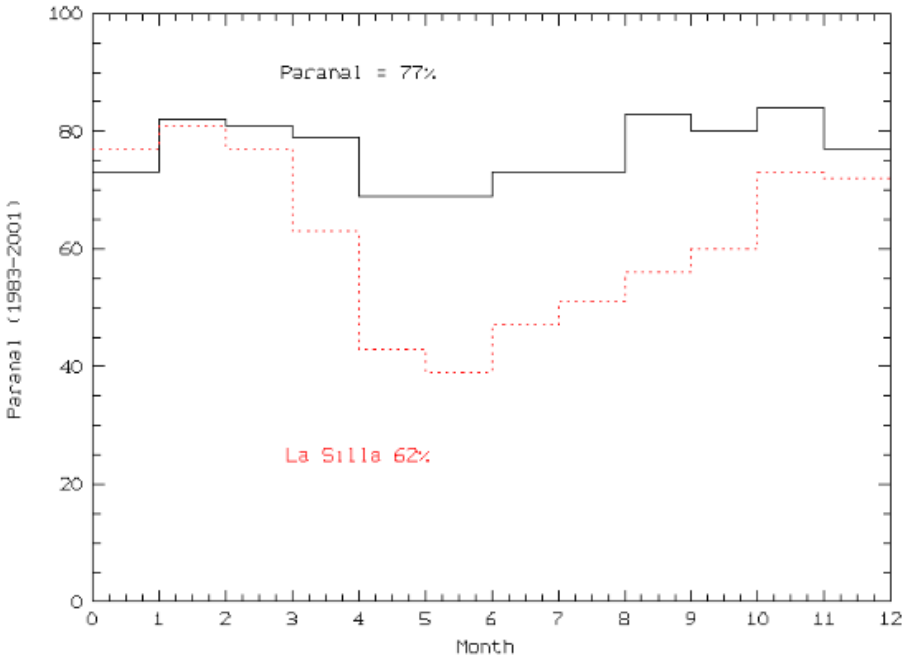

Figure 4.3: Average monthly fraction of nights where observations took place at both ESO's Paranal and La Silla observatories in the period between 1983 and 2001. The values quoted inside the plot refer to the annual average. Figure obtained from private communication with Didier Queloz.

possible to use real weather information from observatories on a much finer temporal resolution to improve the simulation. However, since the software is designed to operate on time-scales of a minimum of 4 months, it is unlikely that such implementation would yield a substantial improvement on the simulation, and the overall results are likely to be comparable.

Moon

The influence from the presence of the Moon is dependent on both its phase and proximity to the field in question. It is unavoidable that the general level of the background light will increase if the Moon is also present in the night sky. This increase is determined by a model of Krisciunas & Schaefer [1991], which is based on observations from the Mauna Kea summit. It is a function of the Moon's phase, zenith distance and angular separation to the sky position, as well as the local extinction coefficient.

The model starts by converting the dark sky brightness at zenith (in V magnitudes) to nanoLamberts (B_{zen}) using the expression

$$B_{zen} = 34.08 \exp(20.7233 - 0.92104 V_{zen}), \tag{4.1}$$

as first presented by Garstang [1989]. The dark sky brightness V magnitudes used in this simulation are 21.9 for La Palma [Benn & Ellison, 1998], 21.7 for La Silla [Mattila et al., 1996] and 21.6 for Paranal [Patat, 2003].

From this result, the dark sky brightness (B_o) as a function of zenith distance (Z) can be determined by the expression shown in equation 4.2, where k is the local extinction coefficient in units of magnitudes per airmass and χ is the optical path length along the line of sight in units of air masses, given by $\chi = (1 - 0.96 \sin^2 Z)^{-0.5}$. The local extinction coefficient has been taken to be 0.08 magnitudes/airmass, determined based on the analysis of the NGTS prototype raw flux measurements. Once the sky brightness as a function of zenith distance is determined it can be reverted again to V magnitudes (V_o) using equation 4.1.

$$B_o(Z) = B_{zen} 10^{-0.4k(\chi-1)} \chi. \tag{4.2}$$

The contribution from atmospheric scattering of the Moon light is now considered. Based on the relation presented by Schaefer [1990] we use the expression

$$I^* = 10^{-0.4(m+16.57)}, \tag{4.3}$$

which relates the V magnitude of the Moon (m) and its illuminance (I^*) in units of footcandles. In turn, the V magnitude of the Moon is a function of the lunar phase, α, given by $m = -12.73 + 0.026|\alpha| + 4 \times 10^{-9}\alpha^4$.

At this point, a scattering function is required, since the contribution of the moonlight depends on the angular separation between the Moon and the sky position being considered ρ. This function, $f(\rho)$ [Rozenberg, 1966], is simply the sum of the Rayleigh scattering function from atmospheric gases, $f_R(\rho)$, and the Mie scattering function for aerosols, $f_M(\rho)$, given by

$$f(\rho) = f_R(\rho) + f_M(\rho) = \left[10^{5.63}(1.06 + \cos^2(\rho))\right] + \left[10^{6.15-\rho/40}\right]. \tag{4.4}$$

Finally, the brightness due to the contribution from the Moon, B_{moon}, can be determined using

$$B_{moon} = f(\rho)I^* 10^{-0.4k\chi_{moon}} \left[1 - 10^{-0.4k\chi}\right], \tag{4.5}$$

where χ_{moon} is the airmass of the Moon. Once again this brightness can be converted to V magnitudes using equation 4.1 and a difference between the dark sky brightness and the sky brightness due to the presence of the Moon in magnitude units can be found. A limit can therefore be set to the maximum change in the sky brightness allowed for a measurement to take place.

It is important to note that this model of the sky brightness due to the Moon does not apply to lunar angular separations below 10°, where the scattering functions presented are no longer valid. Krisciunas & Schaefer [1991] tested the model against collected data and the results are plotted in Figure 4.4. It is possible to see that good agreement between the data points and the model takes place at low brightness, and that the predictions for high illumination levels suffer from a larger variance. Nevertheless, the authors present a formula that "(...) has the advantages of having the correct functional dependencies, yet being easy to use and accurate to better than 23%" [Krisciunas & Schaefer, 1991]. For the simulation described only a direct comparison between different locations on sky is intended, and this level of accuracy is sufficient.

Due to the limitation of the model, a hard limit of 10° lunar separation was introduced in the simulations and a 4.5 magnitude increase in the background sky brightness was set as the maximum threshold. At this level, stars with magnitude I=16 would have approximately a S/N of unity over exposures of 15 seconds.

In order to avoid any incidence of direct moonlight inside the telescope tube

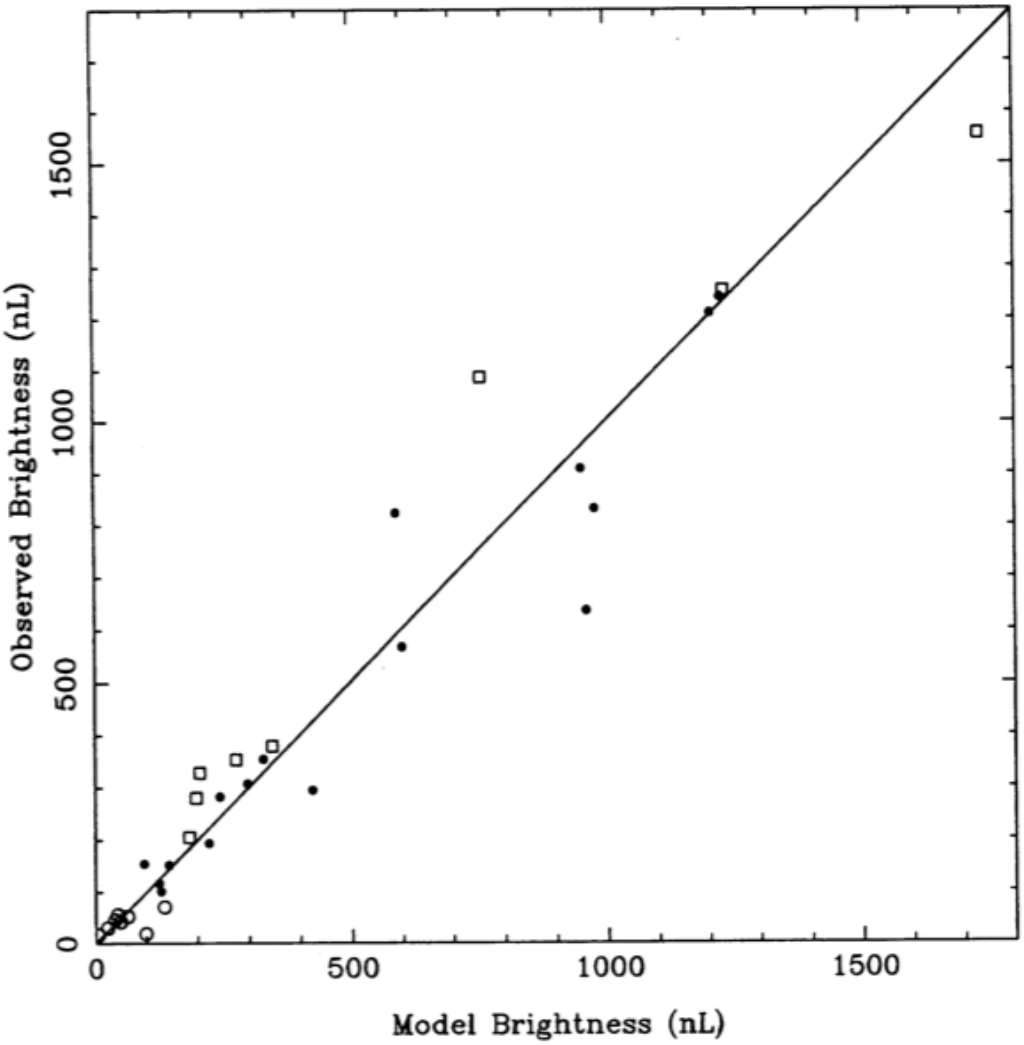

Figure 4.4: Observed values of sky brightness due to the presence of the Moon in the sky (in nanoLamberts) as a function of values from a proposed model. The open circles show points where the brightness of the Moonlight is less than the dark night sky brightness. The square markers and filled circles show data taken at different times. A line of slope 1 is shown for comparison. Taken From Krisciunas & Schaefer [1991]

and thereby minimise any internal reflections the design of the NGTS telescope assembly incorporates a baffle of 40cm in length. Geometrically, this extra tube length ensures that fields with an angular separation from the Moon larger than 28° are shielded from this scenario. This is not a perfect solution, and therefore there is no hard rejection of this separation in the simulations. We simply include lines that indicate fields that come within this separation at times during the observing year.

Zenith distance

As mentioned in Section 4.1, the choice to employ a staring strategy is typically associated with the aim of improving photometric quality. This then implies that the choice of field must take into account the effects of the atmosphere in the form of the airmass and scintillation. Section 3.6.1 contains details regarding the issue of the atmospheric extinction as a function of airmass, where there is a reduction in the stellar flux of over 10% from airmass 1 to airmass 2. Section 2.3 describes the effects of scintillation, which is a strong function of airmass (clear from the $\chi^{7/4}$ term in equation 2.5).

The best location to observe a given field in terms of potential data quality is at zenith. Therefore, choosing a field with a large difference between its declination and the local latitude would significantly reduce the inherent potential data quality, i.e., if the telescope is located at latitude $-30°$ degrees, choosing a field close to the celestial South pole ($\approx -90°$ declination) would have the advantage that this field is visible all year but would be observed always at airmass 2.0, where the stellar flux is reduced due to atmospheric refraction and the scintillation would seriously limit the precision of the photometry. Moreover, fields that have equal declination to the local latitude will be observed through the entire range of airmass on a given night and restricting the telescope observations to times when the field is above a specific altitude may be desired. This option was included in the simulation as an input parameter, where the zenith distance of each location is calculated and any values above a given threshold are rejected.

This restriction then limits the minimum number of fields selected for a given year to avoid times where the telescope is idle because no selected field is visible. If the zenith distance is restricted to 30°, a minimum of 6 fields separated by 4 hours in RA (60°) are required for declinations corresponding to the local Latitude. Naturally, a small zenith distance restriction will also impact the overall coverage of a given field, since it would only be sampled for a small fraction of the night and a shorter period during the year. The simulation can be used to assess the impact of such choices.

Galactic plane

Typically wide-field surveys tend to not observe close to the galactic plane. This is simply to avoid the high density of stars that cause large fractions of targets to suffer from *blending* from background sources. This is the case when the flux from a star of interest is contaminated by the light from another nearby star. This is a common source of false positives in the search for planetary transits, since the deep eclipse of binary systems can appear shallower, and hence planet-like. Additionally, the galactic plane contains a high number of giant stars and, hence, the increased number of targets does not necessarily correspond to a high increase in the quantity of targets of interest.

The simulation takes this into account by rejecting any positions on sky that fall under a particular distance from the galactic plane. The galactic latitudes of each location of interest were computed based on their right ascensions and declinations and any that fall under a specific threshold rejected. An angular separation of 10° from the galactic plane was used as an avoidance region.

The exact decision of this minimum distance is to be decided by the NGTS team. Stellar blending is always present in wide-field surveys independently of the location of the chosen field. However, the fraction of stars that suffer from this issue is a function of galactic plane distance and the distance to the galactic centre, where once again the stellar density increases further. It is possible to simulate the expected amount of blending present in a given field, using a stellar catalogue as an input, and assess the stellar *crowding* of a particular location. This particular step was done by Simon Walker as part of the research conducted during his PhD.

With the objective of estimating stellar blending for a given galactic latitude the following approach was taken. A sample image from the NGTS prototype data and an isolated star were selected as the basis to measure the PSF distribution. Several stars were used and the results were found to be consistent. Using the aperture size chosen for the analysis of the prototype data (4 pixels in radius), the flux from the star was measured with the aperture placed at the centre and at increasing offsets of 0.1 pixels in four orthogonal directions from the centre. This is a method to sample the PSF of this star and, assuming local isotropy, the results are interpolated to form a model of it. This shape is then assumed for all stars and a correspondence between the instrument PSF and the aperture size is found. Using stellar magnitudes to obtain the total flux it was possible to generate a corresponding expected PSF for the instrument and, thereby, estimate how much light is contributed by a given source at any radial distance from its centre.

Using a central coordinate a simulated image with the final instrument's

Right Ascension (h:m:s)	Declination (d:m:s)	Galactic Longitude (hours)	Galactic Latitude (degrees)	Blending fraction (%)
06h26m33.3s	+33d:03m15.8s	12	10	16
17h08m16.3s	-23d:01m51.4s	0	10	35
07h12m02.2s	+37d:02m46.6s	12	20	9
16h34m12.3s	-17d:01m43.1s	0	20	10

Table 4.1: Table showing the predicted fractions of blended stars in a given NGTS telescope FOV for fields at separate galactic coordinates. These numbers refer to stars brighter than I=16 and fainter than I=8.

FOV of 7.23 squared degrees can be generated using input from a stellar catalogue. This particular computation used the UCAC catalogue [Zacharias et al., 2000] as an input of magnitudes in the I band for all the stars within the FOV centred at the chosen coordinate. The choice of this optical band was based on the proximity to the color of stars of interest (late K and M dwarfs) but, despite not having been decided yet, the wavelength range of the instrument will likely cover a large portion of the range from 600-900nm. At this point, for each aperture centred on every star, the light contribution from every other star in the field can be computed and a *blending factor* calculated. This is simply the fraction between the contaminating light from every other star and the total flux from the star centred on the aperture. At this point, a threshold of 5% blending was chosen to distinguish blended from unblended stars and the percentage of blended stars provides an indicator of crowding. This threshold is chosen as a test of the proximity of other nearby stars. Despite the fact that a change in the apparent flux of 5% causes any transits of the star of interest to have an apparent depth change of the same percentage, any variability from the either star (stellar pulsations or deep eclipses) is a potential source of false positives. Moreover, any degradation of the seeing conditions during an observation will increase this blending percentage. For a given list of locations on sky of varying galactic latitudes and longitudes this parameter was be computed.

Table 4.1 contains a list of fields for which this step was performed, with the corresponding galactic coordinates and blending percentages for stars in the $16 > I > 8$ range. The results provide information on the expected crowding, which aid the choice of fields to observe. Fields at 10 and 20 degrees away from the galactic plane at extreme separations from the galactic centre were tested to define the range of possible crowding levels. The stellar density is not a linear function of either galactic latitude or longitude, with an exponential increase at low longitudes and latitudes, as modelled by Bahcall & Soneira [1980].

Section 4.3 shows the result of the simulation as a tool to select the fields that will maximise the science output of the NGTS instrument.

4.3 Field selection strategy for NGTS

The simulation described in Section 4.2 results in the plot shown in Figure 4.5. The coordinates of the Paranal observatory were used, as well as the relevant weather information to compute the expected maximum number of hours of observation in a single year for every location by the final instrument. A maximum zenith distance of 60° was used, since the observatory enclosure's design blocks the view of any telescope at elevations under 30° and an exposure time of 600 seconds (10 minutes) was set. This choice of exposure time is purely based on computational grounds as it sets the time resolution of the simulation.

The Figure shows the maximum number of hours a telescope can observe any location on the sky. The blue region marks any coordinates that are under 10° galactic latitude, whilst the black cross markers representing fields at an angular separation of 20° from the galactic plane. The white star shows the location of the galactic centre, the green line represents the path of the Moon on the sky throughout the year, while the purple lines delimit any fields that never come within 28° of the Moon. As mentioned in Section 4.2, this is the minimum angular separation required to avoid direct moonlight illumination of the telescope tube when using a 40cm long baffle. The white dots show the locations of known SuperWASP planets and the blue horizontal line indicates the fields that cross the zenith at Paranal.

It is clear that there is a discontinuity between the coverage of fields south of the zenith and those north, related to the influence of the presence of the Moon. It is also immediately possible to see that fields around the region of 10-12 hours in right ascension and between -35 and -50 degrees in declination offer the highest coverage possibility. This is, however, not surprising since the weather conditions at Paranal are uniform throughout the year (figure 4.3) and this location points at fields primarily available in the Winter months, during which the nights are longer. However, this also coincides with the RA range that is likely to suffer from the lunar presence, suggesting that the influence of the Moon has been potentially underestimated. An additional advantage towards selecting fields at declinations below the local latitude is that these are better suited for follow-up from Chilean observatories. The northerly direction of the wind present at these locations often forces the telescopes to observe towards the south direction due to pointing limitations.

Further study is necessary to determine the real influence of the moonlight

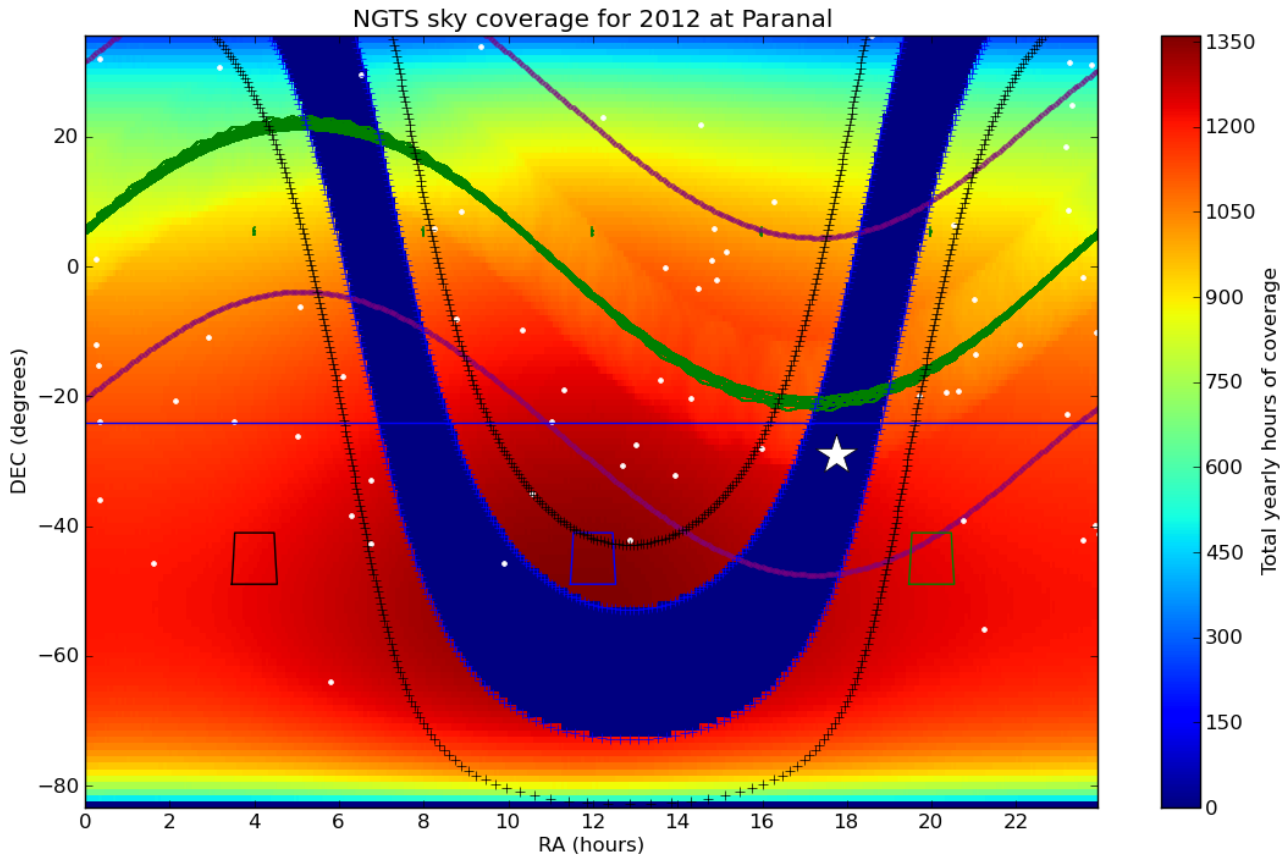

Figure 4.5: Annual sky coverage for the NGTS instrument. This is the result of the simulation described in Section 4.2 when applied to a telescope at ESO's Paranal Observatory. The Figure shows the maximum number of hours the telescope can observe any location on the sky visible with the NGTS instrument. The blue region marks any location that is less than 10° from the galactic plane, with the black cross markers representing fields at an angular separation of 20°. The white large star shows the location of the galactic centre. The green line represents the path of the Moon on the sky throughout the year, while the purple lines delimit any fields that never come within 28° of the Moon. The white dots show the locations of known SuperWASP planets for comparison and the blue horizontal line indicates the fields that cross the zenith at Paranal. Three suggested field choices are also indicated, assuming the telescopes will be set up in a 4×3 arrangement.

in terms of the increase of noise a given light curve can suffer from a change in the background light. A choice of exposure time for the final instrument will determine the limiting magnitude of the telescopes, which in turn will determine the maximum allowed increase in the background light due to the moonlight. Furthermore, light scattering inside the telescope tube may prove to be a limiting factor, but the instrument has been designed such there is scope for additional baffling if necessary.

Nevertheless, Figure 4.5 can still be used to assist in the selection of the locations on sky the telescopes can observe. Due to the physical limitations of minimum observable elevations as a consequence of the design of the building a minimum of three fields for each telescope, separated by 8 hours in RA, must be selected. This ensures that each field is observed for as long as possible, thereby complying with the aims of the project. This choice is dominated by the selection of a field inside the 8h $<$ RA $<$ 16h range which, in order to avoid direct moonlight incidence and overcrowding from the galactic plane proximity, is restricted to a small area. Figure 4.5 shows three suggested locations. These demonstrate the size of the FOV of the full instrument, assuming a 4×3 arrangement of the telescope fields, and provides a picture of the separation requirement between locations. Any deviations in RA would have to be relatively minor to ensure that the central field remains clear of the galactic plane and the lunar avoidance region, but there is no specific condition that requires all three to be located at the same declination. Indeed, the example fields at RA=4h and RA=20h are situated at locations relatively unrestricted. Note, however, that larger differences between the declination of the fields and the local latitude imply a lower maximum elevation and hence a higher average airmass for the data collection.

Figure 4.5 shows that the choice of positions to observe is a trade-off between the influence of the moonlight and stellar crowding, taking into consideration the maximum elevation achieved by each position. The results of this simulation will be used by the team to make field selections.

4.4 WASP field selections for staring strategy

In early 2011 the team responsible for the maintenance and operations of the SuperWASP facility in the northern hemisphere (La Palma, Spain) took the decision to change the observing strategy of this instrument onto a staring mode. This was done to gauge the photometric performance of the instrument when the sampling rate of a given field is increased on average by a factor of 6, as well as improve the sensitivity to planets on longer periods. Section 2.6 discusses the impact of this

change. This simulation was used to select the optimal field to be observed from the beginning of March 2011.

Using the same input parameters described in Section 4.3, the simulation was performed for the location of the SuperWASP North facility using the weather information from the weather monitor at this enclosure as described in Section 4.2.

The result is shown in Figure 4.6 where the path of the moon is represented by the black line. The white dots represent known SuperWASP planets. The simulation incorporates a hard limit at 65° declination because the instrument is unable to observe any fields beyond this point due to the design of the enclosure. This plot has also included a purple line representing all the positions on sky that become observable at the beginning of the night on the 1st March 2011. This is a visual aid for the selection of any fields that are optimal for maximum coverage starting on the intended date. Fields to the right hand side of this line will be suitable later during the year. It is clear that, in order to avoid a close proximity to the Moon, fields located after RA=12 hours and high declinations show a higher coverage possibility. These coincide with fields observable during the Summer in La Palma. Contrary to the weather conditions in Paranal, La Palma suffers from considerably worst weather in the Winter and the simulation suggests that *Summer fields* can be observed for a larger number of hours, despite the shorter nights.

In possession of this result, the SuperWASP team selected a telescope pointing that is represented by the blue rectangles in the image. Each rectangle corresponds to the field of view of a single telescope. Despite the fact that all 8 telescopes are mounted on the same assembly, there is some overlap between the locations on sky that are observed. The staring observations only started towards the end of March 2011 (30th) and hence fields with a higher RA with respect to the purple line were chosen.

This is a circumstance where this simulation can prove to be useful and is an example of a case where it has had a direct impact on the observing strategy of the SuperWASP instrument. Section 4.5 describes the development of a natural extension to this simulation, where the probability of finding a planet for a given position is computed as a function of the orbital period of the planet.

4.5 Planetary detection probability simulations

In the planning and design stages of a transit survey a key question is to ask the sensitivity of planet detection as a function of period. More importantly, what is the dependence of this sensitivity as a function of design decisions. This

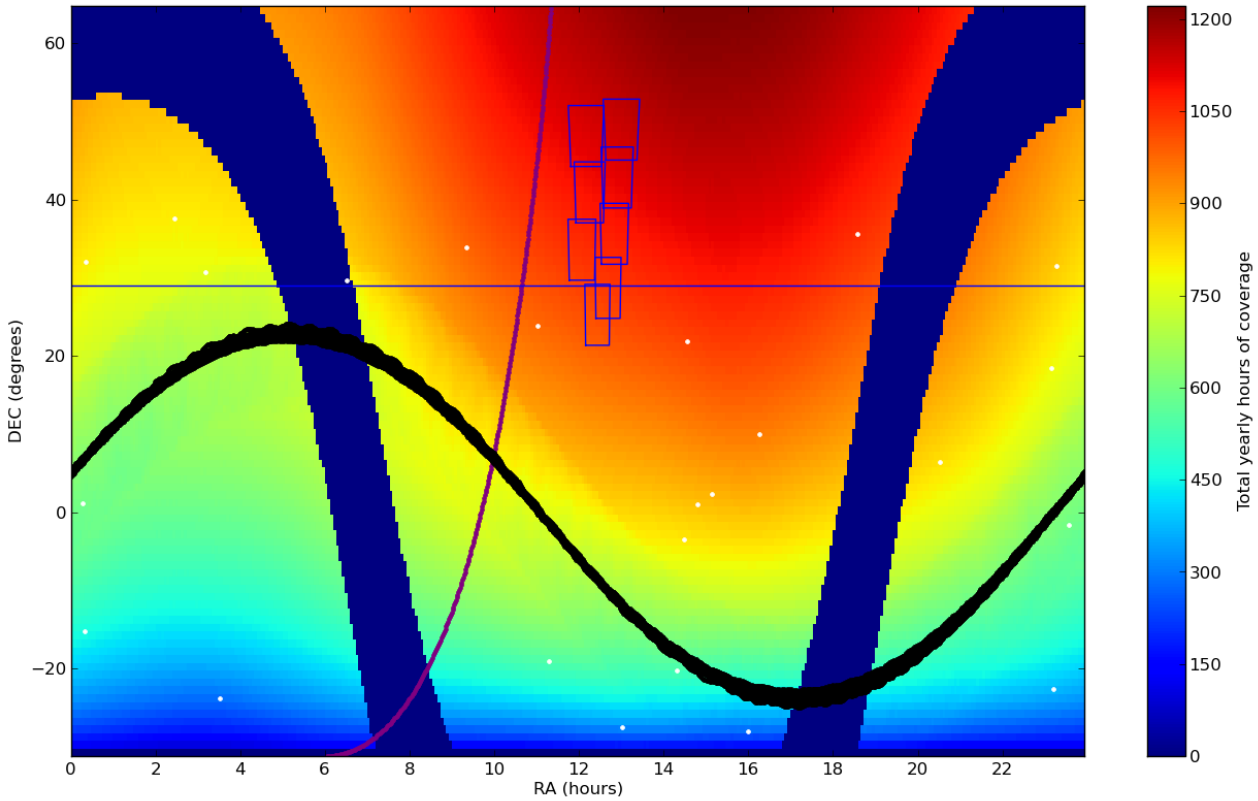

Figure 4.6: Annual sky coverage for the SuperWASP instrument. This is the result of the simulation described in Section 4.2 when applied to the SuperWASP northern hemisphere facility in La Palma (Spain). The Figure shows the maximum number of hours the telescope can observe any location on the sky visible with this instrument. The blue region marks any location that is less than 10° from the galactic plane and the black line represents the path of the Moon on the sky throughout the year. The purple line indicates the positions of fields which would be optimal to start observing in the beginning of March 2011. This is done to aid the SuperWASP North team in the choice of such fields. The white dots show the locations of known SuperWASP planets for comparison and the blue horizontal line indicates the fields that cross the zenith at La Palma. The fields selected by the team are represented by the blue rectangles.

Section describes the development steps of a second software simulation, using common features with the first, but extending the information of sky coverage onto a probability of planetary detection.

For a given set of coordinates this simulation computes the times of every possible measurement over a period of time in accordance to the principles outlined in Section 4.2 and will estimate the probability of finding a planet, if it exists at that location, as a function of its orbital period. The same assumptions for the galactic plane avoidance, lunar presence, weather restrictions and twilight times have been used. The maximum observed zenith distance has been left as an input to the simulation as well as the location of the observatory. The principles of the calculation of the probability are described in the following Sections.

Period range

This simulation will calculate a probability of transit detection for a given set of possible orbital periods. Therefore, a range of orbital periods must be defined. This can be done simply by defining a set of periods in equal steps. However, since transit detections typically imply phase folding the data points according to any trial period and looking for a dip at a particular phase, it is essential to define the periods in equal steps in phase. This method will define the period steps in terms of a constant shift in phase, ensuring that short periods are well sampled whilst avoiding long computations over the longer periods where a small variation reveals no significant change in the phase.

This simulation has tested periods between 0.3 days and 15 days. This is the *period range* $(t_1 - t_0)$ for which a phase ϕ can be found for a given period P according to

$$\phi = \frac{(t_1 - t_0)}{P}. \tag{4.6}$$

A constant phase step of 0.01 was chosen and, using this equation, the increment in orbital period corresponding to this change in phase can be found. This step was found to sample the period range such that it resolves well any pathological periods whilst being computationally manageable.

For a given period P and corresponding phase ϕ there is a larger period P' with a corresponding frequency ϕ' such that $\phi - \phi' = 0.01$. From equation 4.6, it follows that P' is given by

$$P' = \frac{P(t_1 - t_0)}{(t_1 - t_0) - 0.01P}. \tag{4.7}$$

This relation was used to generate a set of test periods that represent equal changes in orbital phase.

Phase coverage

For a planet with a short orbital period, it is likely that multiple transits will be observed over a season. Therefore, a transit signal is improved if the data from all transits is combined into a single case. This is often the method used to search for transits in a light curve, commonly known as *phase folding* the data. This is done by taking the ratio between the time of an observation since a reference date and the orbital period. The integer part of this result will give the cycle number a measurement was made whilst the decimal part will give its fraction along that particular cycle (the phase). Naturally, all measurements belonging to a planetary transit will occur close to a particular point in this phase.

At this point, the simulation generates a phase map of all the measurements taken throughout the duration of observations. Each particular data point occupies a single location in phase space for every possible orbital period, and hence a phase coverage map as a function of period can be generated. This is equivalent to phase folding the data points over every considered period and provides information regarding how well sampled the entire orbital phase is for every period. In other words, if photometric measurements were made once per night at the same time during the night, a transiting planet with true orbital period of precisely 1 day would have a poorly sampled phase coverage, since every measurement would be located at the same point in phase. Therefore, the chances of observing the transit taking place are very small. On the other hand, if the true period of the planet was not a multiple of an integer day, the phase coverage would be more uniformly populated, thereby increasing the chances of the transit being observed.

Generally, a well sampled phase coverage correlates well with the probability of finding a transiting planet with that period. Regardless of the observing strategy employed, however, transiting planets with orbital periods matching periodic events in astronomical observations (such as the day/night cycle) are less likely to be found. Planets in orbital periods of integer days that happen to transit during the day time at the location of the observatory will never be found with that particular instrument. These *pathological periods* are unavoidable in ground-based surveys of this kind. These special periods have the power to increase significantly the sensitivity of shallow transits if the phase is favourable (transits occurring always during the night), but correlated systematics are likely to dominate signals with these periods.

Planet detection probability

At this point, in the possession of a map of the phase coverage per period, the question of what the chances are of finding a planet is placed. Assumptions must be made with regards to the minimum amount of coverage inside the transit necessary to detect a transit. This number was assumed to be 15 hours, provided that this coverage originates from a minimum of 3 separate transits. This was based on previous experience from the SuperWASP project, where evidence of multiple transits is crucial as well as a well sampled transit once the data are phase folded. Assuming a sampling rate of one hour, this corresponds to 15 data points inside a transit which, assuming the typical duration of such transits is 3 hours, is equivalent to an average of 5 transits.

In order to estimate the number of data points in transit (and therefore the total exposure time inside transits), a transit duration must be provided. This value, however, is dependent on the period of the planet, inclination of the orbit and the projected radius of the planetary and stellar disks. Using the method From Winn [2010]; Seager [2010b], the duration of a planetary transit T_{tot} was predicted using

$$T_{tot} = t_{IV} - t_I = \frac{P}{\pi} \sin^{-1} \left[\frac{R_*}{a} \frac{\sqrt{(1 + (R_p/R_*))^2 - b^2}}{\sin i} \right], \tag{4.8}$$

where P is the period of the planet and a is the orbital separation between the planet and the host star, which can be determined from the period using Kepler's Third Law [Kepler, 1619]. Using the symbol convention shown in Figure 1.8b presented in Section 1.3, the duration of a planetary transit is simply the time between contacts t_I and t_{IV}. In this equation, R_* is the stellar radius, R_p is the planetary radius, b is the impact parameter and i is the orbital inclination. These parameters are given as inputs for the simulation but for the cases presented in this thesis, the inclination was assumed to be 90°, the planetary radius used was that of Neptune ($0.35R_J$) and the stellar mass and radius of a typical K star ($0.7\mathrm{M}_\odot$ and $0.75\mathrm{R}_\odot$ respectively).

Using equation 4.8 it is possible to estimate the predicted transit duration of a planet for each period and place windows with the equivalent frequency range on the phase coverage map. For each period 500 transit windows were attempted, placed randomly along the full phase and the number of points inside this window (and whether they come from a minimum of a given number of separate events) determined whether a detection of the transit is achieved. The probability of finding a planet for that given period is simply the ratio of the number of windows that revealed a detection and the total number of attempts.

Visual results

In order to confirm that the simulation is working as expected, the typical outcome is shown in Figure 4.7. The simulation was executed for the duration of the year 2012 for a field located at 16h in right ascension and a declination of -30 degrees observed from Cerro Paranal.

The top left panel displays the measurements made throughout the year as a function of the date. The blue lines show the twilight times, the green points represent photometric measurements, the red points any measurements rejected because of the several constraints and the yellow points show any times where the target is above the horizon during times of daylight. The top right panel shows the phase coverage map described previously. Data points are plotted in phase as a function of orbital period. It is possible to see that pathological periods show large gaps in the phase coverage.

In order to visually assess the uniformity of this phase coverage for any given period, the panel on the bottom left of Figure 4.7 shows the density distribution of the data points for every period. This is done by calculating the histogram for each case using bins of size 1×10^{-3} cycles (which gives a total of 1000 bins) and plotted as a function of period again. It provides a visual inspection of how uniform each phase coverage is, which is particularly useful in situations where the number of measurements is small. In the case shown, the large number of elements ensures a relatively uniform coverage for most periods. The phase coverage plots in these two panels are particularly useful an interactive plotting package where particular periods can be inspected in more detail.

The remaining panel presents the crucial result from the simulation, where the probability of finding a planet as a function of period is shown. Any pathological periods show a characteristic sharp decrease in probability due to the extreme non-uniform phase coverage. For this particular execution of the software, a maximum zenith distance of 60° was used, as well as a sampling rate of one hour. This is not a realistic exposure time, but may be the time scale required to detect planetary transits. This has also been the time scale used to gauge the precision of the SuperWASP instrument in Chapter 2. Comparisons between the results shown in the bottom right panel of the Figure for different input parameters provide an insight into how a particular design decision may affect the planet probability catch as described in Section 4.6.

The probability curve presented shows that a staring strategy is necessary to extend the range of known long period transiting planets discovered by ground-based surveys. Intensive coverage is also crucial to maximise the amount of coverage

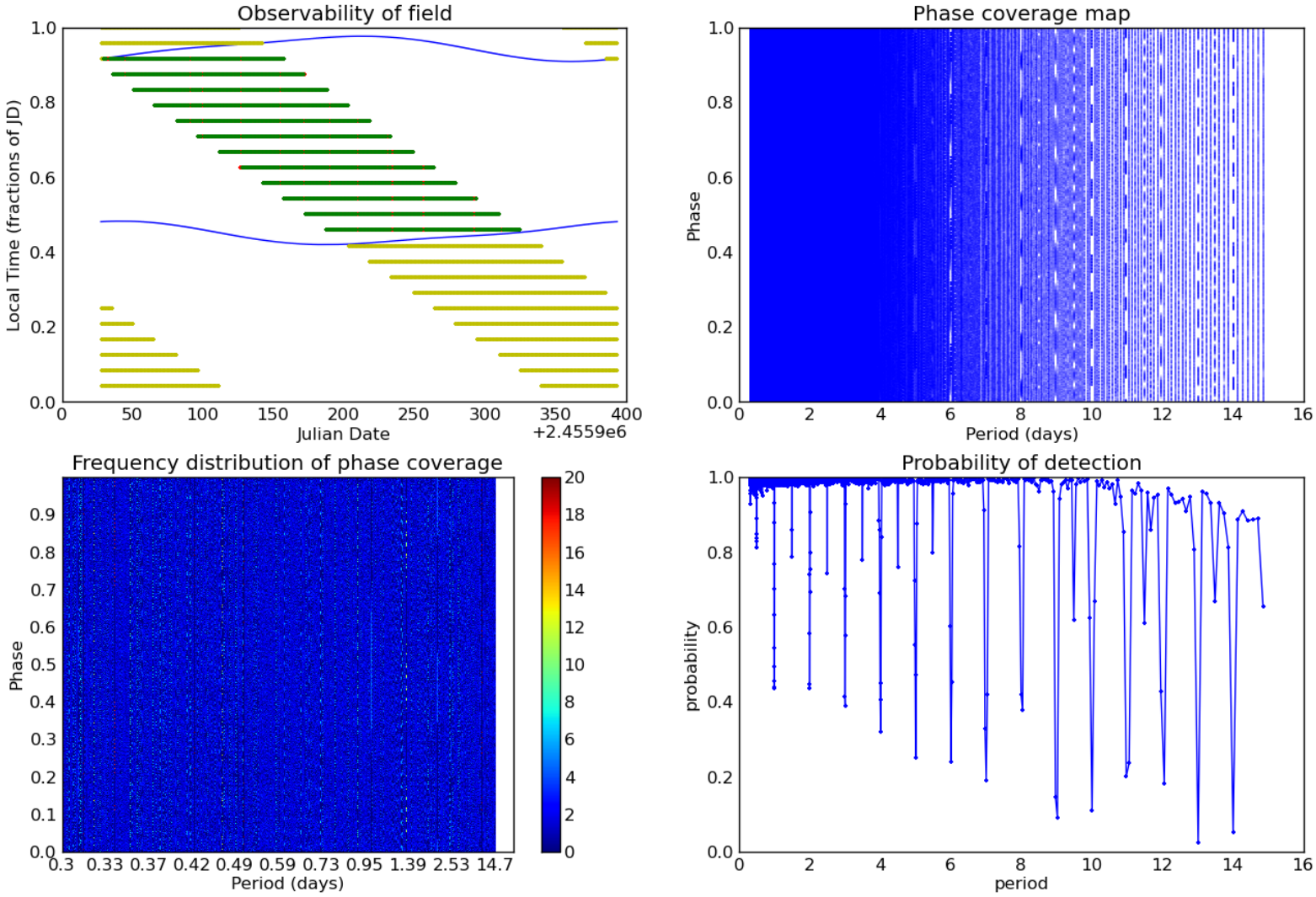

Figure 4.7: This Figure shows the general outcome from the planet detection probability simulation described in Section 4.6. The top left panel shows the annual distribution of measurements in terms of the time they happen during the day. The blue lines show the twilight times, the green points represent photometric measurements, the red points any measurements rejected because of the several constraints and the yellow points show any times where the target is above the horizon during times of daylight. The top left panel shows the phase coverage map for this particular run. This map shows the position in phase of each photometric measurement as a function of period. The bottom left panel is used to assess the uniformity of this coverage, in the form of a series of histograms of the phase distribution as a function of period. Finally, the bottom right panel shows the crucial result of the simulation, where the probability of transit detection is presented as a function of orbital period.

during transits and hence increase the chances of detecting shallow eclipses.

4.6 Window function dependence on input parameters

The simulation software described in Section 4.5 is designed to provide a probability of finding a planet at a given location as a function of its orbital period. However, it can also be used to compare any changes in the probability as input parameters are varied, such as the maximum zenith distance allowed, the location of the telescope, the location on sky, the minimum exposure time during transit and the minimum number of observed transits.

Zenith distance restriction

The plot presented in Figure 4.8 shows an example of such study, where the effect of changing the maximum zenith distance a field is allowed to be observed at is simulated. Naturally, restricting observations to a higher elevation will reduce the number of photometric measurements but will improve the average precision of the measurements (this effect is not accounted for in the simulation). Indeed, if the team decide to select 6 fields per camera separated by 4 hours in right ascension, contrary to the suggested pattern of only 3 fields shown in Figure 4.5, it would be ideal that each field would be observed with the maximum zenith distance restricted to 30°. However, as shown in Figure 4.8, observing 6 fields per year would restrict the number of observations of each field and would result in a loss of sensitivity of long period planets. Once again, this is under the assumption that 15 hours of coverage are indeed necessary to detect a transit. This is unlikely to be the case for large planets.

Using a restriction in zenith distance would be desirable to limit the impact of scintillation. However, the Figure shows that if the zenith distance is restricted to 30° (cyan line) the chances of finding planets in orbits longer than 4 days begin to decrease, reaching zero probability for planets in 8 day orbits. Using the maximum allowed zenith distance by the building design (blue line) shows a high sensitivity to planets in the entire considered period range.

Telescope location

In order to commission the final instrument at ESO's Paranal observatory, the team was required to request authorisation from the European Southern Observatory in the form of a proposal that was based on our *white book*. This document

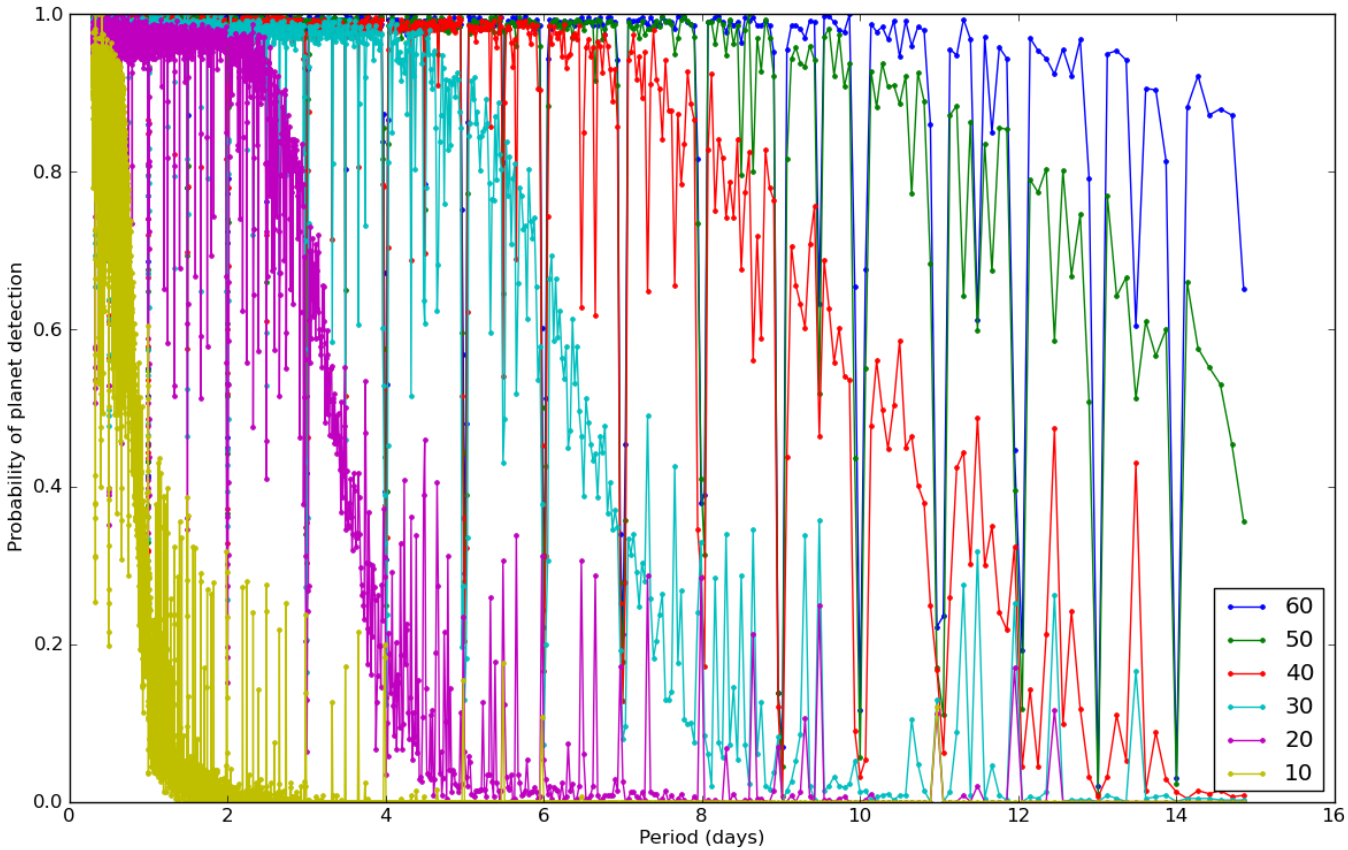

Figure 4.8: Probability of planetary transit detection as a function of period for different restrictions on the maximum zenith distance allowed. The 6 curves represent the zenith distance restrictions, where the values are given in the legend in degree units.

describes the project, its current status and addresses a number of issues. These included the science goals of the project and how these integrate the long term strategy of the ESO initiatives. NGTS is designed to find transiting planets around bright stars, which will serve as good candidates for follow-up with facilities such as the VLT and the E-ELT.

One of the questions that needed to be addressed in this document involved justifying the choice of location. The observatory at Cerro Paranal is one of the best sites on the planet for ground-based astronomical observations, due to its high altitude, low humidity and remoteness, but ESO's other optical telescopes are located in another excellent location, the La Silla Observatory. The fundamental difference between different sites is uniquely related to the weather conditions associated to each. Figure 4.3 shows the monthly average percentage of good nights each of the two observatories delivers over the course of one year. It is clear that, despite the two locations being comparable in the Summer months with Paranal having a slight advantage, La Silla exhibits a significant decrease in the number of observable hours during the Winter.

This simulation played a crucial role in the justification for the commissioning to be done at Cerro Paranal, based on the effects of the loss of nights during the Winter at La Silla. The software was executed for both locations choosing 2 separate fields, ideally observed during the Summer and Winter months in Chile. These were fields located at right ascension of 16 hours and declination of -30 degrees for a Summer field and right ascension of 6 hours and declination of -30 degrees for the Winter field. The probability of planetary detection curves for both situations are shown in Figure 4.9. The right hand panel displays the results of the probability as a function of period on both locations for the Summer field. Despite the fact that Paranal exhibits a higher probability for long period planets, the two results are comparable up to periods of around 13 days. However, the left hand panel shows the results for the Winter field, where the probability curve for Paranal shows a significantly higher sensitivity for periods higher than 10 days.

Moreover, the sensitivity gain between the two sites can be demonstrated in terms of the ratio of the probabilities of finding a planet as a function of period assuming all other parameters are constant. Figure 4.10 contains curves that show the ratio of the probabilities between the two sites for the case of the Summer field (blue) and the Winter field (red). It once again shows that fields observed in the Summer have comparable chances of finding planets across the period range, but the gain for fields observed in the Winter months at Paranal is considerable for any periods above 9 days. The probability of finding a planet displaying an orbital

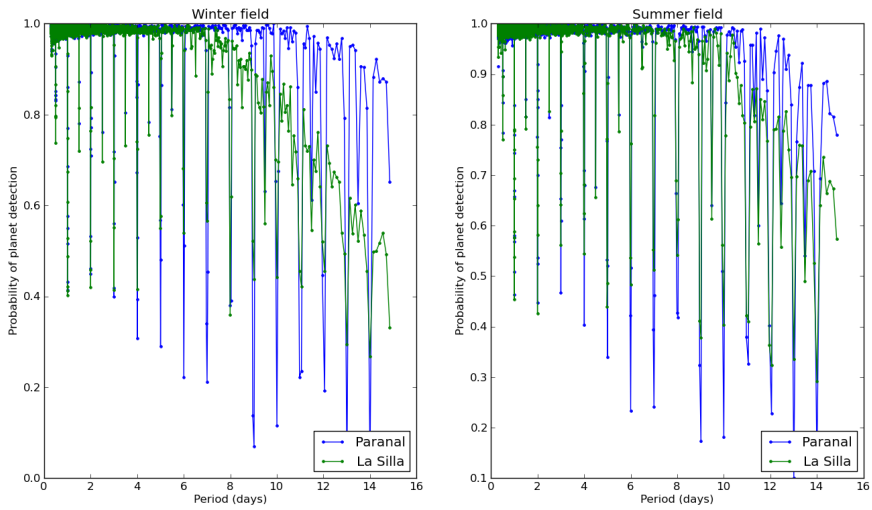

Figure 4.9: Probability of planetary transit detection as a function of period between La Silla and Paranal observatories. The two panels show these probability curves for a Winter field (left) located at RA=16h, DEC=-30d and a Summer field (right) located at RA=6h, DEC=-30d.

period of 15 days is estimated to be twice as likely if the survey is commissioned at Cerro Paranal, thereby demonstrating the clear advantage of this site in comparison to the alternative. A previous version of this Figure was included in the NGTS white book submitted for approval by the ESO science committee.

The results of this simulation show that, in order to find transiting planets in long periods, ground-based surveys must maximise sky coverage for each chosen field, and therefore be located at the best possible sites on the planet.

Detection thresholds

All the results shown so far have assumed that 15 hours of coverage during transit are required for a detection. This is unlikely to be the case for Jupiter-sized planets, where potentially a single transit achieves enough precision. Members of the team have suggested that, if a clear single transit is observed and immediately thought to be a strong candidate, radial velocity follow-up can be triggered straight away. A series of spectra for a candidate can confirm the sub-stellar nature of the planet and provide a period, allowing the prediction of the next transit, which could be observed using larger telescopes. This would extend the sensitivity of NGTS to planets over long period (several weeks to months). On the other hand, Earth-sized

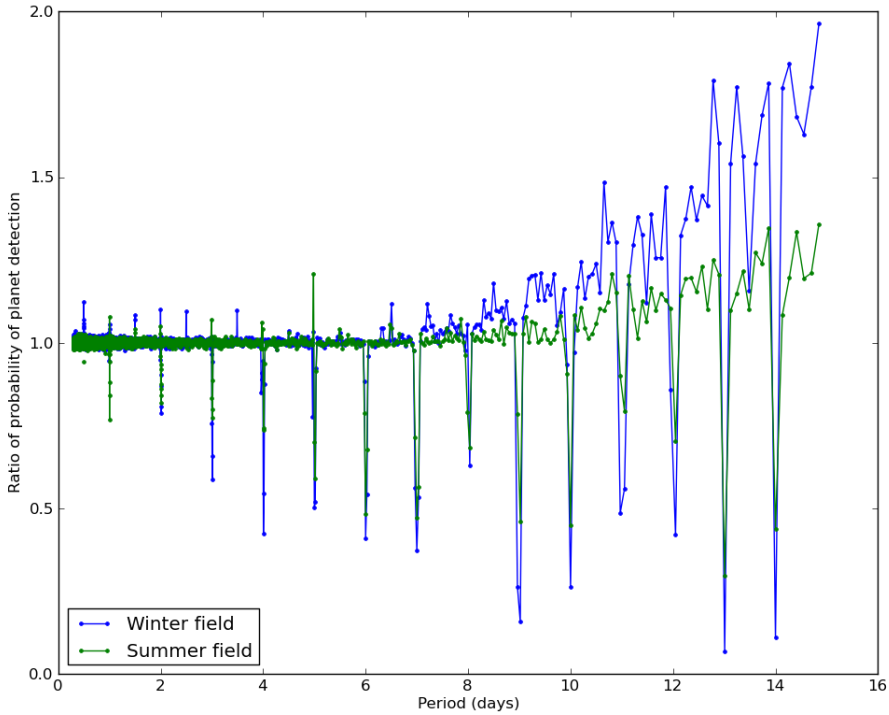

Figure 4.10: Ratio of the probability of planetary transit detection as a function of period between La Silla and Paranal observatories. The two curves show the ratios of the probability curves shown in Figure 4.9 for the Winter and Summer field cases.

planets may require longer coverage due to the shallower nature of these transits.

The simulation was used to explore how the window function depends upon such assumptions. Several runs of the simulation were executed using different restrictions on the minimum number of transits required and the minimum amount of exposure during transit. Specifically, combinations of 1, 3 and 10 minimum transits with 2, 15 and 30 hours of minimum coverage were used, and the results are shown in Figure 4.11

The several panels of the Figure show how the various assumptions affect the window function, and the relations between them. The overall planet probability when a minimum of 30 hour coverage inside transit is required is relatively insensitive to the restriction on the minimum number of transit observed. This is likely because the typical transit duration implies that 30 hours of coverage are likely to belong to close to 10 transits. On the other hand, under the assumption that only 2 hours are required for a detection, corresponding to essentially the duration of a single transit, the results are completely dominated by the requirement to detect multiple transits. This case demonstrates that, for examples where a single transit provides enough S/N for a convincing detection, it is perhaps preferable to bypass the requirement for multiple transits to be observed and select candidates for follow-up immediately. Interestingly, a more stringent restriction on the minimum number of individual transits significantly affects the probability of planet detection close to pathological periods. The examples seen in the top panels of Figure 4.11 show that for these integer periods the results are affected by the high probability that a large number of transits may not be visible at all during the entire observing season.

4.7 Future Work

The NGTS facility has been designed to be flexible in terms of observing strategy. Every telescope is assembled on a separate mount to allow precise auto-guiding to take place. This will allow each telescope to maintain all stars in the same pixel on the chip, whilst allowing reliable acquisition of fields for different nights. The effects of differential refraction have been also considered and is reflected on the choice of CCD+telescope assembly. These were selected such that the maximum expected deviation of stellar position due to differential refraction effects over the entire FOV is under the pixel scale up to a maximum airmass of 2. Hence, the effects of wavelength The single mount per telescope design also provides the possibility of using each telescope for a different function, with a different individual observing strategy, i.e, a single telescope could perform an all sky survey with a given sampling

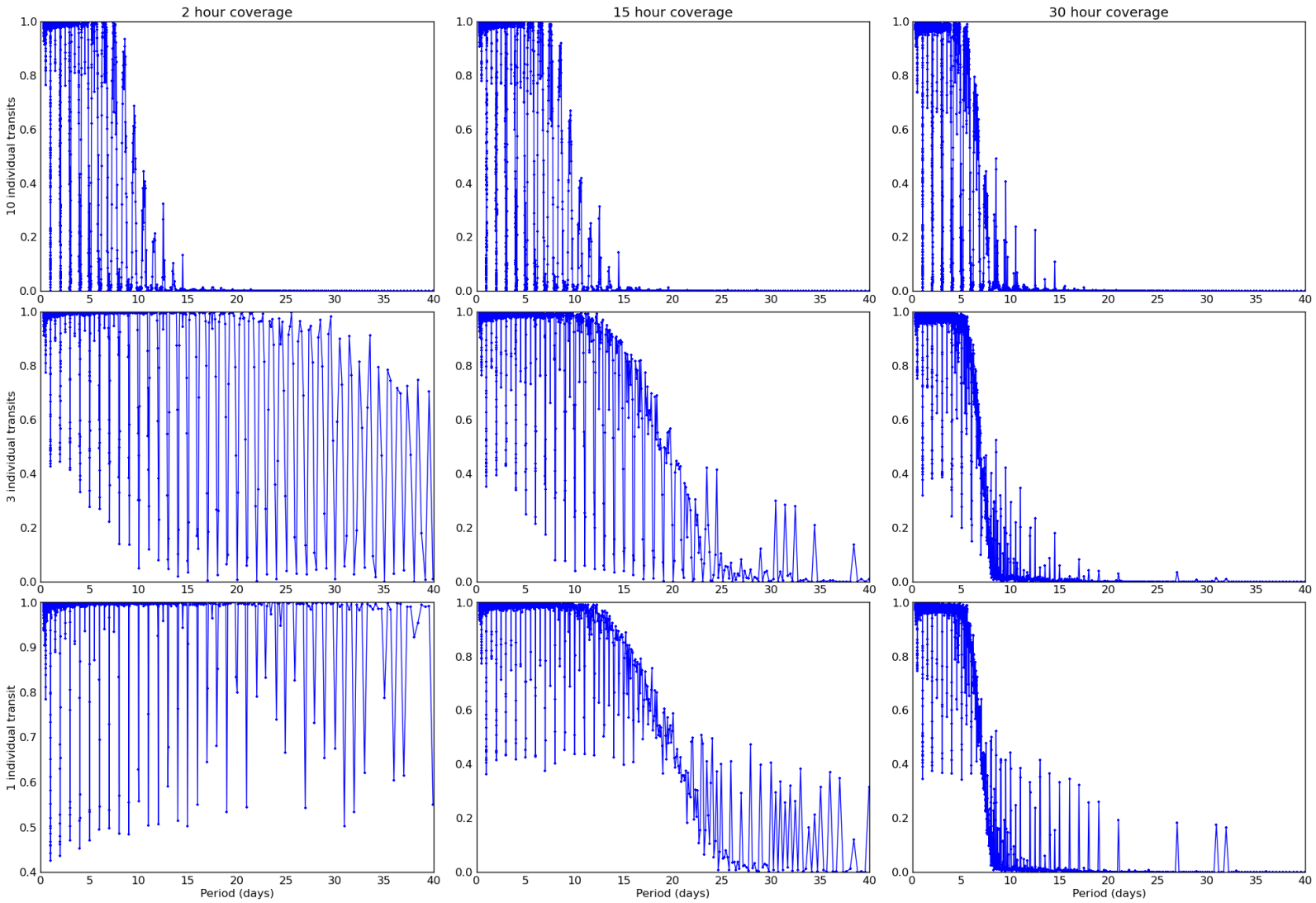

Figure 4.11: This Figure contains the NGTS window functions for a combination of minimum number of detected transits and exposure time during transit. The several panels show the results assuming 1, 3 and 10 transits required for a detection, combined with a minimum of 2, 15 and 30 hours of coverage inside transit. The vertical axes represent the discovery probability while the horizontal axes the period of the planet.

frequency per field whilst the other telescopes operate under a staring strategy policy. Indeed, as the research into the mass-period distribution of exoplanets reveals new insights into the period distribution of Neptune-sized planets, the observing strategy could be modified without the need to perform any major hardware changes.

The transit detection threshold in terms of a fixed number of points present inside the transit window is potentially too simplistic. We have explored the consequences of different detection threshold assumptions on the window function, but a more realistic approach can be used. Assuming a given stellar type and magnitude, calculations of the expected noise per measurement can be made using a model similar to that presented in Section 2.3. This would incorporate information on the airmass each photometric data point is taken through and its impact on the data quality, which the simulation currently does not take into account. Each simulated measurement would then have a corresponding photometric precision and the transit detection threshold could be defined in terms of the minimum required S/N, in such a way as to attribute a large weight to data points taken under optimal conditions. This method would also allow a direct comparison with preliminary results from the finished instrument. Alternatively, this software can be used in conjunction with other simulations that focus on the photometric precision for each target star.

Chapter 5

Conclusions

5.1 Summary of conclusions

This thesis presents multiple studies of improvements to current and future ground-based transiting planet surveys. The work focuses on the world-leading survey SuperWASP and the development of the Next Generation Transit Survey, a new ground based wide-field survey to search for planetary transits soon to be commissioned at ESO's Paranal observatory in order to benefit from the high quality of this site. A detailed description of an enterprise to perform transmission photometry of inflated hot-Jupiters WASP-15b and WASP-17b using the multiband photometer ULTRACAM on the NTT is also presented.

5.1.1 Analysis of the noise sources of SuperWASP

Chapter 2 presents a study of the systematic effects within the SuperWASP instrument. A noise model based on that presented by Southworth et al. [2009] was developed in order to determine the expected performance of the telescopes and compare with the real data quality. Using the fractional RMS over the time scale of a single night as an indicator of photometric quality, the data sets from 2007 show a large deviation from the theoretical noise curve. This is due to a known issue related with temperature dependent telescope focus solved in 2008 during a hardware maintenance period. A similar test with data from 2009 for the same camera was performed and the results show that the hardware maintenance has indeed solved the issue. The effects of this maintenance are also seen in the overall quality control diagnostics from the SuperWASP pipeline. Calculations of the median of the fractional RMS of all the light curves in a specific brightness range ($11.6 > V > 10.0$ magnitudes) for each field every night are performed and stored.

Therefore, time series of the photometric quality for each camera have been plotted where a clear improvement in the precision for cameras 144, 147 and 148 is seen after the hardware upgrade.

The fractional RMS of the latest data sets show that the implementation of detrending algorithms such as that developed by Tamuz et al. [2005] is having a small impact on the overall data quality of the bright stars and that the current performance of the telescopes is close to the maximum expected precision. These Figures also reveal that the instrument is consistently achieving sub-percent photometric precision on single exposures. Despite this, there is evidence of a source of systematic noise affecting the light curves of the brightest stars in the field as the fractional RMS of these is still above the expected level from the noise model.

Correcting for flat-fielding errors

The implementation of detrending algorithms is key to minimising the effects of systematic noise sources. However, these are typically designed to remove trends that are similar (even if with different amplitudes) between large numbers of stars. Thus, any sources of noise that are spatially dependent across the chip due to localised features will not be dealt with. A study of a set of *detector maps* produced from the average of the fractional residuals of the light curves in CCD coordinates reveals the presence of a variety of features. Note that these maps are produced using the final product of the software pipeline, and therefore any features visible are present in the light curves used to search for planetary transits. These maps were used to identify non-linear pixels that have not been flagged in the bad pixel masks, as well as several issues with the software reduction. However, the dominant large scale features have been found to be related to the wavelength dependence of the inter-pixel variations of the CCDs. The flat-field frames used by the instrument are obtained during twilight, where the dominant wavelength is shorter than the typical wavelength of the target stars SuperWASP observes. Additionally, the broadband nature of the filter used makes the instrument particularly susceptible to any wavelength dependent phenomena. This study used the sky background from science images from various nights with different lunar phases, which correspond to different wavelengths of the background light, to investigate the behaviour of features seen in the detector maps and has revealed that the current flat-fielding strategy is introducing a component of red noise into the light curves.

We suggest a set of possible improvements to minimise this problem. A set of lab flats at different wavelengths can be combined with the twilight flats to remove this pattern from this calibration step. Alternatively, a set of sky flats with narrow

band filters can achieve the same result. Using the night sky frames to generate flat field frames from the sky background light during dark nights can also be attempted, as this would provide a flat field that is produced using light of similar wavelength to that of the stars. However, this requires a large set of frames during dark time where the sky background level is low, and the feasibility of this method is uncertain. The structure in the flat fields is time-dependent on time scales likely to be shorter than those required to accumulate enough photons in the night sky flats such that the data is not dominated by the photon noise in this calibration step.

This study has also identified the presence of a particularly serious feature of yet unknown origin. Examples of elliptically shaped features in all CCDs can be seen in the detector maps, which cover areas of hundreds of pixels and have depths of around 1%. These are potentially capable of introducing periodic dips of the typical transit depth into the light curves of any star that drifts across them, thereby becoming a potential serious source of false positive cases. Several examples have been found to appear and/or disappear at specific times during an observing season where no correlations are found with degrading weather conditions or to times where any maintenance was done. In addition, some examples are found to move in CCD coordinates between seasons. This is observed by comparing detector maps produced with data sets from different observing seasons, showing a temporal evolution of this feature in particular.

The current planet searching algorithms used by the project are designed to exclude any candidates that show flux decreases in periods of 1 ± 0.05 days. This was implemented because a large number of light curves were being selected for visual inspection with periodic signals of approximately integer days that were found not to be related to astrophysical phenomena. It is possible that these false positives are simply stars that drift across features in the CCD every night and that a suitable efficient removal of such features would allow the instrument to be sensitive to periods close to one day without being overloaded with false cases.

The possibility that the detector maps can be used as the basis for an extra detrending step in the SuperWASP software pipeline is discussed. In principle, these consist of a measurement of any systematic effects still present in the final product of the software pipeline fixed in detector space. Hence, there is a possibility that they can be used to decorrelate the light curves and provide an improvement. We have tested this hypothesis by obtaining the detector map values for pixels where each measurement on a given light curve was performed and create a *detector map series*. This is essentially a time series containing the detector map values for the location of each measurement. It also provides a measurement of the predicted amplitude of

the systematic noise introduced by the features seen in the maps. Hence, a direct comparison between the measured fractional RMS for each star and this predicted signal can be done. The results demonstrate that the detector map features have a negligible effect on the bulk of the un-binned light curves, and only a few bright stars achieve a precision similar to the level where the detector map could have an impact, once the data are binned. It is, therefore, clear that using the detector map to decorrelate the light curves will not make a significant improvement to the overall sample of targets.

The SuperWASP North team decided to modify the observing strategy of the instrument to a staring mode in order to test what precision can be achieved in single transits whilst extending the sensitivity to longer period planets. Data for this case was collected between March and June 2011 for a single location, selected using a simulation described in Chapter 4. This experiment in particular has the potential to be affected by the systematic noise visible in the detector maps, since the sampling rate of any star is increased and therefore the precision achieved in time scales of one hour is also improved. The improvement in the binned data is clear with respect to the non-staring data from 2009 but for stars brighter than V = 12 magnitudes the fractional RMS is underestimated by the noise model, suggesting the presence of an additional source of noise. It is now possible to see that the RMS of the bright stars in time scales of one hour is comparable with the noise expected from the detector map features. Nevertheless, the attempt to use this map to decorrelate the light curves has yielded no significant improvement. The distribution of the result of using the detector map to decorrelate this data set indicates that approximately 50% of stars show an improvement independently of brightness. This is consistent with multiplying each light curve by a random function of negligible amplitude and this shows that the detector maps are not likely to be suitable for decorrelating the light curves at this time. Several reasons are suggested that can explain this:

- It is possible that an unknown source of systematic error is limiting the precision at the 1mmag level, thereby causing the detector map to be an ineffective means of compensation.

- The typical fractional RMS of the detector map series for a staring field appears to be larger than that of the non-staring cases. This is likely to be related to the fact that the non-staring data was taken in 2009 whilst the staring fields are all observed in 2011, where only half a year of data were used for the creation of the detector map. The detector maps require a very large number of measurements to achieve the S/N necessary to visualise the features

seen, typically entire seasons. The noise present in the 2011 detector maps is likely larger that any other previous year, which leads to a larger fractional RMS of the detector map series generated from it. It is possible that a map created with the full data set for 2011 (not yet processed completely) would provide a more accurate measurement of these features and would potentially serve as the basis for an improvement in the photometry of bright stars.

- Using the detector map as a basis for decorrelating every star may be unsuitable in principle, since this would be compensating for a feature resulting from a wavelength dependence, whose amplitude is likely to be different for every star. A more profound understanding may be required in order to scale the detector map series to the color of every star and make this decorrelation a viable step.

The analysis done throughout Chapter 2 is relevant to any enterprise in astronomy using CCDs aiming to reach photometric precisions of 1 mmag or better. Despite the fact that at this time the amplitude of the detector map features seem to be negligible with respect to the bulk of the targets observed by the SuperWASP project, knowledge of such noise sources has had an impact on the design of the Next Generation Transit Survey. This project is designed to observe at longer wavelengths, with its filter bandpass between 600 and 900 nm, and similar wavelength dependent features from those seen in the detector maps have been found in the prototype instrument to be much weaker in amplitude. Moreover, the NGTS survey is designed to have guiding capabilities, which will potentially eliminate the effects of any systematic effect fixed in detector space completely.

5.1.2 Transmission photometry of exoplanets

Chapter 3 contains a description of an effort to perform transmission photometry of inflated exoplanets. This technique aims to measure a wavelength dependence of the depth of planetary transits due to the presence of opacity sources in the atmospheres. Fortney et al. [2008] predicts that hot-Jupiters fall into two distinct categories based on the irradiation levels of their atmospheres which determines the presence of a temperature inversion. However, recent observations have been found not to agree with this prediction and most observations of this kind find evidence of a broadband structure in the atmospheres of these planets thought to be due to Rayleigh scattering.

We have used the fast multiband photometer ULTRACAM on ESO's 3.6m NTT telescope, using several filter combinations to probe for the presence of a

temperature inversion (due to TiO absorption), Rayleigh scattering or absorption due to a broad NaI feature. We select our targets based on the expected transit depth difference due to one planetary scale-height, despite previous observations suggesting that the detected difference can correspond to a heigh of several times this parameter. We describe the preparations for the observations in order to maximise the photometric precision, including a simulation to determine the optimal defocus to use.

Primary transits of our selected targets, WASP-15b ad WASP-17b, are analysed and a clear systematic signal is noticeable close to the meridian transition. We propose an airmass correction with a linearly changing extinction coefficient as we see a clear distinction between the data before and after the meridian as a function of airmass. The airmass corrected raw fluxes then reveal the extent of the systematic error and a description of a series of tests is presented, which are aimed at understanding the origins of this *meridian feature*. We find that the systematic noise is a multiplicative signal that is different in shape between the 3 bands of ULTRACAM but similar in shape between all the stars in the same band. It is, however, sufficiently different such that a differential photometry approach is unable to correct for it. We find a direct correlation with parallactic angle, suggesting that it is related to the rotation of the field of view with respect to the telescope.

Despite being unable to reject any effects from the rotation of the telescope vignetting pattern with respect to the camera as a source of potential systematic errors, we find that the likely cause for the meridian feature is extra vignetting from the telescope's guide probe. A simple test performed by the ULTRACAM team reveals that, due to the wider field of view of the instrument when compared to the resident photometer at the NTT, the guide probe's angle of avoidance used for the observations of the planetary transits was not large enough to avoid the introduction of a vignetting pattern. This pattern is found to be dependent on the position of the guide probe with respect to the observed field, and it is particularly serious close to specific corners of the chip, depending on the position of the probe. We analyse the results of this test in more detail and find that the fractional decrease in flux across the CCD is different between the different bands and at a level consistent with the observed systematic errors found in the raw fluxes. We also find evidence of a spatial dependence of around 0.5 mmag between different locations on the chip for a given position of the guide probe. This level is also consistent with the amplitude of the residual systematic noise visible in the differential photometry light curves. We therefore conclude that the major contributor towards the systematic effects is likely to be extra vignetting from the telescope's guiding probe. It is still unclear

the reason for a difference in the strength of the vignetting between the different arms of the instrument, as this vignetting would be expected to be the same for all CCDs, since it is generated before the beam enters the camera. This may be due to any issues with the light splitting inside the instrument, and can explain the dramatic differences in the shapes of the meridian feature between each band. Moreover, the guiding probe can have an impact throughout the entire data set, and not simply at the closest approach to the local meridian, and thus these data are deemed unsuitable for measurements in the context of performing transmission photometry of the planets observed.

Using previously published parameters for WASP-17b [Anderson et al., 2011] and limb-darkening coefficients from the calculations by Claret & Bloemen [2011], we plot the differential magnitude light curves of this planet using 3 comparison stars for all 3 arms along side the model transit. This demonstrates that the systematic errors are strongly dependent on the choice of comparison star, but nevertheless the examples using each comparison star suggest a level of consistency which motivated a further test. The light curves were again fitted allowing the planetary radius to vary. The results show a distribution of planetary radii as a function of wavelength where the values are consistent with each other within the estimated errors, but also suggest a Rayleigh scattering dominated atmosphere with a broad NaI absorption feature for WASP-17b. The possibility that these data can be used to contribute to transit timing variation measurements is still to be assessed, provided care is taken to ensure that the shapes of the ingress and egress of the transits are not significantly affected by the systematic errors.

5.1.3 Observing strategy simulations

In Chapter 4 we describe the development of a software package designed to provide the NGTS consortium with a tool to make informed decisions regarding observing strategy choices. This should help maximise the chances of finding planets.

Sky coverage simulation

Since the project is designed to employ a staring strategy, where a given location on sky is observed for as long as possible before moving onto another, an informed choice must be made in order to minimise any idle telescope time and to maximise the quality of the observing conditions. The first aspect of this software package deals with this problem, attempting to calculate the number of hours per year the telescope is capable of observing for any given location on sky.

In order to tackle this question, information regarding the twilight times, weather conditions, galactic plane and lunar avoidance angle and the Moon's contribution to the sky background has been used to impose restrictions on observations. A given maximum zenith distance (adjustable) has been applied, which ultimately determines the number of observed field per year. Using a 60° maximum zenith distance implies that a minimum of 3 fields separated by 8 hours in RA are required. We find that the choice of fields around right ascensions of 13 hours is severely constrained by the presence of the proximity of the galactic plane and the lunar avoidance angle. We suggest a possible set of three locations that satisfy most conditions.

In early 2011 the SuperWASP North team decided to modify the observing strategy of the instrument to a staring mode in order to test the improvement in photometric precision over time scales comparable to the typical planetary transit as well as improve the instrument's sensitivity to longer period planets (up to 15 days). The team requested this software to be used in order to select the best field to observe during the months of March to June 2011. Using similar constraints applied to the SuperWASP North facility in the island of La Palma, Spain, the resulting plot shows the locations that are more likely to provide the maximum coverage under optimal conditions. Using this information, the team selected a specific pointing and observations were taken during the intended months, whose results are used in the analysis of the SuperWASP noise sources in Chapter 2.

Planet probability simulation

The second part of this software package is designed to calculate the probability of finding planets for a given location on sky as a function of the orbital period. Using the same restrictions as those used in the sky coverage simulation, and selecting a sampling rate based on an estimated time scale of interest, this software generates a phase coverage map, where every measurement contributes a point in phase for each period of interest. This map is then used to estimate the probability of finding a planet for each period by randomly placing windows of a transit duration along the entire phase. A given minimum exposure time inside a transit, as well as a minimum number of unique transits, is set as the detection requirement, thereby producing a probability curve for each strategy.

We improve the simulation by using equal steps in phase space to avoid under-sampling short periods and over-sampling the longer period range. This simulation can then be used to test how the probability of finding a specific type of planet depends upon changes in the strategy of the survey. We give many examples of

implementations of this code.

In particular, the choice of location for the telescopes is critically important to the success of the project. The possibility to commission the instrument at ESO's Paranal Observatory required authorisation from the scientific committee and, hence, justification of the scientific advantages over other sites was necessary. This simulation played a crucial part in that process, producing a plot of the planet probability function as a function of period for both Paranal and La Silla observatories, showing that the favourable weather conditions at Paranal lead to a factor of 2 higher probability of detecting planets in orbits of 15 days, with further improvements at higher periods.

5.2 Future work

The analysis of the SuperWASP detector maps has demonstrated that the current flat field strategy is introducing a source of systematic noise fixed in detector coordinates, potentially capable of imprinting daily transit like features into the light curves. We have argued that these could be partly responsible for the unmanageably large numbers of false positive integer day period planetary candidates submitted for visual inspection by the transit searching algorithms, which has prompted the SuperWASP team to force a rejection of any one and half-day period candidates. A potential test would be to use the detector maps to apply a correction to the light curves of a particular field and run the transit search algorithm without this rejection. The results can potentially reveal a significant decrease in the number of false positives with integer periods, making the project sensitive to planets in this range again.

Initial attempts to use the detector maps to correct for these features have revealed that the quality of the light curves in time scales of one hour is still not enough to be comparable with the typical correction the detector map can provide. However, the recent staring strategy data does indeed reach levels comparable with the noise in the detector maps, but the full data set for this year is yet to be available at this point. Due to this fact, the detector map produced for the 2011 year is limited by the lower data quantity and hence may not be suitable for this correction. Moreover, several fields must be tested for this hypothesis to be confirmed. A future project involves the use of the entire 2011 data set for the purpose of creating a detector map with comparable quality to previous years and re-attempt the analysis described in Section 2.6 for the 2011 data set.

Additionally, using the entire SuperWASP data set for any camera may pro-

duce a *master detector map*, which will contain features that are present throughout the lifetime of the instrument. This may result in a high S/N calibration tool for these systematic effects. Naturally, any features that show any temporal evolution will not be present, but nevertheless a substantial improvement to the light curves is possible.

The analysis of the systematic effects seen in the light curves of the planetary transits of WASP-15b and WASP-17b have shown that these data are unsuitable for the purpose of transmission studies. However, it is possible that they can be used for the purpose of transit timing variation measurements. ULTRACAM is particularly suited to this purpose, due to its high temporal resolution capability. This possibility is, however, dependent on determining whether the ingress/egress of the transits are particularly affected by the systematic noise present. Since this noise is highly dependent on which comparison star is chosen, a comparison of the results between light curves using each comparison star may reveal a level of consistency that would provide confidence that this is possible.

This data set can also potentially provide an improved ephemeris and period since the S/N in time scales of minutes is higher than any other previous observation of the primary transit for this planet.

The transit detection threshold in terms of a fixed exposure time inside the transit is potentially too simplistic in our simulations. We have explored the consequences of different detection threshold assumptions on the window function, but a more realistic approach can be used. Assuming a given stellar type and magnitude, calculations of the expected noise per measurement can be made using a model similar to that presented in Section 2.3. This would incorporate information on the airmass each photometric data point is taken through and its impact on the data quality, which the simulation currently does not take into account. Each simulated measurement would then have a corresponding photometric precision and the transit detection threshold could be defined in terms of the minimum required S/N, in such a way as to attribute a large weight to data points taken under optimal conditions. This method would also allow a direct comparison with preliminary results from the finished instrument. Alternatively, this software can be used in conjunction with other simulations that focus on the photometric precision for each target star.

Bibliography

Aerts, C., Christensen-Dalsgaard, J., Kurtz, D. W., 2010, Asteroseismology

Aigrain, S., Favata, F., 2002, A&A, 395, 625

Aigrain, S., Favata, F., Gilmore, G., 2004, A&A, 414, 1139

Akerlof, C., et al., 1999, Nature, 398, 400

Anderson, D. R., et al., 2010a, A&A, 513, L3

Anderson, D. R., et al., 2010b, ApJ, 709, 159

Anderson, D. R., et al., 2011, MNRAS, 416, 2108

Bahcall, J. N., Soneira, R. M., 1980, ApJS, 44, 73

Bakos, G. Á., Lázár, J., Papp, I., Sári, P., Green, E. M., 2002, PASP, 114, 974

Bakos, G. Á., et al., 2010, ApJ, 710, 1724

Batalha, N. M., et al., 2011, ApJ, 729, 27

Beatty, T. G., Gaudi, B. S., 2008, ApJ, 686, 1302

Beaulieu, J. P., et al., 2010, MNRAS, 409, 963

Beerer, I. M., et al., 2011, ApJ, 727, 23

Benedict, G. F., et al., 2002, ApJ, 581, L115

Benítez-Llambay, P., Masset, F., Beaugé, C., 2011, A&A, 528, A2

Benn, C. R., Ellison, S. L., 1998, New Astronomy Reviews, 42, 503

Bertin, E., Arnouts, S., 1996, A&AS, 117, 393

Birney, D., Gonzalez, G., Oesper, D., 2006, Observational Astronomy, Cambridge University Press, second edn.

Bodenheimer, P., Hubickyj, O., Lissauer, J. J., 2000, Icarus, 143, 2

Bond, I. A., et al., 2004, ApJ, 606, L155

Borsa, F., Poretti, E., 2012, Memorie della Societa Astronomica Italiana Supplementi, 20, 25

Borucki, W. J., et al., 2006, ISSI Scientific Reports Series, 6, 207

Borucki, W. J., et al., 2010a, ApJ, 713, L126

Borucki, W. J., et al., 2010b, Science, 327, 977

Borucki, W. J., et al., 2012a, ApJ, 745, 120

Borucki, W. J., et al., 2012b, ApJ, 745, 120

Brown, T. M., 2010, ApJ, 709, 535

Brown, T. M., Gilliland, R. L., 1994, ARA&A, 32, 37

Burrows, A., Sudarsky, D., Hubeny, I., 2004, ApJ, 609, 407

Burton, J. R., Watson, C. A., Littlefair, S. P., Dhillon, V. S., Gibson, N. P., Marsh, T. R., Pollacco, D., 2012, ArXiv e-prints

Butters, O. W., et al., 2010, A&A, 520, L10

Campo, C., et al., 2010, in AAS/Division for Planetary Sciences Meeting Abstracts #42, vol. 42 of *Bulletin of the American Astronomical Society*, p. 1091

Casertano, S., et al., 2008, A&A, 482, 699

Charbonneau, D., Brown, T. M., Latham, D. W., Mayor, M., 2000, ApJ, 529, L45

Charbonneau, D., Brown, T. M., Noyes, R. W., Gilliland, R. L., 2002, ApJ, 568, 377

Chauvin, G., Lagrange, A.-M., Dumas, C., Zuckerman, B., Mouillet, D., Song, I., Beuzit, J.-L., Lowrance, P., 2004, A&A, 425, L29

Christian, D. J., et al., 2006, MNRAS, 372, 1117

Claret, A., 2000, A&A, 363, 1081

Claret, A., Bloemen, S., 2011, A&A, 529, A75

Collier Cameron, A., Pollacco, D., Hellier, C., West, R., WASP Consortium, SOPHIE and CORALIE Planet-Search Teams, 2009, in IAU Symposium, vol. 253 of *IAU Symposium*, p. 29

Collier Cameron, A., et al., 2006, MNRAS, 373, 799

Collier Cameron, A., et al., 2010, MNRAS, 407, 507

Colón, K. D., Ford, E. B., Morehead, R. C., 2012, ArXiv e-prints

Cremonese, G., et al., 1997, ApJ, 490, L199

Croll, B., Lafreniere, D., Albert, L., Jayawardhana, R., Fortney, J. J., Murray, N., 2011, AJ, 141, 30

Crossfield, I. J. M., Hansen, B. M. S., Barman, T., 2012, ApJ, 746, 46

Cumming, A., 2004, MNRAS, 354, 1165

de Mooij, E. J. W., Snellen, I. A. G., 2009, A&A, 493, L35

de Mooij, E. J. W., de Kok, R. J., Nefs, S. V., Snellen, I. A. G., 2011, A&A, 528, A49

Deeg, H. J., Garrido, R., Claret, A., 2001, New Astronomy, 6, 51

Deming, D., Seager, S., Richardson, L. J., Harrington, J., 2005, Nature, 434, 740

Deming, D., et al., 2011, ApJ, 726, 95

Dhillon, V., Marsch, T., Ultracam Team, 2002, The Newsletter of the Isaac Newton Group of Telescopes, 6, 25

Dhillon, V. S., et al., 2007, MNRAS, 378, 825

Doyle, L. R., et al., 2011, Science, 333, 1602

Dravins, D., Lindegren, L., Mezey, E., Young, A. T., 1998, PASP, 110, 610

Dumusque, X., et al., 2011, A&A, 535, A55

Einstein, A., 1936, Science, 84, 506

Evans, J. W., et al., 2005, in Coulter, D. R., ed., Society of Photo-Optical Instrumentation Engineers (SPIE) Conference Series, vol. 5905 of *Society of Photo-Optical Instrumentation Engineers (SPIE) Conference Series*, p. 303

Evans, T. M., Sackett, P. D., 2010, ApJ, 712, 38

Everett, M. E., Howell, S. B., Kinemuchi, K., 2012, PASP, 124, 316

Faedi, F., West, R. G., Burleigh, M. R., Goad, M. R., Hebb, L., 2011, MNRAS, 410, 899

Ferguson, H., et al., 1995, in American Astronomical Society Meeting Abstracts, vol. 27 of *Bulletin of the American Astronomical Society*, p. 1294

Fleming, S. W., Kane, S. R., McCullough, P. R., Chromey, F. R., 2008, MNRAS, 386, 1503

Ford, E. B., Quinn, S. N., Veras, D., 2008, ApJ, 678, 1407

Ford, E. B., Colon, K. D., Blake, C., Lee, B., Mahadevan, S., 2010, in American Astronomical Society Meeting Abstracts #215, vol. 42 of *Bulletin of the American Astronomical Society*, p. #421.10

Fortney, J. J., Lodders, K., Marley, M. S., Freedman, R. S., 2008, ApJ, 678, 1419

Fossati, L., et al., 2010, ApJ, 714, L222

Fressin, F., et al., 2012, Nature, 482, 195

Garstang, R. H., 1989, PASP, 101, 306

Gautier, T. N., Kepler Science Team, 2010, in AAS/Division for Planetary Sciences Meeting Abstracts #42, vol. 42 of *Bulletin of the American Astronomical Society*, p. 1084

Gautier, III, T. N., et al., 2012, ApJ, 749, 15

Gibson, N. P., et al., 2010, MNRAS, 404, L114

Gilliland, R. L., McCullough, P. R., Nelan, E. P., Brown, T. M., Charbonneau, D., Nutzman, P., Christensen-Dalsgaard, J., Kjeldsen, H., 2011, ApJ, 726, 2

Gillon, M., Courbin, F., Magain, P., Borguet, B., 2005, A&A, 442, 731

Giorgini, J. D., et al., 1997, in M. F. Bietenholz, N. Bartel, M. P. Rupen, A. J. Beasley, D. A. Graham, V. I. Altunin, T. Venturi, G. Umana, & J. E. Conway, ed., Bulletin of the American Astronomical Society, vol. 29 of *Bulletin of the American Astronomical Society*, p. 1099

Greiss, S., et al., 2012, AJ, 144, 24

Harrington, J., Luszcz, S., Seager, S., Deming, D., Richardson, L. J., 2007, Nature, 447, 691

Hebb, L., et al., 2009, ApJ, 693, 1920

Hebb, L., et al., 2010, ApJ, 708, 224

Heller, R., Mislis, D., Antoniadis, J., 2009, A&A, 508, 1509

Hellier, C., Anderson, D. R., Collier-Cameron, A., Miller, G. R. M., Queloz, D., Smalley, B., Southworth, J., Triaud, A. H. M. J., 2011, ApJ, 730, L31

Hellier, C., et al., 2009, Nature, 460, 1098

Hellier, C., et al., 2010, ApJ, 723, L60

Henry, G. W., Marcy, G. W., Butler, R. P., Vogt, S. S., 2000, ApJ, 529, L41

Herrero, E., Morales, J. C., Ribas, I., Naves, R., 2011, A&A, 526, L10

Høg, E., et al., 2000, A&A, 355, L27

Holman, M. J., et al., 2010, Science, 330, 51

Horne, K., 2001, in Dent, W. R. F., ed., Techniques for the Detection of Planets and Life beyond the Solar System, p. 5

Horne, K., 2003, in Deming, D., Seager, S., eds., Scientific Frontiers in Research on Extrasolar Planets, vol. 294 of *Astronomical Society of the Pacific Conference Series*, p. 361

Howard, A., Marcy, G. W., Johnson, J. A., Morton, T. D., Isaacson, H., 2012, in American Astronomical Society Meeting Abstracts, vol. 219 of *American Astronomical Society Meeting Abstracts*, p. #405.01

Howard, A. W., et al., 2010, ApJ, 721, 1467

Howell, S. B., 2000, Handbook of CCD Astronomy, Cambridge University Press, first edn.

Hubbard, W. B., Fortney, J. J., Lunine, J. I., Burrows, A., Sudarsky, D., Pinto, P., 2001, ApJ, 560, 413

Huitson, C. M., Sing, D. K., Vidal-Madjar, A., Ballester, G. E., Lecavelier des Etangs, A., Désert, J.-M., Pont, F., 2012, MNRAS, 422, 2477

Ida, S., Lin, D. N. C., 2004, ApJ, 604, 388

Janesick, J., Blouke, M., 1987, S&T, 74, 238

Janson, M., Bergfors, C., Goto, M., Brandner, W., Lafrenière, D., 2010, ApJ, 710, L35

Kalas, P., Graham, J. R., Clampin, M., 2005, Nature, 435, 1067

Kalas, P., et al., 2008, Science, 322, 1345

Kane, S. R., 2007, MNRAS, 380, 1488

Kane, S. R., Collier Cameron, A., Horne, K., James, D., Lister, T. A., Pollacco, D. L., Street, R. A., Tsapras, Y., 2004, MNRAS, 353, 689

Kane, S. R., Collier Cameron, A., Horne, K., James, D., Lister, T. A., Pollacco, D. L., Street, R. A., Tsapras, Y., 2005, MNRAS, 364, 1091

Kane, S. R., Mahadevan, S., von Braun, K., Laughlin, G., Ciardi, D. R., 2009, PASP, 121, 1386

Kane, S. R., Ciardi, D. R., Gelino, D. M., von Braun, K., 2012, MNRAS, 425, 757

Kepler, J., 1619, Harmonices mundi libri V, Forni, reprint edn.

Kipping, D. M., 2008, MNRAS, 389, 1383

Knutson, H. A., Charbonneau, D., Noyes, R. W., Brown, T. M., Gilliland, R. L., 2007, ApJ, 655, 564

Knutson, H. A., Charbonneau, D., Allen, L. E., Burrows, A., Megeath, S. T., 2008, ApJ, 673, 526

Koch, D. G., et al., 2010, ApJ, 713, L79

Kovács, G., Zucker, S., Mazeh, T., 2002, A&A, 391, 369

Kovács, G., Bakos, G., Noyes, R. W., 2005, MNRAS, 356, 557

Krisciunas, K., Schaefer, B. E., 1991, PASP, 103, 1033

Kristensen, L. K., 1998, Astronomische Nachrichten, 319, 193

Laughlin, G., Chambers, J. E., 2001, ApJ, 551, L109

Lecavelier Des Etangs, A., Pont, F., Vidal-Madjar, A., Sing, D., 2008a, A&A, 481, L83

Lecavelier Des Etangs, A., Vidal-Madjar, A., Désert, J.-M., Sing, D., 2008b, A&A, 485, 865

Lindegren, L., 2009, American Astronomical Society, IAU Symposium #261. Relativity in Fundamental Astronomy: Dynamics, Reference Frames, and Data Analysis 27 April - 1 May 2009 Virginia Beach, VA, USA, #16.01; Bulletin of the American Astronomical Society, Vol. 41, p.890, 261, 1601

Lissauer, J. J., et al., 2011, Nature, 470, 53

Lissauer, J. J., et al., 2012, ApJ, 750, 112

Lister, T. A., et al., 2007, MNRAS, 379, 647

López-Morales, M., Coughlin, J. L., Sing, D. K., Burrows, A., Apai, D., Rogers, J. C., Spiegel, D. S., Adams, E. R., 2010, ApJ, 716, L36

Lynch, D., Livingston, W., 2001, Color and Light in Nature, Cambridge University Press, second edn.

Maciejewski, G., et al., 2010, MNRAS, 407, 2625

Mandel, K., Agol, E., 2002, ApJ, 580, L171

Manfroid, J., 1996, A&AS, 118, 391

Marois, C., Macintosh, B., Barman, T., Zuckerman, B., Song, I., Patience, J., Lafrenière, D., Doyon, R., 2008, Science, 322, 1348

Marois, C., Zuckerman, B., Konopacky, Q. M., Macintosh, B., Barman, T., 2010, Nature, 468, 1080

Martinez, P., Klotz, A., 1998, A Practical Guide to CCD Astronomy, Cambridge University Press, first edn.

Mattila, K., Vaeisaenen, P., Appen-Schnur, G. F. O. V., 1996, A&AS, 119, 153

Mayor, M., Queloz, D., 1995, Nature, 378, 355

Mayor, M., et al., 2003, The Messenger, 114, 20

Mayor, M., et al., 2011, ArXiv e-prints

Meschiari, S., 2012, ApJ, 752, 71

Michael, S., Durisen, R. H., Boley, A. C., 2011, ApJ, 737, L42

Migaszewski, C., Slonina, M., Gozdziewski, K., 2012, ArXiv e-prints

Milne, E. A., 1921, MNRAS, 81, 361

Moehler, S., Freudling, W., Møller, P., Patat, F., Rupprecht, G., O'Brien, K., 2010, PASP, 122, 93

Monet, D. G., et al., 2003, AJ, 125, 984

Mordasini, C., Alibert, Y., Benz, W., 2009a, A&A, 501, 1139

Mordasini, C., Alibert, Y., Benz, W., Naef, D., 2009b, A&A, 501, 1161

Morton, T. D., Johnson, J. A., 2011, ApJ, 738, 170

Moutou, C., et al., 2005, A&A, 437, 355

Narayan, R., Cumming, A., Lin, D. N. C., 2005, ApJ, 620, 1002

Narita, N., et al., 2005, PASJ, 57, 471

Newberry, M. V., 1992, in Worrall, D. M., Biemesderfer, C., Barnes, J., eds., Astronomical Data Analysis Software and Systems I, vol. 25 of *Astronomical Society of the Pacific Conference Series*, p. 307

Nymeyer, S., et al., 2011, ApJ, 742, 35

Ochsenbein, F., Bauer, P., Marcout, J., 2000, A&AS, 143, 23

O'Donovan, F. T., et al., 2006, ApJ, 651, L61

Oshagh, M., Haghighipour, N., Santos, N. C., 2011, in Sozzetti, A., Lattanzi, M. G., Boss, A. P., eds., IAU Symposium, vol. 276 of *IAU Symposium*, p. 448

Paardekooper, S.-J., Leinhardt, Z. M., Thebault, P., Baruteau, C., 2012, ArXiv e-prints

Paczynski, B., 1991, ApJ, 371, L63

Paczynski, B., 1996, ARA&A, 34, 419

Pál, A., et al., 2008, ApJ, 680, 1450

Patat, F., 2003, A&A, 400, 1183

Pepe, F., et al., 2000, in M. Iye & A. F. Moorwood, ed., Society of Photo-Optical Instrumentation Engineers (SPIE) Conference Series, vol. 4008 of *Society of Photo-Optical Instrumentation Engineers (SPIE) Conference Series*, p. 582

Pepe, F., et al., 2004, A&A, 423, 385

Perryman, M., 2011, The Exoplanet Handbook, Cambridge University Press, first edn.

Perryman, M. A. C., et al., 2001, A&A, 369, 339

Pollacco, D., et al., 2008, MNRAS, 385, 1576

Pollacco, D. L., et al., 2006, PASP, 118, 1407

Pont, F., Zucker, S., Queloz, D., 2006, MNRAS, 373, 231

Pont, F., Knutson, H., Gilliland, R. L., Moutou, C., Charbonneau, D., 2008, MNRAS, 385, 109

Pont, F., Husnoo, N., Mazeh, T., Fabrycky, D., 2011, MNRAS, 414, 1278

Pont, F., et al., 2007, in Afonso, C., Weldrake, D., Henning, T., eds., Transiting Extrapolar Planets Workshop, vol. 366 of *Astronomical Society of the Pacific Conference Series*, p. 3

Protopapas, P., Jimenez, R., Alcock, C., 2005, MNRAS, 362, 460

Quist, C. F., 2001, A&A, 370, 672

Ragozzine, D., Wolf, A. S., 2009, ApJ, 698, 1778

Redfield, S., Endl, M., Cochran, W. D., Koesterke, L., 2008, ApJ, 673, L87

Rozenberg, G. V., 1966, Twilight: A study in atmospheric optics, New York, Plenum Press, first edn.

Schaefer, B. E., 1990, PASP, 102, 212

Seager, S., 2010a, Exoplanet Atmospheres, Princeton University Press, first edn.

Seager, S., 2010b, Exoplanets, University of Arizona Press, first edn.

Seager, S., Mallén-Ornelas, G., 2003, ApJ, 585, 1038

Seager, S., Sasselov, D. D., 2000, ApJ, 537, 916

Ségransan, D., et al., 2011, A&A, 535, A54

Sing, D. K., López-Morales, M., 2009, A&A, 493, L31

Sing, D. K., Vidal-Madjar, A., Désert, J.-M., Lecavelier des Etangs, A., Ballester, G., 2008, ApJ, 686, 658

Sing, D. K., et al., 2011, MNRAS, 416, 1443

Smalley, B., et al., 2011, A&A, 526, A130

Smart, W. M., 1933, MNRAS, 94, 115

Smith, A. M. S., et al., 2006, MNRAS, 373, 1151

Snellen, I. A. G., Albrecht, S., de Mooij, E. J. W., Le Poole, R. S., 2008, A&A, 487, 357

Southworth, J., 2008, MNRAS, 386, 1644

Southworth, J., 2009, MNRAS, 394, 272

Southworth, J., 2010, MNRAS, 408, 1689

Southworth, J., et al., 2009, MNRAS, 396, 1023

Swain, M. R., et al., 2009, ApJ, 704, 1616

Szymański, M., Udalski, A., Kubiak, M., Pietrzyński, G., Soszyński, I., Woźniak, P., Zebruń, K., 2000, in R. E. Schielicke, ed., Astronomische Gesellschaft Meeting Abstracts, vol. 16 of *Astronomische Gesellschaft Meeting Abstracts*, p. 19

Tamuz, O., Mazeh, T., Zucker, S., 2005, MNRAS, 356, 1466

Tamuz, O., et al., 2008, A&A, 480, L33

Tingley, B., Sackett, P. D., 2005, ApJ, 627, 1011

Todorov, K., Deming, D., Harrington, J., Stevenson, K. B., Bowman, W. C., Nymeyer, S., Fortney, J. J., Bakos, G. A., 2010, ApJ, 708, 498

Tody, D., 1986, in D. L. Crawford, ed., Society of Photo-Optical Instrumentation Engineers (SPIE) Conference Series, vol. 627 of *Society of Photo-Optical Instrumentation Engineers (SPIE) Conference Series*, p. 733

Tody, D., 1993, in R. J. Hanisch, R. J. V. Brissenden, & J. Barnes, ed., Astronomical Data Analysis Software and Systems II, vol. 52 of *Astronomical Society of the Pacific Conference Series*, p. 173

Torres, G., et al., 2011, ApJ, 727, 24

Traub, W. A., 2012, ApJ, 745, 20

Vidal-Madjar, A., et al., 2011, A&A, 527, A110

Wambsganss, J., 1997, MNRAS, 284, 172

Welsh, W. F., et al., 2012, Nature, 481, 475

West, R. G., et al., 2009, AJ, 137, 4834

Willems, B., Kolb, U., Justham, S., 2006, MNRAS, 367, 1103

Winn, J. N., 2010, ArXiv e-prints

Wittenmyer, R. A., Tinney, C. G., Butler, R. P., O'Toole, S. J., Jones, H. R. A., Carter, B. D., Bailey, J., Horner, J., 2011, ApJ, 738, 81

Wolfgang, A., Laughlin, G., 2011, AGU Fall Meeting Abstracts, F6

Wolszczan, A., Frail, D. A., 1992, Nature, 355, 145

Wood, P. L., Maxted, P. F. L., Smalley, B., Iro, N., 2011, MNRAS, 412, 2376

Young, A. T., 1967, AJ, 72, 747

Zacharias, N., Monet, D. G., Levine, S. E., Urban, S. E., Gaume, R., Wycoff, G. L., 2005, VizieR Online Data Catalog, 1297, 0

Zacharias, N., et al., 2000, AJ, 120, 2131

Zhao, M., Monnier, J. D., Swain, M. R., Barman, T., Hinkley, S., 2012, ApJ, 744, 122